Imperial College London
Department of Earth Science & Engineering

Uplift and erosion histories of ancient and modern landscapes: examples from the North Sea, Iceland, and Mars

Gaia Stucky de Quay

A dissertation submitted in fulfilment of the requirements
for the degree of Doctor of Philosophy

June, 2018

Abstract

Ancient and modern landscapes contain records of vertical motions which can be used to probe histories of sub-surface processes. In this work I examine how rates of landscape evolution and styles of erosion can be determined using biostratigraphy and seismic data, cosmogenic dating techniques, and cratering on extra-terrestrial surfaces. I explore three examples, a buried landscape in the North Sea, a modern-day Icelandic river, and finally an example from Mars. First, I examine sedimentary basins fringing the North Atlantic Ocean, which contain excellent evidence that the continental shelf experienced episodic sub-aerial exposure. Stratigraphy, well logs, cores, and seismic data are used to reconstruct a 55 Ma terrestrial landscape buried 1.5 km beneath the North Sea. The best-fitting uplift rate history from extracted longitudinal profiles is staged, similar to that of a buried landscape in the nearby Faeroe-Shetland. These vertical motions are consistent with response to pulses from the incipient Icelandic plume. Secondly, I determine the erosional history of the modern Icelandic landscape. Today, the Icelandic plume is located beneath Iceland. Longitudinal river profiles across Iceland contain broad knickzones such as the Jökulsárgljúfur. High-resolution photogrammetry and ^{3}He exposure ages of terraces indicate retreat rates of $\sim$ 70 cm yr^{-1} in the Holocene. Calibrated drainage inversion indicates that rifting, dynamic support, and isostatic adjustment resulted in tens to hundreds of meters of modern uplift, and that progressive fluvial processes set the pace for erosion in volcanic, postglacial landscapes. Finally, preserved drainage patterns on Martian craters contain longitudinal profiles similar to fluvial terrestrial craters. However, an understanding of the effects of g, climatic and tectonic forcing, and valley formation timescales are lacking. A prominent example of drainage is Warrego Valles, a high-density dendritic system in southern Thaumasia. Spectral analyses indicate its power is greatest at $>$ 10 km wavelengths, and river inversions suggest it was uplifted by the Tharsis Bulge. The results of this work addresses key problems concerning longevity of topography and the roles of denudation, tectonics, and sub-surface processes. Uplift and erosion histories of the North Sea, Iceland, and Mars provide crucial constraints on dynamic support, mantle viscosity and temperature, closure of ocean gateways, rifting and magmatism, and surface processes on solar system bodies.

Declaration of Originality

I hereby declare that this work is original research undertaken by me and that no part of this thesis has been submitted for consideration towards another degree at this or any other institution. Any work in this thesis which is not my own work has been properly referenced.

Gaia Stucky de Quay
June, 2018

Copyright Declaration

The copyright of this thesis rests with the author and is made available under a Creative Commons Attribution Non-Commercial No Derivatives licence. Researchers are free to copy, distribute or transmit the thesis on the condition that they attribute it, that they do not use it for commercial purposes and that they do not alter, transform or build upon it. For any reuse or redistribution, researchers must make clear to others the licence terms of this work.

Gaia Stucky de Quay
June, 2018

Acknowledgements

First and foremost, my deepest appreciation goes to my primary supervisor Gareth Roberts, without which this work would have been not only impossible but also entirely inconceivable. I am indebted to his indispensable advice, constant encouragement, and most importantly, his enthusiastic assent to my indulging in as many study sites as I possibly could. I would like to thank my supervisors Chris Jackson, for his guidance in the North Sea, and Edwin Kite, for encouraging me to reach the final stages of my PhD as well as insightful Mars discussions. I am also grateful for Rebecca Bell's guidance and support as my assessor along the years. I am incredibly grateful to Victoria Fernandes for the inordinate amount of academic and social support provided. Having a field assistant that hand feeds you at regular intervals is a great way to brave the Icelandic weather. I would like to thank my research colleagues Bhavik Lodhia and Jennifer Quye-Sawyer for many helpful discussions to help us cope. I am eternally grateful to Dylan Rood for introducing me to the wonderful world of exposure dating, as well as Jordan Weddepohl and Alex Leggett for their tremendous assistance in the lab and the field. I would like to express my thanks for lab assistance from Jonathan Watson in the Imperial geochemistry lab, as well as Jonathan Treffkorn and Ken Farley for the opportunity to work in the Noble Gas Lab at Caltech. Funding, materials, and permits provided by NERC DTP, PGS, Statoil, BGS, the London Petrophysical Society, Vatnajökull National Park, and the Icelandic Institute for Natural History are immensely appreciated. I would not have made it through without the motivation and support provided by The Greenhouse/JAGER (Roan du Feu, Jone Bosch, Olyx Powell, and Eg), core Cohort 1 members of the NERC DTP (especially Clesh Kolster), and the UCL Earth Science / PHs crew. I would like to deeply thank my amazing family for providing me with the means and motivation to pursue my passion: my mother Bebelle Stucky de Quay for her loving support, my father José Luiz Moutinho for all but forcing me to love science since Day 1, my brother Yago de Quay for always inspiring me to catch up to him, my cousin and best friend Thaïs Bendixen for always believing in me, and my baby brother Theo Stucky who will hopefully be joining his siblings in academia one day.

Last but certainly not least (you even get your own personal page!) I would like to express my most heartfelt gratitude to Rasmus Severinsen and his unwavering support and encouragement throughout all these years, tusind tak min skat!

Contents

1 Introduction **1**
- 1.1 Background . . . 2
  - 1.1.1 Vertical motions & topography . . . 2
  - 1.1.2 Drainage networks as geological tape recorders . . . 3
  - 1.1.3 Landscape evolution principles . . . 4
- 1.2 Objectives . . . 6
- 1.3 Locations & motivation . . . 6
  - 1.3.1 The North Sea . . . 6
  - 1.3.2 Iceland . . . 7
  - 1.3.3 Mars . . . 7
- 1.4 Dissertation Structure . . . 8

2 North Sea drainage: stratigraphic, geochemical, and mapping constraints **10**
- 2.1 Chapter Introduction . . . 10
- 2.2 North Atlantic Ocean and dynamic support . . . 11
  - 2.2.1 Mantle convection and the North Atlantic Ocean . . . 11
  - 2.2.2 Transience of mantle convection . . . 13
  - 2.2.3 Spatial-temporal constraints of the incipient Icelandic plume 13
  - 2.2.4 Manifestations of plume activity in the northern North Sea 15
- 2.3 Stratigraphy of the northern North Sea . . . 17
  - 2.3.1 Sedimentary basins and regional vertical motions . . . 17
  - 2.3.2 The Bressay region . . . 17
  - 2.3.3 Well data . . . 18
  - 2.3.4 Age constraints from biostratigraphic dating . . . 21
- 2.4 Evidence for a terrestrial origin . . . 23
  - 2.4.1 Well cores and cuttings . . . 23
  - 2.4.2 Geochemical analyses . . . 25
  - 2.4.3 Organic matter origin . . . 26
- 2.5 Extracting an ancient buried landscape . . . 27
  - 2.5.1 Combining seismic and well data . . . 27
  - 2.5.2 Regional stratigraphy & Bressay Sandstone . . . 28
  - 2.5.3 Channel incision & 2D mapping . . . 30
  - 2.5.4 Bressay landscape in time . . . 31

2.6 Further evidence of uplift in the North Atlantic Ocean 33
2.6.1 North Bressay survey 34
2.6.2 Stratigraphy & mapping 34
2.6.3 Channel geomorphology 35
2.6.4 Bressay vs. North Bressay system 36
2.7 Chapter summary 37

3 Uplift history and geodynamics of the North Atlantic Ocean 39
3.1 Chapter Introduction 39
3.2 Reconstruction of sub-aerially exposed surface 40
3.2.1 Depth conversion 40
3.2.2 Decompaction 41
3.3 Drainage patterns & river extraction 43
3.3.1 Drainage extraction 43
3.3.2 Longitudinal river profile sensitivities 44
3.3.3 Seismic data and lithology along river 45
3.4 Uplift history & mechanisms 47
3.4.1 Uplift in the Bressay region 47
3.4.2 Inverting for uplift rate 47
3.4.3 Vertical motions of Bressay between 58–55 Ma 48
3.5 Generating uplift in the North Atlantic Ocean 49
3.5.1 Sources of uplift during Paleocene-Eocene 49
3.5.2 Temperature anomalies from the Icelandic plume 51
3.5.3 Staged uplift histories 52
3.5.4 Timing and origin of Icelandic plume pulses 53
3.6 Evidence for regional vertical motions in the North 54
3.7 Chapter Summary 57

4 Iceland fieldwork: geological mapping, sampling, and elevation models 60
4.1 Chapter Introduction 60
4.2 The modern Icelandic landscape 61
4.2.1 Geological setting 61
4.2.2 Glacial vs. fluvial signals 62
4.2.3 Drainage patterns 63
4.3 History of Jökulsá á Fjóllum 65
4.3.1 Jökulsá á Fjóllum and Jökulsárglúfur canyon system . . . 65
4.3.2 Evidence for fluvial erosion in Jökulsárglúfur 67
4.3.3 Rifting and the Northern Volcanic Zone 69
4.3.4 Deriving an erosion history of Jökulsárgljúfur 72
4.4 Sampling of fluvial terraces 73
4.4.1 Cosmogenic ^{3}He dating technique 73
4.4.2 Fieldwork and sampling in Jökulsárgljúfur 74
4.4.3 Sample corrections & field constraints 75

4.4.4 Location within lava flow . . . 76
4.4.5 Correction for non-cosmogenic sources . . . 78
4.4.6 Topographic shielding . . . 80
4.4.7 Ground cover . . . 80
4.5 High-resolution canyon model . . . 82
4.6 Chapter Summary . . . 83

5 Regional uplift in Iceland from fluvial erosion histories 85
5.1 Chapter Introduction . . . 85
5.2 Laboratory analyses of northeast Iceland samples . . . 85
5.2.1 Rock preparation . . . 87
5.2.2 Mineral separation techniques . . . 87
5.2.3 Noble gass mass spectrometry . . . 91
5.3 Exposure age calculations . . . 94
5.4 Erosion rate and knickzone history . . . 98
5.4.1 Waterfall retreat rates in Jökulsárgljúfur . . . 98
5.4.2 Knickzone generation . . . 101
5.5 Regional uplift history . . . 102
5.5.1 Calibration of Holocene erosion . . . 102
5.5.2 Drainage extraction and inversion . . . 103
5.5.3 Spatio-temporal patterns of uplift . . . 105
5.5.4 Measured uplift and canyon denudation . . . 107
5.5.5 Regional uplift sources . . . 108
5.6 Chapter Summary . . . 109

6 Drainage systems on Mars: planetary constraints on landscape evolution 111
6.1 Chapter Introduction . . . 111
6.2 Fluvial history and topographic evolution . . . 112
6.3 Elevation data & drainage mapping . . . 114
6.3.1 Data acquisition . . . 114
6.3.2 Dendritic valley networks . . . 116
6.3.3 Outburst floods . . . 116
6.3.4 Valley formation . . . 117
6.4 Crater drainage . . . 117
6.4.1 Eberswalde & Holden craters . . . 117
6.4.2 Terrestrial craters . . . 122
6.5 Warrego Valles . . . 125
6.5.1 Preserved dendritic drainage . . . 125
6.5.2 Spectral analysis . . . 127
6.5.3 Inverting for uplift history . . . 130
6.5.4 Uplift patterns and sources . . . 132
6.6 Chapter Summary . . . 132

7 Conclusions 135

References **138**

List of Figures

1.1 Schematic diagrams of drainage patterns and parameterss 5
1.2 Venn diagram of three study sites 8

2.1 North Atlantic Ocean topography 12
2.2 Evidence for dynamic support in the North Atlantic Ocean 14
2.3 Paleogeographic reconstruction of North Atlantic Ocean (55 Ma) 15
2.4 Bressay region and its surrounings in the northern North Sea . . . 16
2.5 Location of wells and BBK seismic survey 18
2.6 Well correlation for 7 wells 19
2.7 Paleocene-Eocene chronostratigraphy of Bressay and Judd regions 20
2.8 Gamma-ray data and cores for well 3/28a-4 23
2.9 Cores obtained from well 3/28a-4 at BGS 24
2.10 Geochemical analyses photo examples 25
2.11 GC-MS (partial mass chromatogram) oleanene peaks 26
2.12 Seismic variance and geomorphic features at 1400 ms 28
2.13 Interpreted seismic stratigraphy of the Bressay region 29
2.14 Location of interpreted channel cross-sections (1/2) 30
2.15 Location of interpreted channel cross-sections (2/2) 31
2.16 Extracted Bressay channel surface in two-way time 32
2.17 Geomorphic features in seismic variance of North Bressay 33
2.18 Interpreted seismic stratigraphy of the North Bressay region . . . 34
2.19 Extracted North Bressay channel surface in two-way time 36
2.20 Location of buried channels in the North Atlantic Ocean 38

3.1 Checkshot time-depth data for five wells 40
3.2 Decompaction parameters and porosity as a function of depth . . 41
3.3 Depth converted and decompacted Bressay landscape 42
3.4 Drainage networks in the Bressay region 43
3.5 Longitudinal profiles of rivers in the Bressay region 44
3.6 Longitudinal profiles as a function of geophysical uncertainties . 45
3.7 Seismic and stratigraphic data below Bressay river 46
3.8 Joint inversion for uplift history of two main Bressay tributaries . 49
3.9 Uplift histories for Bressay and Judd 50
3.10 Uplift as a function of excess temperature and low viscosity channel thickness 51

3.11 Reconstructed surface, drainage networks, and longitudinal profiles in North Bressay . . . 55
3.12 Uplift history from joint inversion four rivers in North Bressay . . 56
3.13 Cut-away cartoon of buried channels and the Icelandic plume system . . . 57

4.1 Map of Icelandic geology and topographic relief . . . 61
4.2 Glacial U-shaped valleys in the Trollaskagi Peninsula . . . 63
4.3 Glacial and fluvial erosional landforms in Jökulsá á Brú . . . 64
4.4 Longitudinal river profiles in Iceland . . . 65
4.5 Waterfalls in Iceland . . . 66
4.6 Cross-sections perpendicular to Jökulsá á Fjöllum . . . 66
4.7 Jökulsárgljúfur canyon geology and topography . . . 67
4.8 Three main waterfalls in Jökulsárgljúfur . . . 68
4.9 Examples of fluvial erosion (abrasion and plucking) along Jökulsárglúfur canyon terraces . . . 70
4.10 Columnar basalt morphologies in Jökulsárgljúfur . . . 71
4.11 Hydrological, tectonic, and volcanic structures in Jökulsárgljúfur 72
4.12 Cartoon showing production of ^{3}He from spallation due to cosmic rays . . . 73
4.13 Example sample site showing tools and rock extraction method . 75
4.14 Example of full vertical lava column stratigraphy . . . 76
4.15 Sampling surface of Terrace A within Flow I . . . 77
4.16 Sampling surface of Terrace B within Flow II . . . 78
4.17 Sampling surface of Terrace C within Flow III . . . 79
4.18 Location of shielded sample used for correction of cosmogenic ^{3}He in Jökulsárglúfur . . . 80
4.19 Measurements used to calculate topographic shielding at each sampling site . . . 81
4.20 Precipitation data for Jökulsárglúfur . . . 81
4.21 GPS survey and drone equipment and set-up used to generate UAV DEMs . . . 83
4.22 UAV orthomosaic imagery and elevation model . . . 84

5.1 Rock preparation room laboratory setup and samples . . . 86
5.2 Key stages of mineral separation techniques . . . 88
5.3 Stages of mineral content and quality of sample AE02 . . . 89
5.4 Stages of mineral content and quality of sample BW07 . . . 90
5.5 Laboratory setup at the Noble Gas Lab at Caltech . . . 92
5.6 Scaling factor S_{EL} for variation of production rates with elevation and latitude . . . 94
5.7 Exposure age differences from co-variations of cosmogenic ^{3}He dating parameters . . . 96
5.8 UAV orthomosaic cross-sections and high-resolution river profile 99
5.9 Exposure age of samples as a function of distance from Selfoss and Dettifoss . . . 100

5.10 Location of knickzone $\sim$ 10 ka at Hólmatungur 103
5.11 ASTER and LMÍ variations in drainage extraction 104
5.12 Inverse model spatial smoothing and m parameter tests 105
5.13 Model and observed river profiles from uplift model 106
5.14 Holocene landscape evolution of Iceland 107
5.15 Geological, seismic, tomographic and gravity observations of the Icelandic crust 109

6.1 Global map of Mars with example drainage locations 112
6.2 Examples of channel locations on Mars 115
6.3 Holden Crater drainage with HRSC imagery and elevation 118
6.4 Longitudinal profiles of extracted channels in Holden Crater . . . 119
6.5 Eberswalde Crater drainage with HRSC imagery and elevation . 120
6.6 Longitudinal profiles of extracted channels in Eberswalde Crater 121
6.7 Terrestrial craters in order of increasing size and age 123
6.8 Location of Warrego Valles channels over HRSC imagery. 125
6.9 Longitudinal profiles of extracted channels in Warrego Valles . . 126
6.10 Spectral analyses of Warrego river profile 127
6.11 Observed and model longitudinal profiles from joint inversion in Warrego Valles 130
6.12 2-D uplift history Warrego Valles 131
6.13 Schematic diagram of formation of Warrego Valles and uplift of the Thaumasia Rise 133

List of Tables

2.1 Dinocyst biomarkers of the Paleocene-Eocene boundary 22

5.1 Sample data used to measure cosmogenic ^{3}He exposure ages. . . 97

Chapter 1

Introduction

Understanding how topography grows, is maintained, and decays is a fundamental constraint on most geological processes. It is generally agreed that landscapes are controlled by a combination of sub-plate, tectonic, and erosional processes. As such, quantifying the history of landscape evolution as a function of time and space can provide important clues about the history of mantle convection and tectonic activity. Geological observations that constrain the history of mantle convection are sparse despite its importance in determining vertical and horizontal plate motions, plate rheology, and magmatism. A solution proposed to tackle this challenge is the use of drainage networks, which are systems capable of recording vertical motions on planetary crusts. River geometries have successfully been used to quantify uplift histories, and given the obvious difficulties in directly observing patterns of convective circulation, they provide an appealing means for probing otherwise difficult to measure sub-surface driving forces. Most geomorphological studies focus on present-day drainage systems due to their quantifiable erosional behaviour. I discuss three examples, one from a buried landscape beneath the North Sea, a second from modern-day Iceland, and finally an example from ancient Mars. These drainage systems attest to diverse geological settings and provide us with uplift and erosion histories in a variety of temporal frameworks from thousands to billions of years.

1.1 Background

1.1.1 Vertical motions & topography

Drainage networks have been used to record a variety of geological processes responsible for generating vertical motions such as mantle convection, plate tectonics, faulting, volcanism, glaciation, sea-level changes, climate forcing, and impact cratering (Hoorn et al., 1995; Blum and Törnqvist, 2000; d'Agostino et al., 2001; Mangerud et al., 2004; Rudge et al., 2008; Howard, 2007; Zhang et al., 2011). In this work I focus largely on plate tectonics and convection of the mantle, which are the main mechanisms for transporting heat from the core to the surface of a planet. However, despite their importance, the details of convective circulation and tectonics are not fully understood. Presently, the mantle can be studied through numerical or laboratory models, and results can then be compared to observations from geochemistry, seismology, and geomagnetism (Becker et al., 1999; Gurnis et al., 2000; Stixrude and Lithgow-Bertelloni, 2005; Tackley et al., 2005; Flament et al., 2014). It is also generally recognised that mantle flow can generate vertical motions of the crust, termed 'dynamic topography', across the entire surface of the planet (e.g. Pekeris, 1935; Hager et al., 1985; Forte et al., 1993; Daradich et al., 2003; Hoggard et al., 2017). Dynamic topography is a deformation present at the surface of the Earth which is supported by the vertical stresses at the base of the lithosphere resulting from the underlying flowing mantle (Moucha et al., 2008). This type of topography is in contrast to the more common mechanism of topography supported by crustal isostasy, which is in equilibrium at the surface and can exist even in a static mantle setting (Lithgow-Bertelloni and Silver, 1998). Thus, dynamic topography observed on planetary surfaces can provide clues as to convective circulation processes occurring beneath it. The effects of tectonic plate motions, which are driven my mantle convection, are also considered. By understanding the evolution of topography at the surface of the planet, it is possible to probe the underlying physics of the planetary sub-surface.

1.1.2 Drainage networks as geological tape recorders

Obtaining reliable quantitative estimates of vertical motions of the surface is limited in two ways: small dynamic signals are hard to detect, since uplift and subsidence at the surface are often caused by changes in crustal and lithospheric thickness, and uplift is isostatically amplified by erosion, resulting in poorly constrained denudation. Constraining processes such as uplift rate, rock cooling, and river incision can be estimated using different techniques, such as radiometric dating or sedimentary flux histories (Olsson, 1986; Kirby and Whipple, 2001; Whipple and Tucker, 2002). However, many of these estimates are spot measurements, and suffer from limited spatial coverage. As a result, there is an evident lack of methods for identifying large-scale dynamic topography patterns.

In actively deforming regions, the morphology and evolution of fluvial systems is regulated by surface uplift, and the uplift and tectonic history of these regions is recorded in the geometry of river systems (Gilbert and Murphy, 1914; Howard et al., 1970; Davies, 1974). One proxy for this is measuring longitudinal river profiles (i.e. the elevation of a river bed plotted as a function of distance along the river bed). For instance, in a tectonically stable region with uniform lithology, the river profiles are expected to have a smooth gradual profile extending to base level. Conversely, profiles with divergence from a smooth profile are usually given as evidence for phases of uplift affecting the drainage systems (Tanner, 1971; Stock and Montgomery, 1999; Kirby and Whipple, 2001; Perron and Royden, 2013). When a region is uplifted, there is a resulting rapid change in the gradient of the river near the mouth, or a 'knickpoint', and subsequent erosional processes cause this change in gradient to travel upstream, a process known as knickpoint retreat (Whipple and Tucker, 1999; Stock and Montgomery, 1999; Bishop et al., 2005; Crosby and Whipple, 2006; Pritchard et al., 2009). This suggests complex river profile geometries can provide us with uplift rates, and have been successfully employed as a tool for extracting rock uplift histories on various continents including South and North America, Australia, Europe, Africa, and Asia (Seeber and Gornitz, 1983; Kirby and Whipple, 2001; Cowie et al., 2008; Whittaker et al., 2008; Pritchard

et al., 2009; Roberts and White, 2010; Stephenson et al., 2014; Czarnota et al., 2014; Barnett-Moore et al., 2014; Grimaud et al., 2014; Thiede et al., 2014; Rudge et al., 2015; Glotzbach, 2015; Fox et al., 2015; Rodríguez Tribaldos et al., 2017). These landscape evolution models have been highly successful in quantifying uplift and erosion histories, in particular the inverse modelling of large drainage inventories, which is described below.

1.1.3 Landscape evolution principles

The form that river channels takes as a function of time can be expressed as an interplay between erosion rate, E, and uplift rate, U, which work to decrease and increase river elevations, respectively. The rate of change of elevation $z(x,t)$ at any point on the river can be described as,

$$\frac{\partial z}{\partial t} = U(x,t) - E(x,t) \tag{1.1}$$

where x is the downstream distance from the river source and t is time. The erosional term $E(x,t)$ parameterises a complex set of processes, which can be expressed using the empirical stream power law (Howard et al., 1970; Rosenbloom and Anderson, 1994; Whipple and Tucker, 1999). Thus we can express the rate of change of elevation as,

$$\frac{\partial z}{\partial t} = U(x,t) - vA(x)^m \left(\frac{\partial z}{\partial x}\right)^n + \kappa \frac{\partial^2 z}{\partial z^2} \tag{1.2}$$

where A is the upstream drainage area at any point in the river x, v is the advective constant, m and n are dimensionless erosional parameters, and κ is the rock diffusivity. It is widely agreed that advective retreat of knickzones predominates and that rock diffusivity plays a minor role in detachment-limited systems. See Figure 1.1 for visual explanation of observed drainage variables.

Many geomorphological studies concentrate on determining the values of v, m and n from steady-state river profiles. The value of n is much debated. If $n > 1$, shock wave behaviour is expected under certain circumstances as knickpoints retreat upstream (e.g. Pritchard et al., 2009). Previous work has shown that drainage inventories are best fit when $n \sim 1$, which is consistent with field observations (Whittaker et al., 2008; Paul et al., 2014; Czarnota et al.,

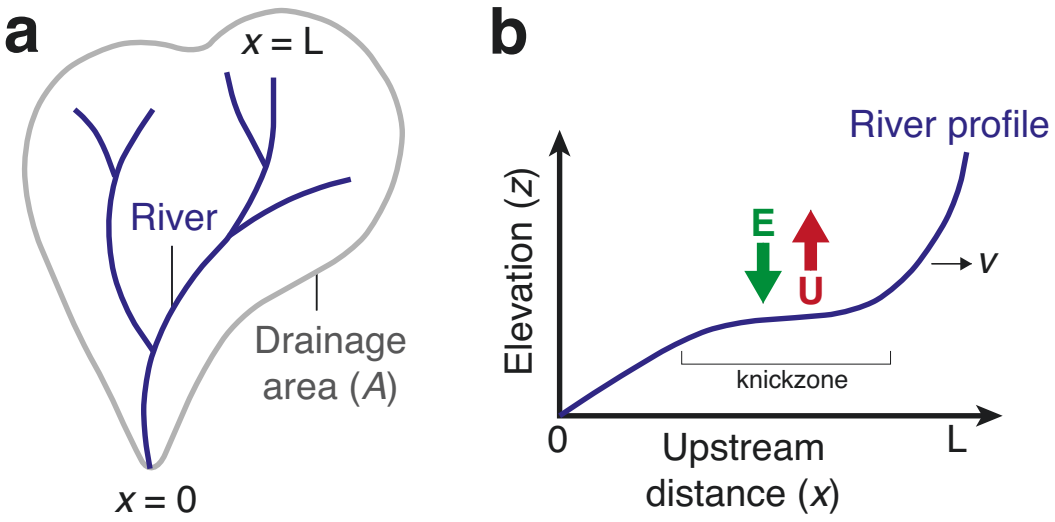


Figure 1.1: Schematic diagrams of drainage patterns and parameters. (a) Planform drainage basin and river channels. (b) Longitudinal profile of river, where driving forces U/E = uplift/erosion. Note departure from smooth graded river corresponds to knickzone. v = erosional parameter related to knickzone retreat velocity.

2014). Note that the term vA^m corresponds to knickzone velocity if n =1. It is argued that values of v and m are primarily controlled by climate, precipitation, bedrock lithology, and sediment transport mechanics (Roe et al., 2002; Murphy et al., 2016; Sklar and Dietrich, 1998; Gallen, 2018). This would suggest v and m could vary significantly over short timescales but can be assumed to be constant however over geological timescales (Paul et al., 2014; Czarnota et al., 2014; Wilson et al., 2014). Currently, slope-area analysis and chi-plots are generally the favoured means for determining values of v and m and their geographical variation (e.g. Schoenbohm et al., 2004; Perron and Royden, 2013). However, since v is related to the velocity of knickpoint retreat, it can be such can be accurately determined from either measured erosion rates or known constraints on landscape erosion duration.

To calculate uplift histories of landscapes, I adopt river inversion models which seek a smooth distribution of uplift rate as a function of space and time that minimize the misfit between suites of observed and calculated river profiles (Roberts and White, 2010; Rudge et al., 2015). For simplicity, this approach assumes that erosional parameters such as v and m do not vary on geologic timescales and are constant within the same drainage system (Paul et al., 2014;

Czarnota et al., 2014; Wilson et al., 2014). This inverse method for understanding landscape evolution is applied to all three drainage systems contained in this study, with parameters calibrated using a variety of techniques ranging from stratigraphy, exposure dating, and crater counting.

1.2 Objectives

This work aims to understand the geological, geodynamic, and geomorphological processes that shape planetary landscapes. It focuses on answering the following three key questions: **a)** How can we deconvolve and quantify erosional processes which shape dynamic landscapes? **b)** How can we use these erosional constraints to obtain uplift histories which vary over different time and length scales? **c)** How can these histories be used to shed light on the driving forces behind present and past landscape evolution? These problems are tackled by combining field studies (e.g. geological and digital mapping), laboratory techniques (e.g. organic geochemistry, cosmogenic dating) and theory (e.g. inverse modeling of fluvial erosion).

1.3 Locations & motivation

Each of the three landscapes in this work contain unique benefits and useful constraints which allow us to determine their uplift and erosion histories. Here I provide a summary of the chosen locations and outline their appeal as study sites for landscape evolution.

1.3.1 The North Sea

In the Bressay region of the northern North Sea, a terrestrial landscape is mapped and extracted which was formed 55 Ma and is now buried 1.5 km below the seabed. The abundant stratigraphic records, high resolution seismic data, and dense network of hydrocarbon wells and cores allow me to precisely determine the morphology, origin, age, and duration of this ancient buried landscape. In addition to this, its excellent preservation state means the original drainage network is highly representative of its shape when it was formed millions of years ago. Its important location on the fringe of the present-day

Icelandic plume suggests its history of vertical motions is most likely a manifestation of dynamic support, providing us with a window to mantle convective processes occurring in the Paleocene.

1.3.2 Iceland

In Iceland, large river networks are deeply incised into the volcanic and glacial landscapes which contain steep canyons, powerful waterfalls, and abundant tracts of preserved fluvial terraces. These accessible knickpoints and their associated terraces, such as Jökulárgljúfur in the northeast, provide an excellent means of quantifying knickpoint retreat rates in the present-day. The young, basaltic nature of the island implies that it is an excellent candidate for exposure dating using cosmogenic ^{3}He, which can be used to calibrate erosion histories. Its accessibility relative to the other study sites (i.e. on the surface of the Earth) allows for high-resolution elevation models of its topography to be constructed using drone technology. Its unique geological setting, both cut by a plate-spreading boundary and over a mantle plume, indicate that it is an exciting laboratory for deconvolving the driving forces acting behind its dramatic topography.

1.3.3 Mars

On Mars, the channels observed are ancient remnants attesting to a very different climate $>$ 3.5 Ga. Dendritic, precipitation-fed valley networks, such as Warrego Valles located south of the Tharsis Bulge, have been preserved due to the negligible atmosphere and volcanic resurfacing on Mars. On Earth, rapid erosion and resurfacing does not allow for preservation of such ancient channels, and so these billion year old channels are an extraordinary opportunity to investigate fluvial processes in a radically different planetary setting and era. Mars is also currently the only planet we know of that has had abundant water flowing on its surface and also to have undergone a complete, irreversible, global climate change. The abundance of high resolution orbital imagery with planet-wide coverage results in readily accessible topographic data. This can be combined with availability of crater count ages of structures to constrain

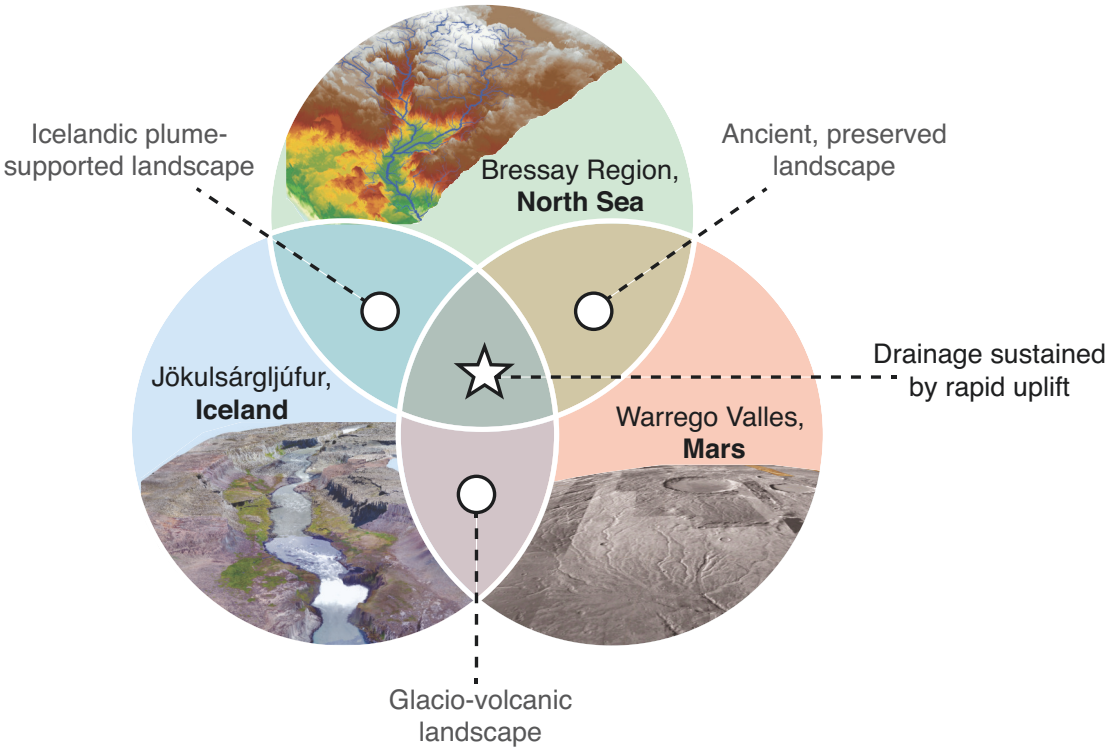


Figure 1.2: Schematic Venn diagram of three study sites included in this thesis and their commonalities: North Sea, Iceland, and Mars. Elevation models and imagery are described within the respective chapters.

large-scale processes which have shaped the martian surface.

Figure 1.2 summarises the commonalities of each of the three landscapes. Importantly, uplift and erosion histories of these regions allow us to test the limits of current landscape evolution models, which can in return help to improve their accuracy and increase the breadth of their applications.

1.4 Dissertation Structure

This dissertation is divided into seven chapters, where the first and last chapters are the introduction and conclusion of the thesis, respectively. The five central chapters are arranged according to the three areas of study: the North Sea (Chapters 2 & 3), Iceland (Chapters 4 & 5), and Mars (Chapter 6). **Chapter 2** focuses on the stratigraphic and biostratigraphic analyses, organic matter geochemistry, and seismic mapping of the buried Bressay landscape into order

to determine the timing, origin, and shape of the ancient landscape. **Chapter 3** then uses this extracted elevation model and combines it with geophysical and geomorphic analyses to reconstruct the surface drainage at the time of exposure. By applying 1-D inverse modelling of river channels, an uplift history is determined which is linked to dynamic support from the Icelandic plume in the Late Paleocene. **Chapter 4** investigates the landscape of the Icelandic drainage system which presently sits on the Icelandic plume. This chapter focusses on field observations from geological mapping, fluvial terrace sampling, and in-situ UAV elevation models. **Chapter 5** outlines the laboratory analyses undertaken to determine ages of fluvial terraces in northeast Iceland, and combines these with generated elevation models to constrain erosion and 2-D uplift histories, underlining the importance of progressive fluvial action in eroding the strongly glaciated, volcanic landscapes. Lastly, **Chapter 6** explores fluvially dissected craters and drainage systems in the volcanic, uplifted southern highlands of Mars. River geometries, analogous to those observed on Earth, show 2-D uplift patterns consistent with uplift radiating from the Tharsis Bulge volcanic centre. The conclusion synthesises the chapters, focussing on the key connection between landscape evolution and sub-surface processes.

Chapter 2

North Sea drainage: stratigraphic, geochemical, and mapping constraints

2.1 Chapter Introduction

Mantle convection and its interaction with the lithosphere are determinants of plate motion, lithospheric rheology, regional uplift and erosion, and magmatism (Schubert et al., 2001; Braun, 2010). The generation of volcanism and rock uplift by mantle convection impacts the circulation and chemistry of the atmosphere and oceans (Sinton and Duncan, 1997; Pálfy and Smith, 2000; Weissert and Erba, 2004). Epeirogenic uplift and erosion generated by mantle convection can determine sedimentary flux histories, which in turn control distribution and evolution of natural resources (e.g. White and Lovell, 1997; Dam et al., 1998; Anell et al., 2009; Poore et al., 2011). Gravity data, seismic imaging, and the location and chemistry of young magmatism provide information about the present-day state of the mantle (e.g. McKenzie, 2010; Rickers et al., 2013; Matthews et al., 2016). Residuals from ocean-age depth measurements indicate that most modern sub-plate support has amplitudes of ± 1 km at wavelengths of 10^3 km. Positive anomalies of 1–2 km are present at wavelengths up to 2500 km close to the Icelandic, Hawaiian, Azorean, and Afar plumes (Hoggard et al., 2016). A sparse suite of uplift and denudation measurements of dynamically supported topography and the history of magmatism contain important clues about the temporal evolution of mantle convection (e.g. White and McKenzie, 1989; Rudge et al., 2008; Hartley et al., 2011; Czarnota et al., 2013; Rowley et al.,

2013).

In this chapter I use a suite of geological observations from the northern North Sea to map a Paleocene-Eocene buried terrestrial landscape, which, combined with geophysical methods presented in Chapter 3, constrain the evolution of the incipient Icelandic plume. Well data and a three-dimensional seismic survey are used to reconstruct a 58–55 Ma landscape now buried $\sim$1.5 km beneath the seabed in the Bressay region (Figure 2.1). Geochemical analyses of cuttings from wells that intersect the landscape indicate the presence of angiosperm debris. These observations, combined with presence of coarse clastic material, interpreted beach ridges, and a large dendritic drainage network, indicate that this landscape formed subaerially. Presence of multiple buried terrestrial landscapes in observed seismic dataset suggest that Cenozoic uplift events were widespread suggesting the spatio-temporal history of uplift across the North Atlantic Ocean can be mapped.

2.2 North Atlantic Ocean and dynamic support

2.2.1 Mantle convection and the North Atlantic Ocean

The history of mantle convection is probably best understood beneath the North Atlantic Ocean and its surroundings where a combination of seismic, topographic, magmatic, thermochronological, and stratigraphic analyses constrain evolution of sub-plate support (e.g. Lawver and Müller, 1994; Japsen and Chalmers, 2000; Jones et al., 2002b; Mudge and Jones, 2004; Storey et al., 2007; Rickers et al., 2013). Figure 2.2 shows regional dynamic topography calculated using long-wavelength (>800 km) free-air gravity anomalies extracted from the GOCE dataset and admittance of 35 mGal km^{-1} (Jones et al., 2002a; Förste et al., 2014). These calculations are broadly consistent with residual ocean-age depth measurements, which indicate that dynamically supported topography of $\sim$2 km is centered on Iceland (Figure 2.2; Hoggard et al., 2016). Positive anomalies extend east to the British Isles and Scandinavian Mountains and west to Greenland. Rickers et al. (2013)'s full-waveform S-velocity model has slow velocity perturbations, -2 to -9% relative to a modified version of the

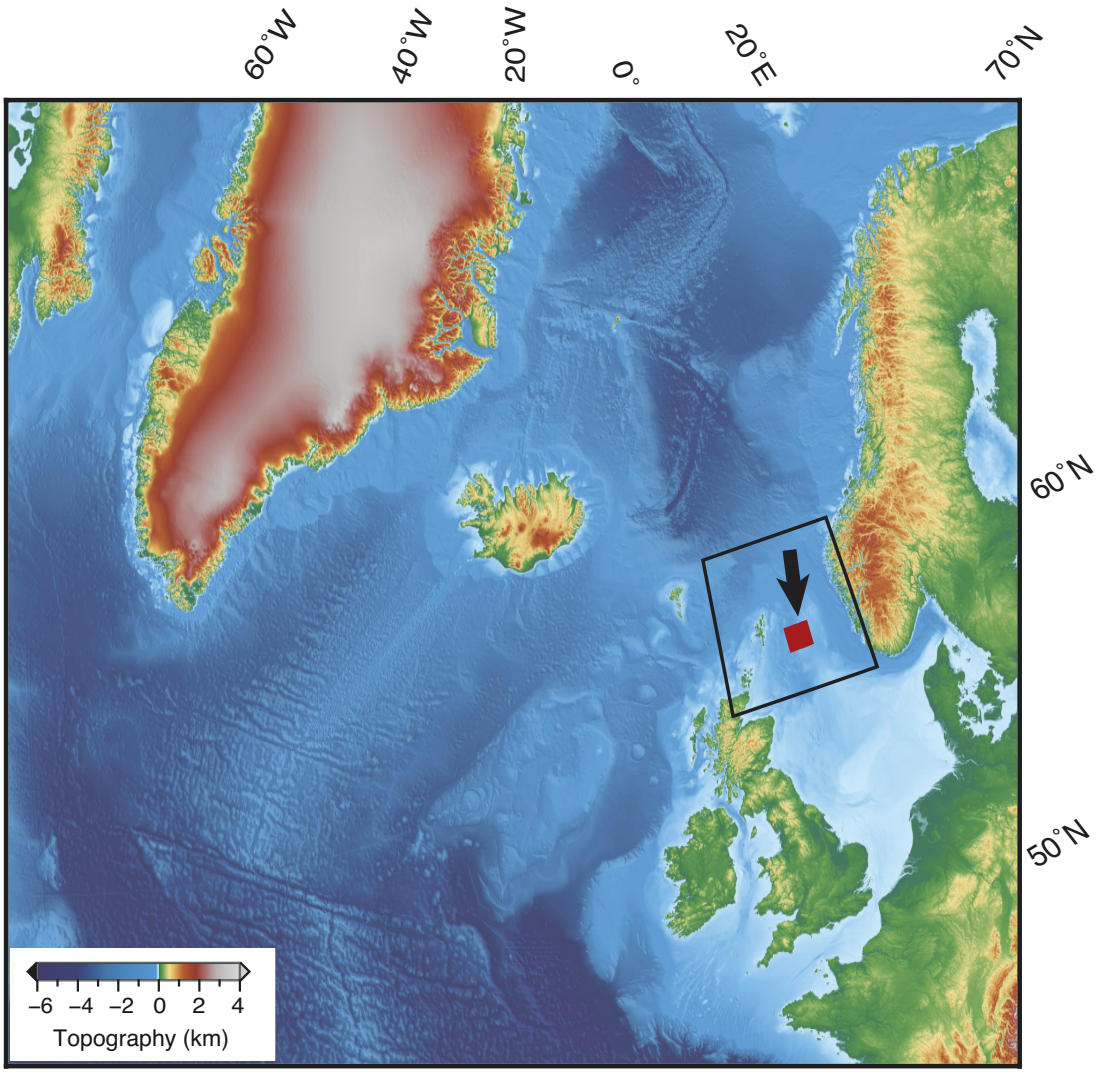


Figure 2.1: Topography of the North Atlantic Ocean. Red square = Bressay study region. (Smith and Sandwell, 1997). Black square = Figure 2.4.

Preliminary Reference Earth Model (PREM), located directly beneath the plate below Iceland, along the Mid-Atlantic ridge, and in promontories that extend to the British Isles and Scandinavia (Dziewonski and Anderson, 1981). These observations indicate that anomalously warm mantle extends >1000 km away from the Icelandic plume today. Recent work has shown that the complex irregular planform shape of the plume (as opposed to a symmetrical, radial extent) is a result of viscous fingering which occurs when a less viscous fluid is injected into a more viscous fluid (Schoonman et al., 2017). The location of thickest oceanic crust, gravity anomalies, shallow low-velocity anomalies in the upper mantle, earthquake hypocenters, intraplate volcanism, and high

$^3He/^4He$ concentrations suggest the center of the plume is close to 65° N, 18° W today (Oskarsson et al., 1985; Einarsson, 1991; Thorbergsson et al., 1993; Breddam et al., 2000; Darbyshire et al., 2000; Allen et al., 2002; Shorttle et al., 2010). The combination of receiver functions, wide-angle seismic data, ocean age-depth residuals, gravity data, and tomographic models indicate that the Icelandic plume supports up to 2 km of modern topography from Greenland to Norway (Figure 2.2; Darbyshire et al., 2000; Jones et al., 2002a; Rickers et al., 2013; Hoggard et al., 2016).

2.2.2 Transience of mantle convection

Given that the Rayleigh number of Earth's mantle is 10^6–10^8, sub-plate support of topography is expected to be time-dependent (e.g. White and McKenzie, 1995). This time-dependent behaviour will punctuate histories of vertical motion generated by lithospheric shortening, stretching and loading (Sclater and Christie, 1980; White and McKenzie, 1989; Medvedev et al., 2013; Green et al., 2013). Seismic and multibeam imaging, gravity data, and geochemical modeling of dredged basalts from oceanic crust close to Iceland record 55–0 Ma of transient plume behaviour (Vogt, 1971; Jones et al., 2002b; Parkin et al., 2007; Parnell-Turner et al., 2014). These observations indicate that transient thermal anomalies occurred every 3–8 Ma and that buoyancy flux has varied through time. The transient behaviour of the plume provides an explanation for punctuated Cenozoic uplift and subsidence of fringing sedimentary basins (e.g. northern North Sea), development of ephemeral landscapes, sedimentary drift and flux histories, magmatism, and oceanic circulation (e.g. Jones and Milton, 1994; Liu and Galloway, 1997; Japsen and Chalmers, 2000; Underhill, 2001; Jones et al., 2002a; Mudge and Jones, 2004; Shaw Champion et al., 2008; Anell et al., 2009; Poore et al., 2009, 2011; Hartley et al., 2011).

2.2.3 Spatial-temporal constraints of the incipient Icelandic plume

The present-day distribution of Early Paleocene igneous rocks suggests that the Icelandic plume extended up to 1000 km away from its centre in southeast Greenland, which is similar to its present-day extent (White and McKenzie,

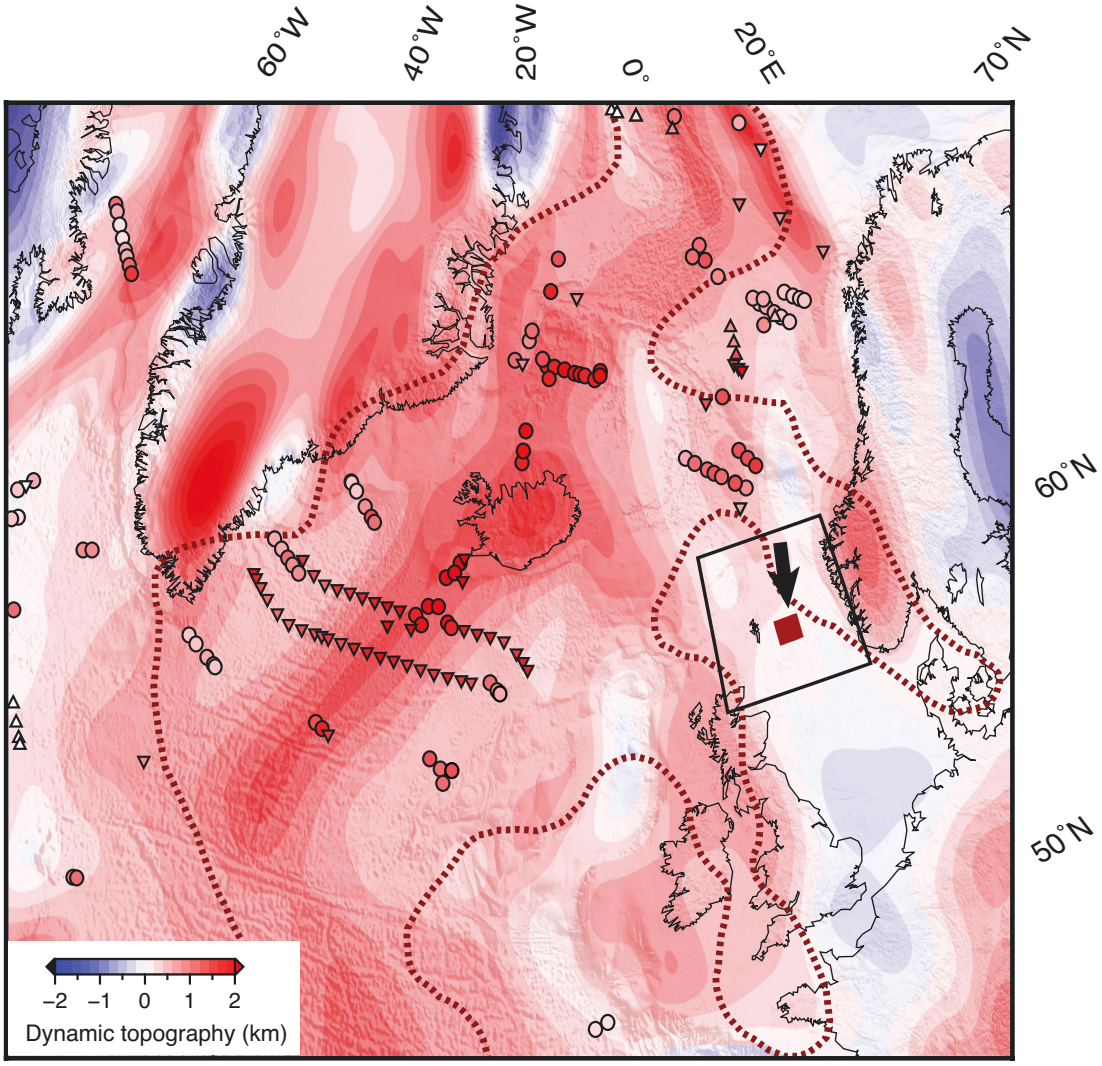


Figure 2.2: Dynamic support of the North Atlantic Ocean calculated using long-wavelength (>800 km) free-air gravity anomalies (obtained from GOCE; Förste et al., 2014) and a constant admittance of Z = 35 mGal km^{-1} appropriate for sub-aqueous regions (Jones et al., 2002a). Dashed red line encompasses S-velocity perturbation <-2% between 100 km and 200 km depth (Rickers et al., 2013). Circles = residual topography from age-depth measurements; upward/downward pointing triangles = minimum/maximum values (Hoggard et al., 2016). Red square = Bressay study region. Black square = Figure 2.4.

1989). Aluminium-in-olivine thermobarometry of a suite of ~61 Ma North Atlantic picrites indicates that the Paleocene Icelandic plume had an excess temperature up to 300 °C (Spice et al., 2016). Other Paleocene-Eocene plume centres have been proposed based on models of plate motion and continental stratigraphy, which place the plume in central Greenland or offshore southern Greenland (see Figure 2.3; Lawver and Müller, 1994; Jones and White, 2003).

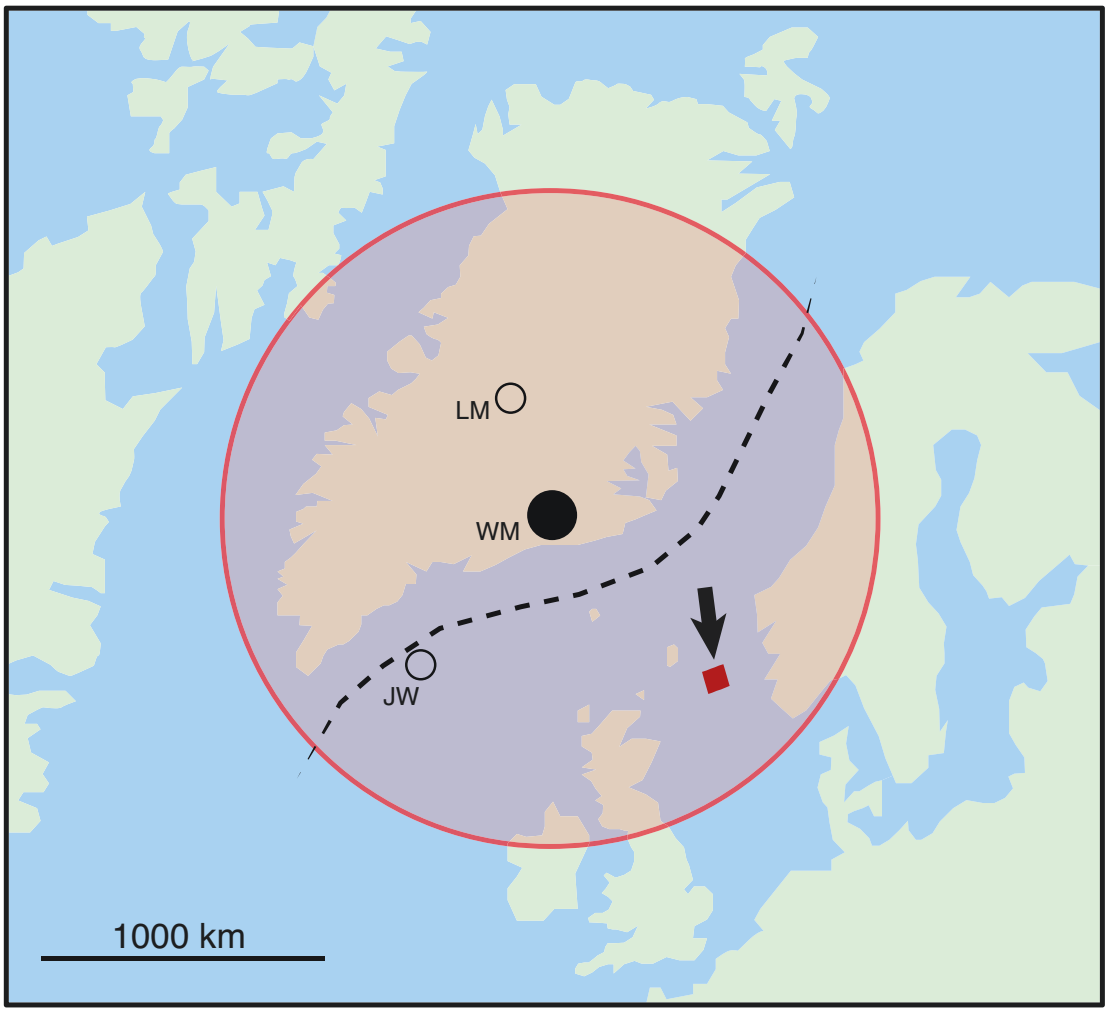


Figure 2.3: Simplified reconstruction of the North Atlantic Ocean at 55 Ma. Black circle labeled WM = centre of White and McKenzie (1989) Icelandic plume; open circles labeled LM/JW = Lawver and Müller (1994)/Jones and White (2003) plume centres; red transparent circle = approximate extent of idealised axissymetric plume; dashed black line = location of continental break-up (White and McKenzie, 1989). Red square = Bressay study region.

2.2.4 Manifestations of plume activity in the northern North Sea

Figure 2.4 illustrates the present-day distribution of Paleocene and Lower Eocene sedimentary and igneous rock in the northern North Sea (Mudge, 2015). The Faeroe Platform is covered by Paleocene lavas. The seismic dataset provided for this study (described in Section 2.5) is located in the Bressay region, which sits on the eastern edge of the deltaic Dornoch Formation. It is flanked by the East Shetland Platform and the Viking Graben. The West and East

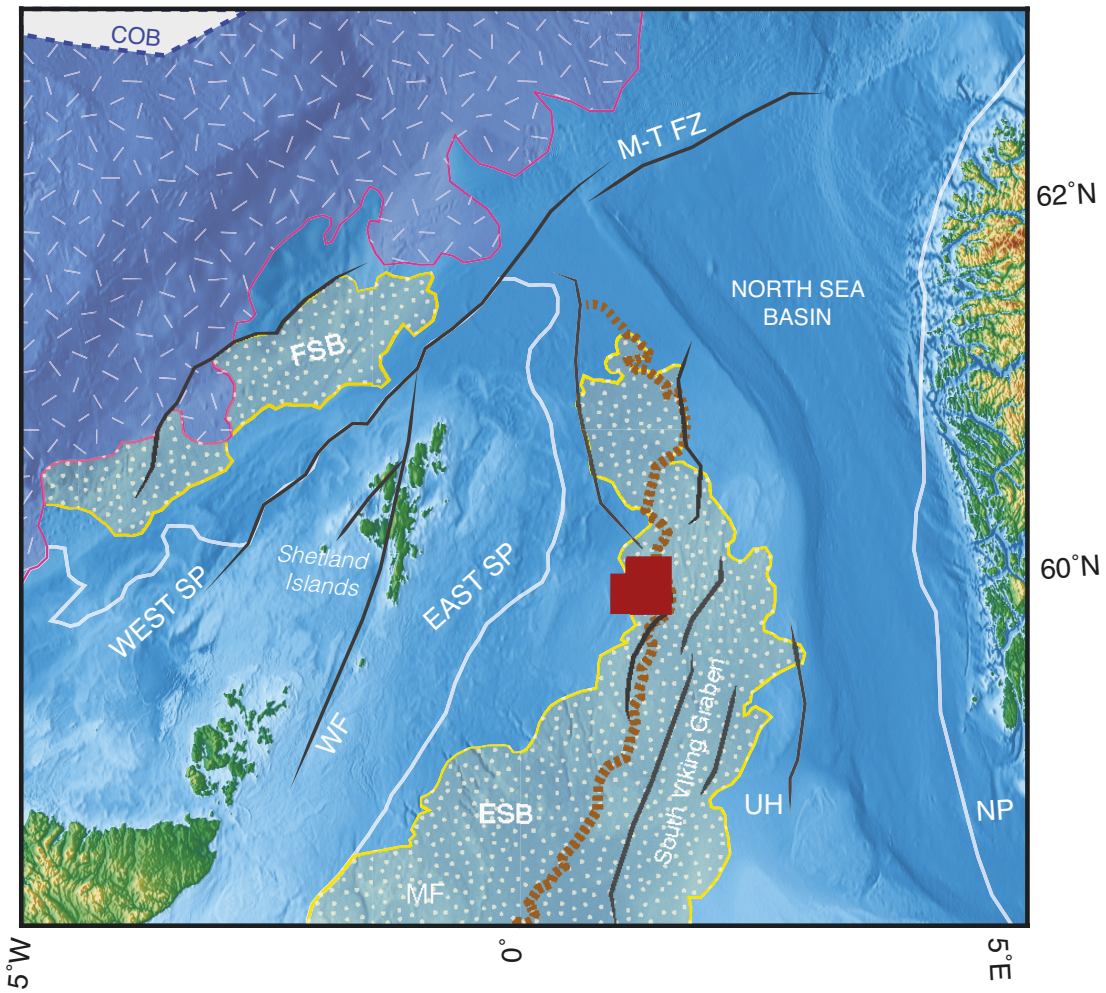


Figure 2.4: Bressay region and its surroundings. Red box = 3D seismic dataset. Yellow stippled areas = slope and basin sands; pink edged polygon = Paleocene lavas; orange dashed line = eastern limit of the Dornoch delta; black lines = faults; COB = continent-ocean boundary, ESB = East Shetland Basin, FSB = Faeroe-Shetland Basin, SP = Shetland Platform, M-T FZ = Møre-Trøndelag Fault Zone, NP = Norwegian Platform, WF = Walls Fault, UH = Utsira High (Mudge, 2015).

Shetland platforms, and the Norwegian platform are devoid of Paleocene or Eocene sedimentary rock (Mudge and Bujak, 2001). The next section discusses the stratigraphy of the North Atlantic Ocean and the constrains on the timing and duration of vertical motions during the Paleocene-Eocene.

2.3 Stratigraphy of the northern North Sea

2.3.1 Sedimentary basins and regional vertical motions

Sedimentary basins in the North Atlantic Ocean reveal stratigraphic sequences in which transient vertical motions (uplift and subsidence) can be observed and quantified (Rudge et al., 2008; Hartley et al., 2011). The Faeroe-Shetland, Moray Firth, and North Sea basins contain coarse Paleocene-Eocene terrestrial sandstones sandwiched between marine mudstones. These observations indicate that these regions experienced a short-lived (< 3 Ma) history of marine-terrestrial-marine conditions close to the Paleocene-Eocene boundary (Mudge and Bujak, 2001; Underhill, 2001; Mudge and Jones, 2004; Mackay et al., 2005; Shaw Champion et al., 2008). In the Judd region of the Faeroe-Shetland Basin, north of Scotland, an erosional unconformity has been mapped at the base of the coarse sandstone Flett Formation. Depth conversion and decompaction of infilling stratigraphy and recorded lignite suggests that the unconformity was created by erosion of a terrestrial landscape with at least 900 m of relief (Shaw Champion et al., 2008; Hartley et al., 2011). Dinoflagellate and pollen chronostratigraphy indicate that this landscape formed at close to 55 Ma. Longitudinal profiles extracted from this surface have almost 1 km of relief and contain three large ($>$ 100 m of relief) knickzones (Hartley et al., 2011).

2.3.2 The Bressay region

A slightly younger and lower relief ($<$300 m) landscape was mapped in the Bressay region using seismic and well data by Underhill (2001). The Bressay region is located on the East Shetland Platform of the northern North Sea. Buried extensional faults and backstripped well data indicate that the East Shetland platform was stretched by a factor $\beta = 1.3 \pm 0.04$ from the Late Jurassic for $\sim$60 Ma (White, 1990; Underhill, 2001). It currently sits on the eastern fringe of the Icelandic plume (Figure 2.3). In this section, gamma-ray data, stratigraphic charts, and biostratigraphic records are combined to generate a stratigraphic framework for the upper 1.5 km of the Bressay region. The following subsection summarises the lithostratigraphy of the Bressay region based on well

reports and published work using the nomenclature of Knox and Holloway (1992) and Underhill (2001).

2.3.3 Well data

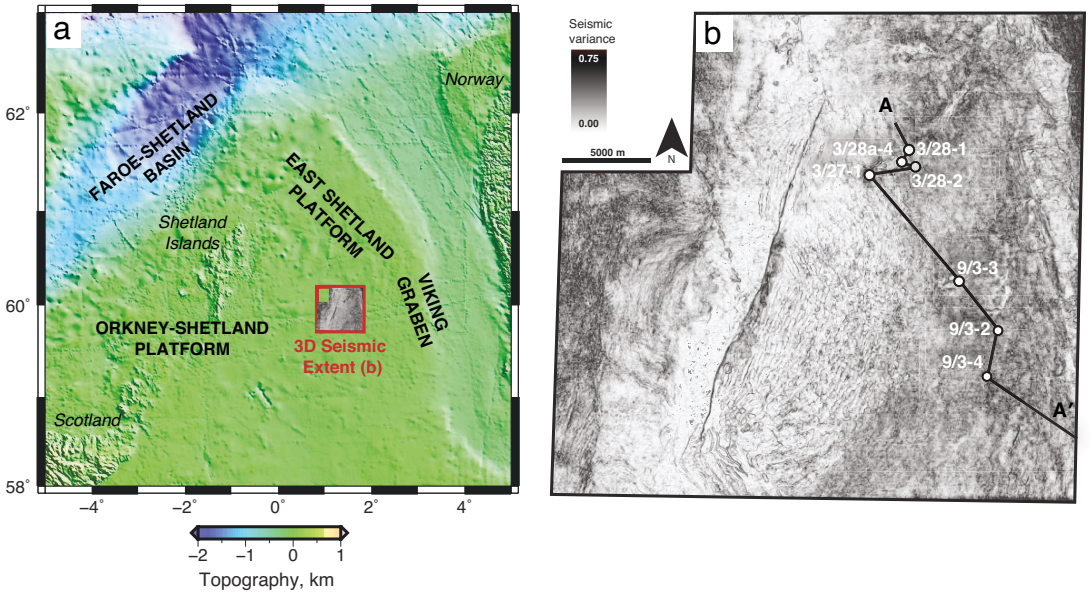


Figure 2.5: (a) Location of the BBK seismic survey and study site relative to North Sea bathymetry (Smith and Sandwell, 1997). (b) Depth-slice of seismic variance (trace-to-trace variability) at 1400 ms from 3-D seismic volume outlined in red in a). White circles = wells used in this study. Regional cross-section along wells = A–A′ (see Figure 2.6).

The location of 7 exploration wells provided by PGS (Petroleum GeoServices) are illustrated in Figure 2.5: 3/27-1, 3/28-1, 3/28-2, 3/28a-4, 9/3-2, 9/3-3, 9/3-4. The locations of the wells are shown relative to the extent of the Bressay seismic survey (BBK). Seismic data are addressed in detail in Section 2.5. A well correlation along the A–A′ line is shown in Figure 2.6. A more detailed study of the Paleocene-Eocene boundary is shown in Figure 2.7 for both the Judd and Bressay regions. At the bottom of the stratigraphy in Figure 2.7, the boundary between the Chalk Group and the overlying Paleocene Montrose Group records the onset of Cenozoic clastic deposition in the basin. The base of the Montrose Group has successions of interbedded chalk and local sandstone. The group is subdivided into the Maureen and Lista Formations. The Lista Formation contains sand accumulations separated by pelagic muds, and the Maureen Formation is generally indicated by a downward change into more

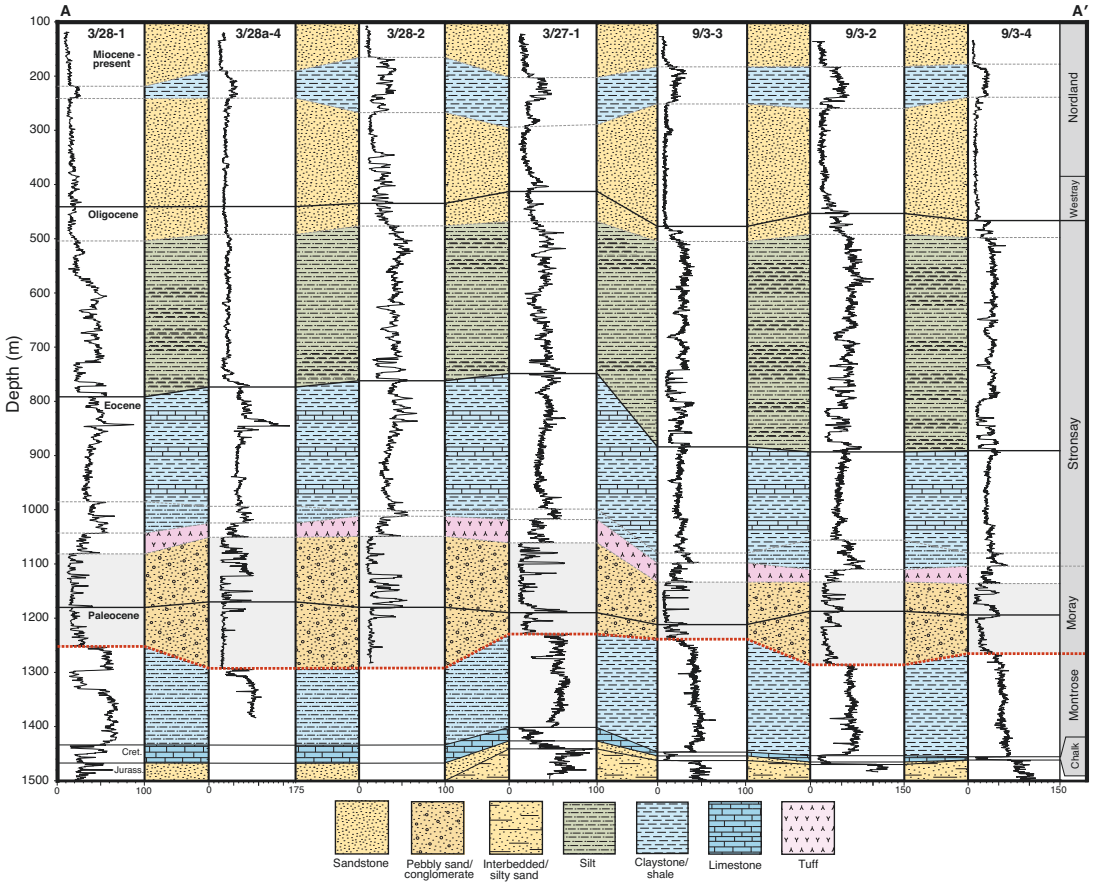


Figure 2.6: Gamma-ray data for 7 wells shown along A–A′ line in Figure 2.5. Dashed grey lines = lithological boundaries; solid black lines = age boundaries; red line = erosional surface.

calcareous sandstone, reworked limestone, or marl (Knox and Holloway, 1992).

The Lista Formation has a sharp contact with the overlying Moray Group. These units are conformable in wells 9/3-2, 9/3-3 and 9/3-4 (see red boundary in Figure 2.6 and). In wells 3/27-1, 3/28-1, 3/28-2 and 3/28a-4 the marine mudstones of the Lista Formation are unconformably in contact with overlying coarse-grained, well-rounded, poorly sorted sandstone and pebbly sandstone containing wood fragments. Heavily oil-stained mudstones occur intermittently throughout this section, which contains the Dornoch Formation and the Bressay Sandstone (see Section 2.4 for detailed core information). Underhill (2001) suggested that the pebbly sandstone facies of the Bressay Sandstone are the basal fluvial infill of incised channels. The Bressay Sandstone's stratigraphic position relative to the deltaic Dornoch Formation is a crucial con-

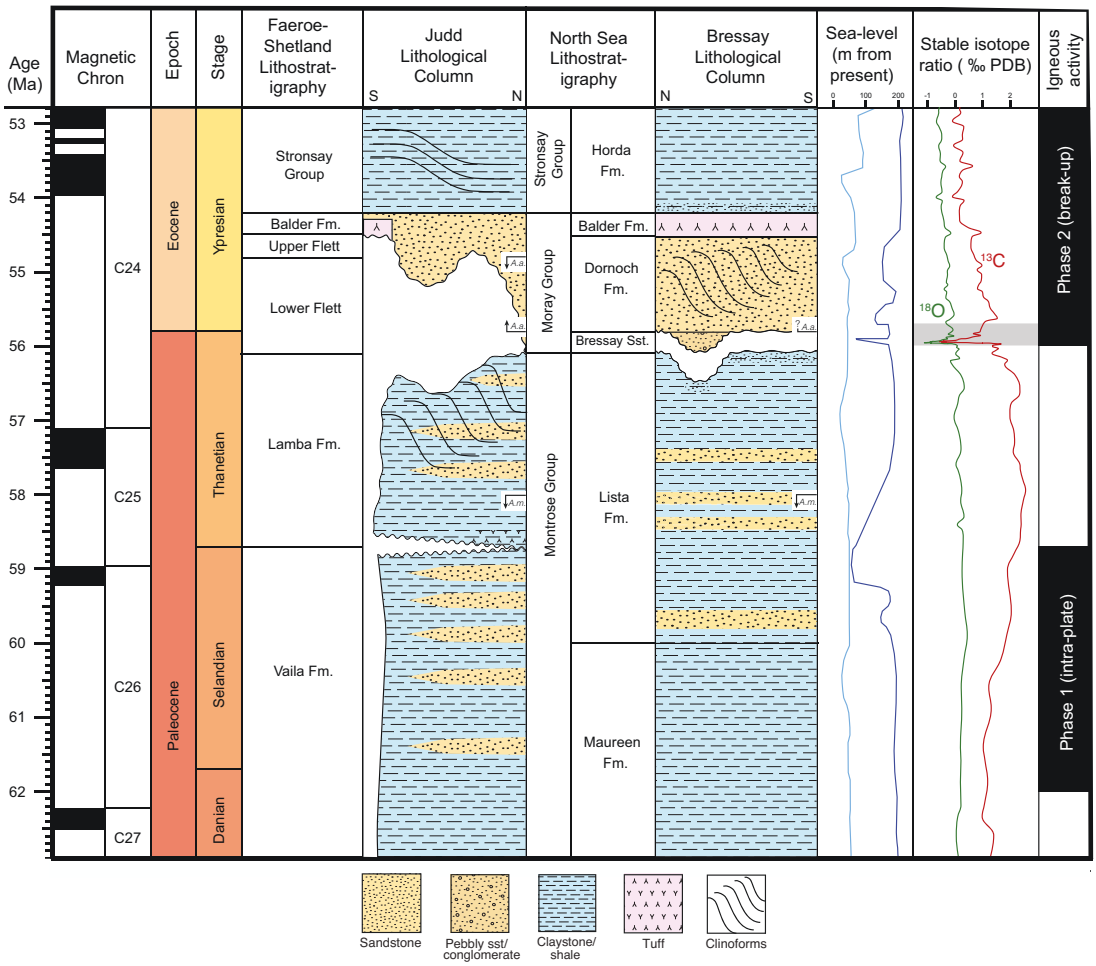


Figure 2.7: Paleocene-Eocene chronostratigraphy of Judd (Shaw Champion et al., 2008) and Bressay regions. Bressay stratigraphy is dated using dinoflagellate cyst records (see Table 2.1). Lithostratigraphy nomenclature is based on Knox and Holloway (1992). Ages for dinocysts *Apectodinium augustum* (*A.a.*) and *Alisocysta margarita* (*A.m.*) are from Luterbacher et al. (2004). Light and dark blue sea-level curves are from Miller et al. (2005) and Haq et al. (1988), respectively. Isotope curves are obtained from Cramer et al. (2009). Grey band = duration of Paleocene-Eocene Thermal Maximum (PETM), ∼170 ka (Röhl et al., 2007). Igneous activity is summarised from Saunders et al. (1997).

straint on the history of Paleocene-Eocene vertical motions and is the focus of this study. I examine the age of this unconformity in more detail in Section 2.3.4.

The Dornoch Formation in wells 9/3-2, 9/3-3 and 9/3-4 is conglomeratic and contains traces of terrigenous plants and pollens. The uppermost unit of the Moray Group is the Balder Formation. It consists of carbonaceous, tuffaceous mudstones, with tuff-rich layers at its base. The formation is roughly uniform

in thickness throughout the study area (∼30 m). The upward gradation from tuff into mudstones most likely reflects a rise in sea-level as well as a decrease in pyroclastic activity (Knox and Morton, 1988). The Stronsay Group overlies the Balder Formation and consists of marine mudstones and subordinate sandstones. This stratigraphy suggests a rapid return to marine conditions by ∼54.5 Ma (Knox and Holloway, 1992). The Stronsay Group extends into the earliest Eocene and is overlain by the Westray Group, which is formed of early Oligocene to mid-Miocene marine mudstones. This stratigraphic sequence is overlain by the Nordland Group, consisting of silty mudstones and siltstones, which were probably deposited in a shallow marine setting (Andrews et al., 1990). In addition to abundant, well-resolved well data presented above, both in the Bressay and nearby regions in the North Atlantic Ocean, biostratigraphic records were made available through PGS and Statoil. In the next section these records are used to constrain the formation age of the Paleocene-Eocene unconformity in the Bressay region to a high temporal precision.

2.3.4 Age constraints from biostratigraphic dating

Three of the wells in our study area, 3/27-1, 9/3-2, and 9/3-4, contain biostratigraphic records and >150 distinct dinoflagellate cysts (dinocysts) species are observed. Palynomorphs, including cysts of marine planktonic dinoflagellates, and spores and pollens of terrestrial plants, are abundant. Of these, dinocysts are the most suitable for dating the Paleocene-Eocene boundary due to their abundance and high temporal resolution (Mudge and Bujak, 1996). Dinocyst appearances from 14 key specimens and associated ages are provided in Table 2.1.

Nine Eocene biomarkers are located within the Stronsay, Balder, and Dornoch Formations. Six of these dinocysts have their first appearance at the Paleocene-Eocene boundary and occur in the uppermost Bressay Sandstone. Dinocysts *Glaphyrocysta ordinata* (*G.o*), *Palaeoperidinium pyrophorum* (*P.p*), and *Ceratiopsis speciosa* (*C.s.*) straddle the Paleocene-Eocene boundary. These 12 markers are dated using ages provided in Bujak and Williams (1985).

Table 2.1: Dinoflagellate cyst biomarkers of the Paleocene-Eocene boundary in the Bressay region. [a]Bujak and Williams (1985), [b]Mudge and Bujak (2001), [c]Luterbacher et al. (2004), [d]Vandenberghe et al. (2012)

Abbreviation	Nomenclature	Depth(m)	Age
A.d.	Areosphaeridium diktyoplokum	930–1110	E.-L. Eocene[a]
T. d	Thalassiphora delicata	1000–1140	L.Paleocene-M.Eocene[a]
D.o.	Deflandrea oebisfeldensis	1060–1130	L.Paleocene-E.Eocene[a]
H.t.	Hystrichosphaeridium tubiferum	980–1100	E.-M.Eocene[a]
D.p	Deflandrea phosphoritica	1000–1180	Eocene-Oligocene[a]
W.a	Wetzelliela articulata	1000–1200	Eocene[a]
L.w.	Lentinia wetzelii	1020–1110	E.Eocene[a]
H.p.	Homotryblium pallidum	1040–1130	Eocene-E.Oligocene[a]
A.h.	Apectodinium homorphum	1070–1190	L.Paleocene-M.Eocene[a]
A.a.	Apectodinium augustum	1180–1190	54.8–55.3 Ma[b] 54.8–55.8 Ma[c] 55.8–56.5 Ma[d]
G.o.	Glaphyrocysta ordinata	1120–1360	L.Paleocene-E.Eocene[a]
P.p.	Palaeoperidinium pyrophorum	1290–1460	Maastrichtian-L.Paleocene[a]
C.s.	Ceratiopsis speciosa	1290–1460	Maastrichtian-L.Paleocene[a]
A.m.	Alisocysta margarita	1000–1470	56.2–? Ma[b] 58.0–59.2 Ma[c] ?–59.7 Ma[d]

However, the two biomarkers most effective for constraining the age of the Paleocene-Eocene Bressay unconformity are *Apectodinium augustum* (*A.a.*) and *Alisocysta margarita* (*A.m.*). *A.a.* occurs in the Bressay Sandstone, above the unconformity, whereas *A.m.* is found in the Lista Formation below the unconformity (Figure 2.7). The age ranges used in this study are based on those presented by Luterbacher et al. (2004), although other ages for these 2 dinocysts have been proposed by Mudge and Bujak (2001) and Vandenberghe et al. (2012), which are slightly younger and older, respectively. Using Luterbacher et al. (2004)'s ages, *A.a.* has its first appearance at 55.8 Ma and last appearance at 54.8 Ma. This is consistent with an Early Eocene age for *A.a.* in the northern North Sea, and is supported by several authors (e.g. Mudge and Copestake, 1992; Gradstein et al., 1992; Mudge and Bujak, 1994; Neal, 1996; Thomas, 1996). *A.m.* occurrences are 59.2 Ma to 58.0 Ma. The unconformity must have developed after the last appearance of *A.m.* (58.0 Ma) and before the last appearance of *A.a* (54.8 Ma). Combined with evidence for terrestrial organic matter, this observation suggests the unconformity developed as a terrestrial erosional surface around 58–55 Ma. Biostratigraphic records provide us with high precision dates for the timing of the Bressay unconformity, and its

morphology and lithology suggest it is most likely terrestrial. In the following section, we provide further evidence in the form of geochemical analyses of cores extracted from the unconformity to further support a subaerial origin for the Bressay sandstone.

2.4 Evidence for a terrestrial origin

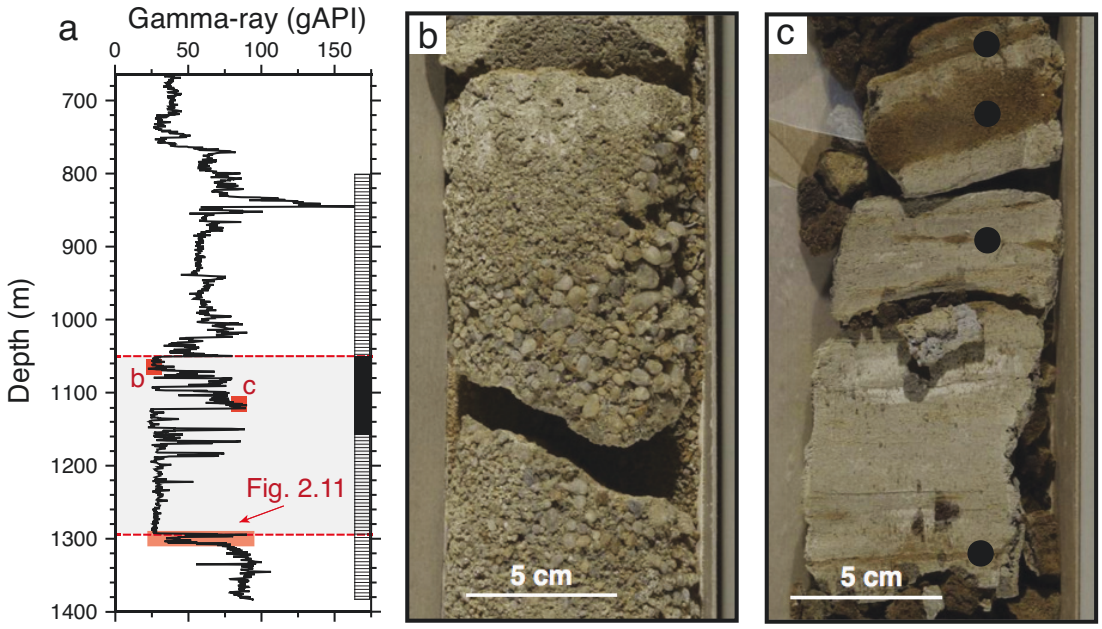


Figure 2.8: (a) Gamma-ray data for well 3/28a-4. Hachures = cuttings; solid black rectangle = core. Grey band = extent of channel fill (i.e. Bressay Sandstone). Red squares = locations of core shown in (b) and (c). Red rectangle = location of cuttings used for analysis shown in Figure 2.11. (b) Core from 1051 m depth. Note coarse sands/pebbles and gamma < 50 gAPI in (a). Core from 1120 m depth. Note shaly facies and gamma > 75 gAPI. Black circles = oil staining. Photographs from (b) and (c) were obtained from British Geological Survey offshore well drillcore database (©NERC).

2.4.1 Well cores and cuttings

To determine the origin of the oldest sedimentary rock (Dornoch Formation/Bressay Sandstone) that infills the unconformity we measured the organic content of core cuttings from well 3/28a-4 at a depth of 1298 m $\pm$10 m. This well conveniently cuts across the thickest portion the Bressay unconformity (see Figure 2.6). The cores were physically examined at the British Geological Survey (BGS)



Figure 2.9: (a) Cores from well 3/28a-4 ranging from depths of 900–1400 m below the seabed at the British Geological Survey (BGS). (b) Sorting of core cuttings into packs of 2–5 g. (c) Examples of samples collected. Note dark shale-rich samples at bottom-right, and pale, sandy samples at top left.

and are shown in Figures 2.8b–c and 2.9a. The large variations in gamma-ray from well 3/28a-4 in Figure 2.8a correspond to high-frequency variations in lithology between interbedded sand and shale. The two type lithologies can be seen in Figure 2.8b–c, including examples of abundant oil content. Samples of 2–5g were collected individually from core cuttings (see Figure 2.9). The samples were evenly spaced out every 10 m above, within, and below the Bressay sandstone, to obtain multiple samples over a range of depths. The organic content of each sample was then transported to and measured at the MAss

Spectrometry and Isotope Geochemistry (MAGIC) Laboratory at Imperial. The laboratory methodology is detailed in the following subsection.

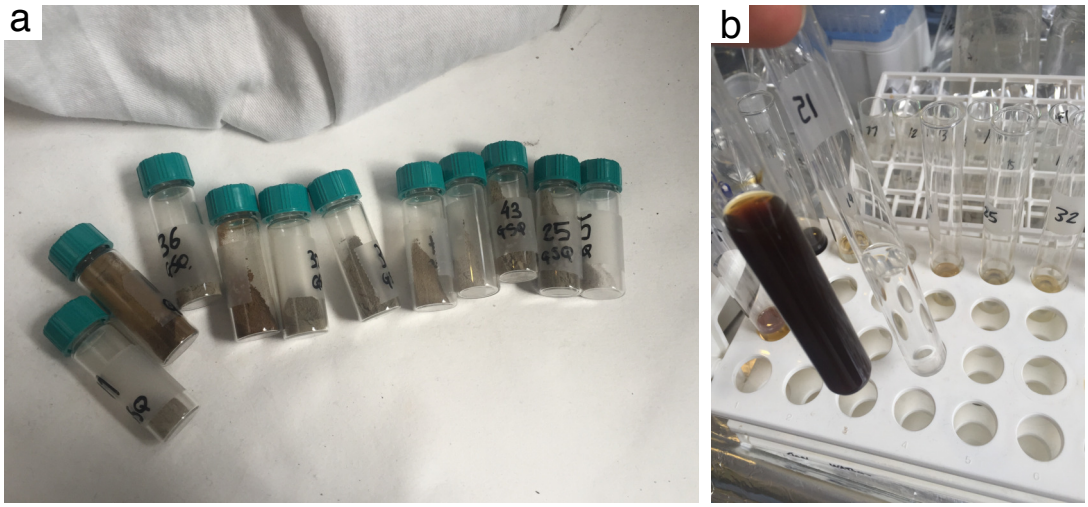


Figure 2.10: Examples of samples at different stages of geochemical analyses. (a) 11 samples after being powdered in a pestle and mortar. (b) Samples in test tubes with 4 ml of dichloromethane (DCM):methanol (93:7 v/v) added. Note dark test tube which corresponds to high organic matter content, and clear test tube corresponds to pure sand sample (no organic content).

2.4.2 Geochemical analyses

Samples of size ~ 1.5 g were powdered in a pestle and mortar and then solvent extracted (Figure 2.10a). Internal standards (squalane and *p*-terphenyl) were added to each sample prior to extraction. The powdered samples were placed in test tubes and 4 ml of dichloromethane (DCM):methanol (93:7 v/v) added (Figure 2.10b). The mixture was then sonicated for 3 minutes, centrifuged, and the supernatant was removed. The extraction process was repeated three times. After extraction, activated copper turnings were added into each sample to remove elemental sulfur and then the combined supernatants were taken to dryness under a stream of dry nitrogen in a pre-weighed vial. The concentrated extracts were fractionated by column chromatography using activated alumina powder in which the total hydrocarbon fraction was eluted using hexane and DCM:hexane (1:1 v/v). The hydrocarbon fraction was concentrated (ca. < 0.2 ml) using dry nitrogen prior to analysis by gas chromatography-mass spectom-

etry (GC-MS).

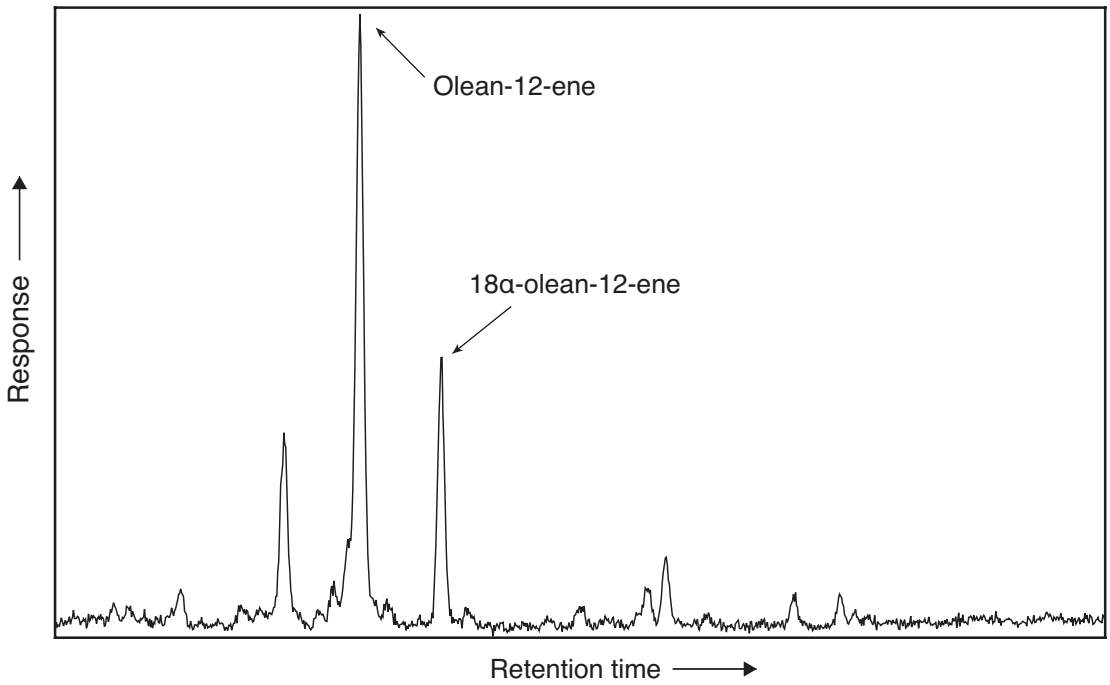


Figure 2.11: GC-MS (partial mass chromatogram *m/z* 218) of hydrocarbon fraction of sample at 1298 m depth displaying two prominent oleanene peaks.

GC-MS analysis was carried out on aliphatic and aromatic fractions of the samples using an Agilent Technologies 7890A gas chromatograph (GC) coupled to a 5975C mass spectrometer. The GC injector was operated in a splitless mode (1μl) with a column flow rate of 1.1 ml min^{-1}. A J&W scientific DB-5MSUI capillary column (30 m, 250 μm i.d., 0.25 μm film thickness) was used for separation and helium employed as a carrier gas. The GC oven temperature was initially held at 40°C for 2 minutes, and then raised to a 310°C at a rate of 5°C min^{-1} where it was held for 14 minutes. Mass spectra were acquired in electron impact mode (70 eV) in the scan range of 50–500 amu and also in selective ion monitoring (*m/z* 177, 191, 205, 217, 218).

2.4.3 Organic matter origin

The abundant presence of oil in the samples resulted in most of the signals from the organic content being drowned out. However, two oleanene isomers (olean-12-ene and 18α-olean-12-ene) were identified in one of the extracts. This

extract was collected from a depth of 1298 m, which corresponds to the base of the unconformity. The partial mass fragmentogram (*m/z* 218) of the hydrocarbon fraction of the extract that contains the oleanenes is shown in Figure 2.11. Oleanenes in oils have been linked to angiosperm debris in Cenozoic or Cretaceous source rocks and to deltaic depositional settings (Eneogwe et al., 2002). The occurrence of the two oleanene isomers in this sample likely favours a terrestrial origin for the organic matter, deposited either in a lacustrine, fluvial, estuarine, or deltaic/shallow marine environment (Adedosu et al., 2010). These observations are consistent with well logs that document the presence of spores, pollens, wood, coals, and lignites within the sandstone deposited directly above the Paleocene-Eocene unconformity. With the samples available we cannot rule out reworking of more proximal material. However, the presence of different types of organic matter and an upward coarsening of clastic material observed in most wells (e.g. Figure 2.6) suggests that the unconformity developed in a subaerial environment. Having established its age and terrestrial origin, the next section uses seismic data to map and extract Bressay's Paleogene erosional surface.

2.5 Extracting an ancient buried landscape

2.5.1 Combining seismic and well data

Until now the shape of the Bressay erosional surface has been poorly constrained, which has made it difficult to test models of its subaerial formation. Fortunately, 900 km^2 of new three-dimensional seismic data (BBK survey) were available for mapping courtesy of PGS and Statoil in addition to the seven commercial wells described in Section 2.3. Having constrained the presence of a $\sim$ 58–55 Ma terrestrial erosional surface, we now incorporate seismic reflection data and well correlations in Figure 2.6 to map its geometry across the Bressay region. The seismic survey is centred at $\sim$1° E, 60° N and includes 2434 in-lines and 2248 cross-lines covering $\sim$ 30$\times$30 km. The survey extends to $\sim$ 5 km beneath the seabed. Note that wells penetrate only the shallowest 1.5 km (Cretaceous and younger stratigraphy). Figure 2.12 shows a horizontal slice through seismic variance (trace-to-trace variability) at a depth of 1400 ms

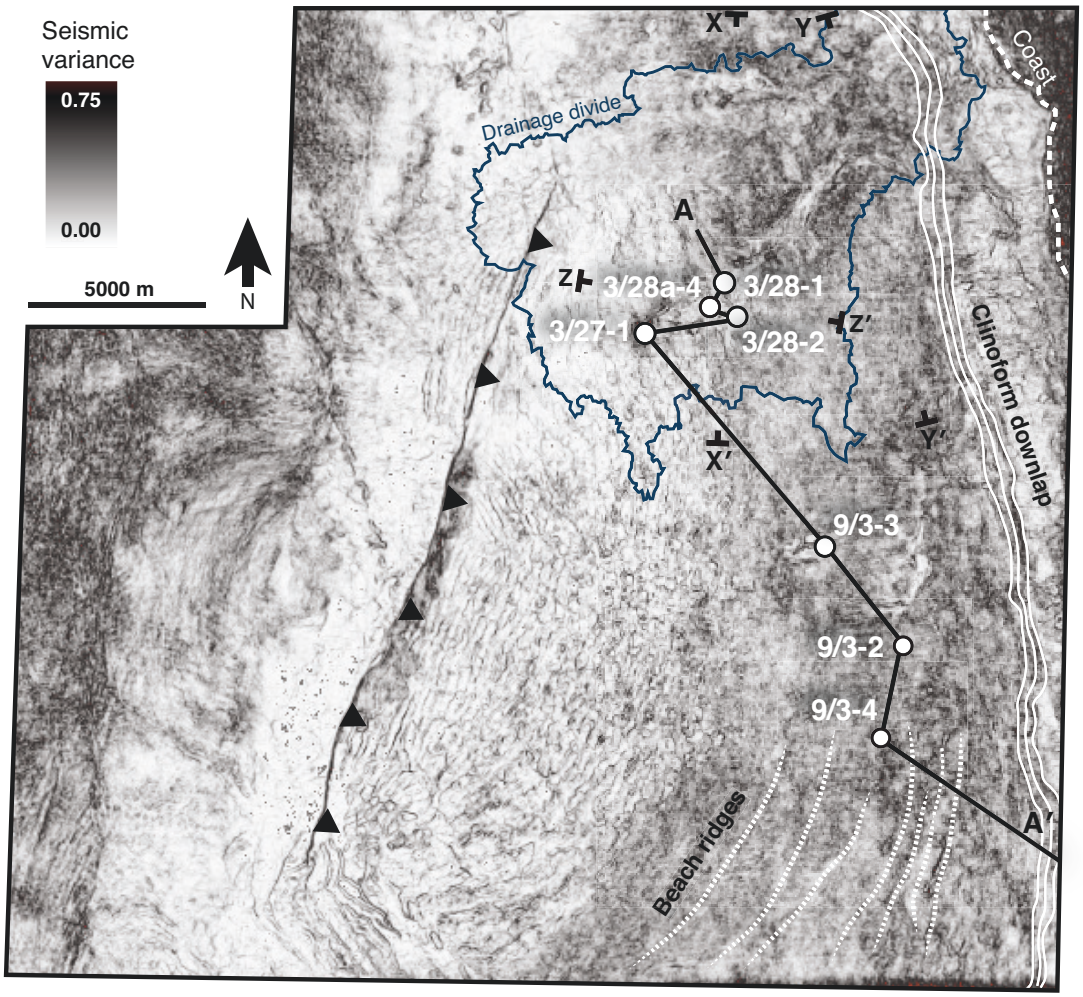


Figure 2.12: Depth-slice of seismic variance (trace-to-trace variability) at 1400 ms from 3D seismic volume. White circles = wells used in this study. Regional cross-section along wells = A–A′ (see Figures 2.6 and 2.13). Cross-sections along channel = X–X′ , Y–Y′ , and Z–Z′ are shown in Figures 2.14 and 2.15.

(∼1.3 km) in two-way time (TWT), which intersects the contact between the Paleocene-Eocene unconformity.

2.5.2 Regional stratigraphy & Bressay Sandstone

To map out the Bressay unconformity, we combine seismic and well data. In Figure 2.12, which is a depth-slice of the variance at the depth of interest (where channels are located), evidence for a drainage system can be seen at the NE corner. Other geomorphic features, such as a paleo-coastline, clinoform downlap, beach ridges, and a thrust fault are also mapped at this depth. Figure 2.13 shows an interpreted cross-section along the line A–A′ shown in Figure 2.12. In

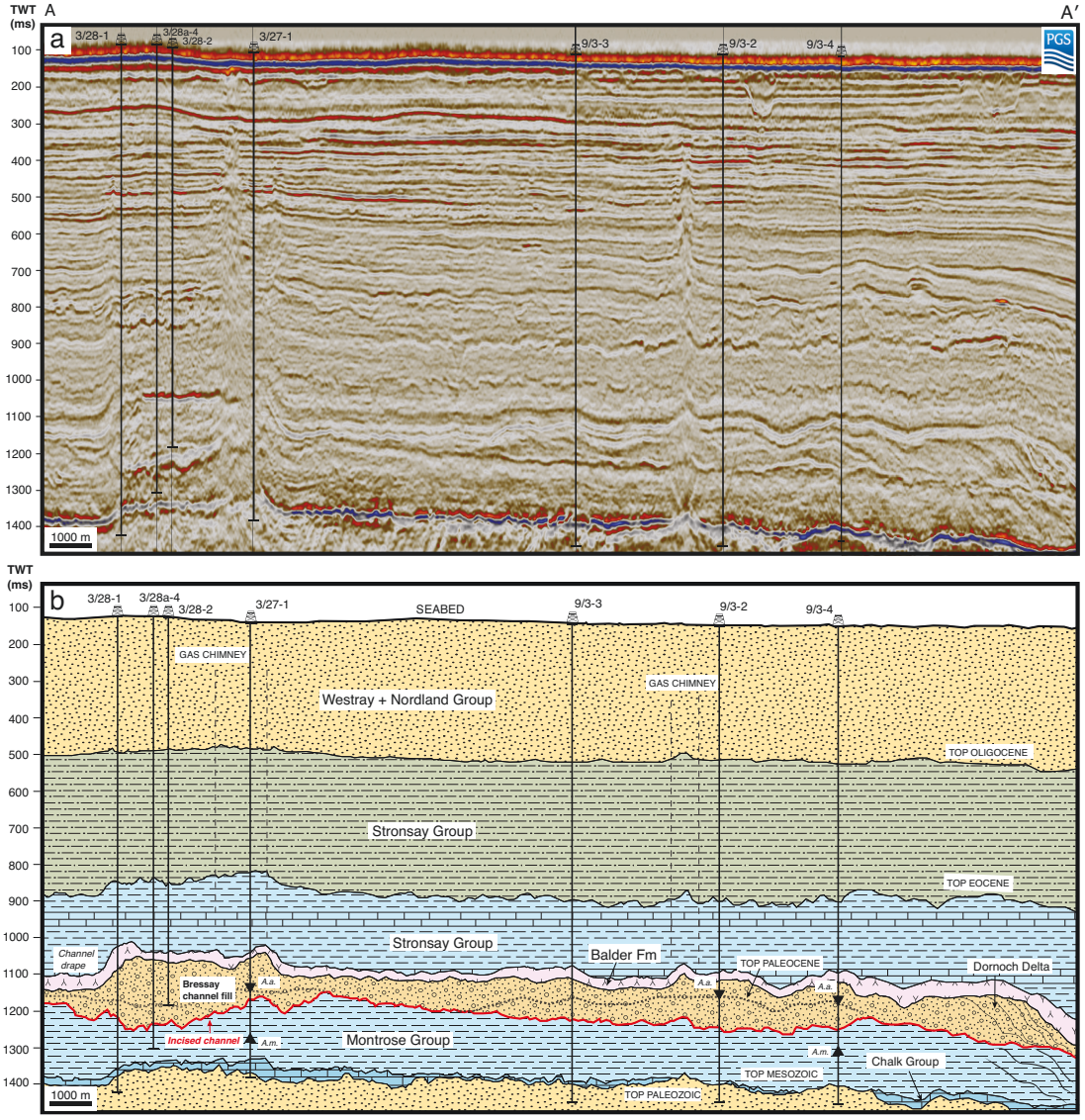


Figure 2.13: (a) Vertical seismic slice along A–A′ trace from Figure 2.12. TWT = two-way time. (b) Interpreted stratigraphy. Red line = unconformity; solid vertical lines = well paths; dashed vertical lines = gas chimneys; dotted line = Paleocene-Eocene boundary. Lithological key is shown in Figure 2.7. Up/down pointing black arrows = location of dinocysts *A.m./A.a.* that constrain the age of the unconformity.

some places gas chimneys make interpretation challenging and velocity pull-up is observed in the chalk unit beneath them. Stratigraphy is generally sub-parallel, which indicates that Cenozoic horizontal shortening is modest. The unconformity is highlighted in red and incision is most pronounced at 1200 ms depth towards the left-hand side (north). The unconformity sits atop the Montrose Group, which contains dipping impedance contrasts to the southeast which are interpreted as clinoforms. The deltaic Dornoch Formation with

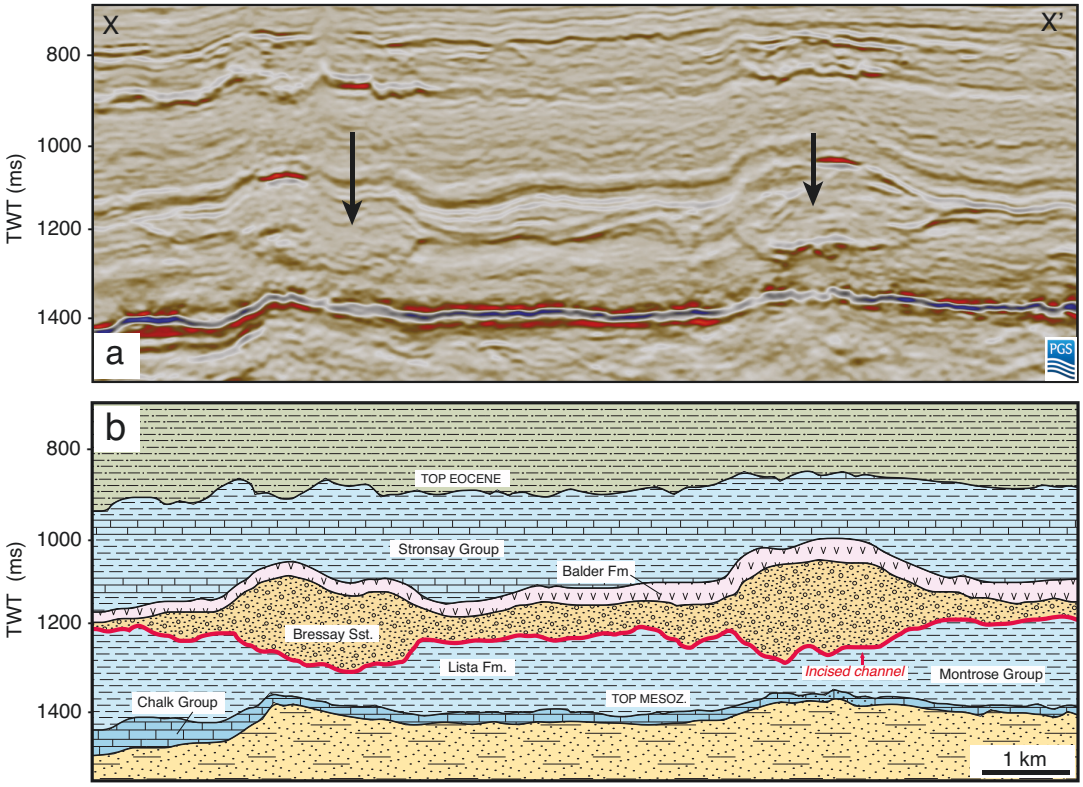


Figure 2.14: Cross section X–X′ of seismic data shown in Figure 2.12; black arrows = channels. (b) Interpreted seismic and well data. Red line = incised surface.

clinoformal geometries sits atop the unconformity. The black arrows show the first occurrence of *A.a.* and the last occurrence of *A.m.* in wells 3/27-1, 9/3-2, and 9/3-4. The V-shaped features, which have high variance at contacts with underlying stratigraphy, are most likely fluvial channels. Patches of high variance in Figure 2.12 outline a dendritic pattern in the northeast that is in the same location as the drainage network mapped by Underhill (2001).

2.5.3 Channel incision & 2D mapping

Figures 2.14 and 2.15 show cross-sections through tributaries of the drainage network. The Bressay Sandstone has a maximum thickness of ∼250 ms in these channels and incises into the Lista Formation. Cross-sections X–X′ and Z–Z′ show steep and narrow valleys. Cross-section Y–Y′ is located in the far northeastern part of the survey and shows that the valley here is wider and its walls have lower slopes. The Balder Formation drapes the Bressay Sandstone and Dornoch Formation and mirrors the relief of the underlying unconformity.

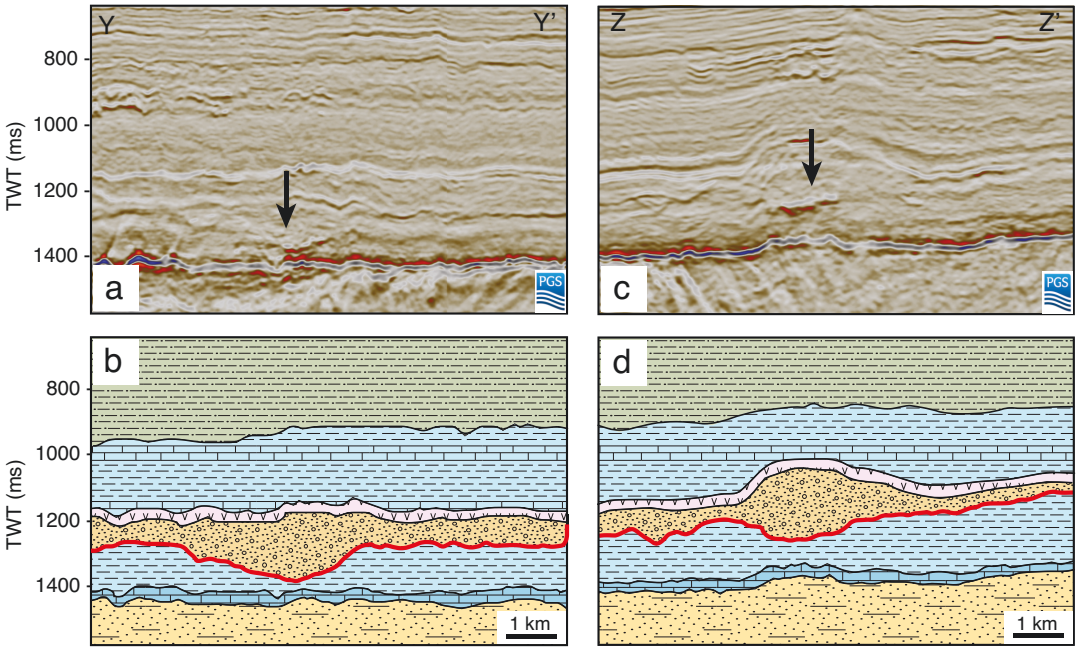


Figure 2.15: a)–b) Cross section Y–Y′ and c)–d) Z–Z′ of seismic data shown in Figure 2.12; black arrows = channels. (b) Interpreted seismic and well data. Red line = incised surface.

This relief is probably caused by differential compaction due to the sandy fill of incised valleys compacting less than adjacent mudstones.

The unconformity was mapped across the study area using every in-line and cross-line (i.e. no autotracking). The resultant landscape is shown in Figure 2.16. It has a resolution of $\sim$12 $\times$ 12 m. Two large catchments drain towards the east. The valley located towards the northeast of the surface has a relief of $\sim$250 ms. The mapped drainage network has a dendritic pattern upstream and a widening central valley downstream.

2.5.4 Bressay landscape in time

The observations described above differ from Underhill (2001)'s work in three subtle but important ways. First, it is shown that the Paleocene-Eocene unconformity does not sit atop the Dornoch Formation, rather that the Dornoch Formation was deposited on top of the unconformity. Secondly, although mapped as a dendritic drainage network by Underhill (2001), remapping of the southeast quadrant indicates that these features tend to be unconnected and

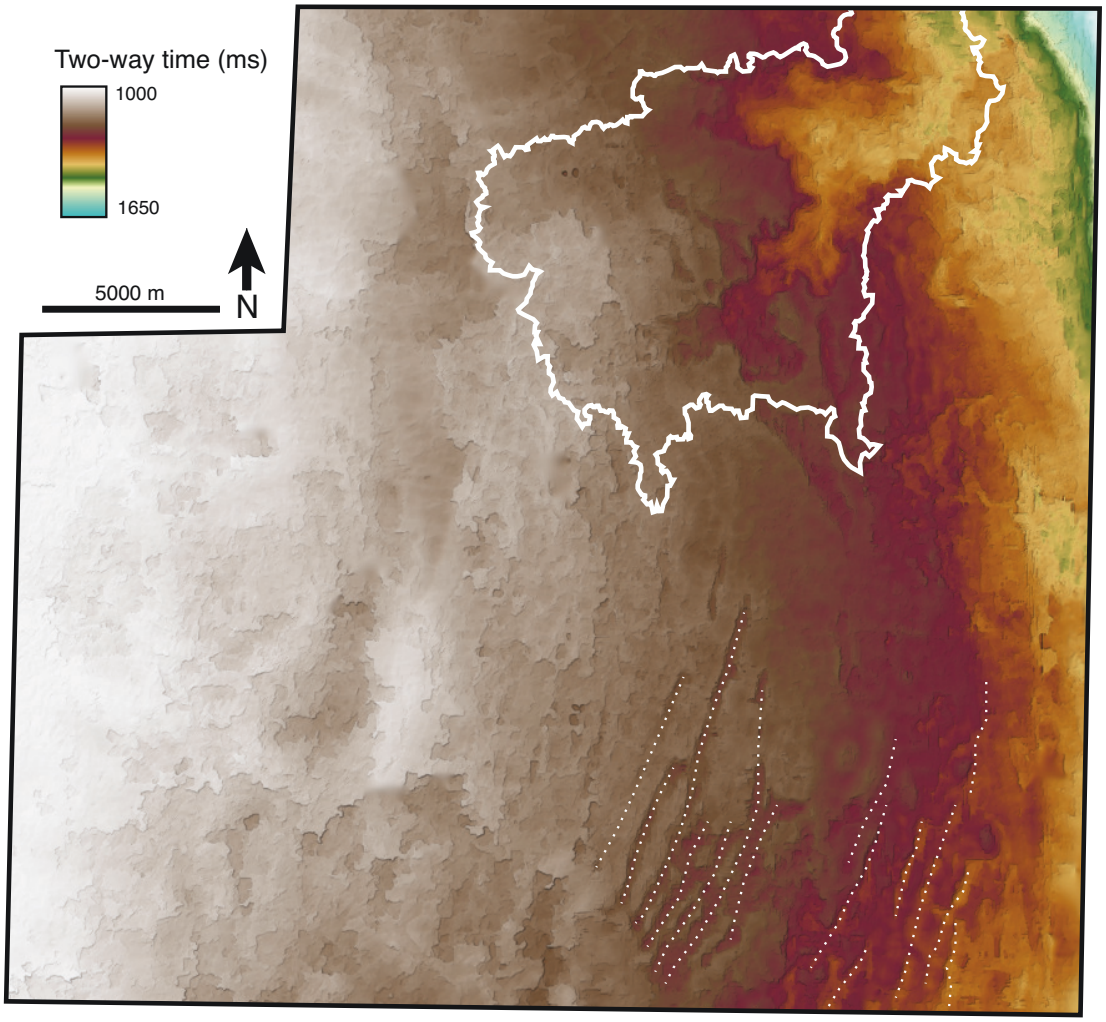


Figure 2.16: Extracted Bressay channel surface in two-way time. White outline = extent of drainage basin. White dotted lines = beach ridges and troughs.

subparallel to the paleo-coastline. They are more likely beach ridges (e.g. Jackson et al., 2010). Finally, remapping the top of the Dornoch Formation indicates that it possesses no coherent or connected drainage network. These observations combined with dinocyst records indicate that the Paleocene-Eocene unconformity is 0.1–1.3 Ma older than suggested by Underhill (2001) and Rudge et al. (2008) i.e. 54.7–54.5 Ma.

To examine the geomorphology of the Bressay landscape as it formed, the extracted surface must be depth-converted and the infilling rock decompacted to determine its thickness at time of deposition. This is the focus of Chapter 3. The

next section describes additional similar surfaces which have been observed in the North Sea.

2.6 Further evidence of uplift in the North Atlantic Ocean

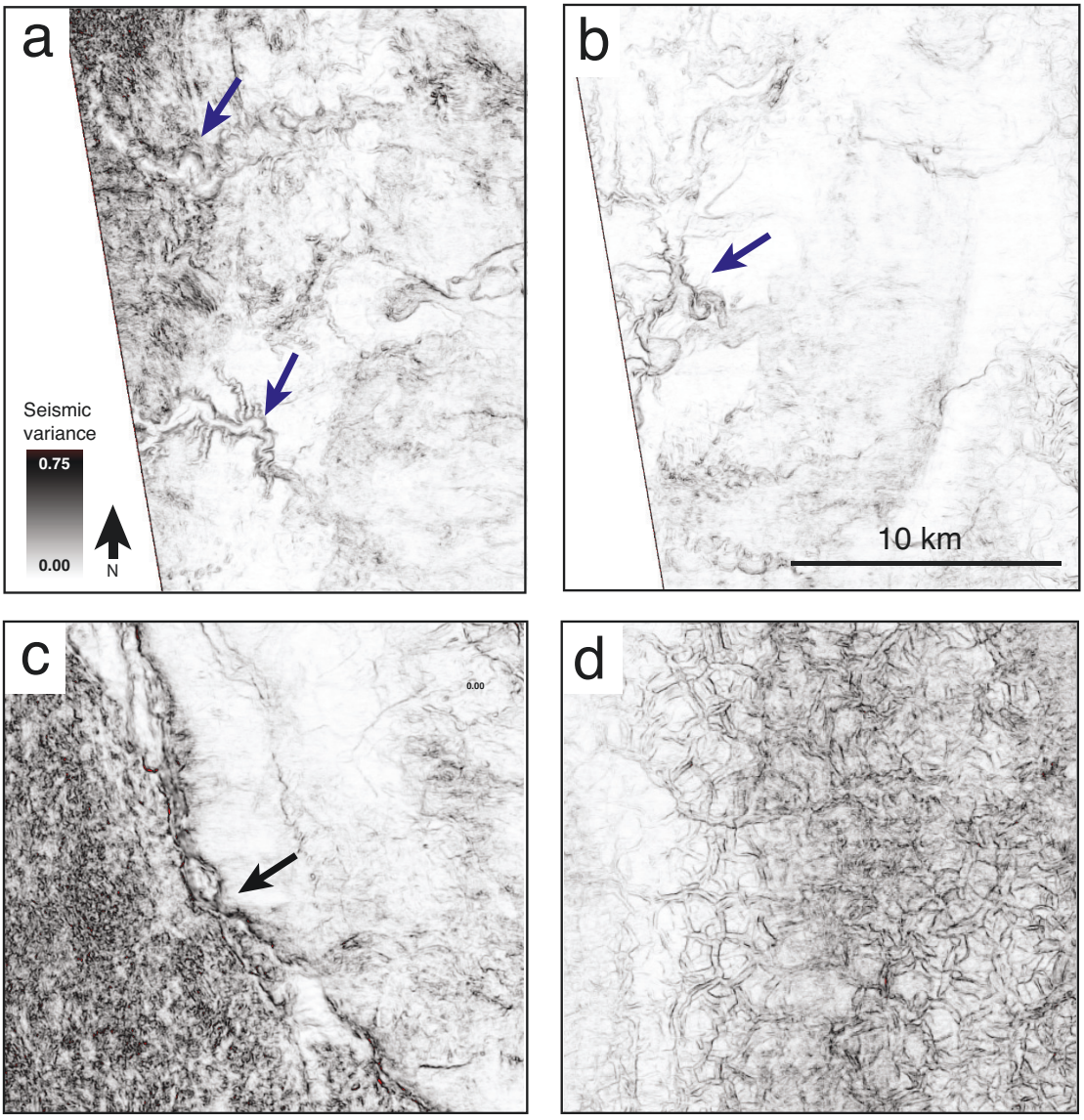


Figure 2.17: Depth-slice of seismic variance (trace-to-trace variability) at various depths showing different features in North Bressay 3-D seismic volume. (a) and (b) located at depths = 550 and 600 ms, respectively. Blue arrows = location of meandering features. (c) Black arrow = large unconformity (depth = 610 ms). (d) Regional polygonal faulting (depth = 400 ms).

2.6.1 North Bressay survey

Observations of publicly available regional seismic data suggest that presence of terrestrial channelized surfaces may be widespread in the North Atlantic. A new seismic survey was made available for analysis by PGS and Statoil (MC3D15010), located directly north of the Bressay region. Evidence for dendritic and meandering drainage is evident from examining seismic variance at a depth of $\backsim$ 600 ms (Figure 2.17a,b). This depth coincides with the strongest reflector visible in seismic cross-section in Figure 2.18a, where evidence for valley incision can be observed (see red arrows in Figure 2.18b).

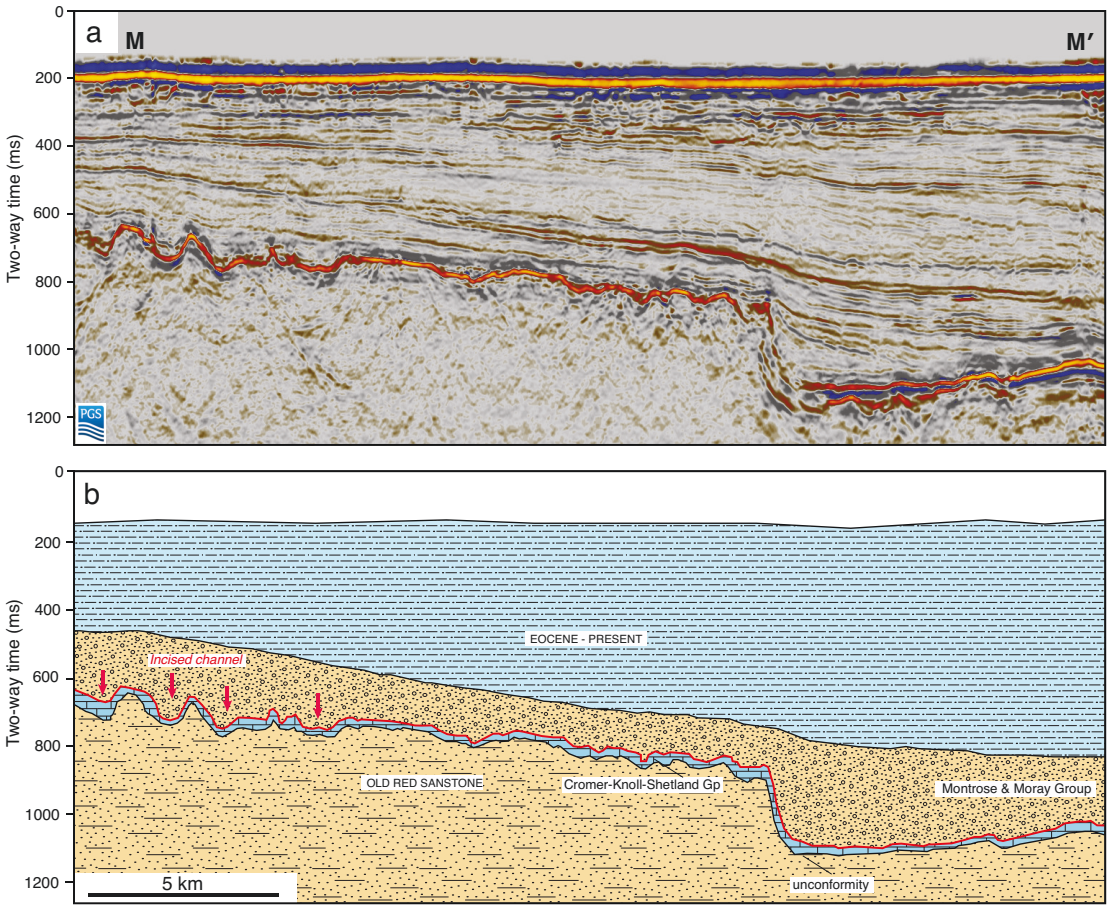


Figure 2.18: (a) Vertical seismic slice along M–M′ trace from Figure 2.19. (b) Interpreted stratigraphy. Red line = unconformity. Lithological key is shown in Figure 2.6.

2.6.2 Stratigraphy & mapping

The stratigraphy of the North Bressay survey can be approximated from well logs in the southeast of the seismic extent (gamma-ray logs and stratigraphic

logs). These indicate the incised layer is of Cretaceous age (Cromer-Knoll-Shetland Group), and the overlying deposits are of Paleocene-Eocene age (Moray and Montrose Groups; cf. Bressay and Judd Region). Well logs suggest the incised Cretaceous layer is composed of limestones and is overlain by interbedded sand and shales with coarse, pebbly sandstone with coarsening towards lower depths. Below the Cretaceous, the logs report sandstones which are most likely of the Old Red Sandstone (Jurassic) Group. Above the Montrose and Moray, a succession of undifferentiated marine mudstones is logged up to the seabed. Only two wells intersect the seismic survey. These are located $>$ 20 km away from the incised features observed in Figures 2.17a,b and 2.18. Importantly, a large unconformity (see Figures 2.17c and 2.18) occurs along the survey which runs N–S and separates the east (well locations) and west (incised features). This makes correlation of reflectors challenging and yield less reliable age constraints. This issue is discussed further in Section 2.6.4

2.6.3 Channel geomorphology

The strong reflector in Figure 2.18a was mapped in two dimensions at a resolution of 10 m. Results using auto-tracking and a high grid resolution of in-lines and cross-lines yield similar results due to the continuity of the mapped surface. The resulting mapped surface in two-way time shown in Figure 2.19 contains a pronounced drainage system in the northwest comprising multiple tributaries. Unlike Bressay, these channels show evidence of high-frequency meandering. Overlapping and interconnected meanders record channel avulsion events (e.g. southernmost channel in Figure 2.19). The channels drain from higher elevations ($\sim$ 600 ms below seabed) toward the east ($>$ 700 ms). Incised valleys appear to stop along a paleo-coastline, and localised deposits at the mouths of channels are most likely deltaic in origin (blue arrow in Figure 2.19). These geomorphologic features, combined with stratigraphic evidence for coarse fluvial sediments in overlying sediments, strongly support formation in a subaerial environment akin to that mapped in the southern Bressay.

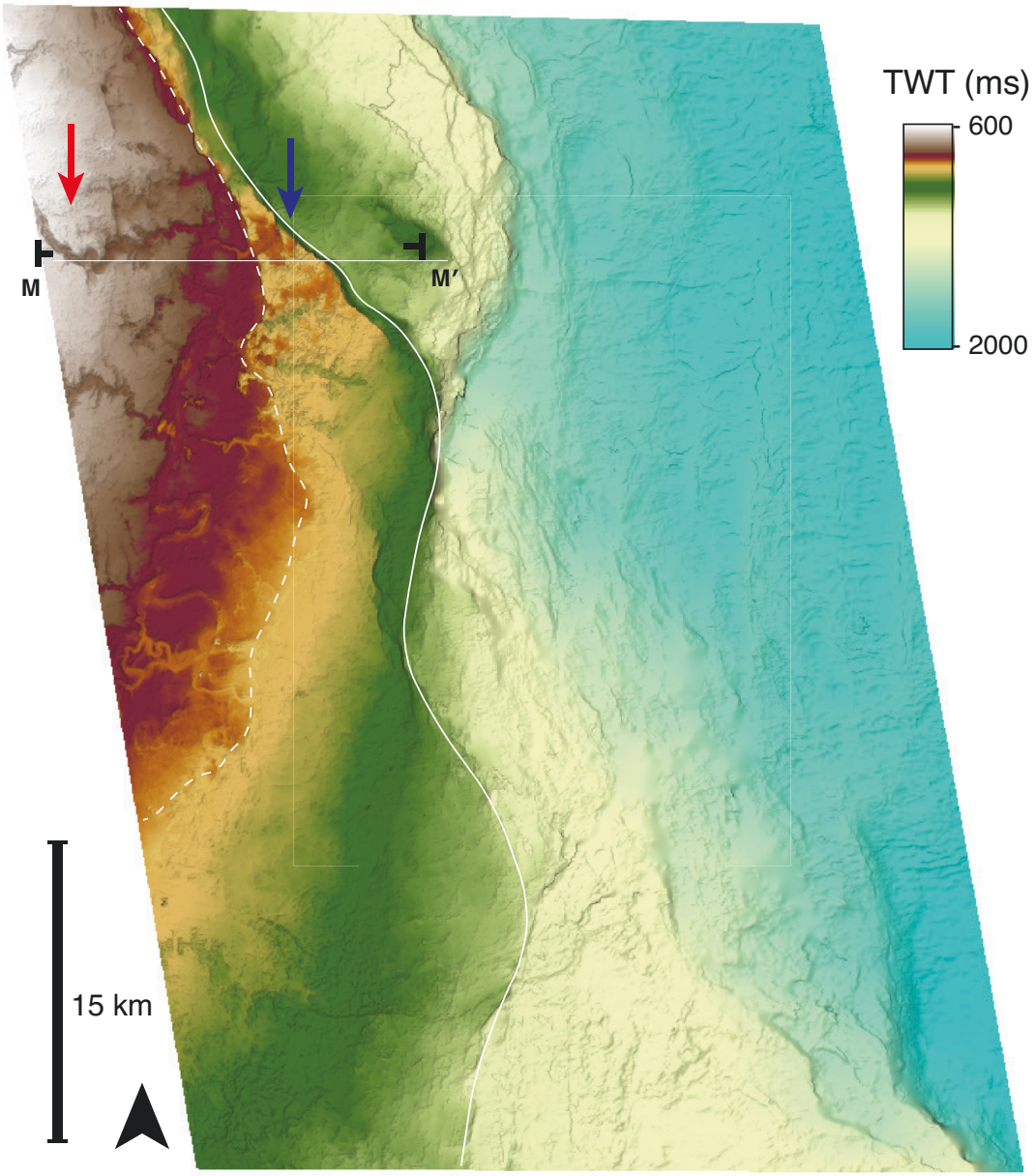


Figure 2.19: Extracted North Bressay channel surface in two-way time. Solid white line = unconformity. White dotted line = paleo-coastline. Red arrow = incised channels. Blue arrow = depositional features. M–M′ cross-section is shown in Figure 2.18.

2.6.4 Bressay vs. North Bressay system

The Bressay and North Bressay drainage systems are located 30 km apart. They share key commonalities in their morphology (incised valleys sloping eastward into paleo-coastlines), stratigraphy (coarse, pebbly channel infill), origin (terrestrial), and age (late Paleocene/ early Eocene). The North Bressay has a larger extent, greater resolution, more clearly defined valleys, a greater

number of individual basins, channels, and tributaries, presence of offshore deposits, shallower depth (= higher vertical resolution), and absence of gas column disruptions. However, the North Bressay survey lacks well data that intersects the channelized surface, and the large unconformity means correlation of seismic horizons along large distances is challenging. The lack of biostratigraphic records also suggests that a high-precision time constraint of the formation of the surface is difficult to obtain. Further, the channels are not contained within the survey, such that the the heads (and the upstream drainage area contribution) cannot be mapped or quantified.

Despite these challenges, both channels have similar approximate ages, morphologies, relief, orientation, and lithology, which suggest a common origin. The existence of a second survey with channelized surfaces is an exciting prospect that implies preservation of these ancient landscapes may be more common and widespread that originally thought. Due to its excellent biostratigraphic records and abundance of available intersecting cores, the Bressay channel will be the focus of the geomorphological and geodynamical analysis presented in the following chapter. Its precise temporal constraint, accurate morphology, and well-defined terrestrial origin suggest that inverting for uplift rates might be fruitful.

2.7 Chapter summary

In this chapter I combined well logs, stratigraphic records, seismic data, biostratigraphic markers, core data, and geochemical analyses of the Bressay region to identify, map, and extract an ancient terrestrial surface. This surface was incised subaerially at ~58 Ma for up to 3 Ma, after which it subsided and was buried under 1.5 km of marine sediments. An additional similar landscape was detected north of Bressay (NB; Figure 2.20). The abundant dataset associated with the Bressay landscape suggest it is an excellent candidate for river inversion analysis. In the next chapter I use these data and combine results with those from the nearby Judd buried landscape (J; Figure 2.20) to estimate the history of vertical motions of the northern North Sea as the Icelandic plume impinged upon the lithosphere 55–58 Ma.

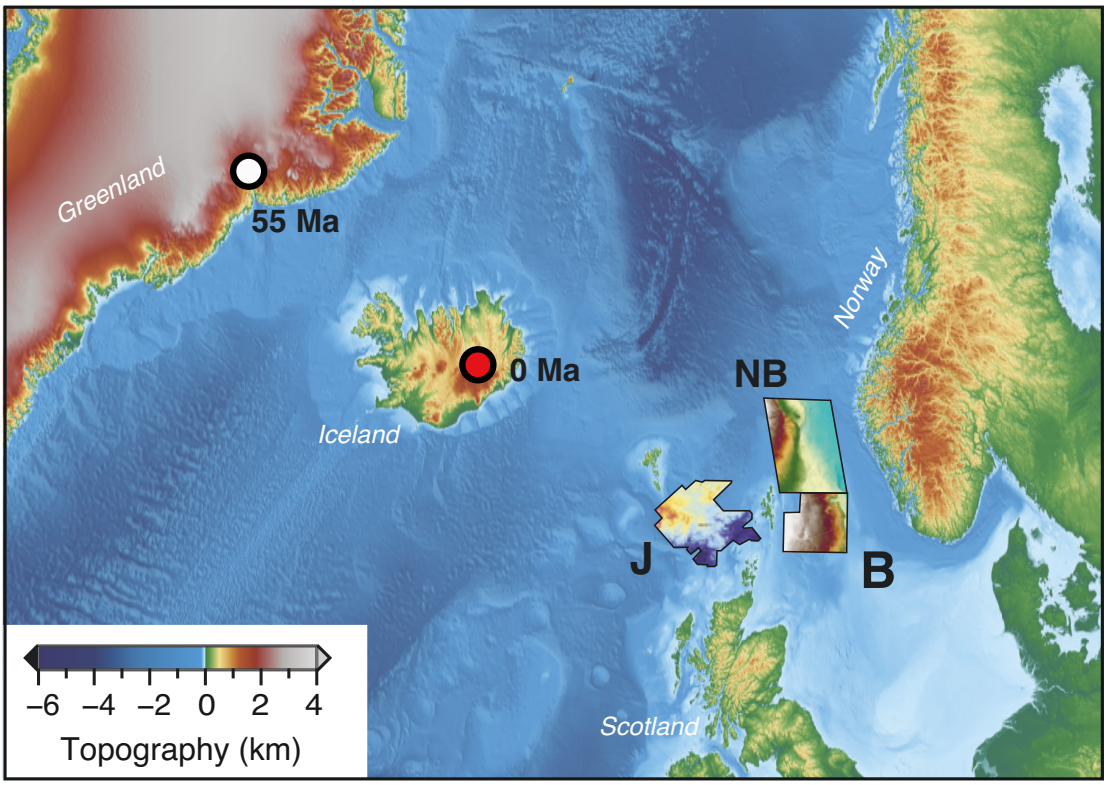


Figure 2.20: Schematic of buried terrestrial channel locations mapped in the North Atlantic Ocean. J = Judd region, B = Bressay region, NB = Borth Bressay region. Red circle = present-day Icelandic plume. White circle = Icelandic plume at 55 Ma.

Chapter 3

Uplift history and geodynamics of the North Atlantic Ocean

3.1 Chapter Introduction

The Bressay region contains a buried, terrestrial landscape which formed around 55–58 Ma (Chapter 2). Similar reconstructed landscapes in the North Atlantic Ocean were proposed by Shaw Champion et al. (2008) to be a manifestation of uplift sourced from the incipient Icelandic plume. In order to assess the origin and evolution of the ancient Bressay landscape, I map drainage inventories and extract histories of uplift. In order to recreate the landscape as it was when exposed on the surface of the earth, it is first necessary to restore it to its original relief. This requires knowledge about the seismic velocities of the region, as well as a quantitative understanding of the amount of post-depositional compaction. The geometry of the extracted drainage system and its knick-points following this correction contains important information about vertical motions. These are the crucial observations used to constrain the timing and duration of uplift in relation to the Icelandic plume. Importantly, these can be used to determine velocities and temperatures of the incipient Icelandic plume (e.g. Rudge et al., 2008; Hartley et al., 2011). The presence of multiple buried terrestrial surfaces of similar age and morphology peppered accross the North Atlantic Ocean indicates that uplift was widespread and that the behaviour of the Icelandic plume can be constrained both in time and space.

3.2 Reconstruction of sub-aerially exposed surface

3.2.1 Depth conversion

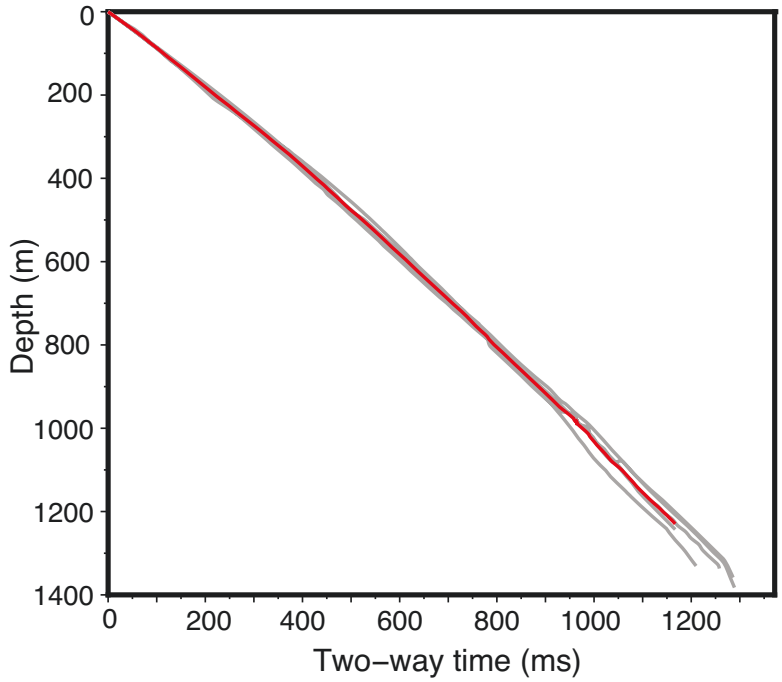


Figure 3.1: Checkshot time-depth data for five wells in Bressay region, 3/27-1, 3/28a-4, 9/3-2, 9/3-3, and 9/3-4, are shown in grey; red line = mean values.

To convert the landscape from two-way travel time, t, to depth, z, I use checkshot measurements. Five of the seven wells in this study have checkshot data, and all are almost vertical such that measured depth is approximately true vertical depth. Observed time-depth pairs for five wells are shown as grey lines in Figure 3.1. Time-depth data for wells intersecting channels and gas columns (3/27-1 and 3/28a-4) are similar to those outside channels (9/3-2, 9/3-3, and 9/3-4) (e.g. Figure 2.12). In addition, seismic data indicates that the Paleogene and younger stratigraphy dips shallowly. Both these observations suggest that a one-dimensional velocity model is acceptable. A quadratic function is fitted to the observed time-depth pairs, such that, $z = 0.0164t^2 + 0.8719t$ (red line in Figure 3.1, $r^2 = 0.99$). A 1σ deviation is used to estimate uncertainty in the time to depth conversion.

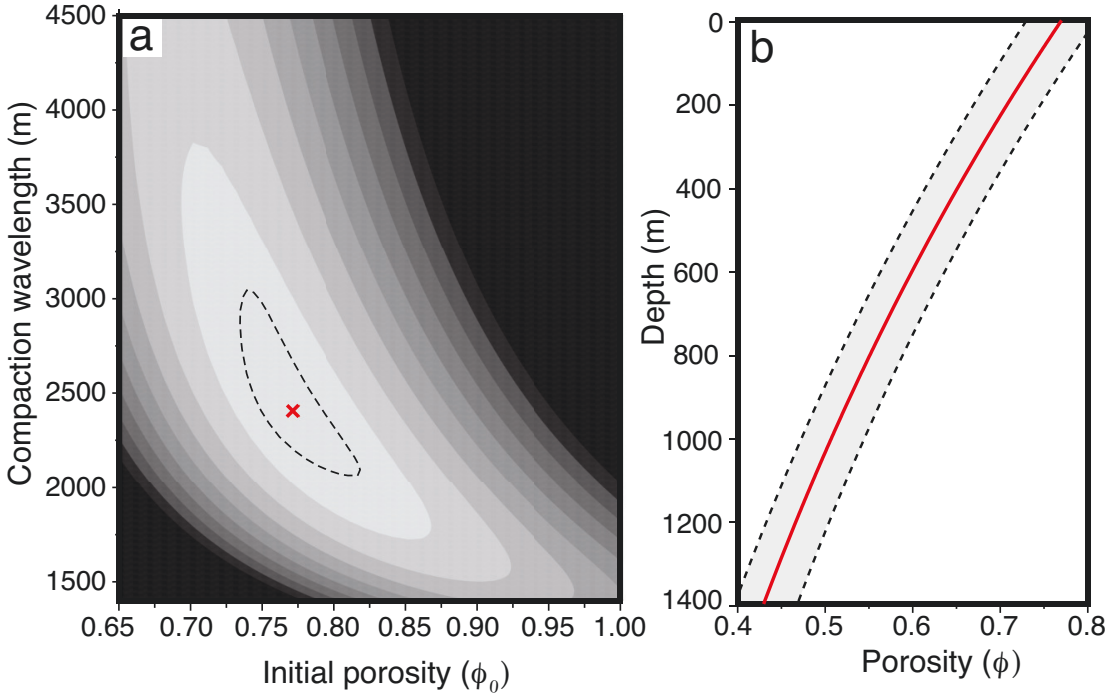


Figure 3.2: (a) Misfit between observed and theoretical time-depth pairs as a function of compaction wavelength (λ) and initial porosity ($\phi_\circ$). Red cross = lowest misfit ($\phi_\circ$ = 0.77, λ = 2400 m); dashed line = error envelope of $\pm 5\%$. (b) Porosity as function of depth for the Bressay region using best-fitting decompaction parameters. Dashed line = $\pm 5\%$ error.

3.2.2 Decompaction

Once the mapped landscape is converted into depth I can then correct for compaction from loading to recover the relief of the landscape. The amount of compaction can be quantified using a well-known relationship between porosity, ϕ, and depth, z,

$$\phi(z) = \phi_\circ \exp\left(\frac{-z}{\lambda}\right), \tag{3.1}$$

where $\phi_\circ$ is initial porosity and λ is compaction wavelength. We use an empirical relationship to constrain $\phi_\circ$ and λ as a function of depth and velocity,

$$\frac{t}{2} = \frac{z}{v_{sg}} + \phi_\circ \lambda \left(\frac{1}{v_w} - \frac{1}{v_{sg}}\right)\left\{1 - \exp\left(\frac{-z}{\lambda}\right)\right\}, \tag{3.2}$$

where constants v_{sg} and v_w are the interval pore fluid sonic velocity (1.5 km s^{-1}) and the solid grain velocity (5.5 km s^{-1} for clastic sediments), respectively (Wyllie et al., 1956; Sclater and Christie, 1980; Christensen, 1982; Czarnota et al.,

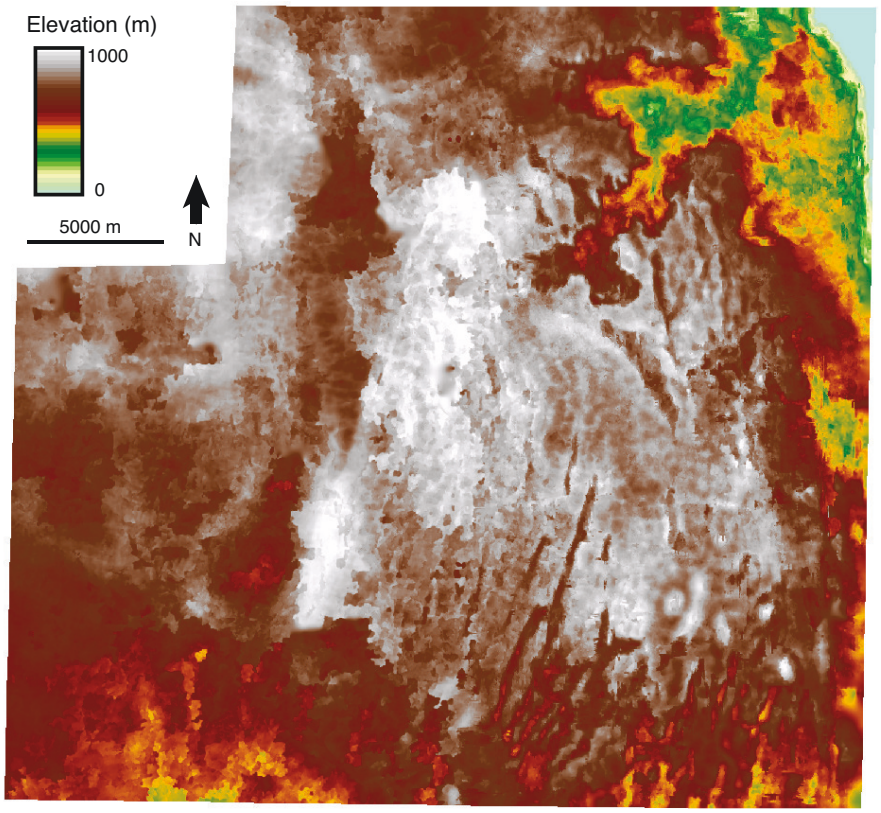


Figure 3.3: Depth converted and decompacted Bressay landscape.

2013). I compare observed and theoretical time-depth values for different combinations of $\phi_\circ$ and λ. Misfit is lowest when $\phi_\circ$ = 0.77 and λ = 2.4 km (rms misfit = 0.37; Figure 3.2a). These values can then be inserted into Equation 3.1 to calculate porosity as a function of depth (Figure 3.2b). I decompacted the sedimentary rock between the eroded landscape and a continuous curvature summit envelope constrained by drainage divide loci (Smith and Wessel, 1990). The volume between these surfaces is a minimum estimate of the amount of material eroded from the Bressay landscape. To decompact, the solid fraction is conserved such that,

$$\int_{z_1}^{z_2} 1 - \phi(z)\mathrm{d}z = \int_{\circ}^{z_3} 1 - \phi(z)\mathrm{d}z, \tag{3.3}$$

where $z_2 - z_1$ is the compacted thickness of the layer and z_3 is the depositional thickness of the layer. Substituting Equation 3.1 in and integrating yields,

$$z_3 = z_2 - z_1 - \phi_\circ\lambda\left[\exp(-z_1/\lambda) - \exp(-z_2/\lambda) + \exp(-z_3/\lambda) - 1\right]. \tag{3.4}$$

Equation 3.4 can be solved by Newton-Raphson iteration for the depositional thickness of the infill of the Bressay landscape, z_3. z_1 and z_2 are the respective

depths of the summit envelope (i.e. thickness of the overburden) and erosional surface. Following depth-conversion and decompaction, the reconstructed landscape shown in Figure 3.3 can be used to extract drainage patterns.

3.3 Drainage patterns & river extraction

3.3.1 Drainage extraction

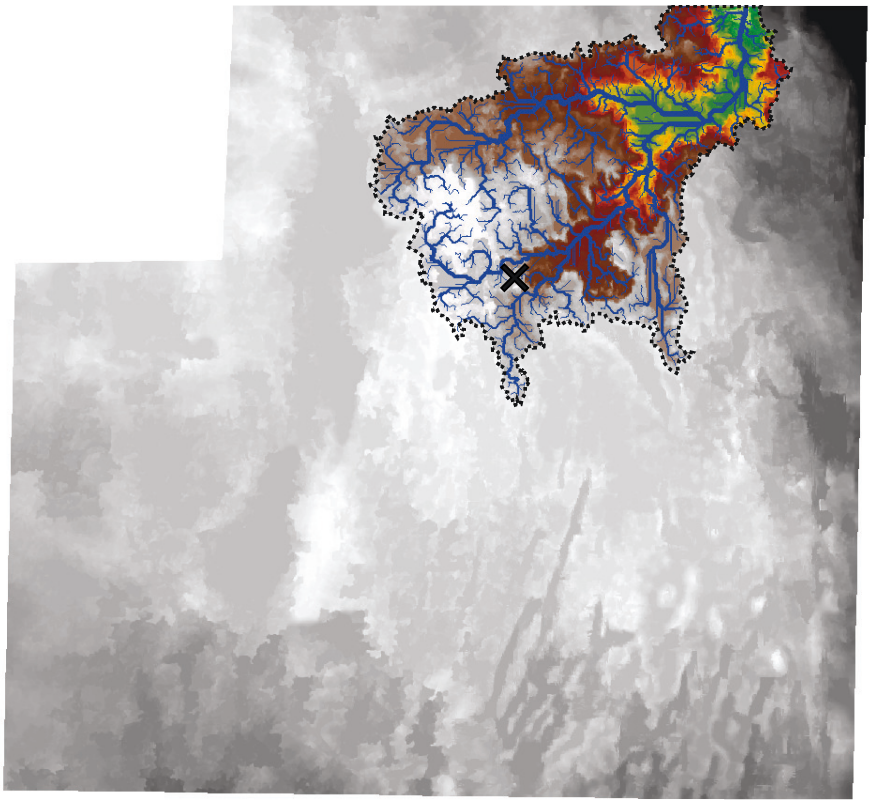


Figure 3.4: Drainage divide (black) and mapped rivers (blue) extracted from Bressay landscape. Outside of Bressay drainage basin is shown as grey scale. Black cross = location of river shown in Figure 3.7.

To extract a drainage network, Esri flow routing algorithms were applied to the digital elevation model (Figure 3.4). First, flow direction is calculated using the steepest descent from each cell in the digital elevation model (Tarboton, 1997). Secondly, flow accumulation to each cell is measured. Finally, flow lengths are calculated and drainage patterns extracted. The drainage inventory includes 87 rivers. Their longitudinal profiles are shown in Figure 3.5. The rivers have up to 350 m of relief and contain knickzones with tens to hundreds of meters of relief, which is much greater than seismic resolution (few meters).

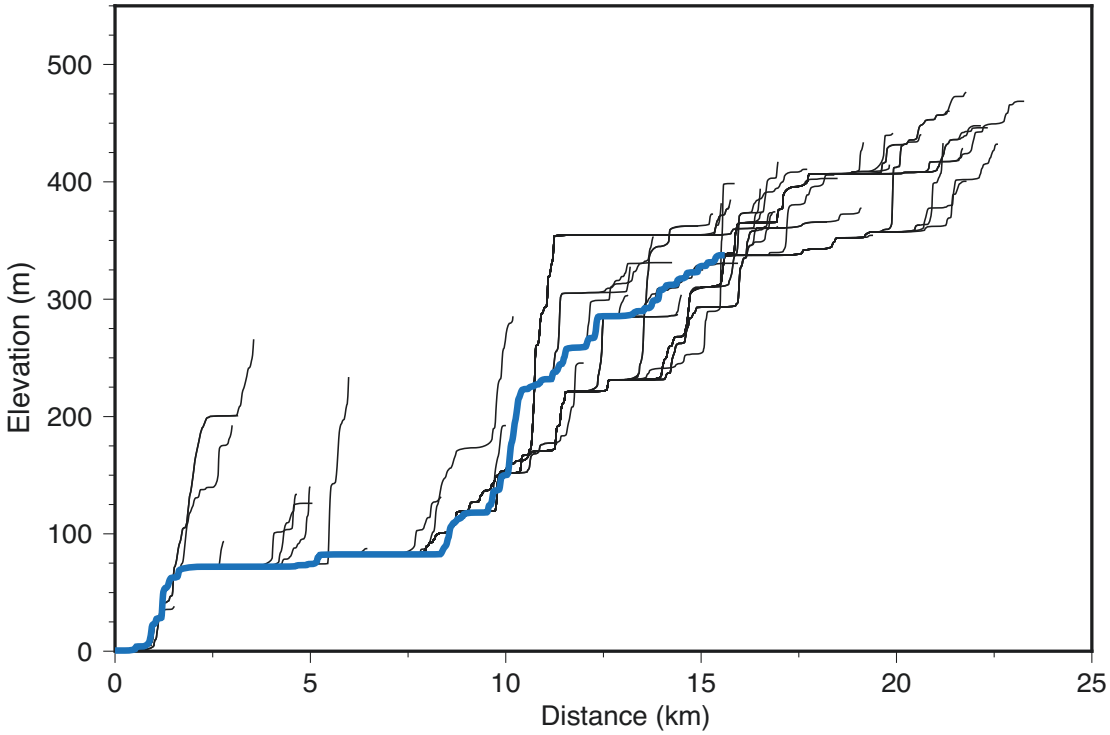


Figure 3.5: Longitudinal profiles of 87 rivers in the Bressay region. Blue river = river indicated by black cross in Figure 3.7 and shown in Figure 3.7.

3.3.2 Longitudinal river profile sensitivities

An important source of uncertainty is the velocity model used to convert two-way time to depth and to determine compaction parameter values. I covaried velocity models and compaction parameters within the uncertainties shown in Figures 3.1 and 3.2 to test their impact on calculated uplift histories (i.e. fastest, best-fitting, slowest velocity models and most compacted, best-fitting, least compacted models). I then re-ran the flow routing algorithms for each of these nine landscapes and re-extracted their drainage patterns. The planforms of the nine drainage networks are very similar. River elevations are stretched or compressed vertically by ± 25 m depending on the velocity and compaction parameters chosen (see Figure 3.6). The location and relief of knickzones are largely unaffected by these uncertainties. These tests indicate that the extracted drainage network and fluvial geometries are largely insensitive to geophysical uncertainties. The next subsection explores the possibility of extracting seismic data along a single channel to confirm its knickzones are real, geomorphic features.

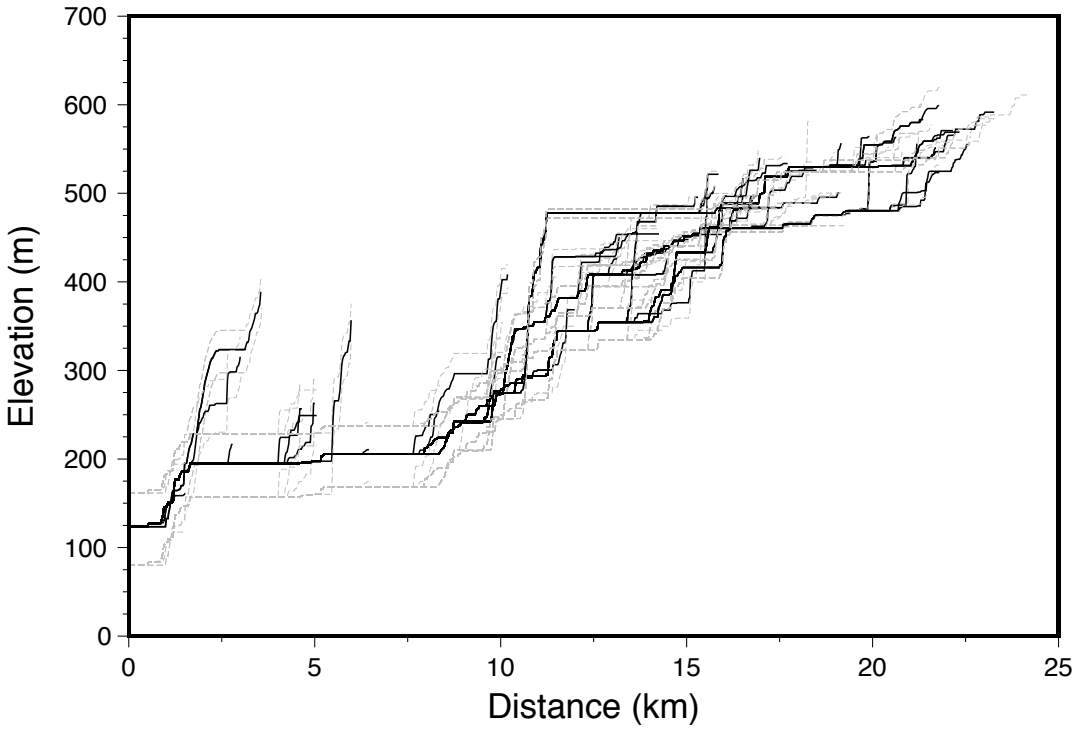


Figure 3.6: Longitudinal profiles of 87 rivers in the Bressay region extracted from surfaces reconstructed with different velocity models and compaction parameters. Black lines = best-fitting velocity and compaction parameters. Grey lines = minimum and maxiumum velocity and compaction parameters.

3.3.3 Seismic data and lithology along river

The lithological and structural characteristics of river substrate and infilling stratigraphy can be explored using seismic data extracted along rivers. A seismic profile, extracted along the river shown in blue in Figure 3.5, is illustrated in Figure 3.7. There is no obvious change in substrate acoustic impedance along the channel, which suggests that lithological contrasts do not play an important role in determining the shape of Bressay river profiles. Instead, I suggest that this landscape was generated by base-level changes (uplift) and erosion 58–55 million years ago.

The gamma-ray log of well 3/28a-4 intersects the channel infill and is shown as an inset in Figure 3.7b. The well log and seismic data are consistent with burial first by sand (e.g. Figure 2.10a; core interval: 1050–1070 m, gamma-ray values: 20–30 gAPI) and then by alternating marine shales (core interval: 1100–

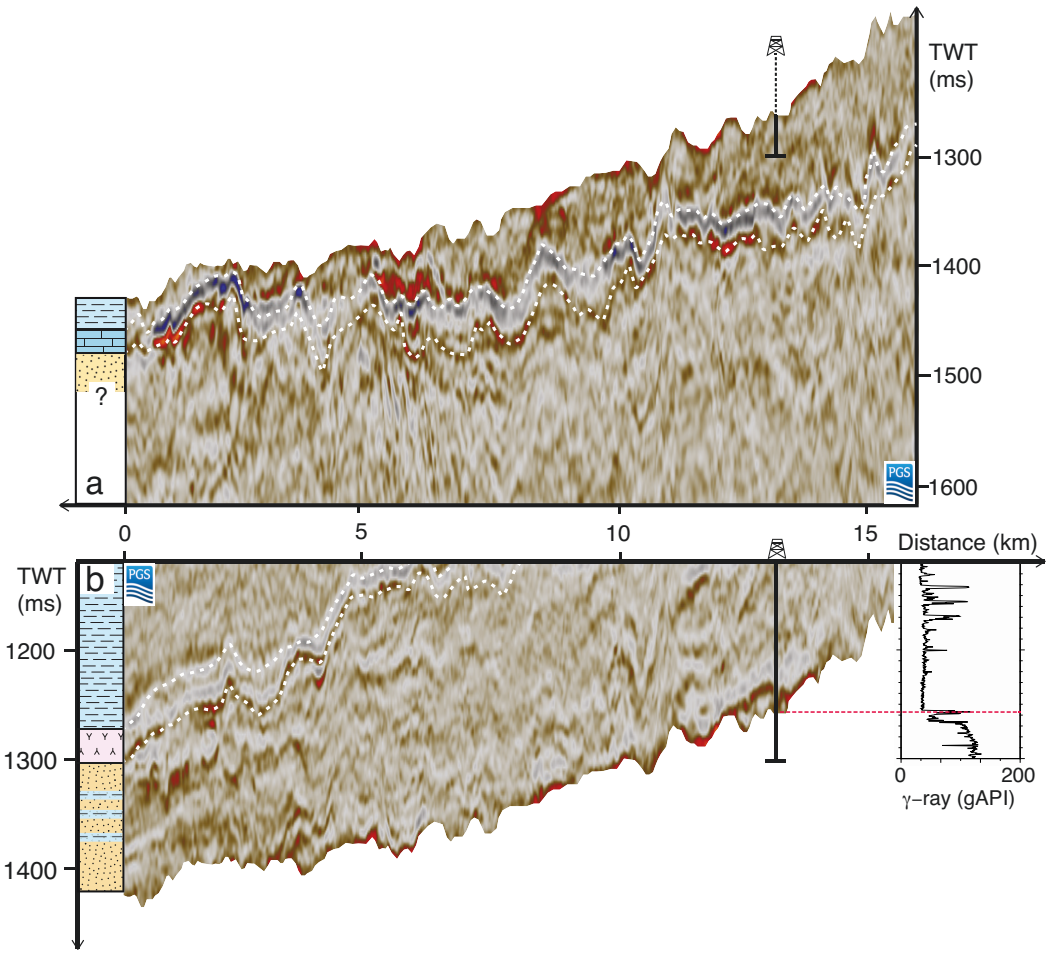


Figure 3.7: (a) Seismic and stratigraphic data extracted beneath the river shown in blue in a) (see cross in Figure 3.4). (b) Seismic and stratigraphic data extracted above the blue coloured river in Figure 3.5. White dotted lines = stratigraphic boundaries. Gamma-ray values for the deepest portion of well 3/28a-4 intersecting the river are shown to the right. gAPI $>$ 100 indicate mudstones and gAPI $<$ 100 suggest sandier lithologies.

1120 m, gamma >100 gAPI) and sand. These observations are consistent with burial first by terrestrial clastic material and suggest that subsequent drowning was staged. The age of dinocysts contained in the underlying and overlying deltaic deposits (Dornoch and Stronsay Formations) constrain the duration of formation of the Bressay landscape to <3 Ma. Relief from drainage patterns extracted from this landscape indicate that the Bressay region was uplifted by at least 350 m. The shapes of the river profiles extracted from the Bressay landscape imply that uplift was episodic and that inverting for an uplift rate history might be fruitful.

3.4 Uplift history & mechanisms

3.4.1 Uplift in the Bressay region

In the previous chapter, well reports, presence of angiosperm debris in core samples, dinocyst biostratigraphy, and remapping of stratigraphy using PGS's three-dimensional BBK survey indicated that the Bressay region was uplifted, eroded by a fluvial drainage network, and then rapidly drowned between 58–55 Ma. The erosional landscape was extracted by mapping a stratigraphic unconformity, which is overlain by the conglomeratic Bressay Sandstone, the sandy Dornoch Formation, the Balder Formation, and the marine Stronsay Group. These observations show that total cumulative (i.e. peak) uplift occurred before 54.8 Ma (i.e. youngest reported age of *A.a*), suggesting it is older than previously thought (*cf.*Underhill, 2001; Rudge et al., 2008). In the previous section, I used checkshot data to convert seismic data to depth and to parameterise decompaction. Importantly, our estimate of maximum relief is 100–150 m more than in Underhill (2001), which I attribute to better seismic data, mapping of every inline and cross-line, and a reevaluation of biostratigraphic data.

3.4.2 Inverting for uplift rate

Pritchard et al. (2009) and Roberts and White (2010) first showed that longitudinal river profiles could be successfully inverted for a history of uplift rate. I use a simplified version of the stream power model to invert rivers draining the Bressay landscape for uplift, U as a function of time, t,

$$\frac{\partial z}{\partial t} = U(t) - vA(x)^m \frac{\partial z}{\partial x}, \tag{3.5}$$

where erosion rate is parameterised using the advective term on the righthand side of Equation 3.5 (Rosenbloom and Anderson, 1994; Whipple and Tucker, 1999). This term controls the velocity of kinematic erosional waves as they propagate upstream. Velocities depend on upstream drainage area, A, which is measured from the extracted landscape and the values of the erosional parameters, v and m. The biostratigraphic records discussed in Section 2.3 indicate that the duration of exposure is < 3 Ma. I use a central value of 1.5 Ma. A joint inversion of the drainage inventory indicates that best-fitting $m = 0.5$,

and a landscape response time of 1.5 Ma yields $v = 1.6$ Ma^{-1} (e.g. Rudge et al., 2015). The inverse problem can be solved by seeking the minimum value of an objective function, H, that incorporates data (rms) misfit, model roughness, and a positivity penalty function, P,

$$H = \left[\frac{1}{N} \sum_{i=1}^{N} \left(\frac{z_i^o - z_i^c}{\sigma_i} \right)^2 \right]^{\frac{1}{2}} + w \left(\frac{\mathrm{d}U}{\mathrm{d}t} + \frac{\mathrm{d}^2 U}{\mathrm{d}t^2} \right) + P, \tag{3.6}$$

where N is the total number of measurements of elevation and distance in our drainage inventory (Roberts and White, 2010). Data variance σ_i is set to 20 m, which is a conservative estimate of the vertical resolution of the seismic data. In practice the model seeks the smoothest uplift rate history that yields the lowest residual misfit between observed and theoretical river profiles (Parker, 1994). In this study, smoothing parameter $w = 0.1$. The model uses Powell's algorithm, a conjugate gradient method, to invert for uplift rate histories, which yields stable solutions (Roberts and White, 2010; Hartley et al., 2011).

3.4.3 Vertical motions of Bressay between 58–55 Ma

I inverted the shapes of longitudinal river profiles draining the Bressay landscape for a history of uplift rate. The calculated uplift history from a joint-inversion of the two main rivers is shown in Figure 3.8. Residual rms misfit is 0.64. Calculated uplift rate history has three phases of increased uplift, labeled 1, 2, 3 in Figure 3.8b. The magnitudes of the uplift events are 100–200 m and total cumulative uplift exceeds 350 m. Calculated uplift rates are 0.5–1 mm/a, with uplift beginning at 56.5 Ma and culminating at 55.0 Ma. Grey band in Figure 3.8b shows uncertainty in calculated uplift for $v = 1.6 \pm 0.1$ Ma^{-1}. If $v = 4.75$ Ma^{-1} (cf. Hartley et al., 2011) calculated uplift occurs within < 1 Ma of peak uplift. A three-stage uplift history was also observed in the Judd region of the Faeroe-Shetland basin (see Figure 3.9). In Judd, cumulative uplift reached $\sim$900 m and the landscape was exposed subaerially for ~ 2.5 Ma, with peak uplift between 56.1–55.0 Ma (Shaw Champion et al., 2008; Rudge et al., 2008; Hartley et al., 2011). Rapid post-uplift subsidence drowned the Bressay and Judd regions.

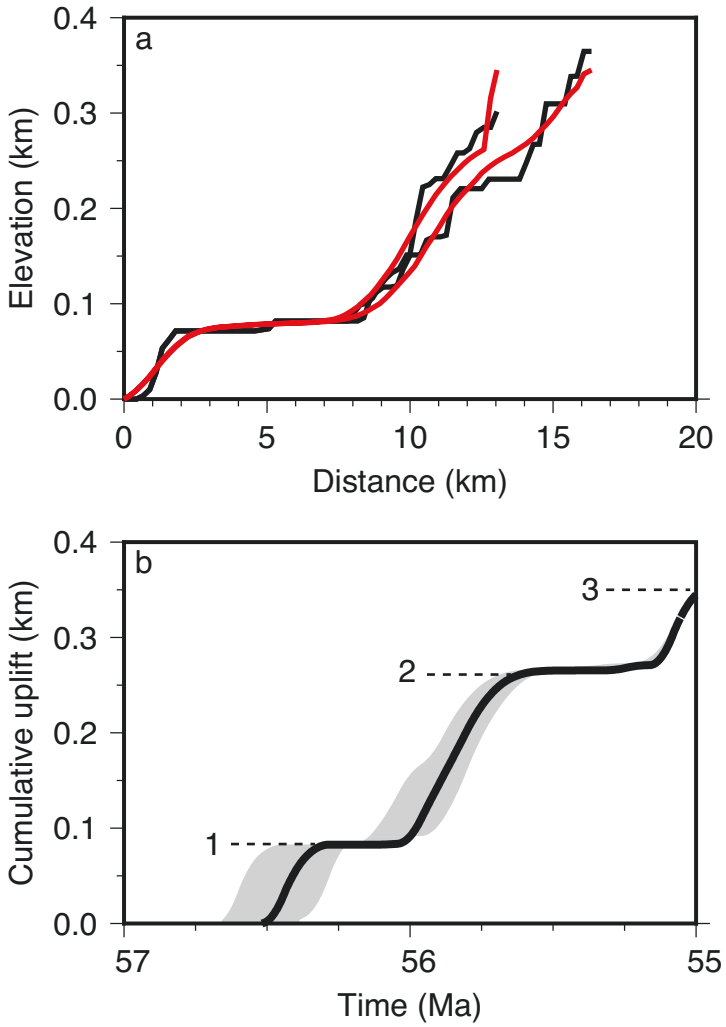


Figure 3.8: Joint inversion of two main tributaries for uplift rate as a function of time. (a) Black = observed river profiles. Red = best-fitting theoretical profiles. (b) Cumulative uplift history that produced theoretical profiles in a). Grey band = range of uplift histories for erosional parameter v = 1.6±0.1 Ma^{-1}. Uplift events are labeled 1, 2, 3.

3.5 Generating uplift in the North Atlantic Ocean

3.5.1 Sources of uplift during Paleocene-Eocene

We consider four processes that could have generated the rapid Paleocene-Eocene vertical motions observed: glacio-eustasy, underplating, crustal shortening, and mantle convection. Glacio-eustasy can generate rapid base level changes when polar ice is present. However, there was probably little polar ice during the Paleocene-Eocene Thermal Maximum (PETM) when glacio-eustatic sea-level probably varied by a few tens of meters at most (Haq et al., 1988;

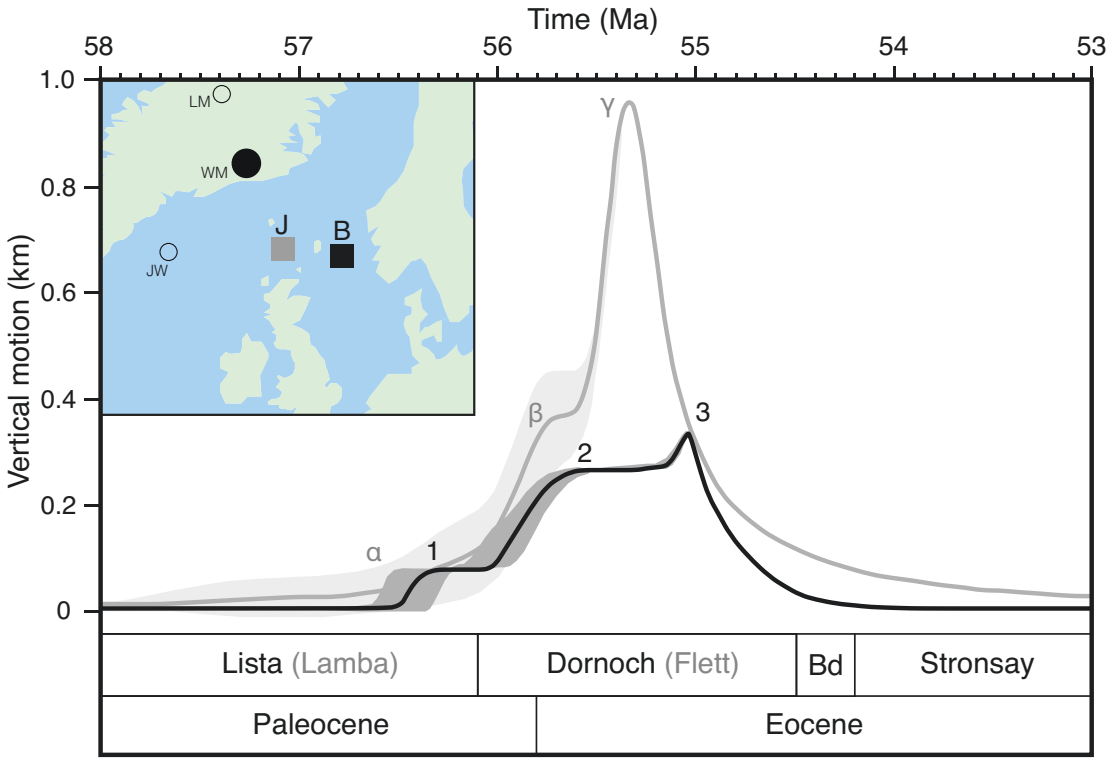


Figure 3.9: Uplift histories for Bressay [black] and Judd (grey; Hartley et al., 2011). Grey bands = uncertainty from erosional parameter values. 1, 2, and 3 = Bressay uplift events. α, β, γ = Judd uplift events. Inset = Paleocene-Eocene paleogeography showing location of uplifted regions: black square = Bressay; grey square = Judd; red circle (WM) = Icelandic plume center from White and McKenzie (1989); LM/JW = plume centers from Lawver and Müller (1994)/Jones and White (2003).

Miller et al., 2005). The growth of relief in the Bressay area appears to be local to the East Shetland Platform, which also indicates that glacio-eustasy is not responsible generating the base level changes observed.

If it is assumed that isostasy applies, a simple isostatic calculation shows that underplating generates air-loaded uplift, $e = t_u(\rho_a - \rho_u)/\rho_a$, where ρ_a and ρ_u are respective densities of mantle (3.2 g/cm^3) and underplate, and t_u is underplate thickness. Using $2.72 \leq \rho_u \leq 2.9$ g/cm^3, which represent the range of densities expected for molten to solid (gabbroic) underplate, yields $0.09t_u \leq e \leq 0.15t_u$ (Maclennan and Lovell, 2002). These simple equations indicate that net uplift following solidification of underplated material is expected to be $\sim 60\%$ of initial uplift, which does not match the rapid post-uplift net subsidence observed. Moreover, to generate the 350 m of uplift observed, $>$ 2 km of underplate is

required. If a large amount of underplating occurred, evidence of melting (e.g. dykes, sills) in well and seismic data would be expected. The well and seismic data contain no evidence of magmatism or significant shortening (e.g. Figure 2.13, Chapter 2). The proximity of Judd and Bressay to the Icelandic plume at $\sim$ 55 Ma indicate that sub-plate support might have played the key role in generating uplift and subsidence.

3.5.2 Temperature anomalies from the Icelandic plume

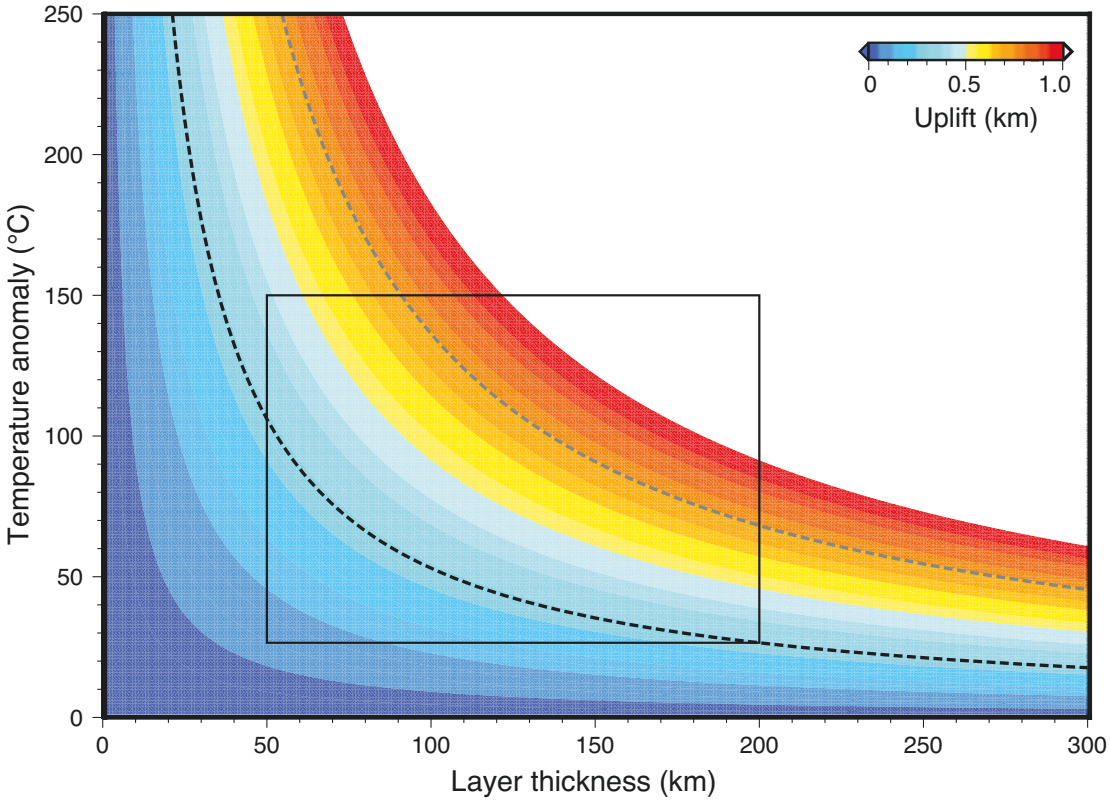


Figure 3.10: Uplift as a function of excess temperature and thickness of low viscosity channel beneath the plate. Black dashed line = 350 m of uplift (Bressay), grey dashed line = 900 m of uplift (Judd). Note strong trade-off between layer thickness and thermal anomaly. Black square denotes geologically reasonable ranges for layer thickness and excess temperature from Rudge et al. (2008).

Stretched and subsided continental lithosphere, such as the Paleocene northern North Sea, has an elastic thickness of a few kilometres, which means that short wavelength changes in sub-plate support should generate observable vertical motions at Earth's surface (Ziegler, 1992; Tiley et al., 2003; Rudge et al., 2008). To investigate the mantle flow required to generate observed uplift and sub-

sidence I calculate excess temperature anomalies and explore the implications for mantle flow using the reinterpreted age of the Bressay landscape. Surface uplift, U, from a subplate thermal anomaly, $\overline{T}$, can be estimated using a simple isostatic calculation,

$$U = \frac{2h\alpha\overline{T}}{1 - \alpha T_{\circ}}, \tag{3.7}$$

where $2h$ is thickness of the anomalously hot layer, $T_{\circ}$ is background temperature, and thermal expansion coefficient $\alpha = 3.3 \times 10^{-5}$ ° C^{-1} (Rudge et al., 2008). If, for example, the background temperature of the plume was 1400 °C ($\sim$ 100–200 ° C greater than normal) and the thickness of the anomalously hot layer is 200 km, the excess temperature, $\overline{T}$, required to produce 350 m of uplift (i.e. peak Bressay uplift) is 50° C. Inspection of Equation 3.7 shows that uplift is insensitive to background temperature. Using a background temperature of 1200°C, for example, changes calculated excess temperature by $< 1°$ C. Results are much more sensitive to the thickness of the hot layer. For example, a 100 km thick layer yields excess temperatures of 100 °C. The upper bound for the temperature of the pulse beneath Bressay is therefore 1450–1500 °C, which is unlikely to have generated much melt beneath modestly stretched lithosphere (White and McKenzie, 1989). Figure 3.10 shows the trade-off between the layer thickness and the thermal anomaly. Peak uplift from the Judd area is $\sim$ 900 m, which indicates a thermal anomaly of 130 ° C for a 200 km thick channel (Hartley et al., 2011). Higher temperatures beneath Judd relative to Bressay are consistent with its closer proximity to the plume centre (see inset in Figure 3.9). Following uplift these regions subsided rapidly in 0.5–1 Ma.

3.5.3 Staged uplift histories

Drainage patterns of Bressay and Judd contain three knickzones that are consistent with a three-stage uplift history (Figure 3.9). The similarity of both uplift histories suggests that they share a common mechanism. Hartley et al. (2011) suggested that the three stage uplift history of Judd was generated by the passage of thermo-chemical pulses beneath the plate originating from the Icelandic plume. The passage of thermal anomalies in a hot channel beneath the plate is attractive because it provides a mechanism for rapid uplift and subsidence. Detailed fluid dynamical modelling (e.g. Larsen et al., 1999) is

beyond the scope of this dissertation; instead, I modify Rudge et al. (2008)'s one-dimensional radial advection model and use our estimates of the time of peak uplift to calculate the age at which the putative thermal anomaly departed the plume centre. Uplift in both regions must have occurred after 58.0 Ma (age of *A.m.* in underlying stratigraphy). Supposing that uplift in Judd and Bressay was generated by the passage of a thermal anomaly it must have travelled between Judd and Bressay before 54.8–55.8 Ma (i.e. age of *A.a* in the Bressay Dornoch Formation). Our observations indicate that the timing of peak uplift in Bressay and Judd is closer than previously thought (cf. Rudge et al., 2008). The maximum difference in age between Bressay and Judd peak uplift is determined by the uncertainty in the age of *A.a* (55.8–54.8 Ma) and the age of infill of Judd stratigraphy constrained by dating of pollen spores (56.1–55.0 Ma: Shaw Champion et al., 2008).

Conservation of mass means that velocity, $u \propto 1/r$, and position of a pulse, r, at a time, t, can be expressed as,

$$r^2(t) = k(t - t_\circ), \tag{3.8}$$

where $t_\circ$ is the time the pulse leaves its origin (Rudge et al., 2008). k characterises the speed of the pulse and has units of diffusivity. Since I have information about uplift at two different positions, I can estimate k using,

$$k = \frac{r_B^2 - r_J^2}{t_B - t_J}, \tag{3.9}$$

where r_B and t_B represents the position and age of peak Bressay uplift, respectively. r_J, t_J are the corresponding parameters for Judd. As $k \propto r^2$, calculated departure time depends strongly on the location of the plume head. Using White and McKenzie (1989)'s plume centre, $r_J = 580$ km and $r_B = 820$ km. However using Lawver and Müller (1994)'s plume centre, $r_J = 1070$ km and $r_B = 1260$ km, and using Jones and White (2003)'s plume centre I obtain $r_J = 770$ km and $r_B = 1100$ km (see inset in Figure 3.9).

3.5.4 Timing and origin of Icelandic plume pulses

Using the uncertainty in age of peak uplift in Judd and the youngest possible age of the Bressay landscape yields $0.2 \leq t_B - t_J \leq 1.3$ Ma. I then use the

uncertainty in the location of the plume centre to obtain three different values for $r_B^2 - r_J^2$ for each of the plume centres. Using Equation 3.9 I obtain three different values for k for each plume centre. Rearranging Equation 3.8 and inserting the range of k and radii values from the respective plume centres indicates that the latest time a thermal pulse could have left the plume centre to generate the Bressay and Judd landscapes is $t_\circ = 57.4 \pm 2.2$ Ma. I suggest that the passage of thermo-chemical pulses from the Icelandic plume could have generated the Paleocene to Eocene vertical motions observed in Bressay and Judd. Our reinterpreted age of the Bressay landscape indicates that these thermal anomalies travelled between Bressay and Judd at rates in excess of $\sim$ 150 km/Ma, which is similar to the mantle flow velocities calculated using the geometry of the V-shaped ridges south of Iceland (Jones et al., 2002b). The simple model used indicates that thermal anomalies directly beneath the plate can travel orders of magnitude faster than plate velocities.

3.6 Evidence for regional vertical motions in the North

In Chapter 2, a buried terrestrial landscape located just north of Bressay was also extracted. Although the North Bressay region lacks intersecting well logs and check-shot data, its proximity to Bressay suggests the velocity models and decompaction parameters used for Bressay in this Chapter are applicable. After depth conversion and decompaction, the surface can be reconstructed and is shown in Figure 3.11a. The total relief of the landscape is 500 m, with rivers draining towards the east towards the paleo-coastline. Drainage systems are extracted for the 6 main basins to obtain a total of 107 rivers. Their longitudinal profiles are shown in Figures 3.11b–g. Large knickzones (30–50 m) can be observed in the larger basins which have reliefs up to 400 m

.

We invert the two main rivers from the two largest basins for an uplift history (Figure 3.12). Three large knickzones correspond to three uplift events, labelled I, II, and III. The lack of biostratigraphy or intersecting wells suggest that the timing and duration of the channelized surface cannot be directly constrained.

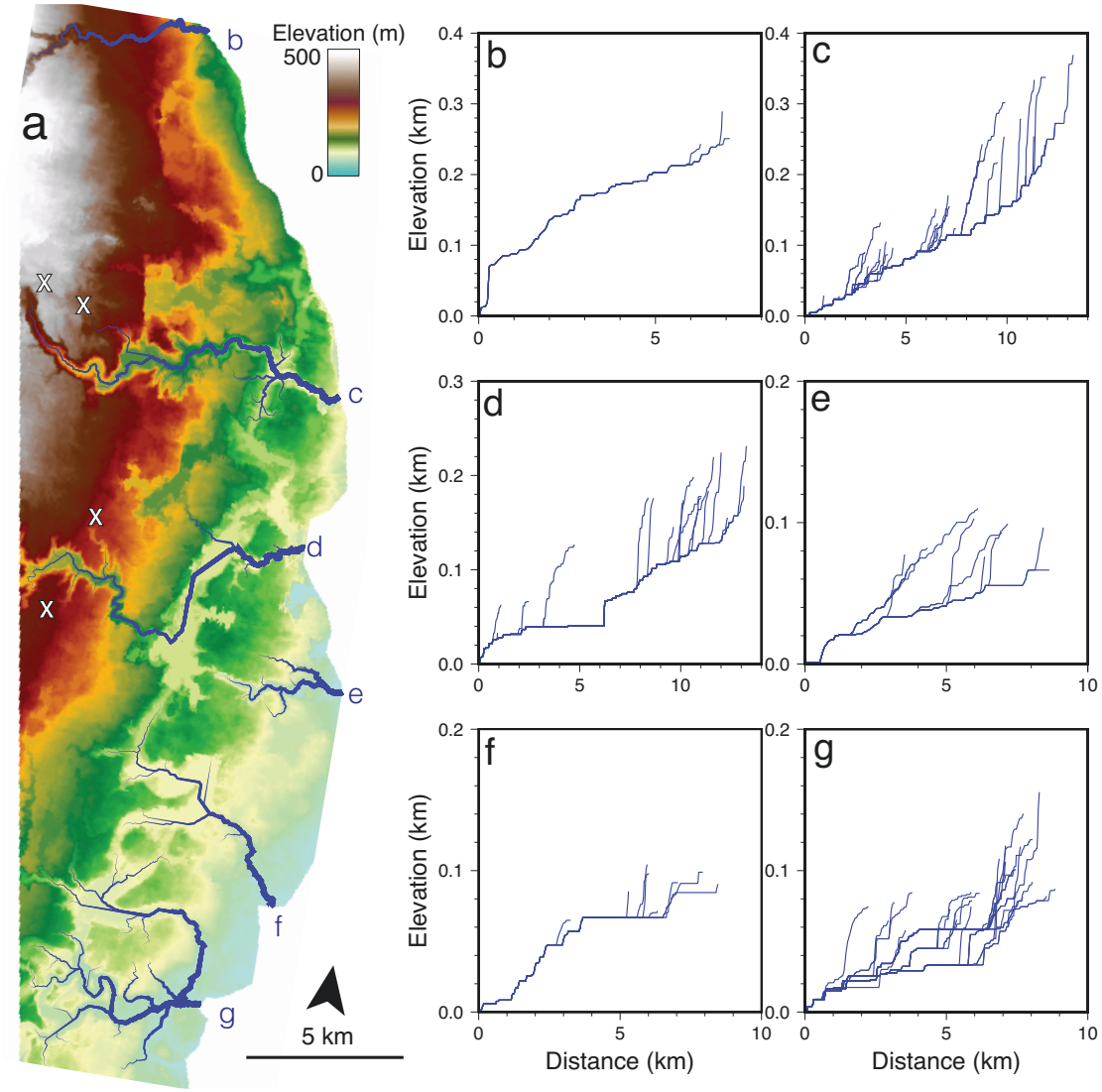


Figure 3.11: (a) Depth-convered and decompacted North Bressay landscape. Blue lines = extracted drainage from 6 main basins (b-g). (b-g) Longitudinal profiles (total = 107) of rivers in North Bressay separated by basins.

However, the overlying sediments are of similar age to those of the Bressay (Late Paleocene-Early Eocene sandstones). Since there are no other heavily channelized surfaces in both regions, and considering their proximity (∼30 km) and presence of coarse sandstones and paleo-coastlines in both, it is likely that they formed around the same time. The duration of exposure (uplift) is a factor of the erosional parameters values, v, which were used. In the Judd region v = 4.75±0.1 Ma^{-1}, whereas in Bressay, v = 1.6±0.1 Ma^{-1}. Using these values implies the landscape formed between 1–3 Ma, which is consistent with

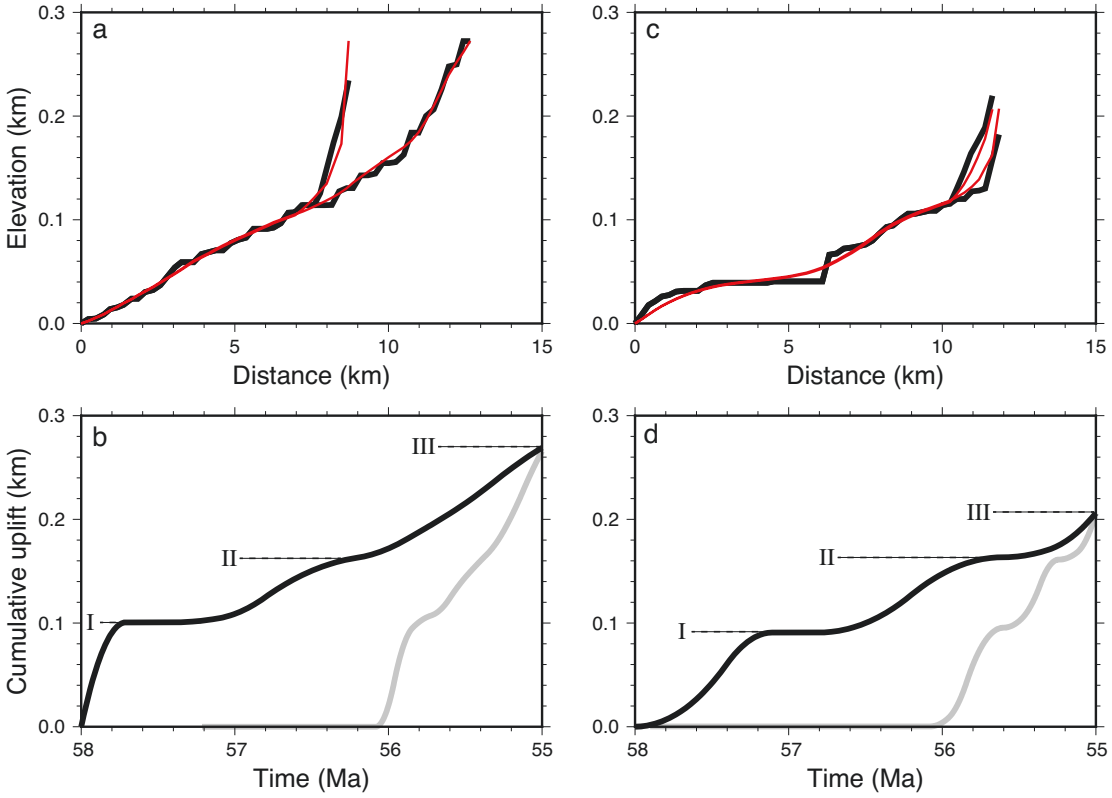


Figure 3.12: Joint inversion of four rivers in the two largest basins in North Bressay for uplift rate as a function of time. (a,b) Two largest rivers in basins c and d, respectively (see Figure 3.11). Black = observed river profiles. Red = best-fitting theoretical profiles. (c,d) Cumulative uplift history that produced theoretical profiles in (a) for basins c and d. Black line = erosional parameter v = 1.6±0.1 Ma^{-1}; grey line = erosional parameter v = 4.75±0.1 Ma^{-1}. Uplift events are labeled I, II, III.

Bressay and Judd exposure times.

The presence of an additional terrestrial channelised surface confirms that regional uplift was widespread and not unique to the Bressay and Judd regions. The geometries, distribution, and ages of these incised landscapes are an important constraint on dynamic support in the North Atlantic Ocean. A continued increase in discovering ancient terrestrial landscapes is a key mechanism for understanding and quantifying mantle convection in both a spatial and temporal context.

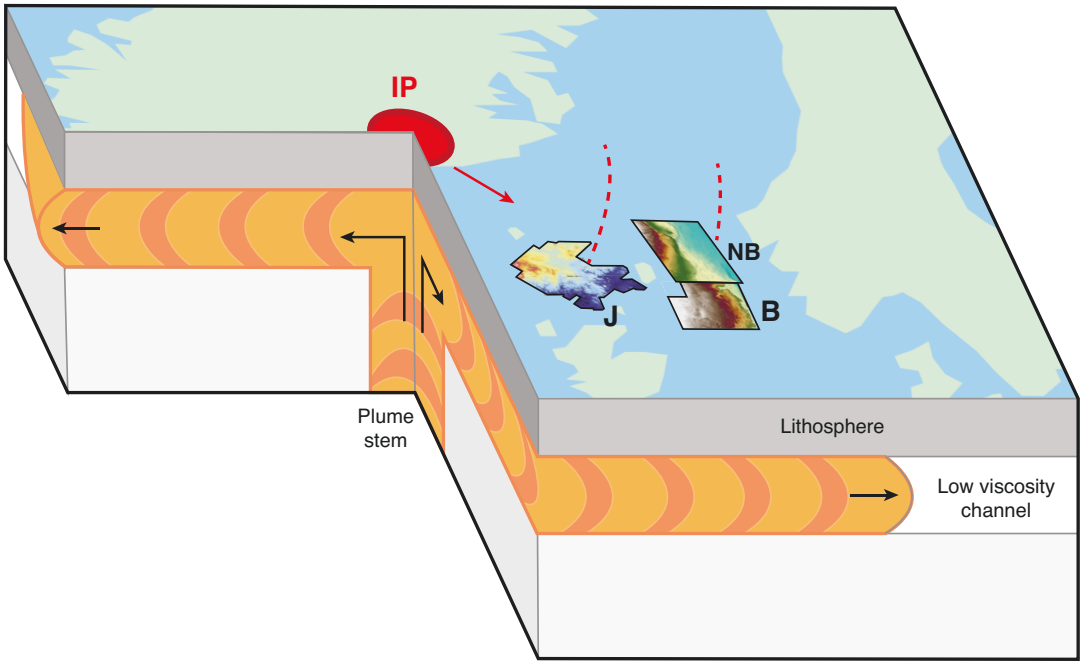


Figure 3.13: Cut-away cartoon showing buried terrestrial channels mapped in the North Atlantic Ocean relative to the Icelandic plume (IP) at ~ 55 Ma. J = Judd region, B = Bressay region, NB = North Bressay region. Red circle = present-day Icelandic plume. Orange layer = idealized plume layer spreading radially from plume stem with thermal anomalies in red. Black arrows = direction of plume flow. Red arrow = planform radial plume flow. Red dashed lines = positions of plume flow during peak uplift of each landscape.

3.7 Chapter Summary

In the previous chapter, it was shown that the Bressay region contains a buried, incised landscape 1.5 km below the seabed. Fluvial drainage patterns, beach ridges, and a paleo-coastline were mapped using the three-dimensional seismic volume, which indicate the erosional surface was generated subaerially and then rapidly submerged. The first and last occurrences of the marine dinocysts *Apectodinium augustum* and *Alisocysta margarita* in underlying and overlying stratigraphy indicate that this landscape formed between 58–55 Ma. Geochemical analyses of cuttings from an interval that includes the erosional surface contain angiosperm (flower plant) debris. Core samples and gamma-ray logs from wells that intersect mapped channels indicate that the landscape was first buried by terrestrial-derived clastic material and then by marine mudstones, which suggest that vertical motions are evident from the Bressay stratigraphy.

In this chapter, checkshot data and well-logs intersecting the mapped channel were used to depth-convert and decompact the buried landscape and flow routing algorithms were used to extract drainage patterns from the landscape. The extracted longitudinal river profiles have three knickzones and a relief of $\sim$350 m. Hundreds of meters of relief, a lack of evidence for shortening in seismic data, and rapid subsidence indicate that lithospheric shortening, glacio-eustasy, and underplating did not create this erosional landscape. River profile shapes are similar to those extracted from a slightly older buried landscape in the Judd region $\sim$400 km to the west.

I inverted the longitudinal profiles of the two main rivers for an uplift rate history. The best-fitting history has three phases of high uplift rates (> 0.5 mm/a), which are slightly smaller than those calculated using the Judd rivers. These observations are consistent with passage of thermo-chemical pulses during inception of the Icelandic plume. The reconstructed uplift history of Bressay contains important information about the velocity and temperature of thermochemical convection generated by the plume. Simple isostatic calculations indicate that the maximum thermal anomalies beneath Judd and Bressay were $\sim$130 °C and 50 °C, respectively. A simple model of radial sub-plate flow suggests that these thermal anomalies departed the plume centre as late as 57.4 ± 2.2 Ma and traveled with a velocity in excess of $\sim$150 km/Ma (e.g. Figure 3.13). The presence of a third ancient buried landscape suggest that a large number of these landscapes may exist. Profiles in North Bressay are similar in magnitude and shape to those in Bressay and also yield a three-stage uplift history. Mapping of ancient buried landscapes is a rich source of geomorphological and geodynamic information, and the large database of buried systems can be used to constrain the evolution of mantle convective processes at a high spatial resolution.

The existence and accessibility of these buried landscapes allow us to probe the behaviour of the Iceland plume in the past, which can be combined with younger constraints to obtain a long-term understanding of its behaviour up to the present-day (Parnell-Turner et al., 2014). However, dynamic support con-

tinues to play an important role in generating uplift in the North Atlantic today. In the next chapter I investigate drainage systems and landscape evolution in Iceland to constrain modern uplift and erosion histories above the present-day Icelandic plume on which it currently sits.

Chapter 4

Iceland fieldwork: geological mapping, sampling, and elevation models

4.1 Chapter Introduction

In actively deforming regions, fluvial systems are strongly regulated by uplift. River geometries record histories of vertical motions that can be used to examine the driving forces generating topographic relief. In the previous chapters, I showed that ancient drainage networks can be used to quantitatively constrain the behaviour of the Icelandic plume. Iceland's dramatic landscapes offer a unique opportunity to disentangle histories of uplift generated by postglacial rebound, volcanism, plate spreading, and dynamic support from the Icelandic plume occurring in the present-day. Broad knickzones observed along Iceland's large rivers, and its powerful waterfalls and deep canyons, hint that regional processes have generated significant relief. However, their histories are poorly constrained. In this chapter I discuss field observations, sampling of fluvial terraces, and high-resolution drone photogrammetry which are used to determine the erosional history of Iceland's largest knickzone located in Jökulsá á Fjöllum, northeast Iceland.

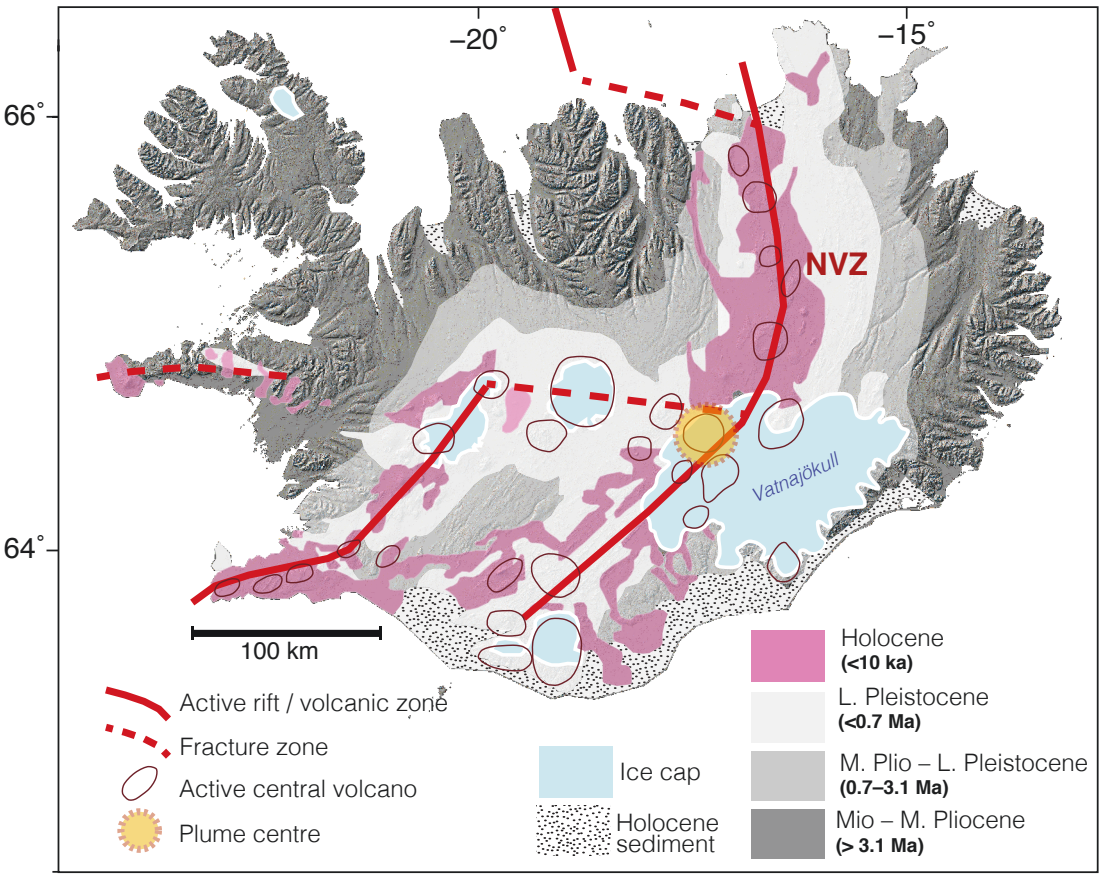


Figure 4.1: Map of Icelandic geology and topographic relief from ASTER GDEM (Jóhannesson and Sæmundsson, 1989; Tentler and Temperley, 2007; Martin et al., 2011). NVZ = Northern Volcanic Zone.

4.2 The modern Icelandic landscape

4.2.1 Geological setting

Iceland is a 100×10^3 km^2 basalt island in the North Atlantic Ocean and is part of a 350×10^3 km^2 basalt plateau which began forming $\sim$ 24 Ma as a product of the interaction between a spreading plate boundary and a mantle plume (Vogt, 1971; Hart et al., 1973; White et al., 1995; Wolfe et al., 1997; Thordarson and Larsen, 2007). The Mid-Atlantic Ridge cuts diagonally across the middle of the island (NE–SW) and forks into two branches in the south forming three components: the Northern, Eastern, and Western Volcanic Zones (Figure 4.1). The island is mainly composed of basaltic rock with ages increasing with distance from the ridge (Figure 4.1). The oldest exposed rocks are 14–16 Ma (Moorbath et al., 1968). The island rises more than 3 km above the surrounding sea floor

and has crustal thicknesses of 10–40 km (Gudmundsson, 2000; Thordarson and Larsen, 2007; Green et al., 2017).

Iceland's topography and geological record contain excellent evidence for regional and local uplift moderated by glacial and fluvial processes (Geirsdóttir et al., 2007; Bjornsson, 2009). Stratigraphic records on- and offshore, crustal thickness, and basalt and ocean chemistry indicate a punctuated history of Neogene uplift and erosion (Jones et al., 2002b; Verhoeven et al., 2011; Shorttle and Maclennan, 2011; Parnell-Turner et al., 2014). Uplift measurements at spot locations from Global Positioning Satellite (GPS) and InSAR data have been used to constrain faulting, seismicity, magmatism, and post-glacial rebound (Sigmundsson et al., 1997; Pagli et al., 2007; Sturkell et al., 2006; Árnadóttir et al., 2009). However, a quantitive understanding of glacial and fluvial processes in Iceland and their relative roles in generating relief is lacking. The next two subsections illustrate regional examples of these processes as observed from fieldwork undertaken in Iceland in June 2017.

4.2.2 Glacial vs. fluvial signals

Geomorphological and stratigraphic evidence for island-wide glaciation prior to 8 ka include hanging and U-shaped valleys, drop stones, moraines, drumlins, and striated bed rock (4.2; Evans et al., 1999; Spedding and Evans, 2002; Kjær et al., 2008). Unloading of the lithosphere during deglaciation has generated up to ~ 100 m of uplift across large parts of the island, providing an important constraint on mantle viscosity (Pagli et al., 2007). The last major deglaciation (Preboreal) in Iceland began at ~ 10 ka, when ice caps that previously extended to the modern coastline began retreating and reached their current extent at ~ 8 ka (Nordhdahl et al., 2008). Large eroded U-shaped valleys (> 500 m height and 1–3 km width) can be observed in the northern, western, and eastern fjords with small alluvial streams post-dating valley formation (see Figure 4.2). In many locations fluvial erosion can exceed 100 m and generate significant relief in the otherwise broad, long-wavelength glacial valleys (Figure 4.3). These observations are consistent with field studies that indicate fluvial erosion can dramatically increase relief in previously glaciated



Figure 4.2: (a)–(b) Glacial U-shaped valleys observed from Þjoðvegúr road, ∼ 20 km west of Akureyri in the Trollaskagi Peninsula in north Iceland. White dashed line = U-shaped valley; white arrow = stream.

landscapes (Koppes and Montgomery, 2009).

4.2.3 Drainage patterns

Stratigraphy and historical accounts indicate that fluvial erosion during high-discharge glacial outburst floods (jökulhlaups) can generate several meters of relief in short amounts of time (Smith et al., 2000; Tomasson, 2002). Although much work has been done to quantify and map glacial outburst floods, not much is known about the time-averaged fluvial erosion processes that have sculpted the Icelandic surface over thousands of years (Baker and Milton, 1974; Alho et al., 2005; Baynes et al., 2015b). Drainage patterns were extracted from ASTER GDEM and LMÍ (Landmælingar Íslands Hæðarlíkan) digital elevation data with 25 and 15 m resolution, respectively (Figure 4.4a). The eight largest

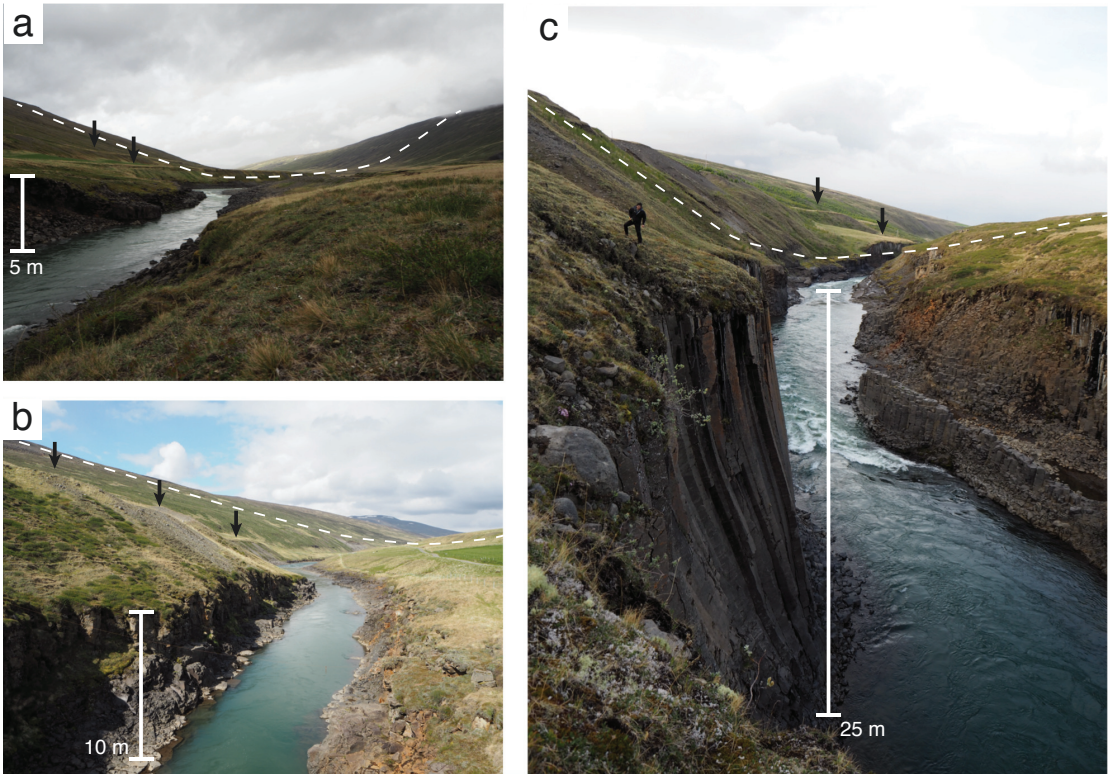


Figure 4.3: (a)–(c) Glacial and fluvial erosional landforms in Jökulsá á Brú, east Iceland. White dashed line = long-wavelength valley; white line = short-wavelength fluvial incision; black arrows = abandoned fluvial terraces.

river basins cover 80% of the surface of the island. Longitudinal profiles of largest rivers show that many of the island's large waterfalls (e.g. Gullfoss & Goðafoss; Figure 4.5) sit within much larger convex-upward changes in slope (i.e. knickzones) that are tens to hundreds of kilometers wide and hundreds of meters high (Figure 4.4b–e).

The pervasiveness of knickzones throughout Iceland's drainage network suggests that its erosional system is responding to regional changes in base level (Howard et al., 1994). To determine the evolution of Iceland's modern landscape I studied the erosional history of its largest knickzone located in Jökulsá á Fjöllum.

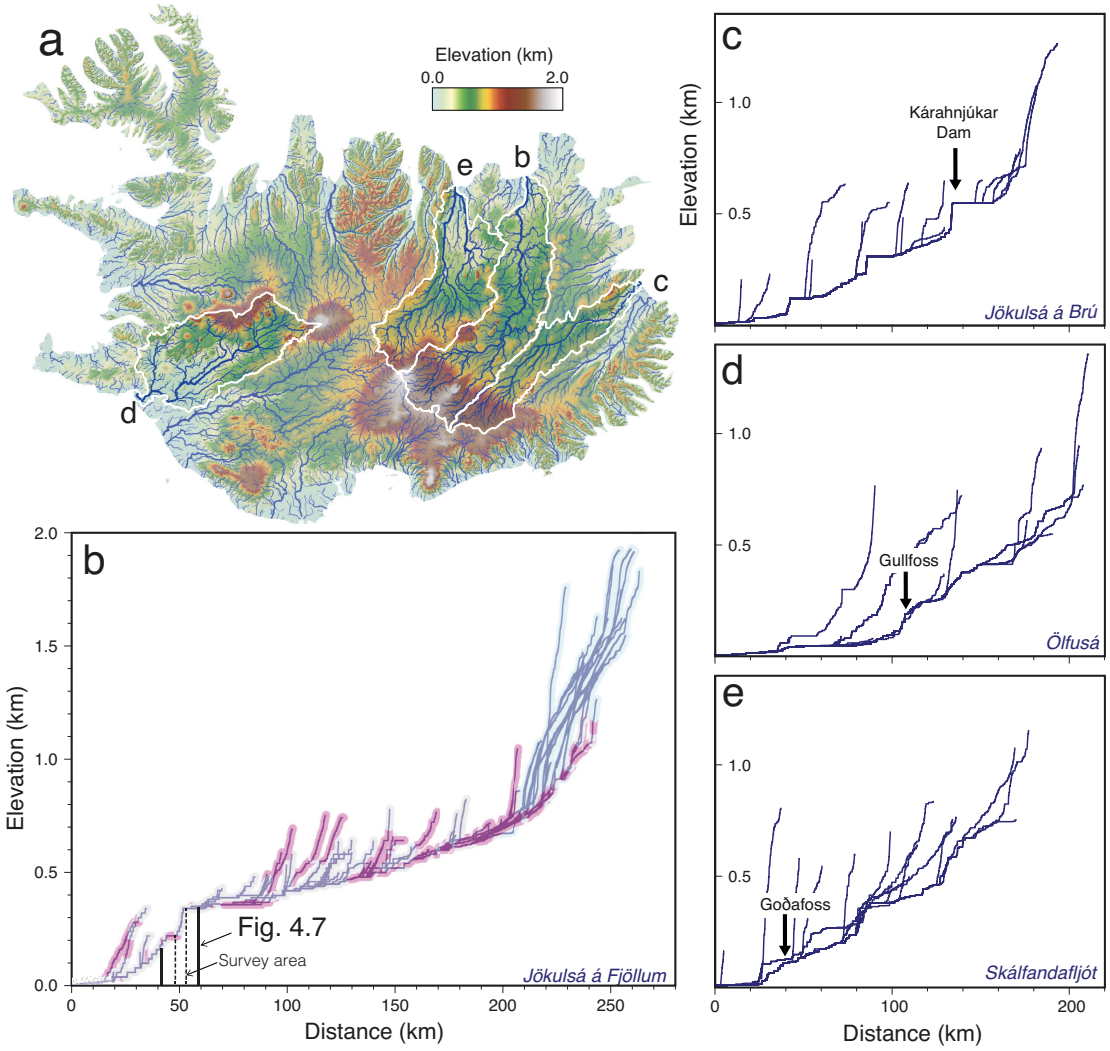


Figure 4.4: (a) Longitudinal river profiles extracted from LMÍ DEM and underlying geology of Jökulsá á Fjöllum. (b)–(d) Longitudinal river profiles of Jökulsá a Brú, Ölfusá, and Skálfandafljót shown in planform in a). Y-axis = elevation (km). Black arrows = waterfalls and dams.

4.3 History of Jökulsá á Fjóllum

4.3.1 Jökulsá á Fjóllum and Jökulsárglúfur canyon system

Jökulsá á Fjöllum flows $\sim$ 200 km from its source beneath the Vatnajökull glacier to the sandur plains in Öxarfjörður in the Arctic Ocean and runs subparallel to the Northern Volcanic Zone, through the Jökulsárgljúfur canyon (Figure 4.6). Total drainage area of the river is $\sim$ 8000 km^2 and maximum annual discharge is $\sim$ 500 m^3 s^{-1} (Baynes et al., 2015a). Cross-sections through the river show relief downstream of its large fluvial knickzones can exceed relief

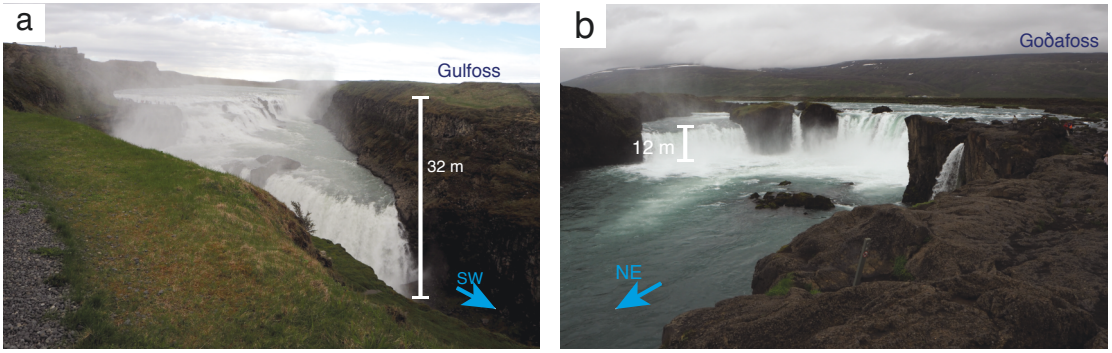


Figure 4.5: Waterfalls in Iceland. (a) Gulfoss, located in the canyon of Hvítá river in southwest Iceland. Blue line = direction of river flow. White line = height of waterfall. (b) Goðafoss, located in the Skálfandafljót river in north Iceland.

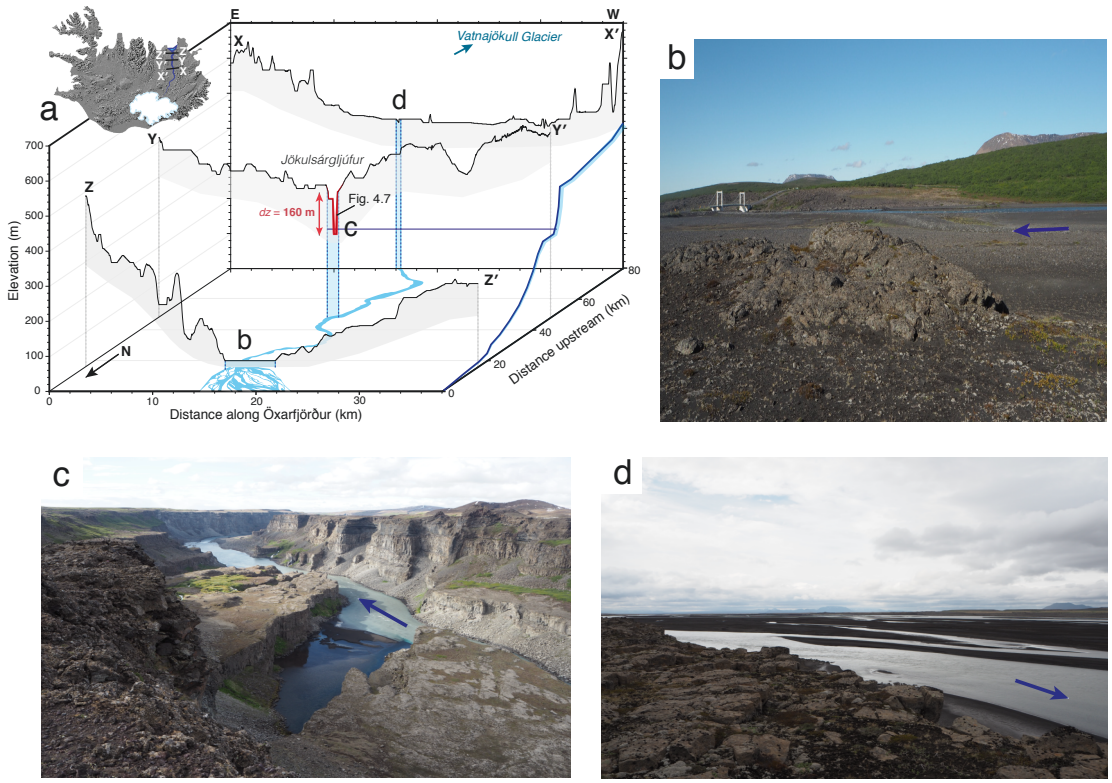


Figure 4.6: Cross-sections perpendicular to Jökulsá á Fjöllum extracted from LMÍ DEM; note inset map shows location of cross-sections. Light/dark blue curves = projected planform/longitudinal profiles of the river. Red = fluvial incision in Jökulsárgljúfur canyon. Note broad U-shaped valley upstream. (b)–(d) Photos of river morphologies in down-, mid-, and upstream are shown in (b)–(d). (b) Flat portion of river mouth (sandur plain). Blue arrow = direction of flow. White bridge = 10 m high for scale. (c) Incised canyon $\sim$ 45 km from mouth. Canyon width = 200 m. (d) Upstream flat, braided, alluvial reach of river. Width of visible stream = 10 m.

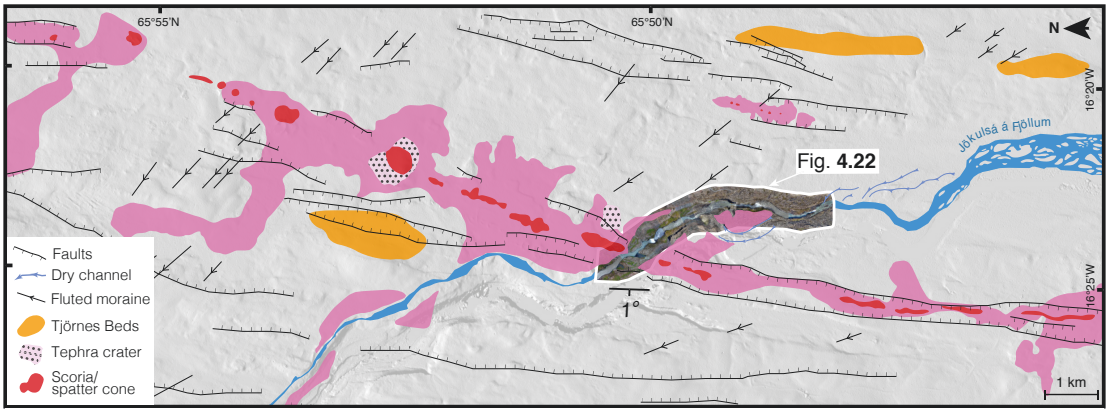


Figure 4.7: Jökulsárgljúfur canyon geology and ArcticDEM topography. White polygon = location of study site and UAV DEM (see Figure 4.22). Pink lithology = Holocene lava field; Grey lithology = Lower Pleistocene basalt (see Figure 4.1).

upstream (Figure 4.6). Upstream at distances > 50 km from the mouth, the river is flat and heavily braided. The surface is covered in post-Holocene deposits and rock outcrops near the river are rarely seen (Figure 4.6d; Jöhannesson and Sæmundsson, 1989). A broad, glacial valley signal can be seen from the topographic cross-section at this distance (Figure 4.6a). The mouth of the river (located in the sandur plains) is also flat, and is flanked by topographic highs from the fissure systems and volcanic centres of the Northern Volcanic Zone (Figures 4.6a,b). At an upstream distance ~ 50 km, reliefs of ~ 160 m are observed in Jökulsá á Fjöllum, corresponding to the Jökulsárgljúfur canyon system (see Figure 4.7). This canyon sits within the broad knickzone in Jökulsá á Fjöllum (see right-side of Figure 4.6a). The following sections will focus on fieldwork (geological and geomorphological mapping, sampling, and in-situ digital modelling) undertaken in the Jökulsárgljúfur canyon, in particular the 5-km long study-site outlined in white in Figure 4.7.

4.3.2 Evidence for fluvial erosion in Jökulsárglúfur

The Jökulsárgljúfur canyon is located on a broad knickzone comprising three large waterfalls: Selfoss (12 m), Dettifoss (48 m), and Hafragilsfoss (26 m) in Figures 4.8a,d,e. The waterfalls are separated laterally by ~ 1 km and have similar shapes. Selfoss has a distinct planform V-shape with discharge being concentrated at its centre (Figure 4.8a). Both Dettifoss and Hafragilsfoss also display a V-shaped morphology, however due to the course of the river, flow

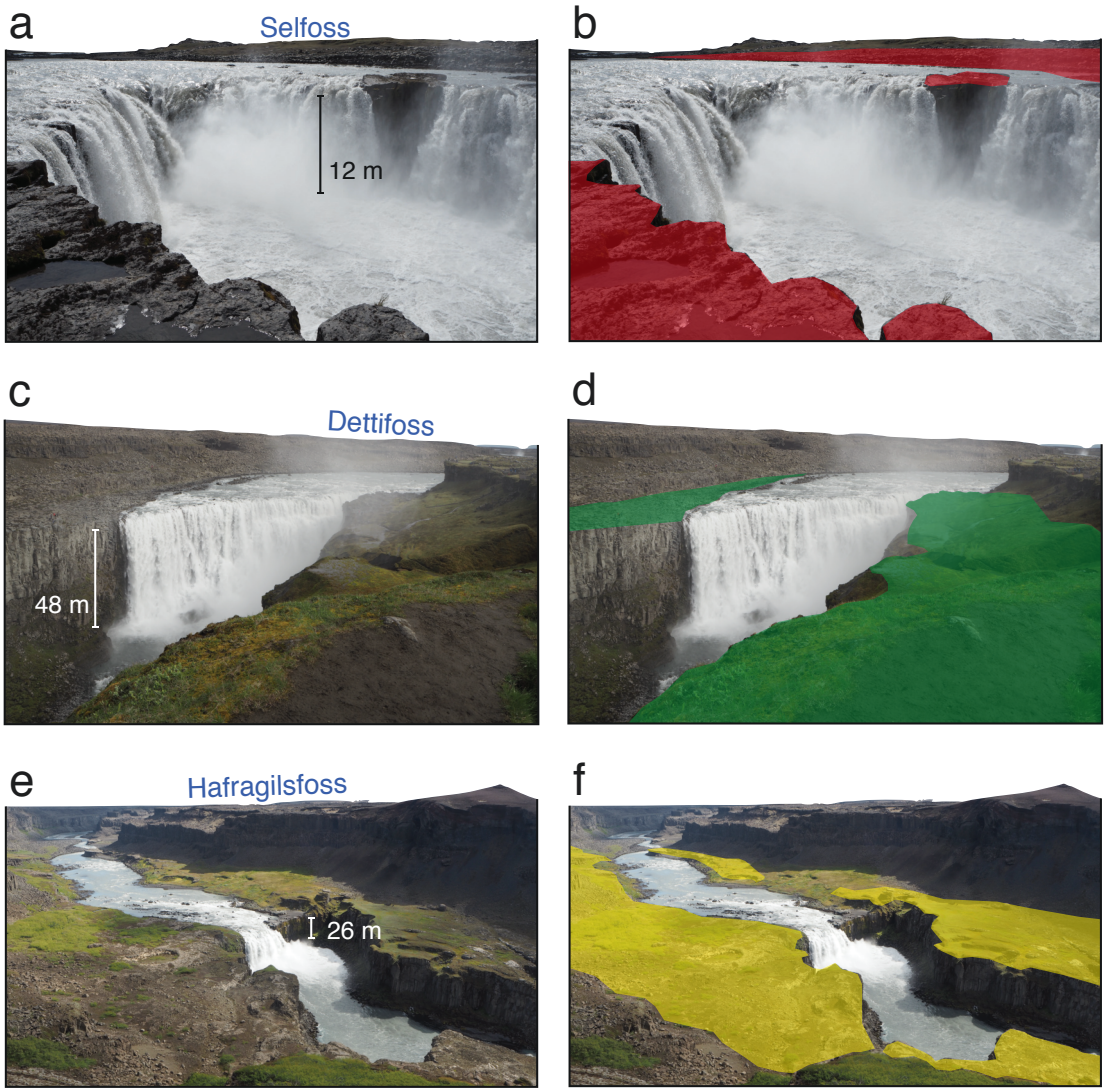


Figure 4.8: Three main waterfalls in Jökulsárgljúfur with increasing distance downstream and their mapped abutting terraces. (a)–(b) Selfoss (12 m); (c)–(d) Dettifoss (48 m); (e)–(f) Hafragilsfoss (26 m). Terraces A, B, C are illustrated in red, green, and yellow, respectively.

is concentrated on one side (Figure 4.8c). Figure 4.8 shows the waterfalls and the prominent fluvial terraces which abut Selfoss, Dettifoss, and Hafragilsfoss. The terraces crop up at the same heights as the top of the waterfalls, and are continuous for several hundred meters downstream on both sides of each waterfall. Terraces A (red), B (green), and C (yellow) correspond to Selfoss, Dettifos, and Hafragilsfoss, respectively.

The three fluvial terraces are horizontal and contain evidence of flutes, scours, tool marks, potholes, and polished surfaces (see Figure 4.9)a–d. These observations suggest that terraces were abandoned due to waterfall retreat and that fluvial abrasion plays an important role in generating relief from vertical incision. Evidence for plucking and recent columnar collapse can also be seen (Figure 4.9e–f). The relative importance of abrasive vs. plucking processes in generating fluvial terraces is not well understood. Importantly, these fluvial features show that significant fluvial erosion is occurring in the present-day and is not limited past episodic flooding.

4.3.3 Rifting and the Northern Volcanic Zone

The canyon has walls up to > 100 m high containing layered basalt flows with thickness between 5–50 m (Figure 4.10). The flows are composed of vertical and subvertical basalt columns. Examples of basaltic morphologies are shown in Figure 4.10. The columns are generally vertical upstream (Figure 4.10a), but tend towards more chaotic orientations with increasing distance downstream. Highly radial and block entablature jointing, as shown in Figure 4.10a,c,d, are most likely the result of accelerated cooling of the upper portion of the lava flow by inundation of the flow surface by water while the flow was still hot, resulting in textural signs of quenching (Lyle, 2000). Note that the terms colonnade and entablature describe the internal structure of lava flows: a regular zone of near-vertical columns at the base, and a zone of more irregular columns, respectively (Figure 4.10a). These important features are described in more detail in Section 4.4.4.



Figure 4.9: Examples of fluvial abrasion along Jökulsárglúfur canyon terraces. (a) Example of sample site AE03. Note flute marks on terrace. White arrow = direction of river flow. (b) High density of scour marks on eastern side of Terrace B. (c) Flutes, potholes, and scour marks on Terrace B close to Dettifoss. (d) Tool marks and flutes at higher state of degradation in Terrace C. (e)–(f) Columnar basalt plucking and toppled blocks on eastern side and western side of Selfoss.

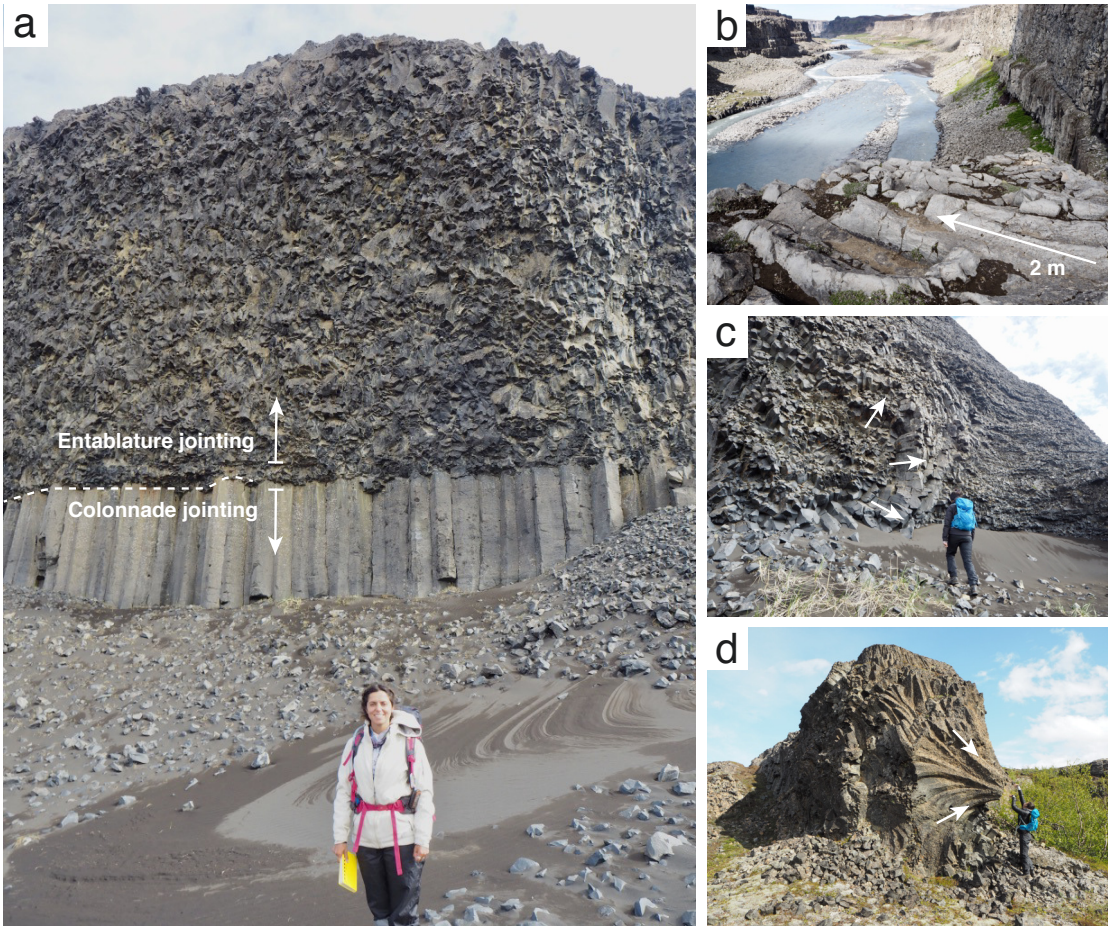


Figure 4.10: Columnar basalt morphologies in Jökulsárgljúfur. (a) Colonnade-entablature structure with strongly defined boundary between both jointing types. (b) Horizontal, curved columns. (c) Radial (outward) columnar jointing; white arrows = joint orientation. (d) Radial (inward) columnar jointing.

The upstream portions of Jökulsárgljúfur canyon consist of simple downcutting of flat, basaltic plateau by Jökulsá á Fjóllum. However, toward the downstream portions (after Hafragilsfoss), several structures intersect and interact with the river. The lower portion of Jökulsárgljúfur canyon cuts diretly across the post-glacial (Holocene) lava remnants ($\sim$ 8.5 ka from tephrochronological dates) which mostly cap or are perched upon the canyon walls (Figure 4.11; Elíasson, 1974). The Rauðuborgir-Randhólar crater row and Sveinar graben are fissure systems associated with the volcanic centres in the Northern Volcanic Zone (see Figures 4.7 and 4.11). The fissures contain crater rows distributed linearly in a roughly N–S orientation for $\sim$ 30 km. Tephrochronological dating suggests they fissures erupted $\sim$ 6 ka, and may have temporarily dammed the river

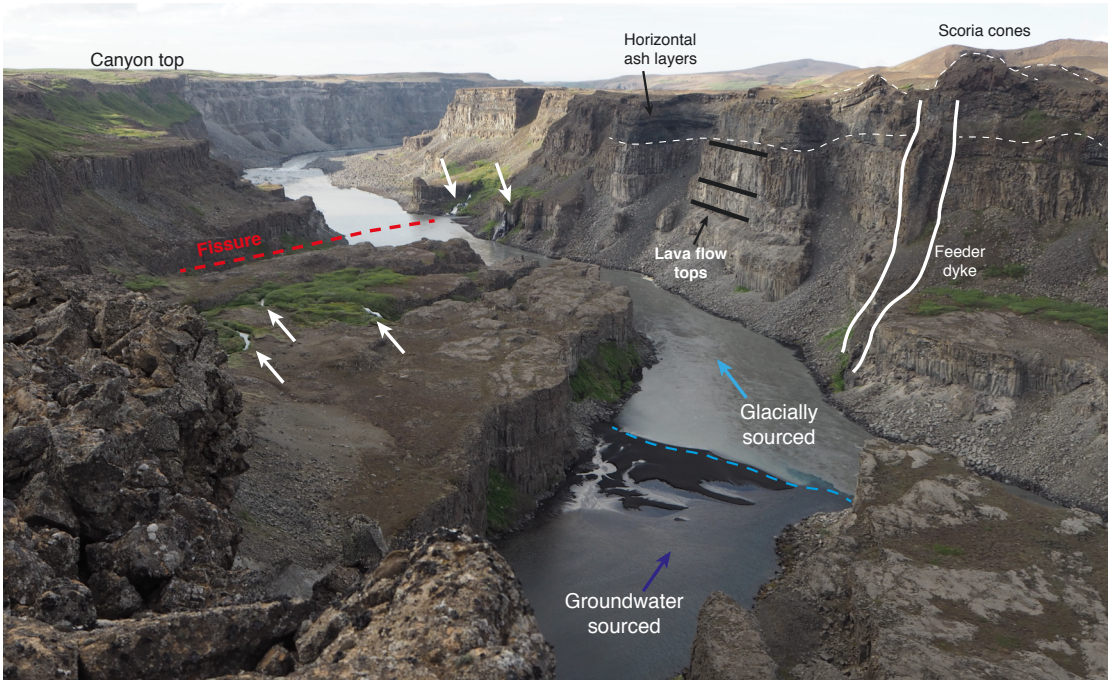


Figure 4.11: Hydrologic, tectonic, and volcanic structures in Jökulsárgljúfur downstream of Hafragilsfoss. White arrows = springs. Dashed blue line = boundary between spring-fed and glacially sourced water.

(Thorarinsson, 1960; Elíasson, 1974). The canyon cuts through one of the cones of the Rauðuborgir-Randhólar fissures, exposing its interior structure and the topmost 100 m of the feeder dyke (Figure 4.11).

After Hafragilsfoss, several springs join the main trunk of the river on both sides of the river. These can be observed both from theatre-headed alcoves and the visible interaction between clear spring water and more opaque, light brown-blue glacially-derived water (see Figure 4.11). Dry valleys cutting in to the main present-day trunk are also observed, which are attributed either to episodic flood spillways or abandoned paleo-river courses.

4.3.4 Deriving an erosion history of Jökulsárgljúfur

A quantitative understanding the erosional history of the canyon can be achieved by dating the abandoned fluvial terraces which are preserved across the 5-km canyon system. In order to do this I sampled various sites along each of the terraces with increasing distance from each waterfall. These samples can then be used to determine exposure ages from fluvial erosion using cosmogenic ^{3}He

dating techniques. The following section will focus on background theory and sampling methods and field constraints required for this technique.

4.4 Sampling of fluvial terraces

4.4.1 Cosmogenic ^{3}He dating technique

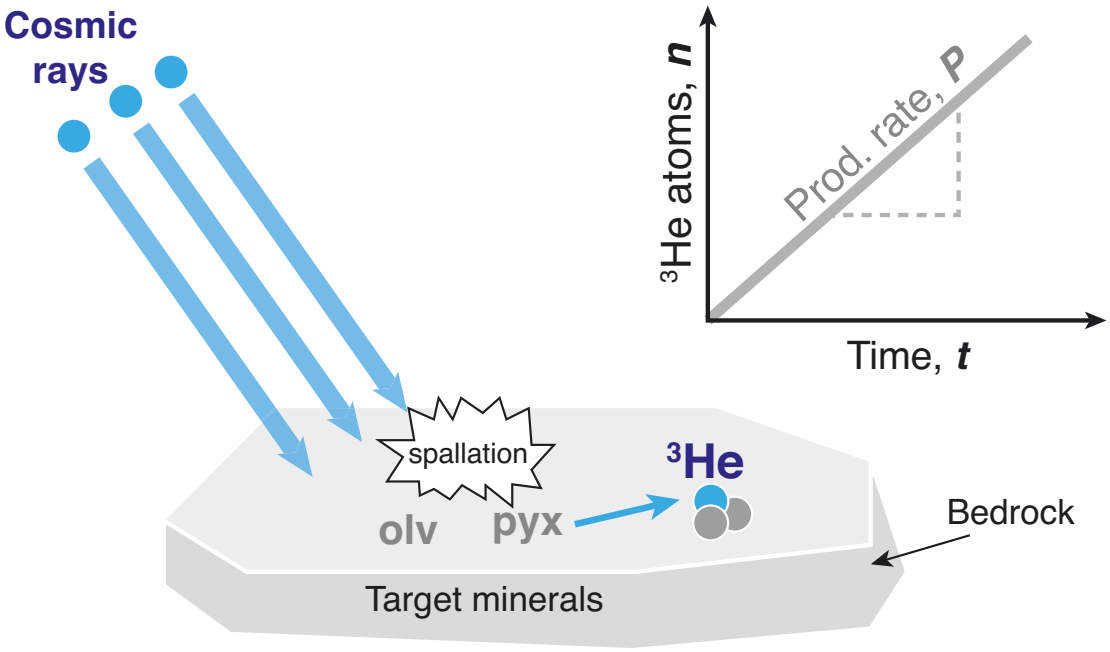


Figure 4.12: Cartoon showing production of ^{3}He from spallation of olivine (olv) and pyroxene (pyx) target minerals in exposed bedrock surface resulting from incident cosmic rays. Blue circles = neutrons; grey circles = protons. Inset shows relationship between ^{3}He atoms, time, and production rate.

Cosmogenic radionuclide dating is a geochronological technique used to estimate the length of time a rock has been exposed at the Earth's surface. Earth is continuously bombarded by cosmic rays sourced from interstellar and circumstellar material swept over by shock waves from supernova explosions (Hayakawa et al., 1958; Drury, 2012). The cosmic rays are composed of high energy particles (protons and alpha particles) and upon atmospheric entry they interact with the atmosphere to produce a cascade of secondary particles. These reactions result in decreasing particle energies as they approach the surface of the Earth (bedrock), where the cosmic ray is predominantly composed of neutrons (Figure 4.12; Masarik and Reedy, 1995). When the neutron collides

with a target atom (e.g. O, Mg, Si, Ca, Fe, Al) it can dislodge one or more protons or neutrons from the atom, producing a different isotope of the original element or a new element (Figure 4.12). This in-situ reaction is termed neutron spallation and results in a continuous accumulation of cosmogenic nuclides with increasing exposure time. ^{3}He has the highest production rate of all cosmogenic nuclides and low detection limit on conventional mass spectrometers so it can be used to date young surfaces ($<$ 3000 kyr) as well as extremely long exposures because it is a stable isotope (Gosse and Phillips, 2001). Due to its isotopic stability, the number of cosmogenic nuclides is essentially directly proportional to the exposure time (see inset in Figure 4.12).

4.4.2 Fieldwork and sampling in Jökulsárgljúfur

Samples were collected along Jökulsá á Fjöllum in northeast Iceland in June 2017. The lithology of Jökulsárgljúfur terraces consists uniquely of coarse-grained basaltic lavas with large, abundant pyroxene and olivine grains ($>$ 250 μm). These target minerals produce ^{3}He cosmogenic nuclides at the surface and canyon ages have approximate ages of a few ka, which suggests the terraces are suitable for ^{3}He dating. ASTER, LMÍ and ArcticDEM digital elevation data, satellite imagery, and field mapping were used to identify suitable sampling sites. Fluvial terraces were identified by their geometries (e.g. close to horizontal, abutting waterfalls) and presence of geomorphological markers such as scour marks, potholes, polishing, flutes, boring, striations (see Figures 4.9a–d). A cordless Milwaukee angle-grinder was used to incise a grid of 5×2 cm rock cuboids within the upper 2 cm of near-horizontal fluvial surfaces (see Figure 4.13). A hammer and chisel were then used to extract the cuboids. A sledgehammer was used when sampling edges of bedrock. Approximately 1 kg of rock was collected for each sample site, although sample sizes varied by $\sim$ 50% depending on rock strength, degradation state, grain size, vesicularity, and angle-grinder battery life. Twenty-five rock samples from three fluvial terraces were extracted at regular distances downstream from the waterfalls for ^{3}He cosmogenic exposure dating. An additional sample was collected 40 km downstream at the mouth of the river, and one from a terrace in Jökulsá á Brú, located in east Iceland.

4.4.3 Sample corrections & field constraints



Figure 4.13: Example sample site showing tools and rock extraction method used for ^{3}He technique. 1 = angle-grinder; 2 = hammer + chisel. Note resulting 'waffle'-cut of 5 $\times$ 2 cm squares, with only upper 2 cm of rock sampled.

Once the samples have been extracted, the number of ^{3}He atoms, n, within each sample can then be measured to deduce the amount of time, t, it has been exposed at the surface (i.e. when the terrace was last eroded and abandoned by the river). This relationship can be written as $t = n/P$ (see Figure 4.12), where P is cosmogenic ^{3}He production rate and is unique to each sampling site as it depends on elevation and latitude. A more in-depth analysis of production rates, and their derivations, quantities, and uncertainties is discussed in Chapter 5. In the following subsections I discuss field observations for the samples which allow us to assess whether any corrections can be applied to ensure the measured number of ^{3}He atoms n is an accurate estimate of t. I include the following considerations: location of the sample within the lava flow column, the presence of non-cosmogenic ^{3}He, shielding of rays due to topographic obstruction, and ground cover above sample site.

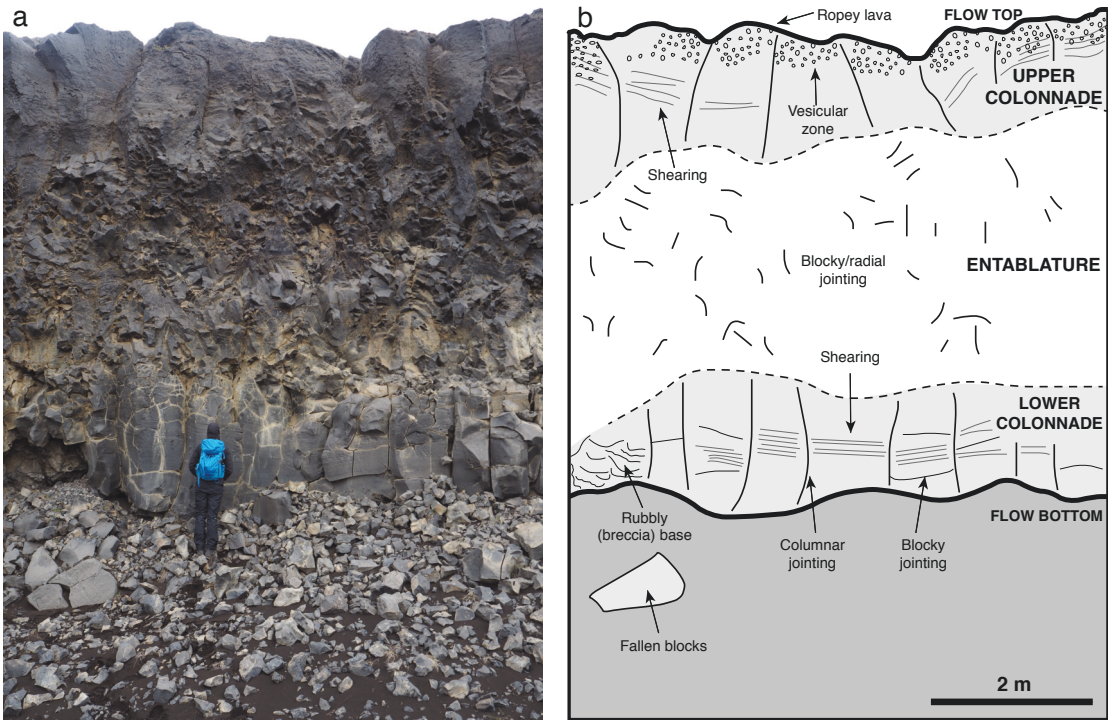


Figure 4.14: Example of full vertical lava column stratigraphy near located in overspill channel near Terrace A in Jökulsárglúfur. Flow bottom characterised by rubbly basal layer and flow top by ropey/vesicular features. Dashed lines = approximate boundaries between zones (Tomkeieff, 1940; Lyle, 2000; Sen and Sabale, 2011)

.

4.4.4 Location within lava flow

The exposure ages obtained from ^{3}He dating measure how long the sampled rock has been exposed at the surface, assuming that at the event of interest, i.e. terrace formation and abandonment, $t = n = 0$. However, if the sample is located close to the surface of the lava flow it is being extracted from ($\lesssim 2$ m; attenuation length of cosmic rays in basalt), it is possible it may have accumulated ^{3}He when the lava flow was first emplaced and exposed up until the subsequent overlying lava flow covered it. This presence of nuclides from exposure prior to the event of interest is termed inheritance. In order to determine whether inherited nuclides are present in the sample, it is necessary to assess its relative height in the lava column and whether it was within > 2 m from the top of the flow.

An example of a typical lava column stratigraphy, from the rubbly, brecciated base, to the vesicular, ropey flow top is shown in Figure 4.14. These main

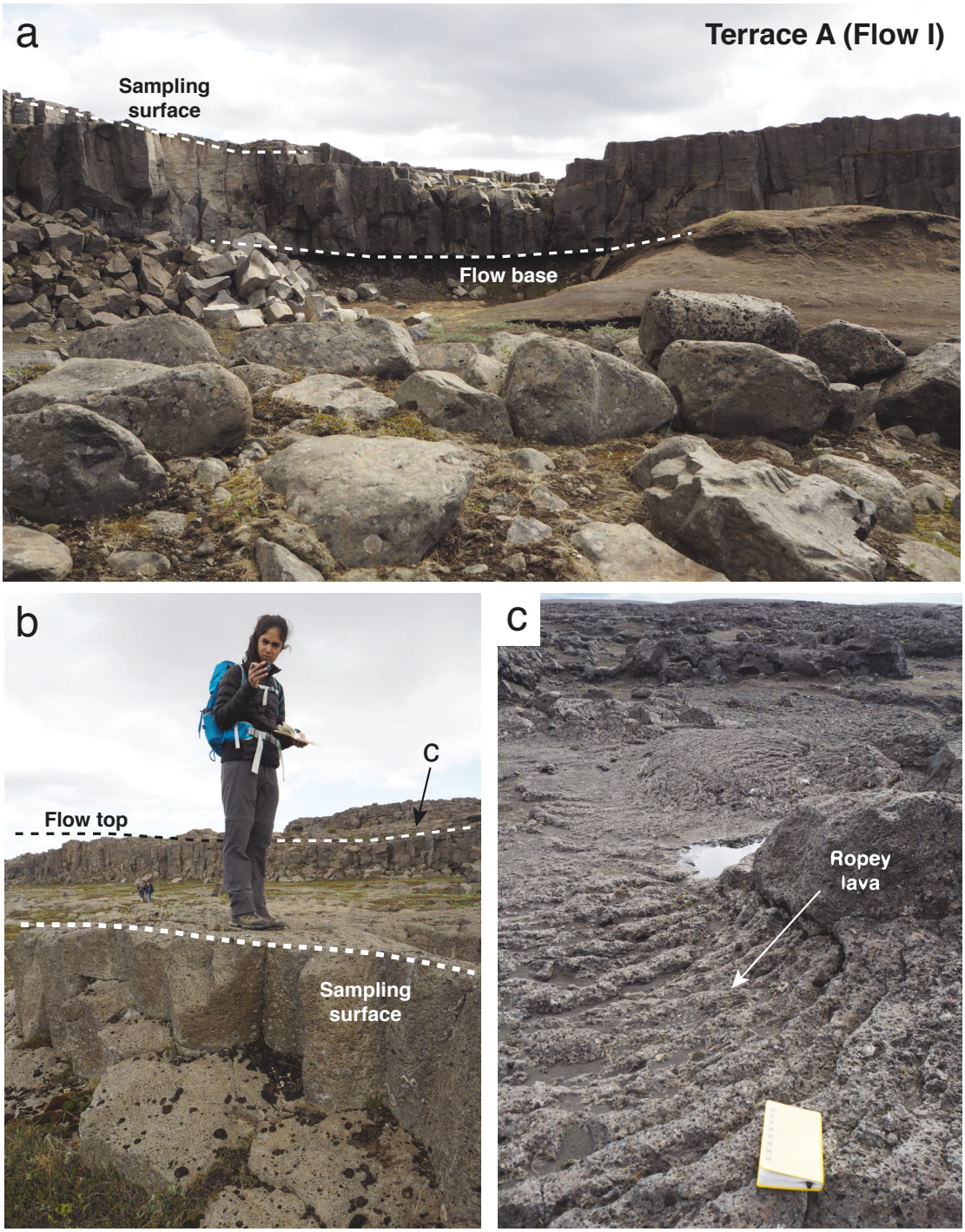


Figure 4.15: Sampling surface of Terrace A within Flow I. Note large (∼ 4 m) vertical distance between flow top and sampling surface.



Figure 4.16: Sampling surface of Terrace B within Flow II. Note large (>15 m) vertical distance between flow top and sampling surface.

structures (colonnade-entablature-colonnade) and associated features (vesicularity, shearing, and jointing) are observed in all visible lava flows and vary only superficially. To determine where each the terraces were located within each flow, I used the sequence in Figure 4.14 to find and map out the top and bottom of each respective flow. Figures 4.15, 4.16, and 4.17 illustrate the relative positions of sampling surfaces and flow boundaries of Terraces A, B, and C, respectively. The sampling surfaces were found to be $\sim$ 4, 15, and 7 m from the top of the flow for Terraces A, B, and C. These depths are much greater than the attenuation length of 2 m suggesting no correction for inherited ^{3}He is necessary.

4.4.5 Correction for non-cosmogenic sources

Another correction that must be made is the potential presence of non-cosmogenic ^{3}He present in the sample. Non-cosmogenic ^{3}He atoms can be radiogenic (produced by a process of radioactive decay), or nucleogenic (natural nuclear reactions of other types, such as neutron absorption). To correct for this unknown non-cosmogenic ^{3}He quantity, I sampled a deep cave located in Terrace

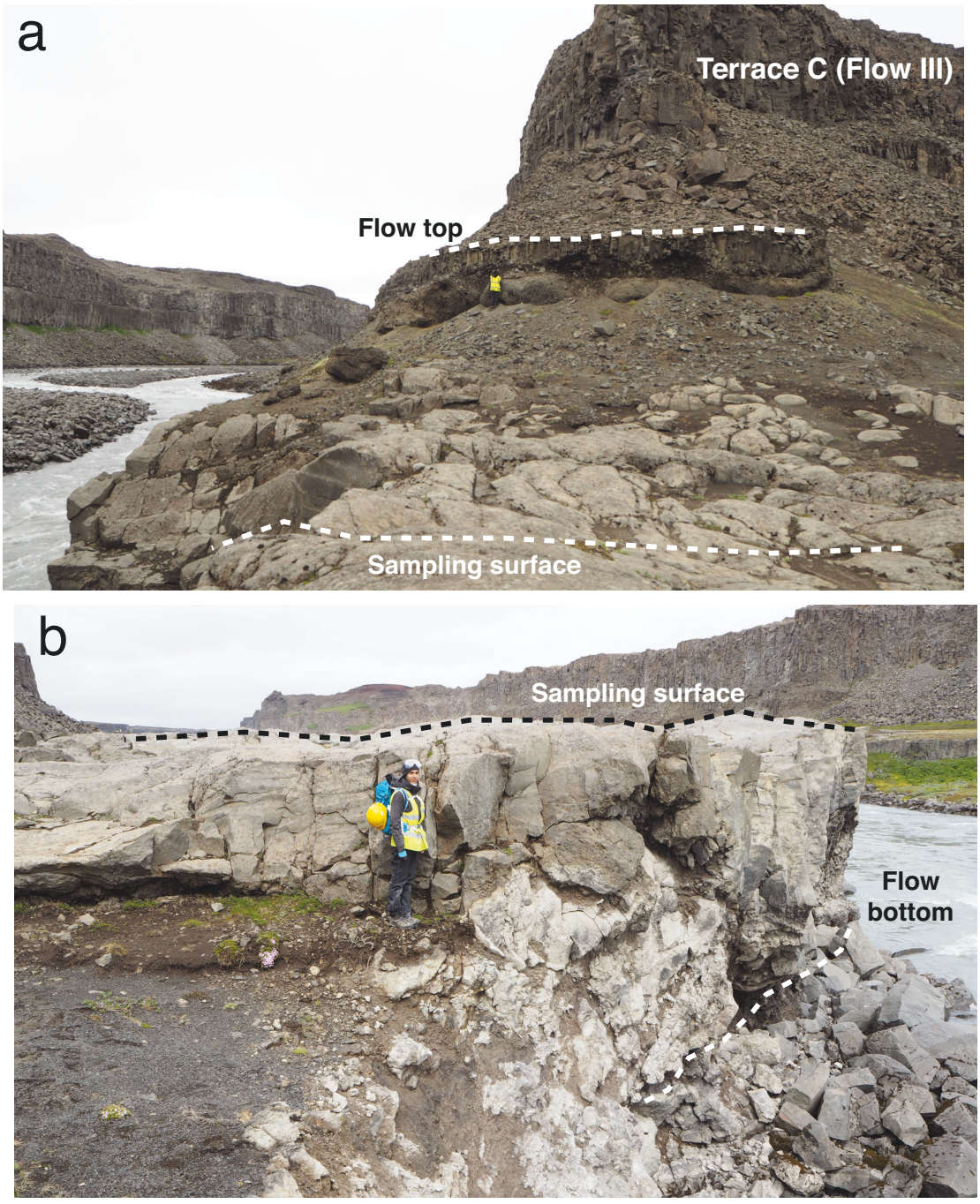


Figure 4.17: Sampling surface of Terrace C within Flow III. Note large (>7 m) vertical distance between flow top and sampling surface.

B (Figure 4.18). Samples from this cave are fully shielded from cosmic rays (> 15 m from lava flow top) and should have no cosmogenic ^{3}He. Thus, any non-zero ^{3}He concentration measured from the shielded sample will correspond to nucleogenic and radiogenic ^{3}He combined. This quantity can be subtracted from the total ^{3}He concentration from each sample to obtain corrected value. Shielding results and values are discussed in detail in Chapter 5.

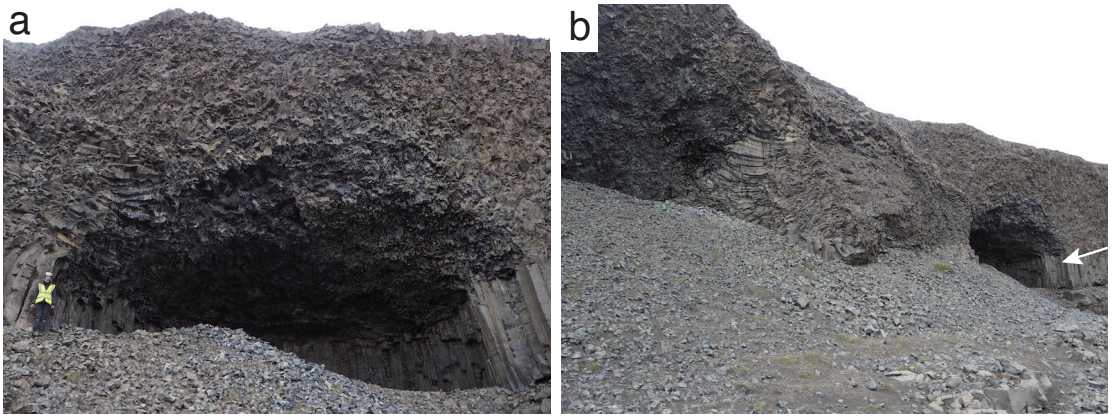


Figure 4.18: Location of shielded sample used for correction of cosmogenic ^{3}He in Jökulsárglúfur. (a) Entrance to cave from eastern side of canyon. Top of cave is ~20 m from top of canyon. (b) White arrow = location of cave on Terrace B.

4.4.6 Topographic shielding

Obstruction of cosmic rays due to nearby topographic features result in lower accumulated concentrations of ^{3}He, especially in sample sites located close to steep canyon walls. The topographic shielding for each sample can be estimated in-situ using a sighting clinometer to measure azimuth, ϕ_i, and inclination, θ_i, of n topographic obstructions along the horizon in a 2π arc from each sample site (see Figure 4.19; Dunne et al., 1999). Topographic shielding is quantified as a scaling factor, and ranges from 0 (fully shielded; e.g. cave) to 1 (no shielding; e.g. plateau). Topographic shielding values and derivations are discussed further in Chapter 5.

4.4.7 Ground cover

The final consideration for sampling sites are whether the sampling surface is or has been covered at any point during its exposure history. Common types of

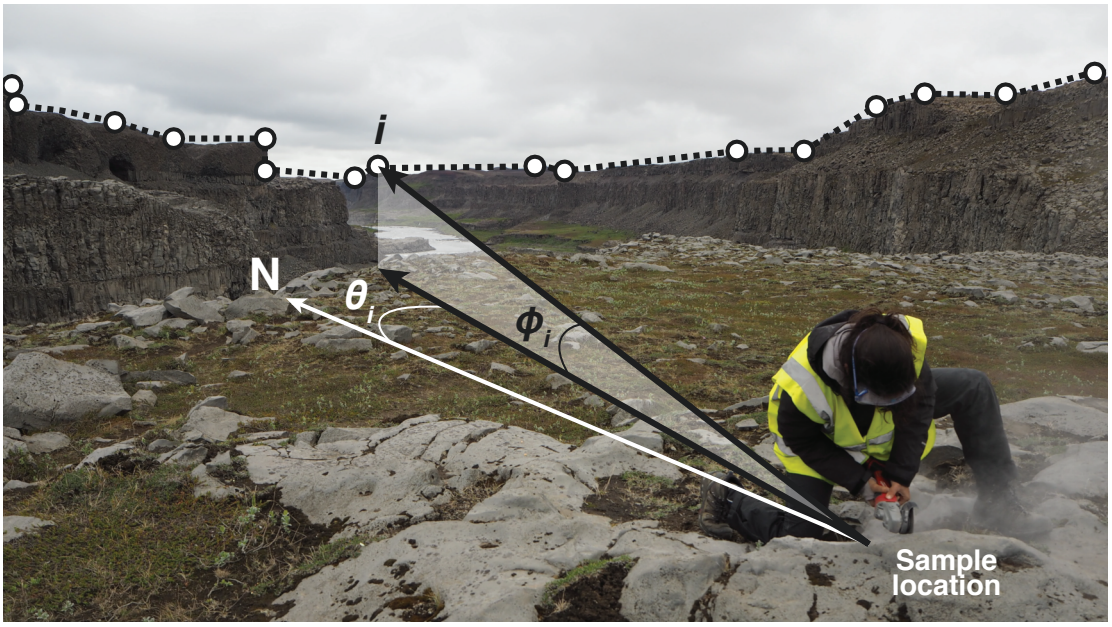


Figure 4.19: Measurements used to calculate topographic shielding from cosmic rays at each sampling site. θ_i = azimuth (degrees from north); ϕ_i = inclination (angle from horizontal). White circles = multiple measurements taken along a 2π arc around sample location.

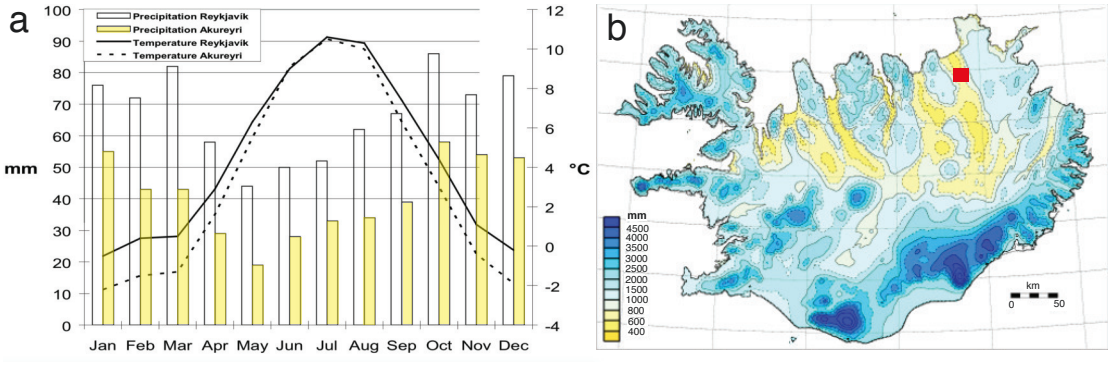


Figure 4.20: Precipitation data for Jökulsárglúfur. (a) Monthly mean temperature and precipitation for 1961–1990 at Reykjavík (southwest Iceland) and Akureyri (north Iceland; proxy for Jökulsárglúfur); modified from Ólafsson et al. (2007). (b) Spatial distribution of precipitation in Iceland estimated with 1 km resolution using an orographic precipitation model (Crochet et al., 2007). Red square = Jökulsárglúfur.

cover consists of soil, sediment, and snow. I avoided sampling where there was evidence for soil and lichen, and no fluvial sediments will have been deposited on terraces after abandonment. However, Jökulsárglúfur is covered in snow during the winter months ($\sim$ 8 months; Einarsson, 1984). Estimates for the average monthly and yearly precipitation for North Iceland from weather gauges and models are shown in Figure 4.20. The average yearly precipitation is $\sim$ 500 mm, of which $\sim$ 50 % falls as snow (Eythorsson et al., 1971; Björnsson, 1980; Ólafsson et al., 2007; Crochet et al., 2007). Without constraints on the ablation of snow, it is estimated snow cover during winter months in Jökulsárglúfur is 12.5 ± 12.5 cm. This correction for snow cover and its uncertainty is quantified in Chapter 5. Note that low density of snow means the corrections are small since cosmic ray attenuation depends on density of obstructing material.

Armed with the measured field constraints discussed above, the suite of samples collected along Jökulsárglúfur canyon can be reliably used to determine exposure ages from ^{3}He concentrations measured in the rock. To complement this high-accuracy sampling technique, the next section describes the usage of UAV (drone) technology to generate a high-resolution digital elevation model of the Jökulsárglúfur study site.

4.5 High-resolution canyon model

A digital elevation model of the Jökulsárgljúfur canyon was generated using a DJI Phantom 4 drone and the Pix4Dmapper software in the field (Figure 4.21). The canyon was mapped as 12 separate flight missions with grids of surface area $\sim$ 400×400 m. Each grid contained 300–400 overlapping (JPEG) photographs. Camera angle was set to 60° to map canyon walls. Flight elevation was $\sim$ 90 m above land and water surfaces, which avoided most waterfall spray. Photographs from each mission were processed using Pix4Dmapper software to produce a high density 3D point cloud, which was used to generate the orthomosaic and elevation model. Ground control points were acquired using three 50 cm square targets for each grid using a Trimble Geo 7x and a Zephyr external GNSS antenna (see Figure 4.21). Elevation models for each grid were georeferenced and corrected for altitude using the ground control

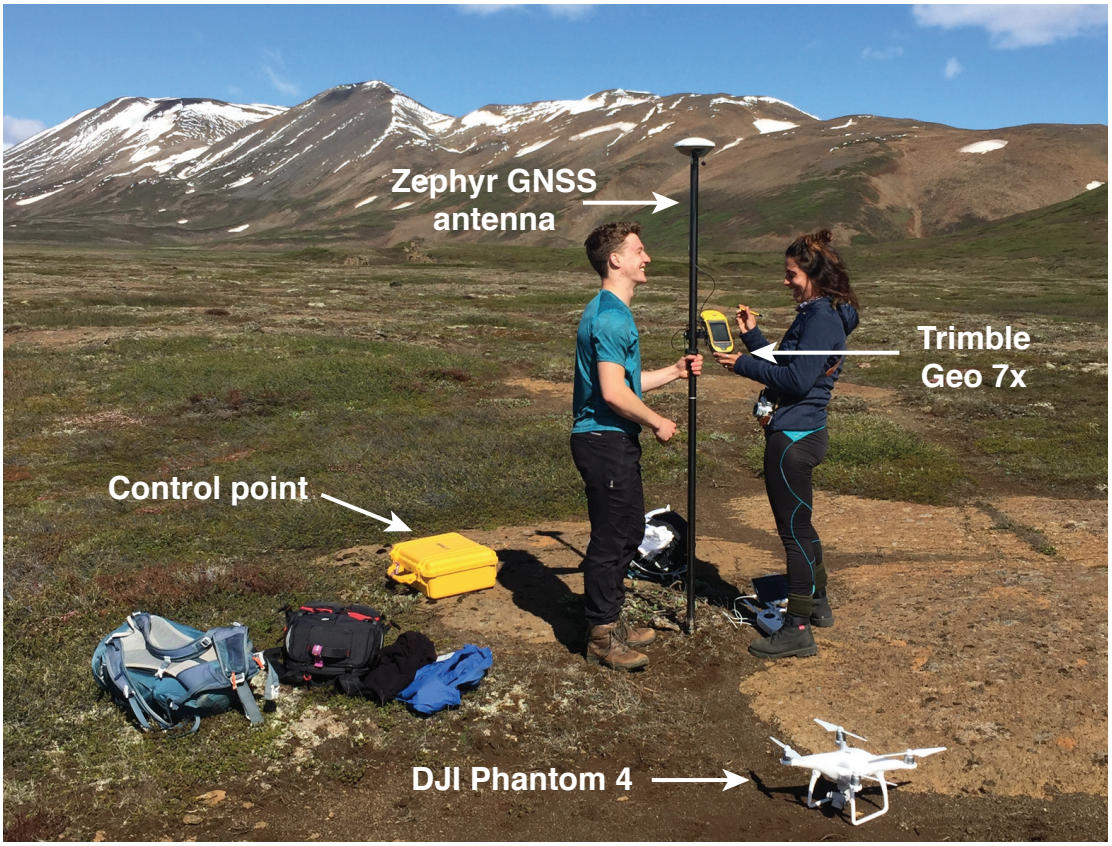


Figure 4.21: GPS survey and drone equipment and set-up used to generate UAV DEMs.

points. Absolute horizontal and vertical errors are 40 cm and 70 cm, respectively. Further processing was performed using ESRI ArcGIS to remove noise due to waterfall spray, clouds, flowing water, and edge effects. The resultant digital elevation model shown in Figure 4.22 has a horizontal and vertical resolution of up to 4 cm. This high-resolution model allows us to calculate the morphology of the terraces and sample locations at unprecedented detail in the following chapter.

4.6 Chapter Summary

In this chapter I outlined observations and measurements from fieldwork undertaken in Iceland in June 2017. Evidence for hundreds of meters of relief and large knickzones from fluvial incision can be seen from large canyons and waterfalls around the island. This suggests the drainage is responding to regional driving processes and changes in base-level. In order to constrain

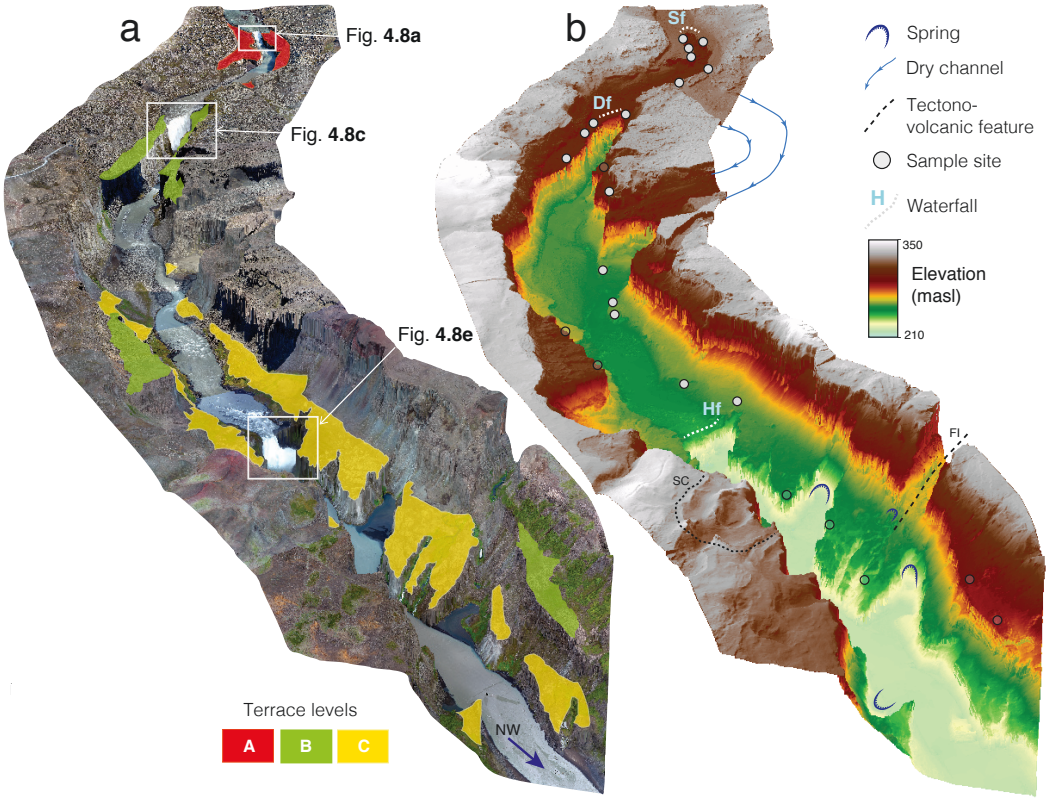


Figure 4.22: (a) UAV DEM of the canyon draped by orthomosaic imagery (2× vertical exaggeration). Coloured surfaces = mapped terraces. DEM is 5 km long in field of view. Blue arrow indicates flow direction. (b) DEM of canyon with key geological/geomorphological observations and sample locations: Sf = Selfoss, Df = Dettifoss, Hf = Hafragilsfoss, Fl = fissure, SC = scoria cone. Filled circles = samples used to calculate retreat rates in Chapter 5.

the regional uplift history, it is necessary to calibrate models of river evolution from field data on erosion rates. Jökulsárglúfur canyon sits on one of the largest knickzones in Iceland, and its well-preserved fluvial terraces provide us an excellent opportunity to determine waterfall retreat rates. This chapter presented field sampling and field constraints to determine high-accuracy exposure dates from ^{3}He dating. This suite of samples can then be combined with high-resolution digital elevation models of the canyon presented above to calculate high-precision retreat rates. The following chapter focusses on the following steps required to determine waterfall retreat rates: laboratory analyses, retreat rate calculations, and calibration of river inversion models to determine modern uplift history from regional drainage patterns in Iceland.

Chapter 5

Regional uplift in Iceland from fluvial erosion histories

5.1 Chapter Introduction

Geological mapping, geomorphological observations, and elevation models of northeast Iceland have shown that fluvial erosion plays an important role in moderating landscape evolution in the present-day. In order to quantify this observation, I sampled river terraces with an aim to measure their exposure ages and thus constrain the erosion rates of the Jökulsárgljúfur knickpoint. This chapter discusses laboratory analyses and measurement techniques used to constrain exposure ages from cosmogenic ^{3}He dating. These results are combined with a UAV photogrammetry model to estimate retreat rates for the Jökulsárgljúfur waterfalls. The ubiquity of large knickzones along all of Iceland's large rivers indicate that inverting for uplift as a function of space and time could yield important information on driving forces generating Icelandic vertical motions. I use measured erosion rates to parameterise the stream power model and calibrate river inversion models. Calculated uplift can then be compared to independent constraints and present-day uplift measurements.

5.2 Laboratory analyses of northeast Iceland samples

In the previous chapters I described how samples were collected from fluvial terraces in Jökulsárgljúfur. This section outlines the steps comprising the lab-based analyses required to accurately measure ^{3}He concentrations from the

samples. This process can be split into two main parts: mineral separation where ^{3}He-bearing olivine and pyroxenes are isolated from the bulk rock, and mass spectrometry where the number of ^{3}He is determined.

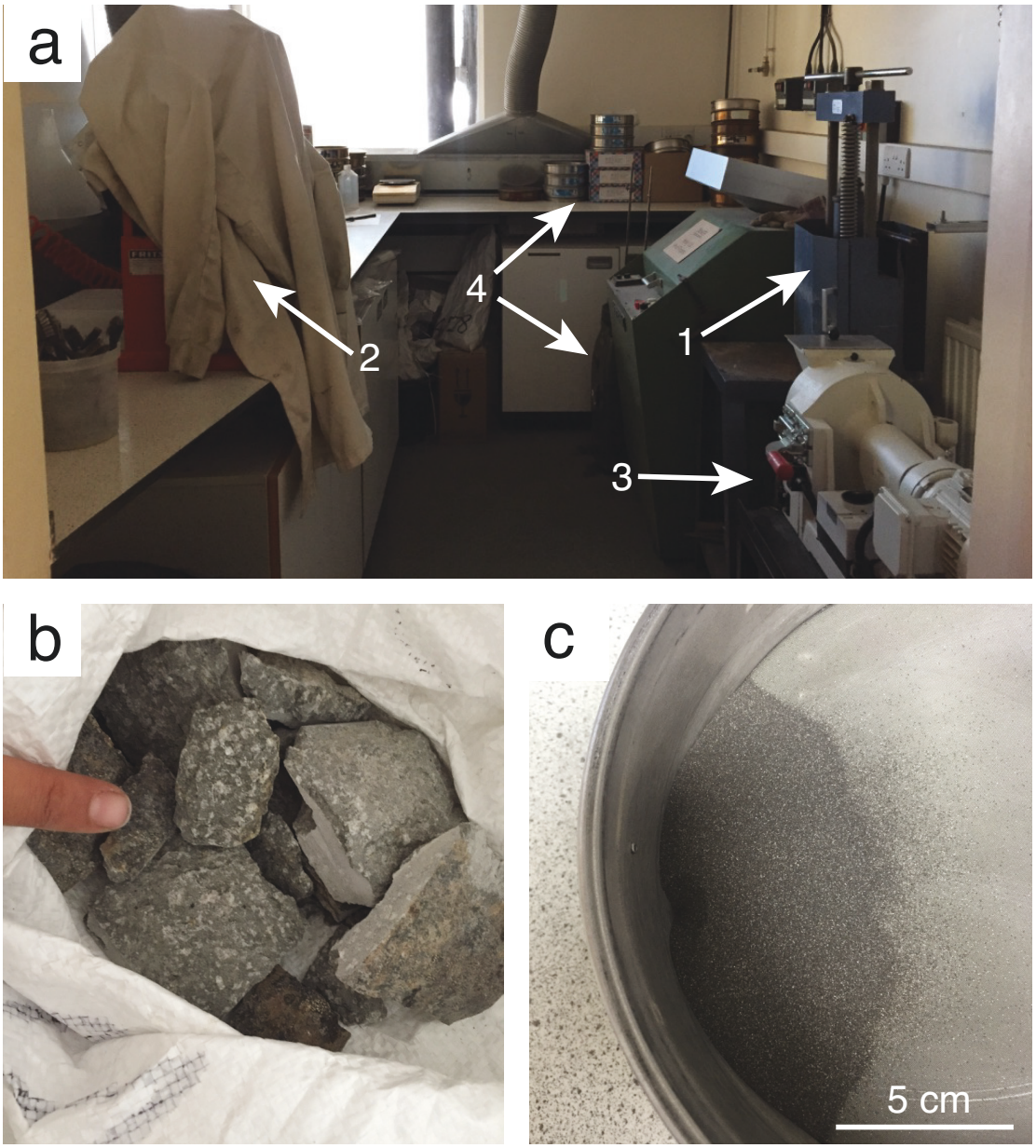


Figure 5.1: (a) Rock preparation room laboratory setup. 1 = splitter; 2 = jaw crusher; 3 = milling machine; 4 = sieve shaker. (b) Rock (cuboid) samples before preparation (5 cm width). Note large (visible) grain size. (c) Rock sample after preparation steps on a 250 μm diameter sieve.

5.2.1 Rock preparation

Collected samples were initially prepared by splitting the rock when rock cuboids > 5 cm and then crushing the rock to gravel-size (see labels 1 and 2 in Figure 5.1a). The sample was recursively milled and sieved on the sieve shaker for 1 minute until grain size $\lesssim 300$ μm (up to $\sim$15 milling runs depending on milling plate separation settings; 3 and 4 in Figure 5.1a). The samples where then sieved for 30 minutes using 500, 250, 150 μm diameter sieves. Example of an initial and prepared sample is shown in Figures 5.1b and c, respectively. All grain size distributions were collected, and samples with 150–250 μm grain size distribution were used for the following steps.

5.2.2 Mineral separation techniques

Once the samples have been crushed to the required diameters, a series of separation techniques can be used to extract the ^{3}He-bearing olivine and pyroxene mineral grains from the basalt.

Washing. First, the samples were washed and dried at $\sim$54 °C to remove adhering dust (Figure 5.2a). Note that temperatures > 60 °C can result in ^{3}He escape and were avoided.

Magnetic separation. The dried, ground sample samples were then magnetically separated by manually scattering them over a large vertical magnet (Figure 5.2b). Magnetic grains adhered to the surface whereas non-magnetic grains were collected at the base. Magnetic grains consist mostly of iron-rich grains from the basaltic ground mass and are largely devoid of olivine and pyroxene grains. This process was repeated twice for accumulated non-magnetic grains to maximise olivine/pyroxene:groundmass ratio.

Density separation. The collected non-magnetic grains were then density separated to isolate high-density (olivine and pyroxene) minerals. Up to 70 g of sample were added to a separating flask filled with 500 mL of diiodomethene (DIM) and stirred frequently for 30 minutes. DIM has a density of 3.325 g cm^{-3} and low viscosity, allowing grains with higher densities $\sim 3.3 - 3.4$ g cm-3

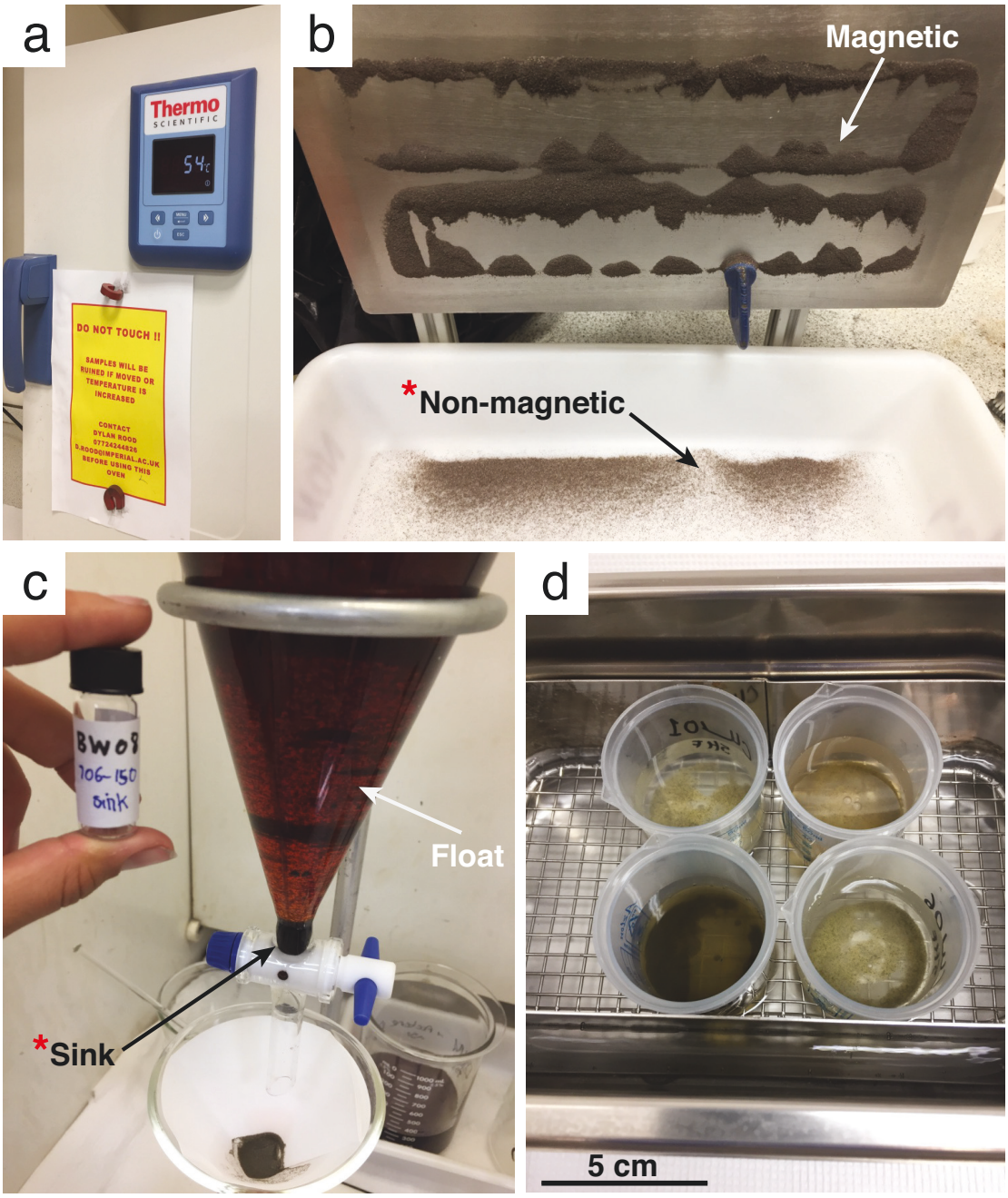


Figure 5.2: Key stages of mineral separation techniques. (a) Oven set to dry samples ~ 54°C after washing. (b) Magnetic separation technique showing distributed grains. Red asterisk = desired sample material. (c) Density separation setup showing float and sink distribution in separating flask. Note filtered sink in beaker below flask. (d) Acid etching of four samples in sonication bath.

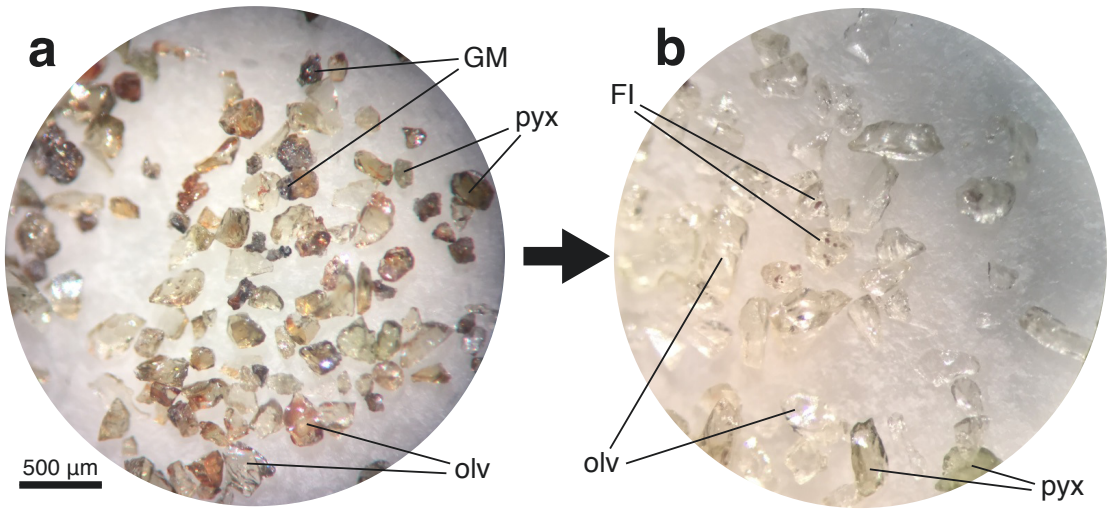


Figure 5.3: Mineral content and quality of sample AE02 (Terrace A) before (a) and after (b) one acid etching, respectively. olv = olivine; pyx = pyroxene; GM = ground mass; FI = fluid inclusions.

(olivines and pyroxenes) to deposit at the bottom of the flask (sink; Figure 5.2c). The sinks were collected using a vacuum filter flask, washed with ethanol, and dried. Typical sink yields ranged between 1–5 g for each 70 g added to DIM-filled flask. Low sink yields ($<$ 1 g) required multiple batches of density separations.

Acid etching. The final step of mineral separation is purification of collected grains. Although grains at this stage are predominantly non-magnetic, high-density olivine and pyroxene grains, microscope observations show presence of adhering groundmass (e.g. Figure 5.3a). Samples were purified by sonication in 2% (vol/vol) 2:1 HF:HNO_3 acid for 1 hour at room temperature (Figure 5.2d). This acid etching procedure works to break up and dissolve groundmass material whilst largely preserving pyroxene and olivine grains. An example of a sample (AE02; Terrace A) before and after acid etching is shown in Figure 5.3. Pre-etching observations show moderate amounts of groundmass (identifiable by its grey 'salt and pepper' texture) which are entirely removed after etching (Figure 5.3b). Final mineral contents for Terrace A and C samples are predominantly clear, glassy olivine with some green, glassy pyroxene (80:20). Samples with abundant adhering groundmass after initial etching were also sonicated in 5% acid up to three times and dry-sieved at 150 μm. An example of this

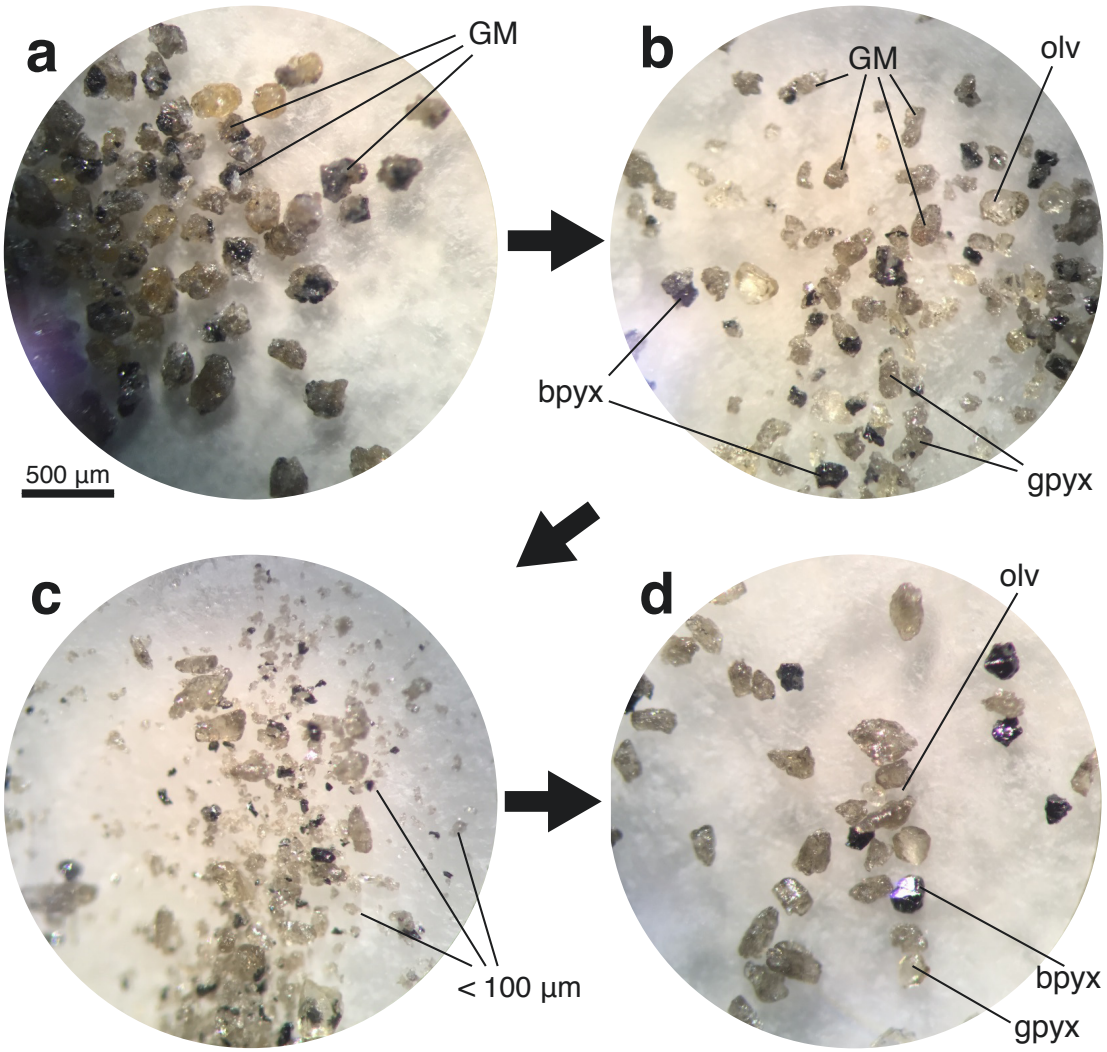


Figure 5.4: Mineral content and quality of sample BW07 (Terrace B) at four different stages. (a) BW07 before acid etching. (b) BW07 after one acid etching. (c) BW07 after second acid etching. (d) BW07 after dry-sieving at 150 μm. olv = olivine; gpyx = green pyroxene; bpyx = black pyroxene; GM = ground mass. Note greater number of stages (cf. Figure 5.3) due to continually adhering ground mass.

longer process is shown in Figure 5.4 for sample BW07 (Terrace B). Mineral contents for Terrace B are mainly green pyroxenes, with some black, metallic pyroxene, and little olivine (70:20:10). Note that some olivine grains contain fluid inclusions (see FI in Figure 5.3b). At this stage, pure olivine and pyroxene sample masses range between 65–1347 mg and are suitable for measuring of ^{3}He content. This analysis was performed at the Noble Gas Lab at Caltech and is outlined in the following section.

5.2.3 Noble gass mass spectrometry

Final sample preparation

The 28 samples were shipped to Caltech and final mineral preparations were done at the lab. To remove mantle-derived ^{3}He trapped in melt and fluid inclusions, the samples were ground with a pestle and mortar submerged in propanol (Figure 5.5a). This method avoids ^{3}He adsorption of Helium from the atmosphere (Protin et al., 2016). Up to 300 μm (where available) of the purified samples were placed into aluminium foil balls and weighed in this final stage.

Mass spectrometer operation

^{3}He concentrations of samples were measured using a MAP 215-50 noble gas mass spectrometer (Figure 5.5c; Blard et al., 2015). Before loading of the samples, the ion gauge and turbo were turned off (including associated valves between charcoal and turbo, including furnace jacket and ion-gauge). The charcoal finger was removed from liquid nitrogen container and heated with a hot air gun (Figure 5.5b). This ensures the charcoal is sufficiently warm that atmospheric volatiles will not adhere to its surface upon exposure. The tree (access point to the furnace and sample dropper) was opened to remove, clean out, and replace the carbon furnace casing. The sample foil balls (12 per run) were then loaded into a dropper, the tree was resealed with a fresh copper gasket, and the dropper magnet was rotated 180°. Valve 10 was opened and closed to diffuse the introduced atmospheric gases across a larger volume, decreasing its pressure and protecting the turbo when it is exposed. With the turbo turned off, the turbo valve was opened to airbrake the turbo. Valve 10 was opened again, and once the turbo started to slow down passively, the turbo

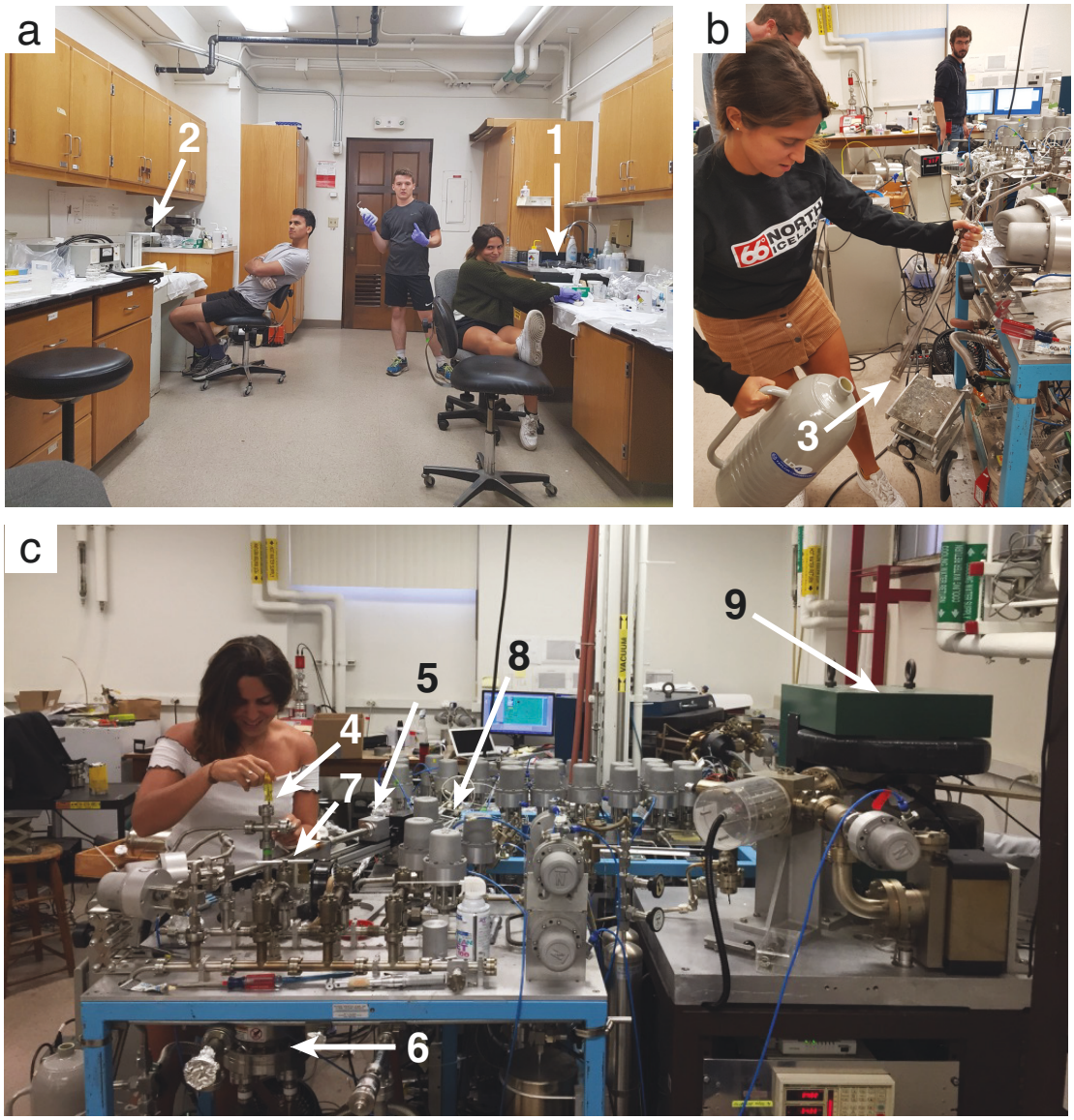


Figure 5.5: Laboratory setup at the Noble Gas Lab at Caltech. (a) Final sample preparation. 1 = grinding station to remove mantle-derived ^{3}He trapped in melt and fluid inclusions; 2 = final weighing of samples and placement into foil balls. (b) De-icing of the charcoal finger in liquid nitrogen before adding samples and turning on furnace. 3 = charcoal finger. (c) Main parts of the MAP 215-50 noble gas mass spectrometer. 4 = tree; 5 = dropper; 6 = furnace; 7 = Valve 5; 8 = system of getters; 9 = mass spectrometer and detection system.

was turned on and allowed to accelerate up to 1500 revolutions/second for 30 minutes allowing the pressure to drop to create a pseudo vacuum. The furnace jacket and ion gauge valves were then opened, and the ion gauge was turned on to reach a pressure reading of 1×10^{-4} Torr. The ion gauge was turned off and the furnace was turned on to 10% of its power for 1 minute, and increased to reach 25% for one hour (final temperature = $\sim 1250^{\circ}$). Once the furnace reached its temperature, the charcoal finger was reheated until the turbo power reading settled at 0.18 A. The furnace was turned off, and the charcoal finger was placed back in a refilled tank of liquid nitrogen and covered in foil. The ion gauge was turned on, and all valves were opened. Sample names, masses, and orders were entered into the computer where the run was initiated.

^{3}He release and detection

The samples were dropped individually into the furnace, which heated the sample and released the volatiles. In this process, the volatiles came into contact with the charcoal which has a high surface area, and is cold and under a vacuum. This freezes out most of the gases, however e.g. CH_4, Ar, and He pass through. When Valve 5 was opened, the gases moved to the analytical equipment where they expanded and interacted with a series of getters (cylinders of stacked plates with high surface area coated in metal alloys) which absorbed anything that was no a noble gas. The charcoal finger also worked to remove organic material, which the getters were unable to do and were damaged by it. The gasses proceeded to further traps which removed H_2O, Ar, etc. The 'clean' gas was then cryo-focused, freezing all the gases ($\sim$ 10 K). This was gradually heated up to 34 K, at which point He was released and could be analysed. The He then entered the mass spectrometer, where it underwent bombardment, acceleration, deflection, and detection. Two detectors were used: in the Faraday detector, ions hit a plate which created a measurable current; in the multiplier, a series of plates were used such that when an He ion hit a plate it released electrons, which subsequently hit a second plate, releasing additional electrons. This process amplified low frequency ion streams to yield a detectable current. These instruments must be sufficiently calibrated as to enable differentiation of detection peaks from He and D (deuterium) as they have

similar molecular masses. This process was repeated for all 12 samples loaded into each mass spectrometer run. A spike of murdering mudpot (MM; collected from Yellowstone) standard gas was introduced into the mass spectrometer in between sample runs as well as blank samples. This allowed for comparison of the signal generated by the sample with the signal generated by an aliquot the standard gas with known Helium abundance split over the same line volume (Amidon et al., 2008). Repeat measurements were made for four samples with large prepared amounts (> 1 g): AE03-2, AW07-2, CW01-2, CW06-2.

Measured ^{3}He concentrations for each sample are shown in Table 5.1. Having constrained the ^{3}He concentrations for each sample, the next step to determine exposure ages is to estimate ^{3}He production rates for each sample. This is the focus of the next section.

5.3 Exposure age calculations

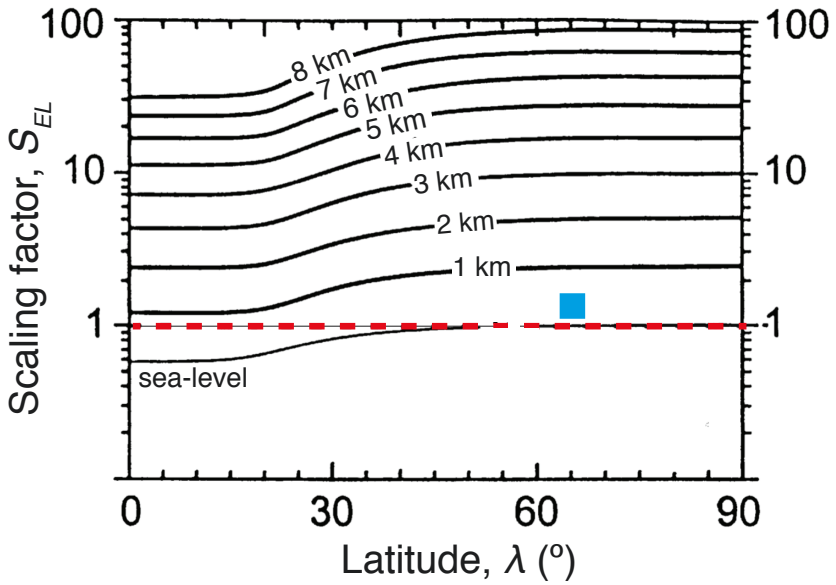


Figure 5.6: Scaling factor S_{EL} for variation of production rates with elevation and latitude using scaling method from Lal (1991) and Stone (2000). Red dashed line = scaling factor 1 (e.g. high latittude, at sea-level). Blue square = approximate scaling for samples in Jókulsárgljúfur. Figure modified from Gosse and Phillips (2001).

In the previous chapter I showed that exposure ages can calculated as $t = n/P$, where n = number of measured ^{3}He atoms, and P is cosmogenic ^{3}He produc-

tion rate. n was constrained in the previous section from mass spectrometer measurements. P can be calculated for each sample site using

$$P = P_{ref} \times S_{EL} \times S_z \times S_{topo} \times S_{snow}. \tag{5.1}$$

I use reference production rate, $P_{ref} = 124 \pm 4$ at g $^{-1}$ yr^{-1}, calibrated for Iceland by independent radiocarbon dating (rocks at high-latitude and at sea-level; Licciardi et al., 2006). Spatial scaling, S_{EL}, varies as a function of elevation and latitude and was estimated using the function given by Stone (2000) who used a modified version of Lal (1991)'s approach (see Figure 5.6). Additional scaling factors S_z, S_{topo}, and S_{snow} depend on sample thickness, topographic shielding, and snow cover, respectively. I solve an expanded version of Equation 5.1:

$$\begin{aligned} P = P_{ref} \times & \left[a + b\exp\left(-\frac{p}{150}\right) + cp + dp^2 + ep^3\right] \\ & \times \frac{\Lambda}{\rho z}\left[1 - \exp\left(-\frac{z\rho}{\Lambda}\right)\right] \\ & \times \left[1 - \frac{1}{2\pi}\sum_{i=1}^{n}\Delta\phi_i \sin^{3.3}\theta_i\right] \\ & \times \frac{1}{12}\sum_{j=1}^{12}\exp\left(-\frac{z_{s_j}\rho_s}{\Lambda}\right). \end{aligned} \tag{5.2}$$

Spatial scaling S_{EL} is calculated using air pressure, p, which is a function of elevation, E, and can be calculated using $p = p_{sl}\exp\{[-gM/RL][\ln(T) - \ln(T - LE)]\}$, where p_{sl} = air pressure at sea-level (1013.25×10^2 Pa), g = gravitation acceleration (9.81 m s^{-2}), M = molar weight of air (28.97 g mol^{-1}), R = gas constant (8.314 J mol^{-1} K^{-1}), L = adiabatic lapse rate (0.0065 K m^{-1}) and T = air temperature at sea-level (288.15 K). Scaling coefficients $a = 71.8733$, $b = 863.1927$, $c = -0.207069$, $d = 2.0127 \times 10^{-4}$, $e = -6.6043 \times 10^{-8}$, which are appropriate for latitudes$>$ 60 $^\circ$ (Stone, 2000). S_z calculates attenuation of cosmic rays in rock as a function of attenuation wavelength, Λ, density, ρ and sample thickness, z. I set $\Lambda = 150$ g cm^{-1} and $\rho = 2.8$ g cm^{-3} (Gosse and Phillips, 2001; Marrero et al., 2016). Topographic shielding, S_{topo}, was estimated from azimuths, ϕ_i, and inclinations, θ_i measured in the field (Chapter 4, Section 4.4.6). Finally, shielding due to snow cover, S_{snow}, was calculated using an estimate of 12.2 $\pm$ 12.5 cm snow cover for 8 months of the year (see Chapter 4, Section 4.4.7).

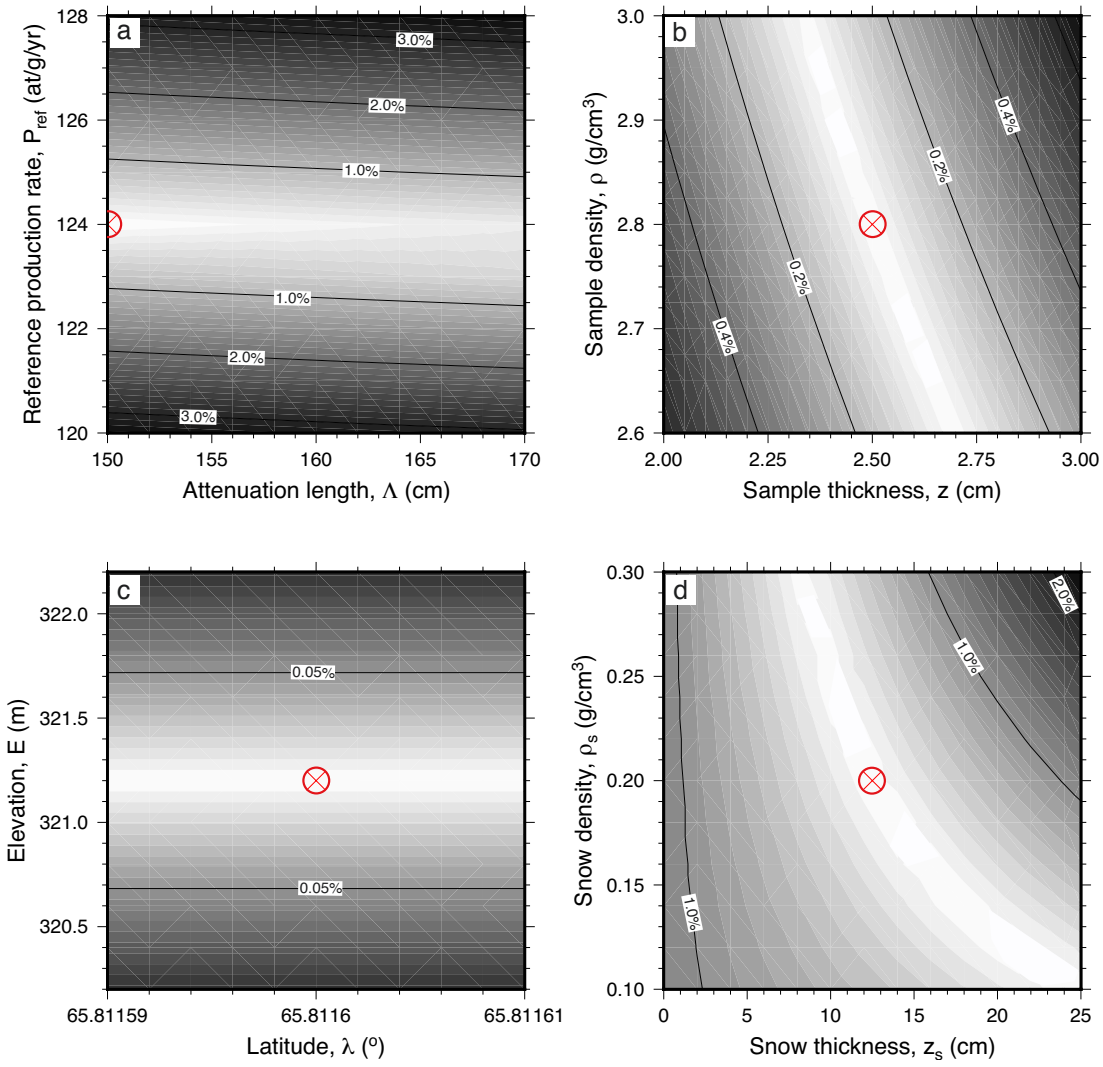


Figure 5.7: Exposure age differences from co-variations of cosmogenic ^{3}He dating parameters for sample AW07. (a) Relative change in exposure age for varying production rate and attenuation length. Red cross-hair indicates mean values used to determine exposure ages. Note >3% error for P_{ref}. (b) Relative change in exposure age for sample thickness and density. (c) Relative change in exposure age due to spatial scaling factors, elevation and latitude. Note 65.81160 $\pm$ 0.00001° corresponds to $\sim \pm$ 1 m error. (d) Relative change in exposure age for snow thickness and snow density.

Table 5.1: Sample data used to measure cosmogenic ^{3}He exposure ages.

Sample name [a]	Latitude (°)	Longitude (°)	Elevation (m)	Thickness (cm)	Topographic shielding factor	Lal/Stone scaling factor	Production rate (at g^{-1} yr^{-1}) $\pm1\sigma$	Olivine + pyroxene mass (g)	Cosmogenic ^{3}He ($\times10^3$ at g^{-1}) [b] $\pm1\sigma$	Exposure age (yr) $\pm1\sigma$
AW01	65.80614	-16.38841	316.5	2	1.000	1.389	167 ± 6	0.307	392 ± 40	2347 ± 257
AE02	65.80826	-16.38830	317.7	2	1.000	1.391	167 ± 6	0.287	526 ± 41	3143 ± 273
AE03	65.80700	-16.38749	317.2	14	1.000	1.390	150 ± 6	0.318	582 ± 45	3880 ± 332
AE03-2								0.439	635 ± 37	4232 ± 295
AE04	65.80593	-16.38647	316.8	2	1.000	1.390	167 ± 6	0.342	446 ± 37	2666 ± 245
AW05	65.80716	-16.38978	316.9	9	1.000	1.390	157 ± 6	0.318	673 ± 43	4291 ± 319
AW06	65.80954	-16.39037	318.2	2	0.999	1.392	167 ± 6	0.347	1028 ± 45	6141 ± 355
AW07	65.81160	-16.38877	321.2	2.5	1.000	1.396	167 ± 6	0.318	1240 ± 59	7418 ± 450
AW07-2								0.263	969 ± 54	5799 ± 386
BE01	65.81844	-16.38345	299.7	2	0.998	1.367	164 ± 6	0.095	216 ± 85	1316 ± 519
BW02	65.81406	-16.38551	300.4	2	0.994	1.368	164 ± 6	0.025	43 ± 302	262 ± 1842
BW03	65.81910	-16.38670	303.7	2	0.993	1.372	164 ± 6	0.383	456 ± 38	2777 ± 252
BE04	65.81608	-16.38339	301.7	2.5	0.988	1.370	162 ± 6	0.276	157 ± 38	965 ± 239
BE05	65.81494	-16.38339	298.2	2	0.995	1.365	163 ± 6	0.101	14 ± 21	87 ± 475
BW06	65.82083	-16.38814	298.6	3	0.957	1.365	156 ± 6	0.037	232 ± 207	1488 ± 1329
BW07	65.83801	-16.41459	284.9	2.5	0.998	1.347	161 ± 6	0.062	1387 ± 144	8611 ± 955
BW08	65.83904	-16.41588	279.3	2.5	0.998	1.340	160 ± 6	0.042	364 ± 182	2270 ± 1141
BE09	65.83015	-16.39092	308.3	11	0.998	1.378	152 ± 6	0.300	1931 ± 65	12664 ± 636
BE10	65.83171	-16.39376	309.0	8	0.998	1.379	157 ± 6	0.317	1698 ± 67	10825 ± 587
CW01	65.82427	-16.38953	247.7	2	0.989	1.299	155 ± 6	0.310	329 ±41	2127 ± 277
CW01-2								0.486	313 ± 31	2027 ± 214
CW02	65.82623	-16.39138	247.6	2.5	0.971	1.299	151 ± 6	0.204	314 ± 48	2079 ± 326
CW03	65.82692	-16.39184	247.5	2	0.982	1.299	154 ± 6	0.406	397 ± 40	2585 ± 278
CW04	65.83094	-16.40128	246.8	2.5	0.968	1.298	151 ± 6	0.320	466 ± 42	3092 ± 718
CW05	65.83022	-16.39786	244.2	2	0.983	1.294	153 ± 6	0.098	302 ± 90	1974 ± 593
CW06	65.83446	-16.40524	238.3	5	0.991	1.287	149 ± 6	0.330	367 ± 45	2455 ± 314
CW06-2								0.480	211 ± 31	1410 ± 214
CW07	65.83537	-16.40770	236.3	13	0.984	1.284	138 ± 5	0.394	214 ± 38	1553 ± 280
CW08	65.83707	-16.40978	231.4	2.5	0.985	1.278	151 ± 6	0.300	233 ± 38	1545 ±258
JF01[c]	66.03254	-16.44017	44	4	1.000	1.052	124 ± 6	0.090	61 ± 92	494 ± 698
JB03[d]	65.10672	-15.53180	353	12.5	1.000	1.439	157 ± 6	0.034	92 ± 221	584 ± 1413
Sh-B[e]	65.82083	-16.38840	-	-	-	-	-	0.337	-	-

[a] First letter = Terrace A/B/C; second letter = East/West side of canyon; appended "-2" indicates repeat sample measured for ^{3}He concentrations.
[b] Cosmogenic ^{3}He concentrations corrected for machine background and non-cosmogenic ^{3}He, with uncertainties propagated in quadrature.
[c] Sample collected from mouth of Jökulsá á Fjöllum.
[d] Sample collected from Jökulsá á Brú.
[e] Shielded sample collected from cave in Terrace B (Figure 4.18).

A systematic sweep of parameters in the production rate model was performed to estimate their contribution to uncertainties in calculated exposure ages (see Figure 5.7). Uncertainties in reference production rates and snow cover contributed the largest systematic error to calculated exposure ages (3.4% and 2.2%, respectively; Figure 5.7). I tested snow densities, ρ_s, and thicknesses, z_s, between $0.1 \leq \rho_s \leq 0.3$ g cm^{-3} and $0 \leq z_s \leq 25$ cm (Gosse and Phillips, 2001). Uncertainties in spatial scaling, sample thickness, and topographic shielding contribute errors <0.5%. The Lifton-Sato scaling schemes were used to test a range of time-dependent cosmogenic production scenarios, which incorpo-

rated temporal and spatial variability of geomagnetic and solar modulation of cosmic ray fluxes (Lifton et al., 2005; Sato and Niita, 2006). The time-dependent production rates were propagated through the CRONUS exposure age calculator(Marrero et al., 2016). Results yielded a maximum difference in exposure ages of 1.8% compared to models that assume constant flux. Samples BE05 and BW02, located close to the crest of Dettifoss, have exposure ages of 0 ka within error, which suggests that vertical erosion rates were sufficiently high that negligible ^{3}He accumulated prior to formation of the terrace.
In Chapter 4, Section 4.4.5, I discussed the collection of a cosmic ray-shielded sample from a cave in the canyon to correct for non-cosmogenic ^{3}He in the terrace samples. The correction is

$$n = n_t - n_s, \tag{5.3}$$

where n is the number of cosmogenic ^{3}He atoms in each sample, n_t is the total uncorrected number of ^{3}He atoms measured, and n_s is the number of ^{3}He atoms measured from the shielded sample , where n_s = $38 \pm 23 \times 10^3$ at. Non-cosmogenic ^{3}He accounts for 3–73% of total ^{3}He measured in samples (mean = 14%). Errors in exposure age, δt, were calculated by propagating errors in measured ^{3}He atoms, $\delta n = \sqrt{\delta n_t^2 + \delta n_s^2}$, and production rate, $\delta P = P_{ref} S \sqrt{(\delta P_{ref}/P_{ref})^2 + (\delta S_{snow}/S_{snow})^2}$, where $S = S_{EL} \times S_z \times S_{topo} \times S_{snow}$, using

$$\delta t = |t| \times \sqrt{\left(\frac{\delta n}{n}\right)^2 + \left(\frac{\delta P}{P}\right)^2}, \tag{5.4}$$

which assumes that uncertainties in spatial scaling, sample thickness, and topographic shielding are negligible. Calculated production rates and uncertainties are given in Table 5.1. Having constrained n and P for each sample, exposure ages t and uncertainties δt were calculated and are shown in Table 5.1.

5.4 Erosion rate and knickzone history

5.4.1 Waterfall retreat rates in Jökulsárgljúfur

Exposure ages of fluvial terraces in Jökulsárgljúfur were measured by cosmogenic ^{3}He dating. These high-precision ages can be combined with high-

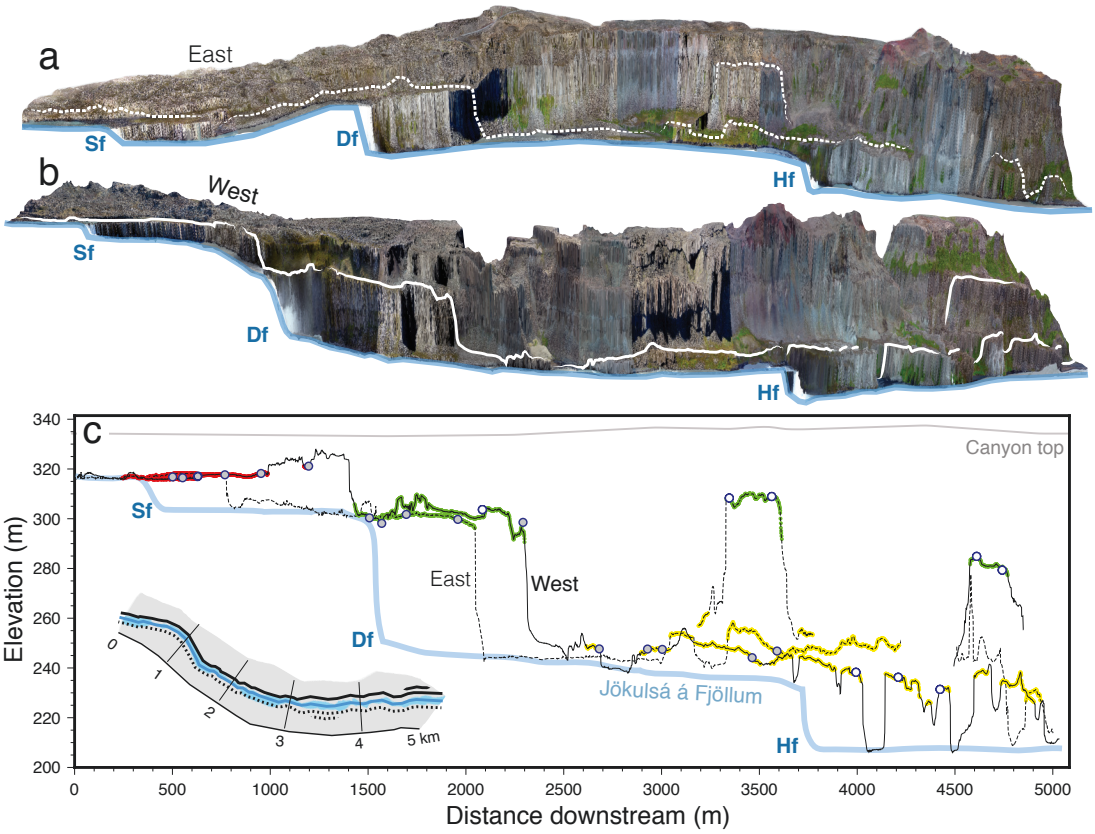


Figure 5.8: (a–b) UAV orthomosaic image (×5 vertical exaggeration) of eastern and western side of canyon. Blue line = modern river. Sf = Selfoss, Df = Dettifoss, Hf = Hafragilsfoss. Dashed/solid white line = fluvial terraces on eastern/western sides of the canyon. (c) Solid/dashed black lines = trace of fluvial terraces on western/eastern side of Jökulsárgljúfur (see inset map for location). Red/green/yellow = mapped and sampled terraces. Grey-filled circles = locations of samples used to calculate retreat rates. Empty circles = additional samples collected (see Table 5.1). Blue = longitudinal river profile.

resolution UAV digital elevation models generated for the Jökulsárgljúfur canyon. River profiles, terrace cross-sections, and locations of samples are shown in Figure 5.8. Exposure ages and downstream distances are shown in Figure 5.9. Calculated exposure ages vary between 0 years and 8 ka and increase further away from waterfalls. Regression of the data yields average knickpoint retreat velocities (Figure 5.9). Samples with mass < 0.05 g result in larger age uncertainties due to the difficulty of detecting low ^{3}He concentrations (e.g. sample BW06 in Table 5.1). Importantly, uncertainties affect absolute ages of terraces but do not change their relative ages which are used to calculate knickpoint retreat rates. Samples collected from terraces abutting Selfoss have exposure

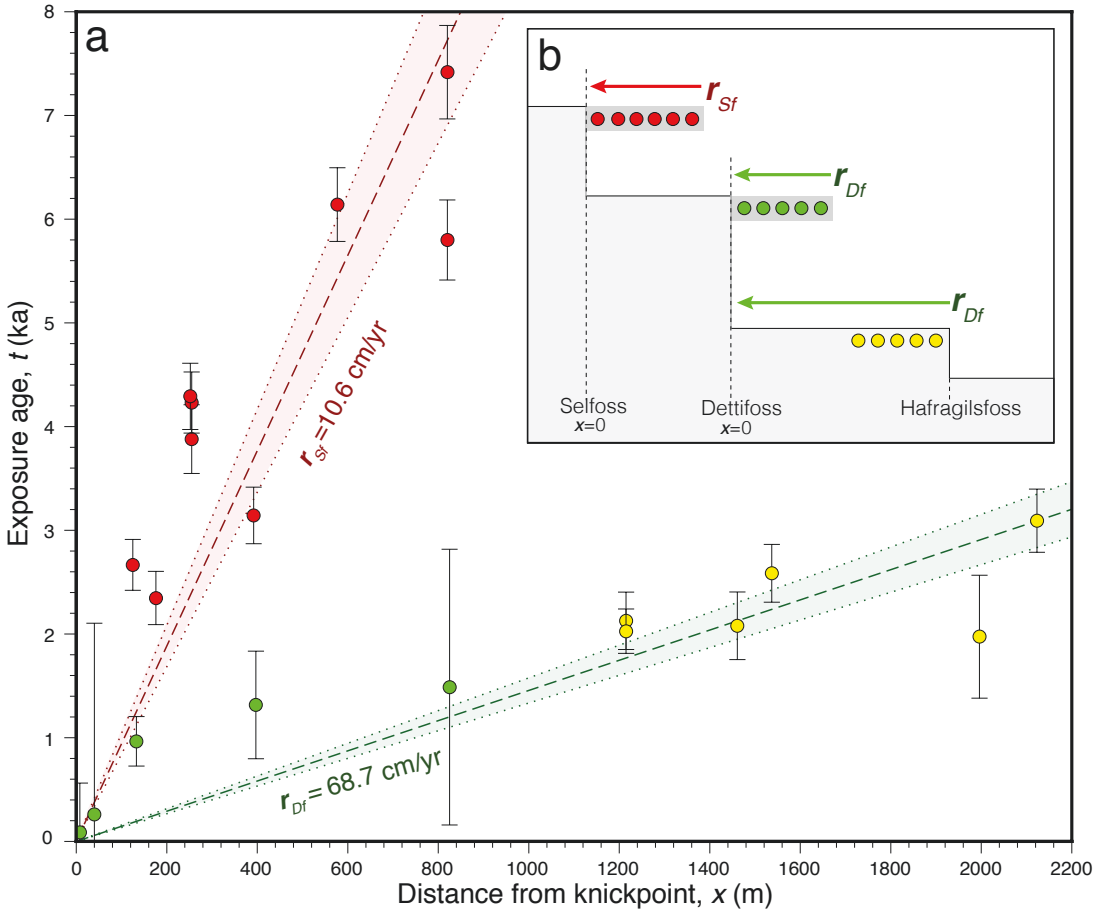


Figure 5.9: (a) Exposure age of samples as a function of distance from Selfoss and Dettifoss. Errors are propagated from measurements of ^{3}He atoms and estimated cosmogenic production rates. Labelled dashed/dotted lines = best-fitting regression lines/$\pm 1\sigma$ of the means. r_{Sf}/r_{Df} = retreat rate of Selfoss/Dettifoss. R^2 = 0.94/0.92 for Selfoss/Dettifoss. (b) Schematic of sample locations and retreat rates for Selfoss and Dettifoss.

ages of 2–8 ka and yield a retreat rate of 10.7 ± 1.0 cm yr^{-1}. Samples from terraces abutting Dettifoss indicate a retreat rate of 68.7 ± 0.1 cm yr^{-1}. Retreat rates calculated for terraces at the top and bottom of the Dettifoss are consistent and exposure ages converge at the modern waterfall.

One key observation is that sample ages are spread over the entire $0 - 8$ ka terrace age range in the canyon. This is contrary to observations made by Baynes et al. (2015b) where terrace ages were found to cluster around 2, 5, and 9 ka ages, suggesting three distinct episodes of erosion. The dataset in this work benefits from a larger sample size and smaller age uncertainties, which

would improve the temporal resolution. These results do not preclude the existence of subglacial megafloods, as these are well documented historically, stratigraphically, and geomorphologically. Rather these erosion rates suggest fluvial processes have progressively generated significant relief over thousands of years, not in 1–3 episodic events.

5.4.2 Knickzone generation

How were Jökulsá á Fjöllum's knickzone and its waterfalls generated? The gradual decrease in ages of terraces towards waterfalls precludes formation in single events, for example during catastrophic megafloods (Waitt, 2009; Alho et al., 2005; Baynes et al., 2015b). Four observations suggest that it is unlikely the Rauduborgir-Kvensödul and Sveinar fissures, which cut across the river downstream of Hafragilsfoss, generated the knickzone or waterfalls. First, the knickzone initiates downstream of the fissures (see Figure 4.4b). Secondly, change in elevation of the longitudinal river profile across the fissures is a few meters (Figure 4.4b). Thirdly, there are waterfalls downstream of the fissures (e.g. Réttarfoss and Vígabjargsfoss). Finally, broad knickzones and large waterfalls (e.g. Goðafoss, Gulfoss) exist along all major Icelandic rivers.

Field and satellite mapping shows many of Iceland's rivers intersect fluted moraines, tephra layers, conglomerate beds, lava flows with a range of jointing and fracturing orientations, and fissure swarms which formed scoria, spatter cones, and dykes (Chapter 4, Section 4.3.3). Jökulsá a Fjöllum's substrate includes basalts that joint and fracture at a columnar (meter) scale, which indicates that substrate plays a role in setting erosion rates at short length scales (Lamb and Dietrich, 2009; Lamb et al., 2015). The collapse of columns generates relief of a few meters to a few tens of meters at wavelengths $\lesssim 10$ m along the river. Jökulsá a Fjöllum's broad knickzone and fluvial terraces cross-cut different lithologies without significant changes in relief and the positions of its waterfalls do not coincide with obvious changes in lithology. No large tributaries join Jökulsá á Fjöllum in Jökulsárgljúfur, although a dry channel west of the canyon has been interpreted as a manifestation of time-dependent discharge (Baynes et al., 2015b). In the northern section of the canyon ground-

water springs merge with Jökulsá a Fjöllum's trunk river (Section 4.3.3; Figure 4.11). These changes in discharge coincide with meter-scale changes in relief of the longitudinal river profile. These observations suggest that substrate and changes in discharge can generate $\sim$ 10 m of relief in Jökulsá á Fjöllum at wavelengths of a few meters to tens of meters. They cannot explain the shape of river's broad knickzone, which has an amplitude of $\sim$ 500 m and wavelength of $\sim$ 100 km.

These observations suggest that the amplitude of Jökulsá á Fjöllum's knickzone is too large to have been generated solely by fissuring, lithological variations, or changes in discharge. The persistence of this broad knickzone in Jökulsá á Fjöllum as well as along all of Iceland's large rivers indicate that inverting for a spatio-temporal history of uplift might yield useful insight into regional topographic support. In the next section I use a simple model of advective retreat to determine the parameters required for drainage inversion.

5.5 Regional uplift history

5.5.1 Calibration of Holocene erosion

In order to calibrate river inversion models, it is necessary to calculate model parameters from the observed values from the field. Using measured erosion rates, I estimate the location of Jökulsá á Fjöllum's knickzone at the end of the Preboreal glaciation by assuming that uplift, $U = 0$, and solving a simplified version of stream power erosional model, such that

$$\frac{\partial z}{\partial t} = -vA(x)^m \frac{\partial z}{\partial x}, \tag{5.5}$$

where $\partial z/\partial t$ is the rate of change of elevation, A is upstream drainage area, x is distance from the mouth of the river, and v and m are positive erosional constants that must be calibrated (Rosenbloom and Anderson, 1994; Whipple and Tucker, 1999). If it is assumed that $m = 0.5$, which is often used for fluvial systems, an appropriate value of v can be determined using knickzone retreat rates from Jökulsá á Fjöllum. Substituting $\mathrm{d}x/\mathrm{d}t = 68.7 \pm 0.1$ cm yr^{-1}, $A = 6.79 \pm 0.4 \times 10^9$ m^2 into $\mathrm{d}x/\mathrm{d}t = vA(x)^m$ yields $v = 8.3 \pm 0.5$ Ma^{-1}. By



Figure 5.10: Location of knickzone $\sim$ 10 ka at Hólmatungur. Blue arrow = river flow. River width = $\sim$ 50 m. Note shallow rapids and volcanic plugs along banks.

solving, $L = \int_{\circ}^{T} vA(x)^m \mathrm{d}t$, it is estimated the position of the knickpoint, L, at time, $T = 10$ ka. Since A is approximately constant for several km downstream Dettifoss, a useful rule of thumb is, $L \approx T\mathrm{d}x/\mathrm{d}t$. Solutions to these simple calculations suggest the knickpoint propagated to its current position from ~ 7 km downstream, close to Hólmatungur where Réttarfoss and Vígabjargsfoss are located today (see Figure 5.10).

5.5.2 Drainage extraction and inversion

Armed with calibrated erosional parameters, it is possible to extract drainage patterns to determine landscape evolution in the last 10 ka. Drainage networks were extracted from the ASTER GDEM (resolution $\sim 26 \times 26$ m) and the LMÍ ($\sim 10 \times 10$ m) datasets using Esri flow routing algorithms (see Chapter 3, Section 3.3.1). ASTERExtracted drainage patterns were compared to satellite imagery and our photogrammetry DEM to ensure fidelity. Basins and individual rivers

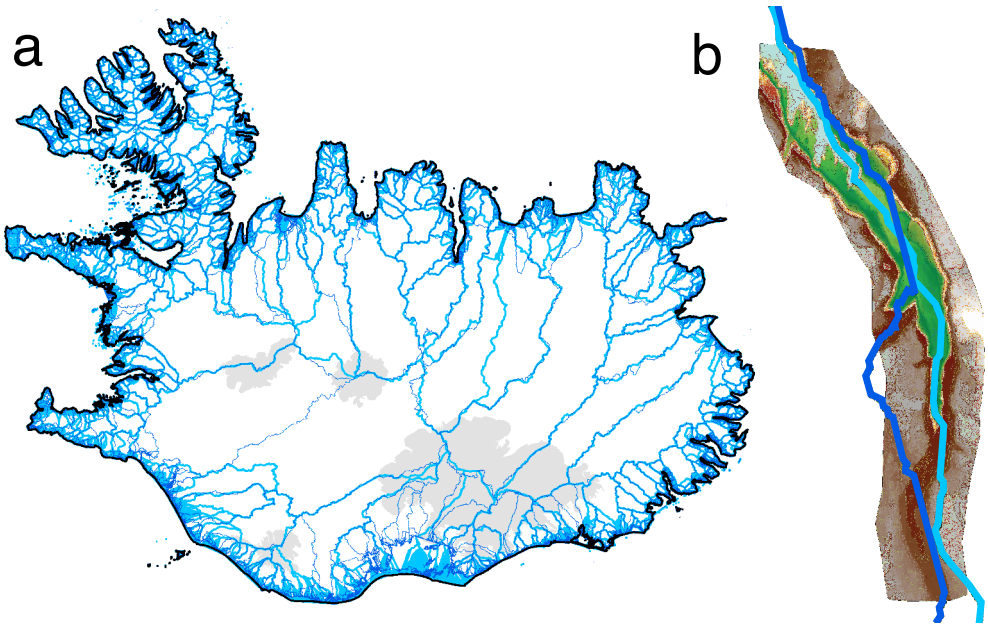


Figure 5.11: ASTER and LMÍ variations in drainage extraction. (a) Mapped drainage basins. Dark blue = ASTER; light blue = LMÍ. (b) Mapped river course over Jókulsárgljúfur canyon. Note ASTER derived river flows through dry valley to the west.

mapped by ASTER GDEM and LMÍ were largely similar further supporting their accuracy (Figure 5.11).

We inverted our drainage inventory of 533 rivers extracted from the ASTER GDEM to calculate uplift rate histories (Rudge et al., 2015). ASTER was chosen due to its superior fidelity in matching regional-scale basins, as opposed to LMÍ which is better at the local (meter) scale (see Figure 5.11). To do so I solved a simplified version of the stream power model, which calculates rate of change of elevation, $\partial z/\partial t$, such that

$$\frac{\partial z}{\partial t} = -vA(x)^m \frac{\partial z}{\partial x} + U(x,t), \tag{5.6}$$

where U is uplift rate, which can vary as a function of space, x and time, t. I use $v = 8.3 \pm 0.5\,\mathrm{Ma}^{-1}$ obtained from maximum measured knickpoint retreat rate at Dettifoss (calibrated in the previous section). Note that this model is described in Chapter 3 for an uplift history only as a function of time (1-D; Section 3.4.2). To invert for a spatio-temporal uplift history a damped least squares approach is used to minimize

$$|M\mathbf{U} - \mathbf{z}|^2 + \lambda_S^2 |S\mathbf{U}| + \lambda_T^2 |T\mathbf{U}|^2 \quad \text{subject} \quad \text{to} \quad \mathbf{U} \geq 0, \tag{5.7}$$

where λ_S and λ_T control spatial and temporal smoothing of the model, respectively (Rudge et al., 2015). Multiple joint-inversions were run which suggest that, for both ASTER and LMÍ derived data, best fitting $m = 0.5$ and $\lambda_S = 1$. The best-fitting, smoothest λ_S was obtained from a systematic sweep of $10^{-2} < \lambda_S < 10^2$ (Figure 5.12a). The best-fitting m was obtained from a systematic sweep of $0 \leq m \leq 1$ and setting $\lambda_S = 1$ and $\lambda_T = 0$ (Figure 5.12). It is acknowledged that m and λ_s trade-off to some extent. Results for river inversion for the last 10 ka are shown in Figures 5.13 and 5.14 and discussed in the next section.

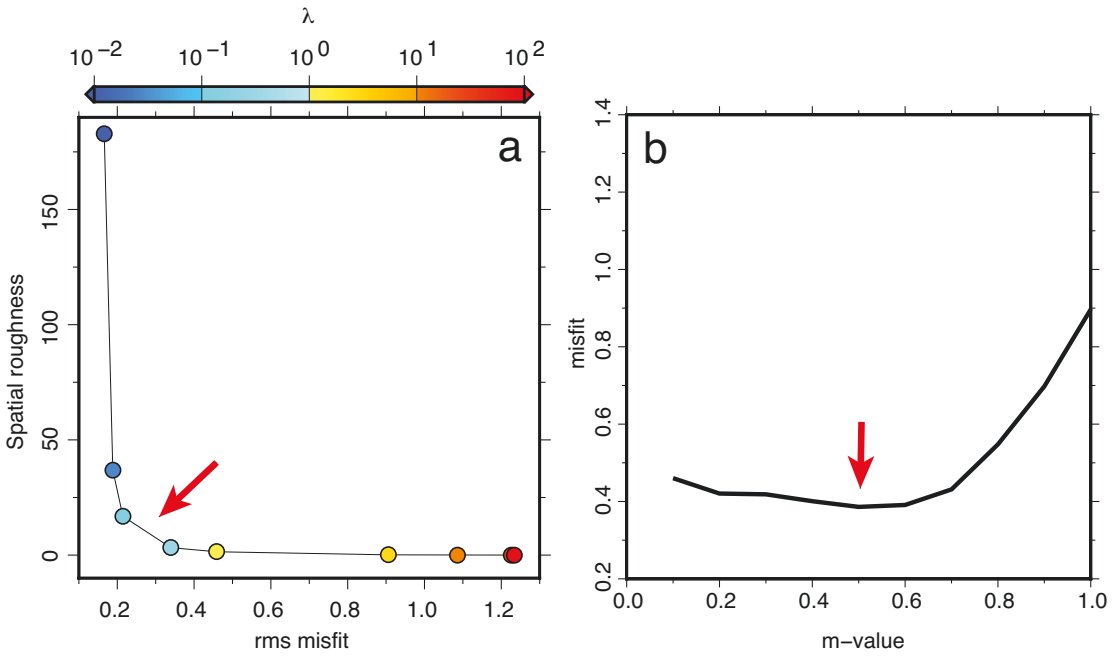


Figure 5.12: Inverse model smoothing and m parameter tests. (a) Misfit as function of spatial smoothing for series of inverse models of river profiles. Colored circles = individual inverse models for different values of λ_S; red arrow = optimal inverse model. (b) Misfit as a function of m parameter from joint inversion of river profiles. Red arrow = lowest misfit (m = 0.5).

5.5.3 Spatio-temporal patterns of uplift

We use the calibrated erosional model to invert our inventory of 533 rivers for a spatio-temporal uplift rate history. Model fits to rivers are good (residual rms misfit = 1.30; Figure 5.13) and cumulative uplift patterns for the last 9 ka are shown in Figure 5.14. Calculated cumulative uplift and uplift rates are

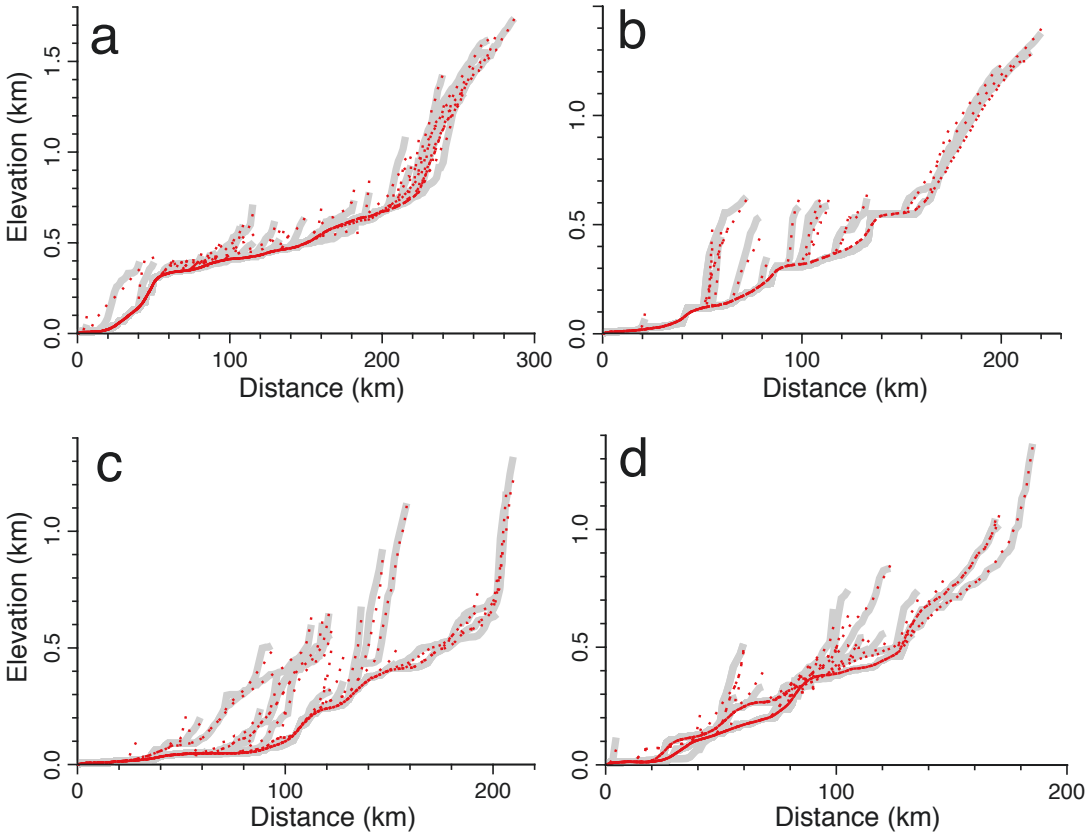


Figure 5.13: Model and observed river profiles from uplift model in Figure 5.14. (a) Gray lines = longitudinal river profiles measured from Jökullsá á Fjöllum catchment; red dotted lines = best-fitting theoretical river profiles calculated from uplift history shown in panel (e). (b)–(d) Observed and best-fitting theoretical river profiles from Jökulsá á Brú, Ölfusá and Skálfandafljót catchments. Global residual rms misfit = 1.30.

greatest in central Iceland where they exceed 100 m and 10 mm yr^{-1}, respectively (Figure 5.14e). Calculated uplift exceeds 50 m in the Eastern and Western Volcanic zones, which are situated above Iceland's rift systems. Independent biostratigraphic and geophysical observations can be used to test the calculated uplift history and examine sources of Holocene uplift. Mapping of paleocoastlines around Iceland indicate uplift rates of 0–15 mm yr^{-1} during the last 8 ka (Le Breton et al., 2010). Average calculated cumulative uplift at these locations is 13 m, which yields an average Holocene-Recent coastal uplift of 13 mm yr^{-1}. Preboreal aged marine mollusc and barnacle shells crop out at elevations of up to 40 m in southern Iceland (e.g. Berufjörður fjord), which suggests average uplift rates of of 7 ± 2 mm yr^{-1} during the last 10 ka (Nordhdahl and Pétursson, 2005). Calculated uplift rates in this region are 6.8 mm yr^{-1}.

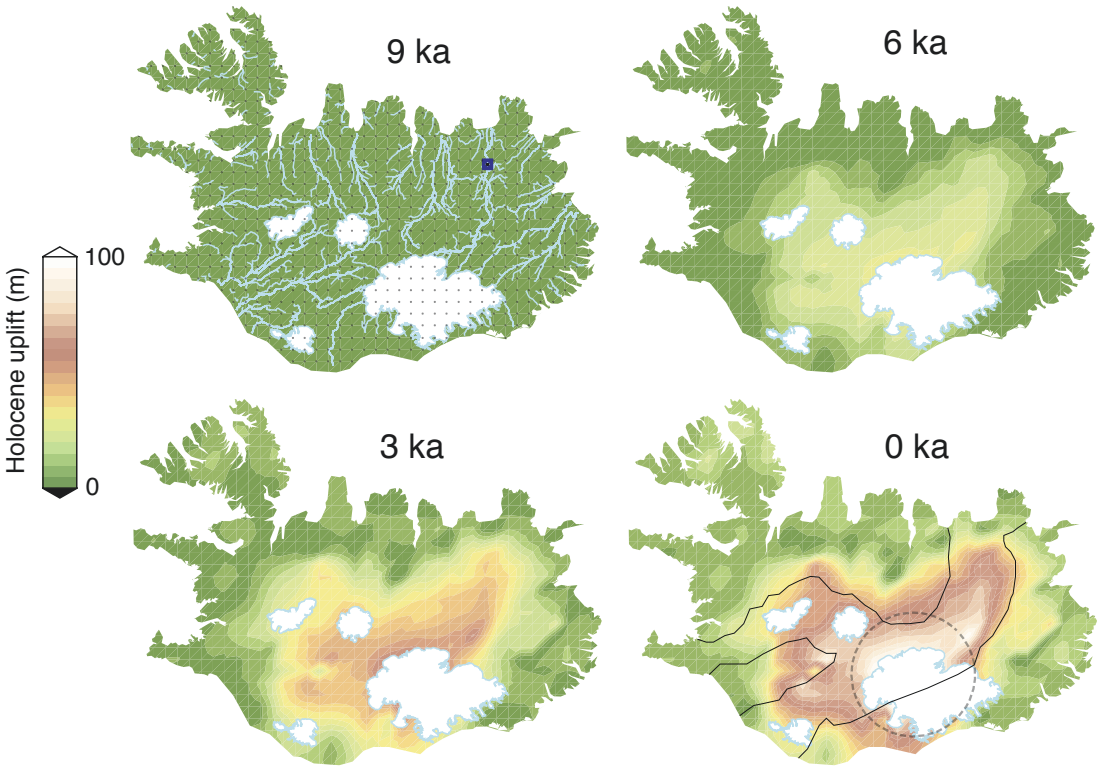


Figure 5.14: Holocene landscape evolution of Iceland. Colour scale = calculated cumulative uplift from 9 ka to present-day; black dots = nodes in uplift model which are spaced 12.5 km apart; blue lines = 553 rivers used in inversion, blue square = location of Jökulsárgljúfur. Solid black lines encloses youngest (<0.7 Ma) rocks and rift zones (Jöhannesson and Sæmundsson, 1989); dashed black circle = location of plume center (Shorttle et al., 2010); white polygons = modern glaciers.

The Plio-Pleistocene Tjörnes Beds Formations in North Iceland contain 1200 m thick sequences of shallow marine sediments and terrestrial deposits alternated with lava flows, which suggest that Iceland has been uplift by hundreds of meters since ~ 5 Ma (Figure 4.7; Verhoeven et al., 2011). Calculated cumulative Holocene uplift in this region is > 70 m.

5.5.4 Measured uplift and canyon denudation

The elevation of the highest terrace and the oldest ages in the canyon indicate that denudation of the Jökulsárglúfur was up to ~100 m since glaciation (Figure 5.9c; topmost terrace = ~315 m, river bottom = ~210 m). Denudational unloading, D, and isostatic adjustment generates rock uplift, U_D. I calculate $U_D = D\rho_c/\rho_a \approx 0.9D$ for crustal and asthenospheric densities of $\rho_c = 2800$ kg m^{-3}, $\rho_a = 3200$ kg m^{-3}, respectively. Using these values yields up to 90 m

of regional rock uplift from denudation of Jökulsárglúfur. Uplift rates are $\lesssim 9$ mm yr^{-1}, assuming unloading rates remained constant for 10 ka. Viscoelastic models indicate that present-day glacial isostatic adjustment exceeds 20 mm yr^{-1} close to Vatnajökull and is negligible ~ 100 km away from the centre of the modern glacier (i.e. close to the canyon; Árnadóttir et al., 2009). These uplift rates suggest the broad area of uplift measured from GPS data in central and southeastern Iceland can be explained by ablation of Iceland's largest glaciers. However, applying corrections for glacial isostatic adjustments to GPS uplift data results in areas of significant residual uplift which cannot be explained by glacial rebound (Schmidt et al., 2012). The largest residual vertical velocities (7–9 mm yr^{-1}) are centred on Jökulsárgljúfur and are consistent with our calculated rates due to denudational unloading of the canyon.

5.5.5 Regional uplift sources

Away from the canyon, regional uplift patterns show highest cumulative uplift which coinciding with spatial distributions of several geological and structural observations. Figure 5.15a shows the location of youngest rocks (< 0.7 Ma), and Figure 5.15b maps loci of active and historical seismicity along Iceland's rift systems (Tryggvason, 1973). Figures 5.15c and d show shear-wave velocity measurements from ambient noise tomography and crustal thickness from seismic refraction results, receiver function analysis, and gravity modelling (Darbyshire et al., 2000; Green et al., 2017). Slow shear-wave velocities correlate very closely with bedrock geology, with contours of the anomalies parallelling the edges of the volcanic zones. Within the seismically slow band (< 2.8 km/s) the lowest velocity centres occur above the centre of the mantle plume and at the top of the western rift. Thickest crust (> 40 km) coincides with the centre of the plume, where active upwelling and high mantle temperatures enhance melt production (Darbyshire et al., 2000). These observations agree with model uplift histories in which a long wavelength (island-wide) component of cumulative uplift with an amplitude of a few tens of meters is required to fit observed longitudinal river profiles, which is most likely a manifestation of dynamic support generated by the Icelandic plume.

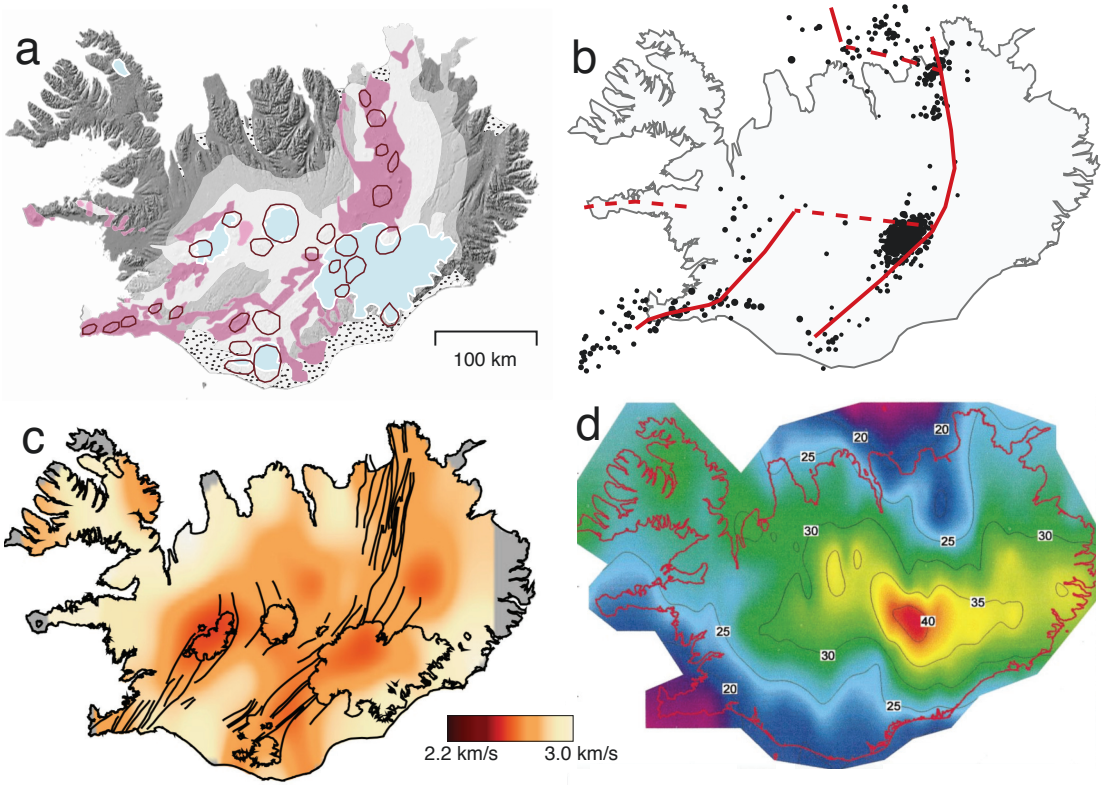


Figure 5.15: Geological, seismic, tomographic and gravity observations of the Icelandic crust. (a) Geology and topographic relief from ASTER GDEM (Jöhannesson and Sæmundsson, 1989; Tentler and Temperley, 2007; Martin et al., 2011). Dark red circles = volcanic centres. See Figure 4.1 for complete key. (b) Earthquakes with magnitude > 2.5 within the last 100 years (USGS Earthquake Catalog). Red lines = rift systems. (c) Shear wave velocities in the upper crust at 3 km depth (Green et al., 2017). Black lines = fissure swarms. (d) Contour map of depth to the Moho. Contours = 5 km (Darbyshire et al., 2000).

5.6 Chapter Summary

Exposure ages of fluvial terraces in Jökulsárgljúfur were measured by cosmogenic ^{3}He dating, which calculates the amount of time rock has been exposed at the Earth's surface. The suite of 26 samples underwent several key stages of preparation where the rock was crushed, magnetic- and density- separated, and sonicated under acid. The purified samples were then transported to Caltech where they were fed into a vacuum where noble gases were extracted at 1250 °C in a MAP 215-50 mass spectrometer. Measured ^{3}He in each sample was corrected using the number of ^{3}He atoms in the shielded sample. Systematic tests of reference production rates, attenuation length of cosmic rays in rock, sample density and thickness, elevation and latitude, snow cover

and its density, were performed. Exposure age results were combined with the 4 cm resolution canyon DEM generated in the field by measuring sample distances downstream. Retreat rates calculated from younging of samples towards waterfalls indicate a knickzone propagation rate of ~ 70 cm yr^{-1} for Dettifoss. Importantly, these results are inconsistent with current models which invoke episodic megaflooding for the formation of Jökulsárglúfur canyon and its waterfall system. This erosion rate was used to calibrate a river inversion model for Icelandic uplift during the Holocene. Results show uplift is broadly consistent with independent measurements from paleo-shorelines and marine fossils. Calculated uplift is highest near rift zones, the Northern Volcanic Zone, and over the Icelandic mantle plume location below Vatnajökull. These observations suggest drainage patterns are responding to these regional processes and that fluvial erosion has played an important role in moderating the post-glacial Icelandic landscape.

In the following chapter, a drainage system from the Martian surface will be explored. In parallel to Iceland, it is dominated by basaltic plains with striking megaflood remnants and glacial landforms. However, it also contains abundant evidence for persistent fluvial erosion over long geological periods. I apply similar tools as those used in Iceland and the North Sea to constrain landscape evolution histories on ancient Mars.

Chapter 6

Drainage systems on Mars: planetary constraints on landscape evolution

6.1 Chapter Introduction

Although presently a cold and dry planet, Mars contains large, complex drainage networks which were once incised by flowing water billions of years ago (Wordsworth, 2016). Once warm and humid enough to support a planet-wide hydrological cycle with hemisphere-covering oceans, deep lakes, and ubiquitous rivers, the planet now has an atmospheric pressure 0.6% that of Earth's and an average surface temperature of -55 °C (McElroy and Donahue, 1972; Kite et al., 2014). This change is thought to have occurred around 4 billion years ago, though the causes are poorly understood (Fanale et al., 1992). Valley networks on Mars would have been dominated by the same driving forces as those on Earth: erosion of the riverbed and changes in base-level (Som et al., 2009). If we can constrain histories of erosion, the uplift histories of the Martian surface can be extracted using similar methodologies which have been applied to terrestrial drainage systems. Several processes could explain changes in base-level on Mars, such as mantle convection, volcanism, and bollide impacts among others. The occurrence of any of these events near or within a drainage system would result in a distinct change in the base-level and thus the gradient of river profiles.

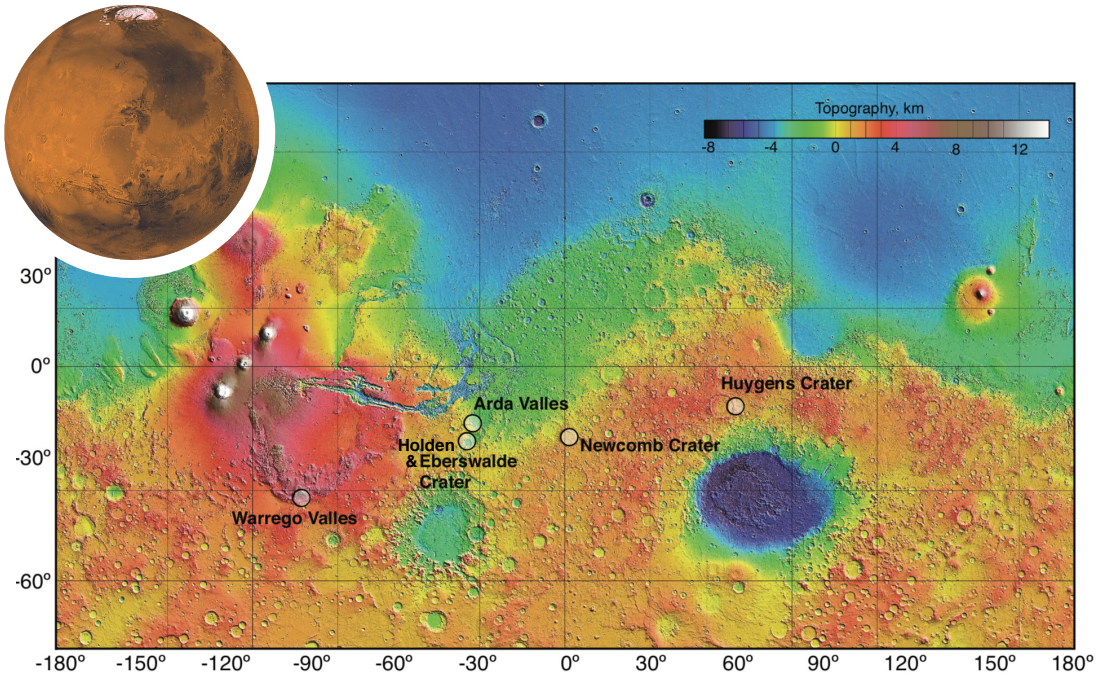


Figure 6.1: Global map of Mars with example drainage locations and study sites superimposed on MOLA altimetry data.

Presently, Mars is the only planet or satellite, other than Earth, for which we have evidence that liquid water has been abundant at the surface (Carr, 1996). This makes it a unique and exciting candidate for testing stream power and landscape evolution models, which have been successful at modelling large drainage inventories on Earth as demonstrated in the previous chapters. In this chapter I explore the various morphologies of Martian drainage networks in the context of potential changes in base-level or uplift events, thus helping to obtain a better understanding of how the Martian crust and drainage system have evolved.

6.2 Fluvial history and topographic evolution

Mariner 9 and Viking Orbiter imagery first revealed valley networks on Mars during the 1970s (Masursky, 1973; Pieri, 1980). During the following decades the increasing resolution of Martian satellite imagery allowed the surface of Mars to be mapped with great detail up to the centimetre scale. These images reveal remarkable landforms which attest to active climatic and geological processes present on Mars. The heavily cratered Martian highlands are dissected

by networks of dry channels and valleys with widths of about 10 km or less, and lengths from < 5 km to up to 1000 km. These channels are no longer active but due to the limited erosional and resurfacing rates on Mars, these ancient landscapes (dated using crater counting techniques) have been able to be preserved despite billions of years of inactivity, wind erosion, and bombardment (Nimmo and Tanaka, 2005). Fluvial activity in these cratered terrains has been dated to up to 3–4 Ga (Jaumann et al., 2015; Wordsworth, 2016). The geometry of channels on Mars has been studied, though predominantly in the context of Mars' ancient climatic history (e.g. Carr, 1996; Hynek et al., 2010; Ansan and Mangold, 2013). As is shown for terrestrial channels in previous chapters, the geometries of these preserved river systems can provide insight into the geological driving forces behind landscape evolution on Mars.

The dominant long-wavelength feature in Martian topography is its 'North-South dichotomy' (see Figure 6.1; Smith and Zuber, 1996). The northern hemisphere is made up of younger, volcanic, smooth lowland plains, whereas the southern hemisphere is much older, rougher, and heavily cratered, with ~ 5 km higher elevations on average (Phillips and Lambeck, 1980). The Tharsis rise is a vast region of volcanism and deformation that appears to interrupt this hemispheric dichotomy (Wenzel et al., 2004). Its domal structure, immense topographic relief, and related gravity field have led several models being proposed for its creation. These models have attributed its formation either to volcanic construction and loading comprising superimposed volcanic plains units, or structural uplift associated with global contraction or local stress fields (Solomon and Head, 1982).

These topographic features illustrate the dynamic nature of the Martian surface. For example, the hemispheric dichotomy has been hypothesised to have occurred either due to thinning of the northern hemisphere crust by mantle convection, or an early period of tectonic plate recycling (Smith et al., 1999). Similarly, the sustained crustal uplift of Tharsis has also been suggested as the result of a mantle plume, or region of convective upwelling, which also provided the heat to fuel the long-lived volcanic activity (Mège and Masson,

1996). Although Mars is presently a dry, cold, and tectonically inactive body, complex topographic features suggest that there is a complex history of uplift and convective processes which can be gleaned from ancient, preserved Martian channels. However, current Martian geomorphic work consists mostly of mapping and quantitative treatment of rivers is limited to more simple analyses (e.g. slope-area), which makes extracting and deconvolving planetary processes over geological time a challenge.

In the next section I discuss some examples of large-scale dissected terrains which highlight the common types of fluvial morphologies on Mars. Section 6.4) then hones in on fluvially modified craters due to their simple and well known base-level history, and their similarity to terrestrial craters. Lastly, in Section 6.5 I focus on Warrego Valles and how its spectral power and drainage networks can be used to extract uplift and erosion histories for ancient Mars.

6.3 Elevation data & drainage mapping

6.3.1 Data acquisition

To map out the channel morphologies, two sets of surface data are required: imagery of the planetary surface which show the location and extent of channels, and digital elevation models to quantity these elevation changes. The Geosciences Node of NASA's Planetary Data System archives and distributes digital data related to the study of the surfaces and interiors of terrestrial planetary bodies. Topographic data has been measured by several instruments at varying degrees of resolution and coverage. The Mars Orbiter Laser Altimeter (MOLA), aboard the Mars Global Surveyor, has lower resolutions of > 500 m and full coverage of the surface (e.g. Figure 6.1). After 10 years of operation, the High Resolution Stereoscopic Camera (HRSC) covers about 70% of the surface by panchromatic images at 10–20 m/pixel, and about 97% at better than 100 m/pixel (Gwinner et al., 2016). These resolutions are on par with global elevation models on Earth (cf. ASTER & SRTM) and indicate similar geomorphological analyses are appropriate.

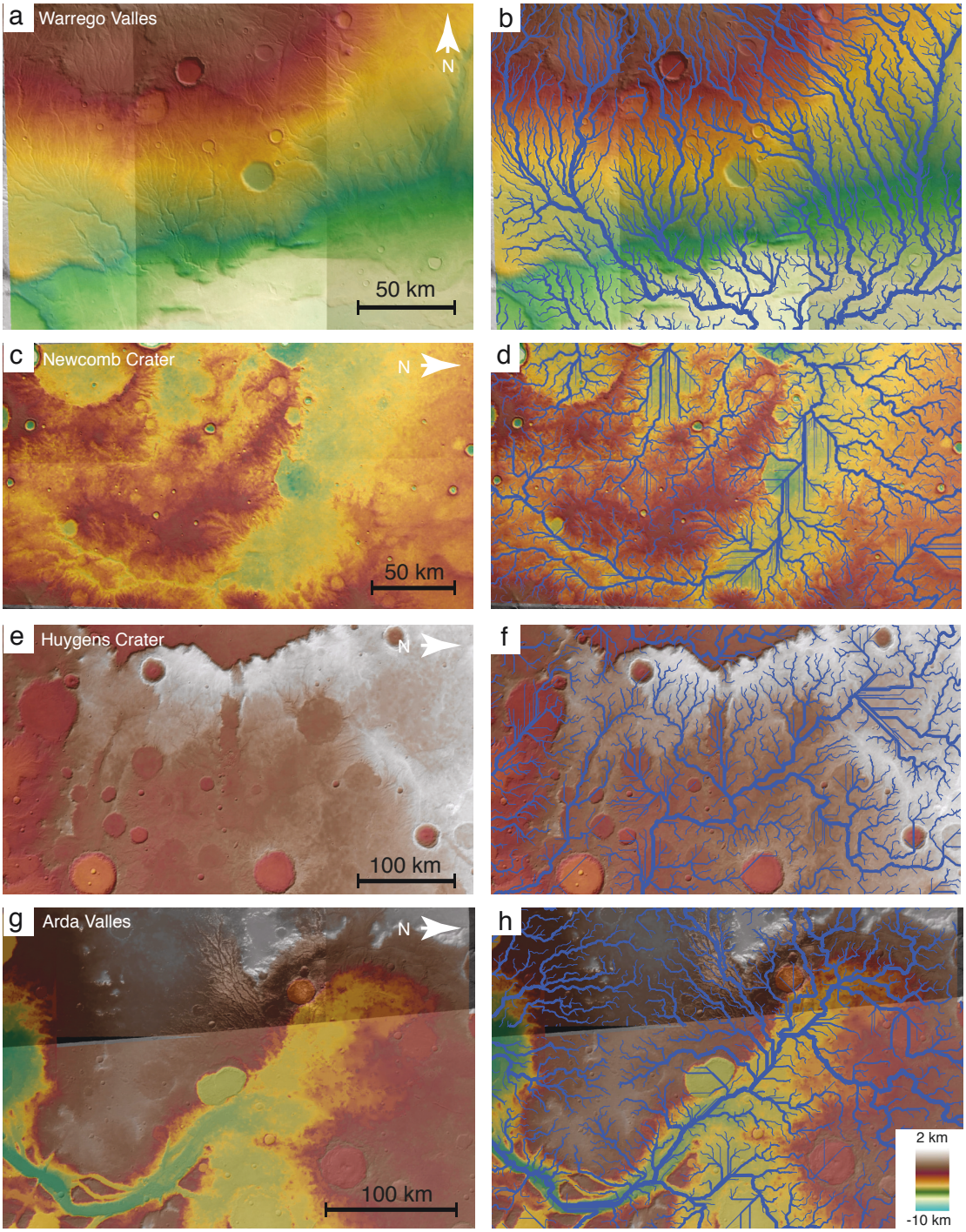


Figure 6.2: Examples of channel locations on Mars. Left-hand panels show HRSC DEM superimposed on HRSC imagery. Right-hand panels show the same locations with mapped drainage. Location names are indicated in top-left corner. See Figure 6.1 for channel locations.

6.3.2 Dendritic valley networks

Drainage patterns were extracted for several channelized regions using HRSC DEM. Their fidelity was checked using HRSC imagery. Figure 6.2 shows the mapped channels of 4 heavily incised locations. The channel features can be clearly seen without the applied drainage on the left hand panels. The calculated drainage networks align well with the observed channels and clearly delineate the distinct basins and drainage into flat regions and crater floors.

There is great morphologic diversity in what is termed a valley. The wide variety in morphologies can include branching networks, fluviatile valleys, dendritic channels, tributaries emptying into large sinuous valleys, parallel gullies, and trellis valley systems (Craddock and Howard, 2002). Small, high-density dendritic valley networks are typified by Warrego Valles. Channels observed in Huygens and Newcomb craters are found to the east of the crater rim of both craters (Figure 6.2c–f). The high topography of the ancient, elevated crater rim resulted in channels that flow away from the crater edge into the Martian plains. The channels are not as clear as the ones observed in Warrego Valles, but significant dendritic features can be observed for both locations. Note that areas which appear to have 'straight' rivers are a result of flow routing algorithms running through a flat area. These straight segments can be seen to occur in flat regions such as crater floors where it is possible that the water could have flowed into, creating crater lakes.

6.3.3 Outburst floods

The channel morphology of Arda Valles differs to that of the three above regions in that it is classified as a large outflow channel (Figure 6.2g,h). Outflow channels are extremely long, wide swaths of scoured ground on Mars, commonly containing streamlined remnants of pre-existing topography and other linear erosive features indicating sculpting by fluids moving downslope (Baker, 1978). Besides their exceptional size, the channels are also characterised by low sinuosities and high width:depth ratios compared both to other Martian valley features and to terrestrial river channels (Baker and Milton, 1974; Carr, 1979). From their geomorphology, locations, and sources, the channels are

today generally thought to have been carved by outburst floods (Carr, 1979; Robinson and Tanaka, 1990; Chapman et al., 2003).

6.3.4 Valley formation

Although outflow channels were formed in single or episodic discharge events, valley networks with dendritic morphologies and high-drainage densities such as Warrego Valles are thought to have been generated by sustained periods of precipitation (Craddock and Howard, 2002). The valley tributaries initiate near peaks of topographic divides (Figure 6.2), which strongly supports an origin due to precipitation as either rain or snow as opposed to groundwater sapping (Wordsworth, 2016). Landform evolution and sediment transport models with wide ranges of input parameters to encompass a range of possible formation conditions have suggested minimum formation timescales of 10^5 yr (Barnhart et al., 2009; Hoke et al., 2011).

Channel formation and wet conditions are not constrained uniquely to the Noachian period ($>$ 3.5 Ga). In the next section I will discuss more recent (Late Hesperian–Amazonian; 3.0 –2.5 Ga) channels formed along crater walls and draining into crater lakes. Channels within a crater contain common base level histories, allowing us to assess Martian channel geometries qualitatively under simple conditions.

6.4 Crater drainage

6.4.1 Eberswalde & Holden craters

Fluvially modified craters show several degrees of gullying and alcove formation on their rims (Grant and Wilson, 2011). These craters have excellent preservation of both erosional and depositional features and are thought to have contained large quantities of water either intermittently or perennially (Cabrol and Grin, 1999). This suggests that the observed channels and alcoves share a common base-level history. Additionally, since the morphologies of fresh impact craters are well constrained both from theoretical modelling and field observations, their initial conditions prior to fluvial erosion are known (i.e.

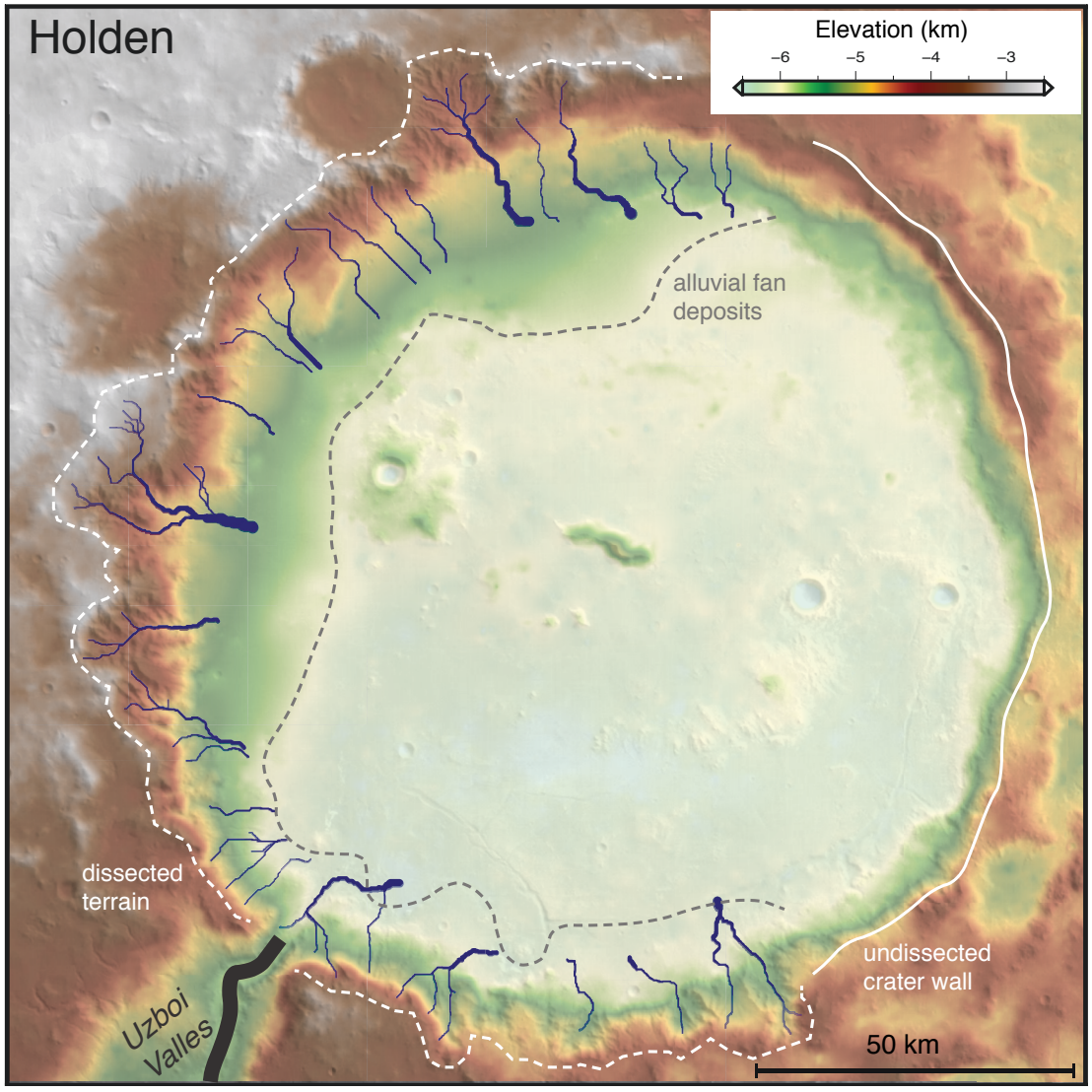


Figure 6.3: Holden Crater from HRSC imagery and elevation. Blue lines = inventory of 54 channels; solid white line = undissected crater rim; dashed white line = dissected crater rim; grey dotted line = alluvial fan deposits; black line = feeder channel.

paleo-topography; Melosh, 1989; Wünnemann and Ivanov, 2003). This makes them a promising site for constraining fluvial histories on Mars.

With the exception of occasional small-scale cratering, their crater centres are generally flat, smooth plains, with overall crater reliefs significantly smaller than those of pristine craters of the same size due to infilling, mantling, and degradation by impacts (Moore and Howard, 2005). Holden crater is a 150 km-diameter crater which contains several incised drainage basins along its rims (Figure 6.3). At the base of these basins, large alluvial fans have been deposited. These are laterally integrated into a the crater floor deposits and

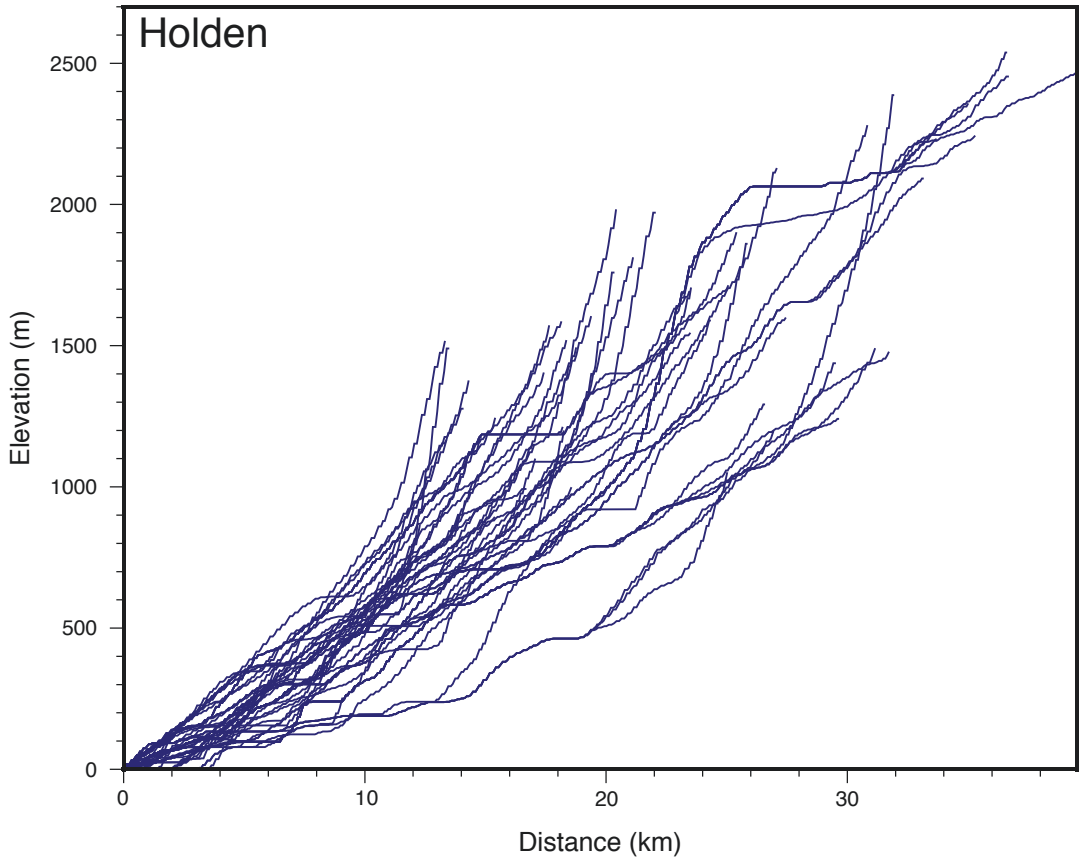


Figure 6.4: a) Longitudinal profiles of extracted channels in Holden Crater. See Figure 6.3 for channel locations.

show evidence of a fluvial-lacustrine system most likely fed by Uzboi Valles (SW side of Holden; Figure 6.3). Longitudinal profiles were extracted to generate an inventory of 54 rivers (see Chapter 3, Section 3.3.1 for drainage extraction methodology). Figure 6.4 shows river profiles which exceed 2 km in height and 30 km in length. Although a long-wavelength, concave-up signal is observed, corresponding to the initial crater wall morphology, the profiles contain multiple knickzones with up to 500 m in height and several km in length.

Eberswalde crater, a 50 km-diameter crater located 30 km north of Holden is shown in Figure 6.5. Although in close proximity to Holden, Eberwalde differs from the former in that its crater walls contain less distinct incised alcoves, its main basin is located outside the crater, and it contains a large preserved deltaic system. High-resolution (few cm) HiRISE (High Resolution Imaging Science Experiment) imagery show these deltaic deposits contain erosion-resistant for-

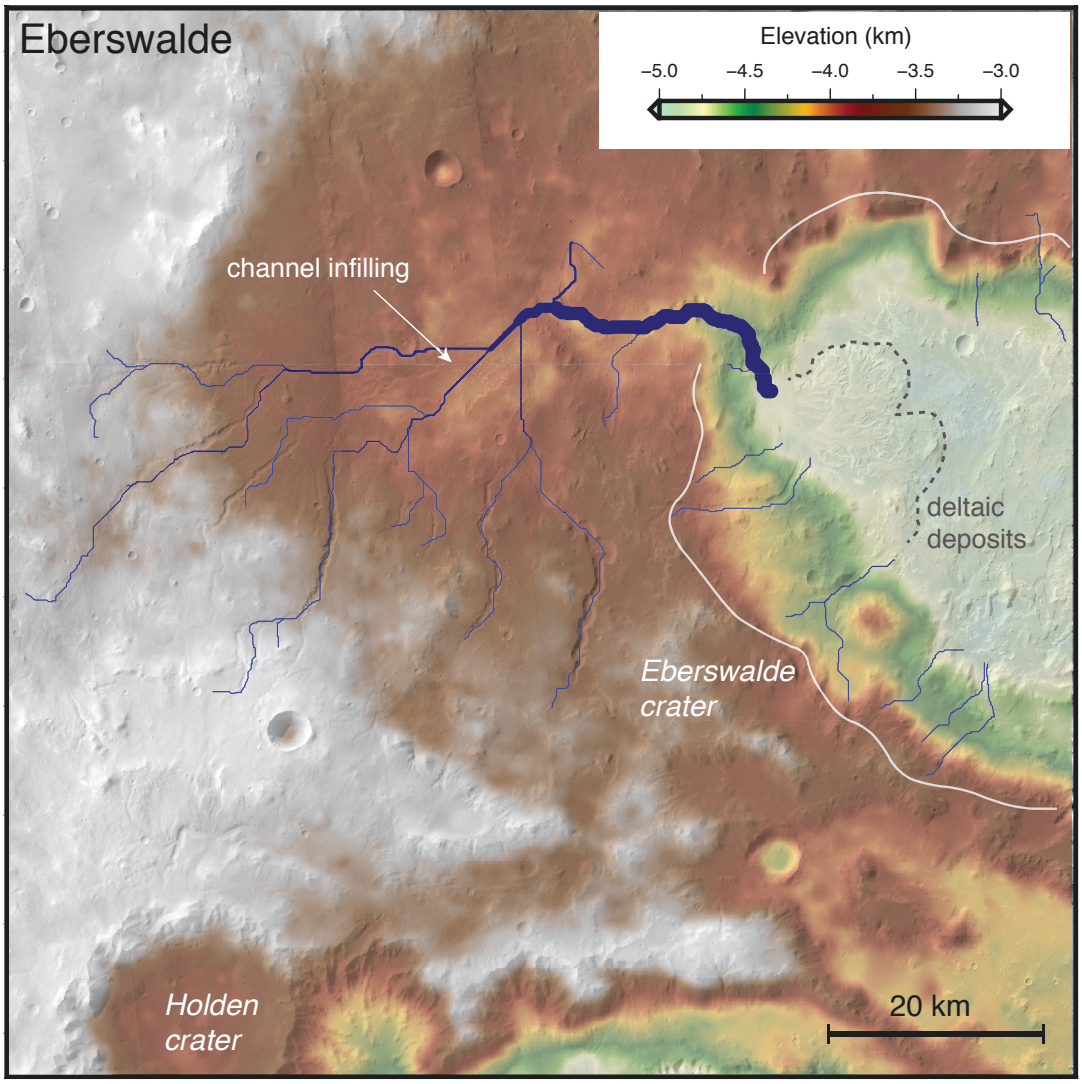


Figure 6.5: Eberswalde Crater from HRSC imagery and elevation. Note northern rim of Holden in bottom centre. Blue lines = inventory of 22 channels; solid white line = crater rim; grey dashed line = delta extent.

mations which are exposed after finer material has been removed from wind erosion, resulting in ridge-dominated inverted topography which can also be observed on Earth (e.g. Niem, 1974; Williams et al., 2009). Longitudinal profiles of channels in Eberswalde indicate the presence of a large knickzone ($\sim$ 1 km height, 20 km length) located at the top of the crater rim (Figure 6.6).

The large knickzone observed in Eberswalde most likely attests to the immaturity of the feeder basin as it breaches the crater rim, suggesting an insufficient amount of time for the channel to generate a graded slope toward the crater

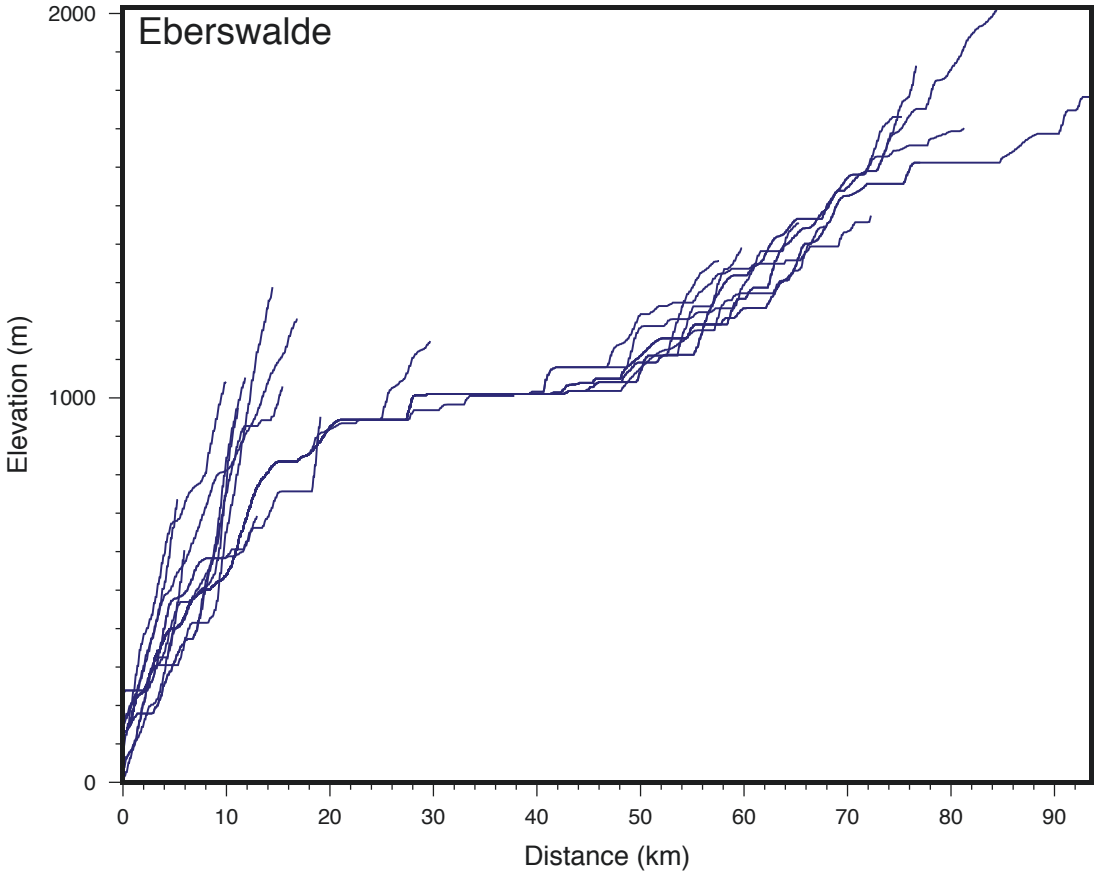


Figure 6.6: Longitudinal profiles of extracted channels in Eberswalde Crater. See Figure 6.5 for channel locations.

floor. In Holden, the lowest portions of river profiles have signals which are covered by alluvial fan deposits containing constant slopes of $\sim$ 2–3°. However, the mid- to upper-reaches of profiles have knickzones that were most likely generated during fluvial erosion since the initial crater walls are graded and otherwise pristine (see NE corner of Holden in Figure 6.3). The lithology of the underlying bedrock is largely uniform (tholeiitic basalt), and there is limited evidence for structural control such as faulting or jointing. As a result, common knickzones (e.g. downstream distance of 14–20 km; Figure 6.4) are best explained by changes in base-level of the crater lake, potentially due to a breaches in the eastern wall.

The two largest sources of error for reconstructing channels profiles as they were formed several billion years ago are post-fluvial cratering and infilling of the channels. Both processes result in flattening of the profiles (sometimes oblit-

erating the entire channel). Tributaries which appeared to be heavily modified by these processes were not included in the inventory so as to ensure profile geomotries and knickpoints were representative of the fluvial processes that formed them.

6.4.2 Terrestrial craters

The fluvially dissected craters described above can be directly compared to terrestrial analogs. On Earth, rapid erosion and resurfacing does not allow for preservation of ancient channels on the surface. Calibrated stream power erosional models suggest that most landscapes on Earth are destroyed within a few tens of millions of years (Hofmann and White, 1982; Bishop, 2007; Burke and Gunnell, 2008; Glotzbach, 2015; Rudge et al., 2015). As a result, large craters preserved on the surface of the Earth have much shorter lifetimes and are generally more heavily degraded.

Meteor Crater. Meteor (Barringer) Crater is a meteorite impact crater 1.2 km in diameter located in Arizona, USA (Figure 6.7a Grieve and Shoemaker, 1994). The crater was formed $\sim$ 50 ka as measured from cosmogenic ^{36}Cl and ^{14}C in rock varnish (Phillips et al., 1991). This young age, combined with the dry Arizona climate, has resulted in its remaining almost unchanged since formation, having been eroded only superficially by fluvial, eolian, and mass wasting processes (Grant and Schultz, 1993). This is reflected in the steep, concave-up profiles which show little to no modification from pristine crater wall morphologies (Figure 6.7b).

Elgygytgyn Crater. Lake Elgygytgyn is 12 km in diameter and is centred within an impact crater with a rim diameter of 18 km located in northeast Siberia (Figure 6.7c; Melles et al., 2011). It formed $\sim$ 3.5 million years ago as measured from laser ^{40}Ar/^{39}Ar dating of impact-melted volcanic rocks (Grieve and Shoemaker, 1994; Layer, 2000). The longitudinal profiles show extensive fluvial erosion and river lengths up to 10 km draining into the lake in the western rims (Figure 6.7d). Large knickzones are observed close to the lake margins whereas

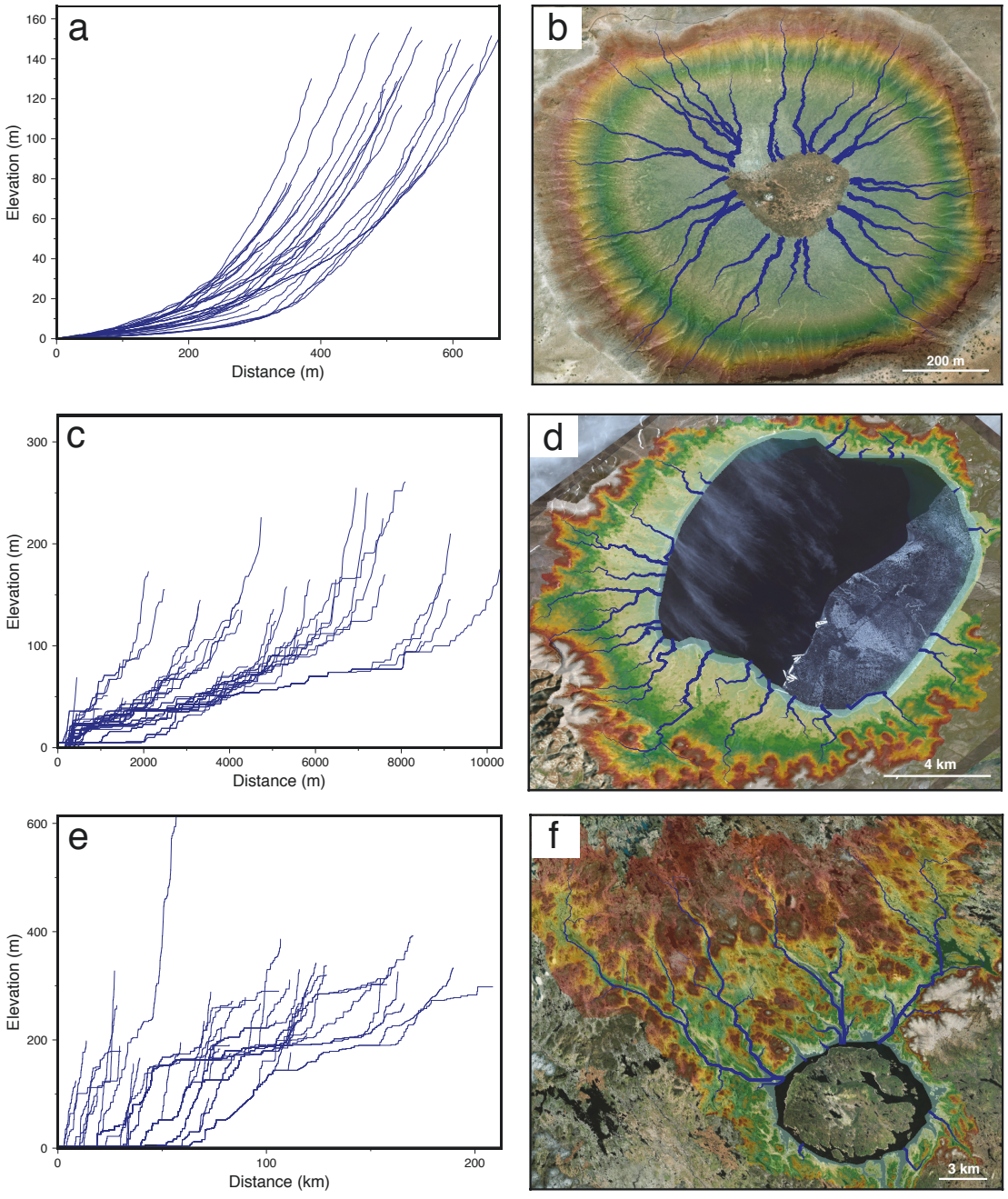


Figure 6.7: Terrestrial craters in order of increasing size and age. (a) Meteor Crater. Blue lines = inventory of 124 channels. (b) Meteor crater longitudinal profiles extracted from photogrammetric DEM and laser scanned interior data (Brown et al., 2008). (c) Elgygytgyn crater lake. Blue lines = inventory of 125 channels. (d) Meteor crater longitudinal profiles extracted from ASTER data. (e) Manicouagan crater. Blue lines = inventory of 128 channels. (f) Manicouagan longitudinal profiles extracted from ASTER data. Underlying imagery for all three craters obtained from ESRI World Imagery basemap.

upstream portions of the rivers have steeper, concave-up morphologies.

Manicouagan Crater. The Manicouagan Crater is located in the Côte-Nord region of Québec, Canada. It formed $\sim$ 215 million years ago as measured from laser $^{40}Ar/^{39}Ar$ dating of glass formed by the impact, and is one of the oldest known impact craters on Earth (Ramezani et al., 2005). The crater is a multi-ring structure $\sim$ 100 km in diameter, containing a 70 km-diameter annular lake, the Manicouagan Reservoir, which surrounds an inner island plateau (Figure 6.7e; Rose, 1955). Extracted drainage patterns deviate strongly from the symmetrical, radial channels observed in the Meteor Crater. Drainage basins extend to 200 km north of the crater, and an abundance of knickzones attest to a highly fluvially degraded history (Figure 6.7f).

Pristine, undissected walls in simple Martian craters resemble those observed in the Meteor Crater (e.g. northeast rim of Holden). However, geometries of Holden and Eberswalde craters profiles are mostly analogous to Elgygytgyn and Manicouagan Crater-type modification. Both comprise well-defined, radial, assymetric drainage basins (few 10s km) and a central crater lake with accumulating sediment layers. These observations support a sustained environment with wet conditions and precipitation for the formation of these younger channels, in contrast to formation by episodic outbursts, groundwater seepage, gullying, or mass-wasting.

In the next section I will discuss one of the most well-defined valley network system on Mars, Warrego Valles, which is older (Noachian age) and is not associated to a crater. Its interesting location in the Martian topography and its highly dendritic morphology make it an exciting candidate for testing models of landscape erosion and uplift on ancient Mars.

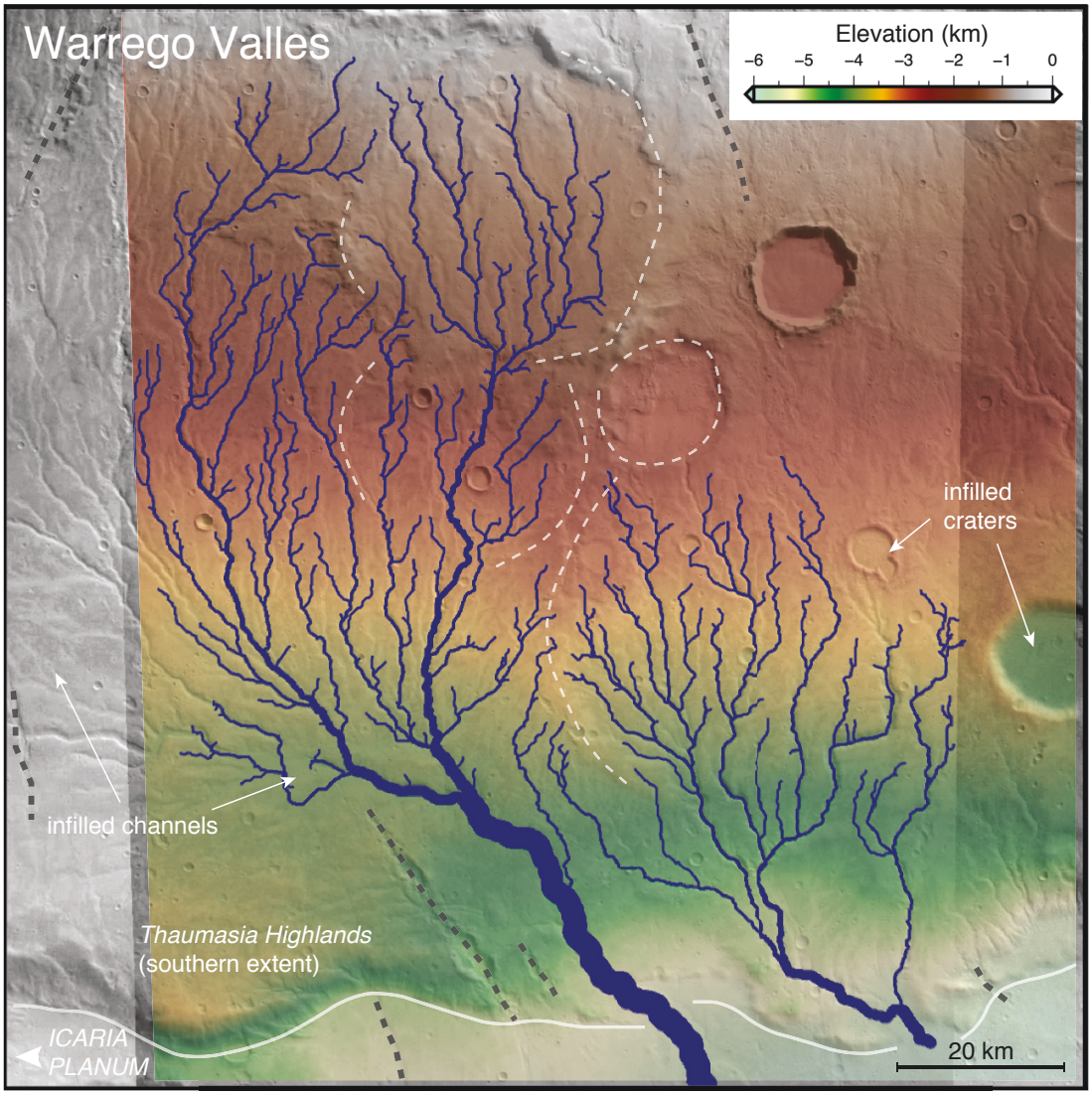


Figure 6.8: Location of Warrego Valles channels over HRSC imagery. White dashed lines = degraded craters. Black dashed lines = faults/joints. White solid line = southernmost boundary of Thaumasia Highlands.

6.5 Warrego Valles

6.5.1 Preserved dendritic drainage

Most valley networks which have been mapped and identified are located primarily in the heavily cratered uplands of Noachian age (4–3.5 Gyr). A remarkable exception to this is Warrego Valles, located on the southeastern part of the Tharsis bulge (Figure 6.1 & 6.8). The Warrego Valles system is characterised by highlands rising to an elevation > 5 km from the southern plains which are heavily dissected and flow southward. A large amount of

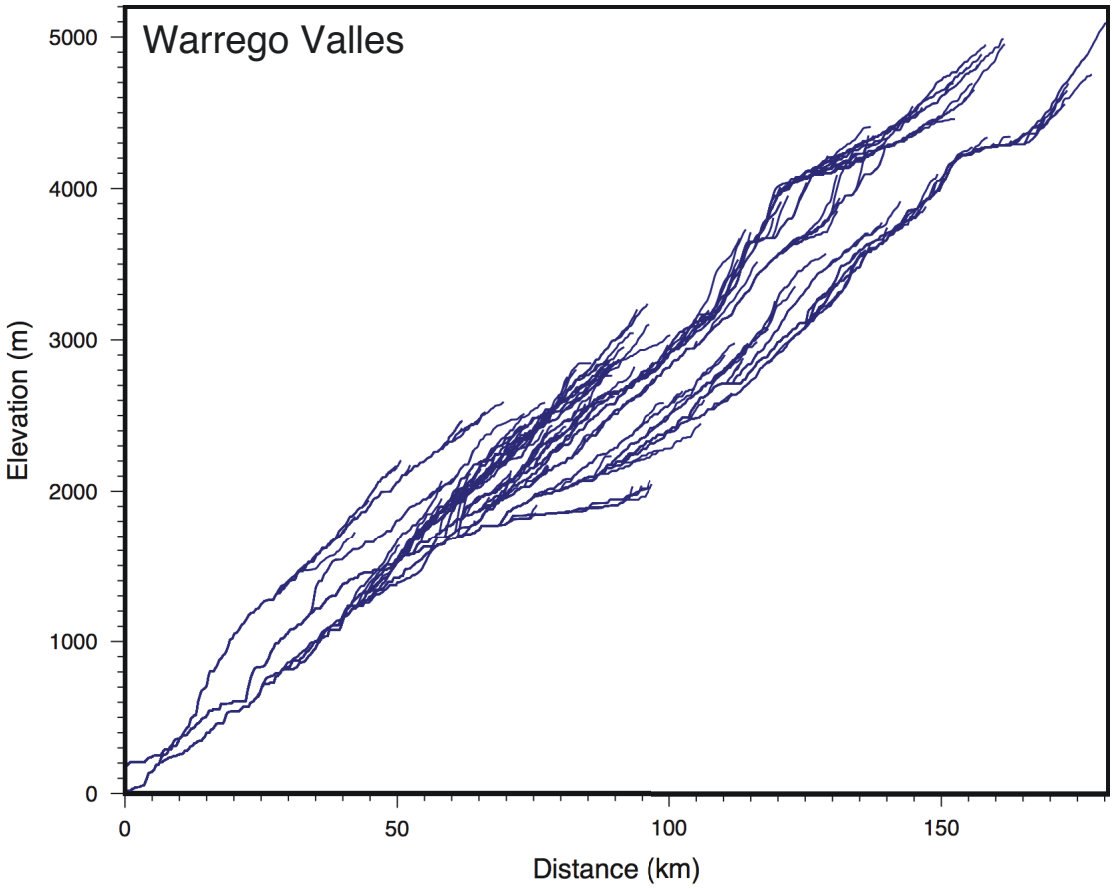


Figure 6.9: Longitudinal profiles of 184 extracted channels in Warrego Valles. See Figure 6.8 for channel locations.

folds, faults, rift valleys and volcanoes have been identified in this region (Schultz and Tanaka, 1994). Most of the valley networks observed in these highlands generally display low degrees of organisation with few branches, however Warrego Valles displays higher maturity, with two well-formed parallel valley systems which join together and terminate in the smooth, southern plains (Ansan and Mangold, 2006). Longitudinal profiles extracted from both Warrego Valles basins show a slightly concave-up shape with large knickzones at upstream distances 50 km and 100–150 km (Figure 6.9). In the next two section I use spectral analyses and joint river inversion methods to assess the Warrego Valles system with an aim to understand its controlling topography.

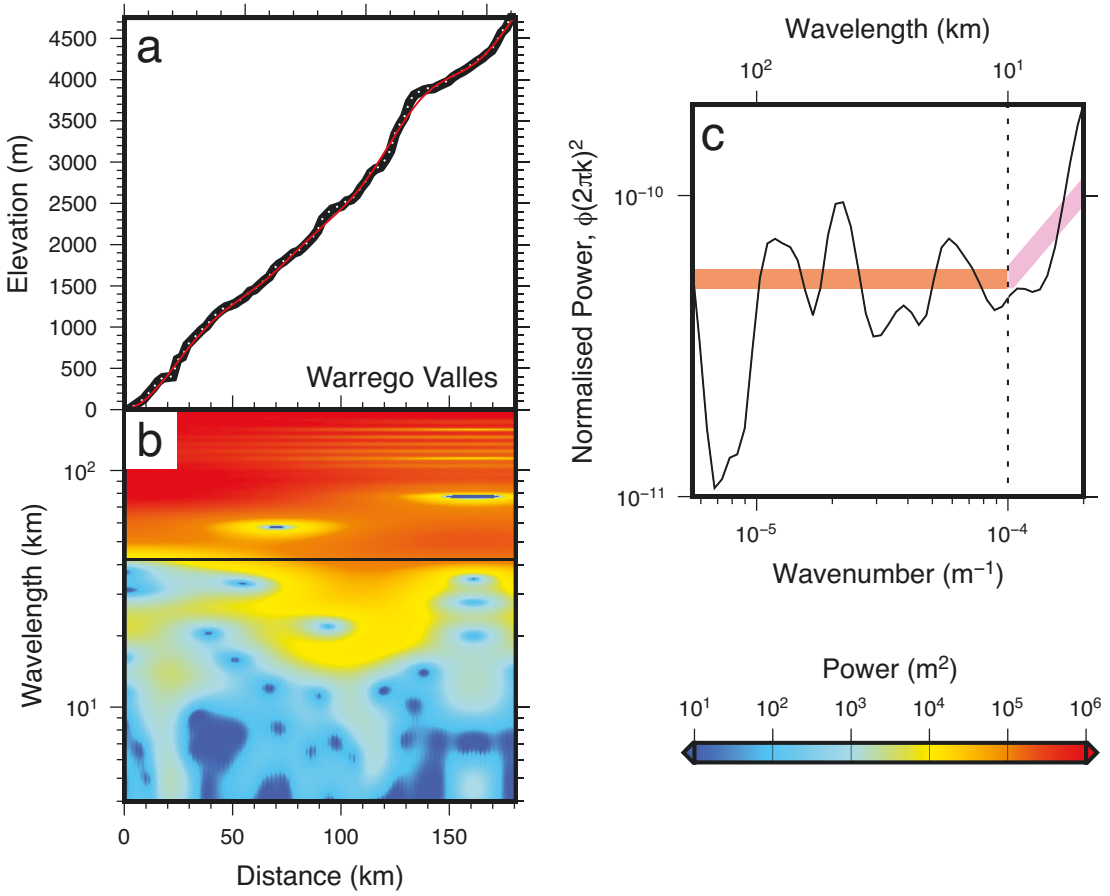


Figure 6.10: (a) Longitudinal river profiles. Black line = observed profile; red solid line = filtered profile calculated using wavelengths $>$ 42 km; white dotted line = inverse wavelet transform. (b) Power of profile elevation as function of distance along river channel and wavelength calculated using Morlet wavelet transform method (Torrence and Compo, 1998). Black solid line = cut-off used to calculate filtered profile for wavelengths of $>$ 42 km. (c) Normalized power spectrum rectified according to scale and multiplied by $(2\pi k)^2$ in order to flatten red noise. Black line = observed, distance-averaged spectrum; red band shows $\phi \propto k^{-2}$ regime; pink band shows $\phi \propto k^{-1}$ regime; vertical dotted line = transition between two regimes.

6.5.2 Spectral analysis

The spectral content of landscapes of landscapes has been examined at a variety of scales (Pike and Rozema, 1975; Bell Jr, 1975; Gallant et al., 1994; Pelletier, 1999; Birnir et al., 2001; Singh et al., 2011). Most landscapes in these studies are observed to be spectrally red such that their power is proportional to k^{-2}, where k is the wavenumber. This behaviour suggests that landscapes are self-similar, i.e. the ratio of amplitude to wavelength of their features is independent of scale (Huang and Turcotte, 1989). Analyses using wavelet transforms have

significant advantages over typical Fourier decomposition, which relies on the assumption of stationarity and lacks information on spatial distribution. Wavelet transforms have the ability to identify dominant wavenumbers (i.e. spatial frequencies) and show how power changes with increasing upstream distance x along a river. The wavelet transform of a longitudinal river profile, $W_x(s)$, is a function of scale s, and can be expressed in discrete notation as

$$W_x(s) = \sum_{x'=0}^{N-1} z_{x'} \psi \left[\frac{(x' - x)\delta x}{s} \right], \tag{6.1}$$

where z_x are discrete elevation measurements equally spaced at intervals δx along the profile. The mother wavelet ψ is scaled by s and translated along the river profile by x' for N data points. The wavelet power spectrum is

$$\phi(s, x') = |W_x(s)|^2. \tag{6.2}$$

The distance-averaged power spectrum, which is related to the Fourier power, spectrum is given by

$$\bar{\phi}(s) = \frac{1}{N} \sum_{x=0}^{N-1} |W_x(s)|^2. \tag{6.3}$$

The wavelet power spectra can be compared with Fourier power spectra by converting scales to wavenumbers and correcting spectral bias ($\phi_s = \phi(s)|s|^{-1}$; Torrence and Compo, 1998). The choice of mother wavelet has an effect on calculated spectra. However, using Morlet or Mth order derivative of Gaussian mother wavelets are similar if M > 6. Spectra are sensitive to discontinuities at the start and end points of a profile. To avoid these artefacts, profiles are mirrored about both z- and x- axes to remove abrupt elevation changes which largely removes edge effects.

Figure 6.10 shows wavelet power spectra for the largest tributary in Warrego Valles. This was calculated using a Morlet mother wavelet (M = 6). It is possible to calculate the inverse wavelet transform by summing the transform over all wavenumbers, k (see white dotted line; Figure 6.10). The original river profile can be recovered with small error, suggesting wavelet transforms are a faithful representation of the river profile. Power spectra indicate that river profiles are

spectrally red such that the greatest power resides at the longest wavelengths. At wavelengths $\sim$ 42 km, there is a sudden decrease in power which varies only slight along the river profile (Figure 6.10b). If power at wavelengths $<$ 42 km is omitted, the recovered profile closely matches the original profiles, with uncertainties of a few meters. Note that high power at short wavelengths is localised and tends to occur at knickpoints. This suggests that the most important power is concentrated at wavelengths $>$ 40 km. This is in agreement with wavelet spectra from terrestrial rivers which also have power concentrated at higher wavelengths, such as the Niger river where most power is concentrated at wavelengths $> 10^2$ km Roberts and White (2017).

Distance-averaged spectra, where power is normalised by multiplying by $(2\pi k)^2$, allows the detailed wavenumber dependency of the spectral power, ϕ, to be isolated (Figure 6.10c). At wavelengths $>$ 10 km $\phi \propto k^{-2}$, which is in agreement with the well-known results obtained by spectrally analysing landscapes. At these length scales, rivers are characterised by red (Brownian) noise and exhibit self-similarity. This behaviour is also consistent with spectral content of observed dynamic topography, which is a dominant controlling process on river morphology. An abrupt transition can be seen at $\sim$ 10 km, where the spectral slope flattens to $\phi \propto k^{-2}$, indicative of pink noise (Figure 6.10c). This abrupt change most likely suggests a transition in the dominant processes from short to longer wavelengths. Importantly, this transition occurs at wavelengths similar to those of some rivers on Earth Roberts and White (2017). These observations suggest Warrego Valles has spectral properties which closely match those on Earth, where more than 90% of power resides in higher wavelengths, with self-similar behaviour occurring at higher wavelengths. These scaling observations are consistent with physically based landscape models in which the channelisation process is driven by white noise but externally forced by large-scale tectonic uplift. In the next section I invert the Warrego Valles drainage basin to obtain an uplift history.

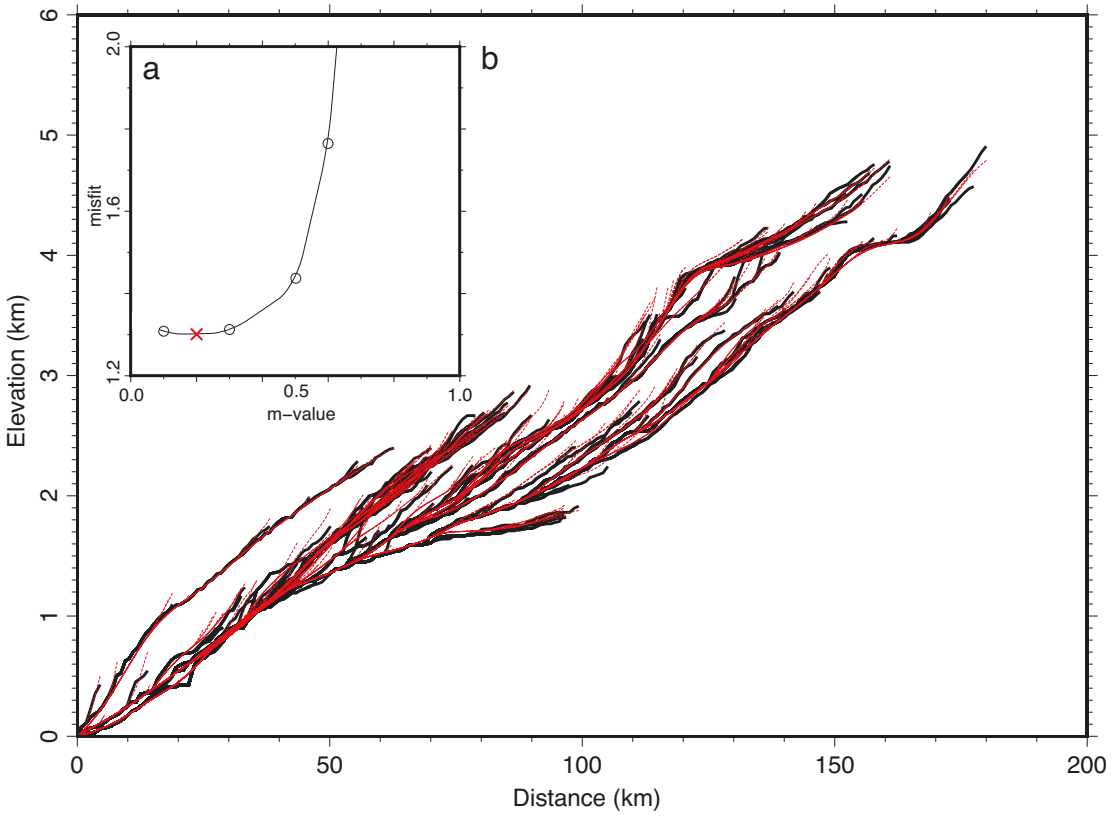


Figure 6.11: Observed and model longitudinal profiles from joint inversion of 184 channel inventory in Warrego Valles. (a) Misfit as a function of m-value. Red cross = best-fitting m = 0.2. (b) Longitudinal river profiles. Black line = observed profiles. Red dotted line = model profiles.

6.5.3 Inverting for uplift history

In previous Chapters, large drainage inventories were successfully implemented as a tool to probe geodynamic and sub-surface processes which drive landscape evolution. Warrego Valles' location on the southern rim of the Tharsis Bulge, which may have been formed from mantle convection, suggests inverting rivers for an uplift history could yield useful insights into its formation and evolution. The valley networks in the Thaumasia region are thought to have been formed from the late Noachian through the early Hesperian ($\sim$ 3.0 Gyr) based on relative chronology and crater counts (Tanaka, 1986; Tanaka et al., 1998; Dohm and Tanaka, 1999). More recent work from buffered crater counting has suggested Warrego Valles may be $\sim$ 3.7 Ga. Note that these

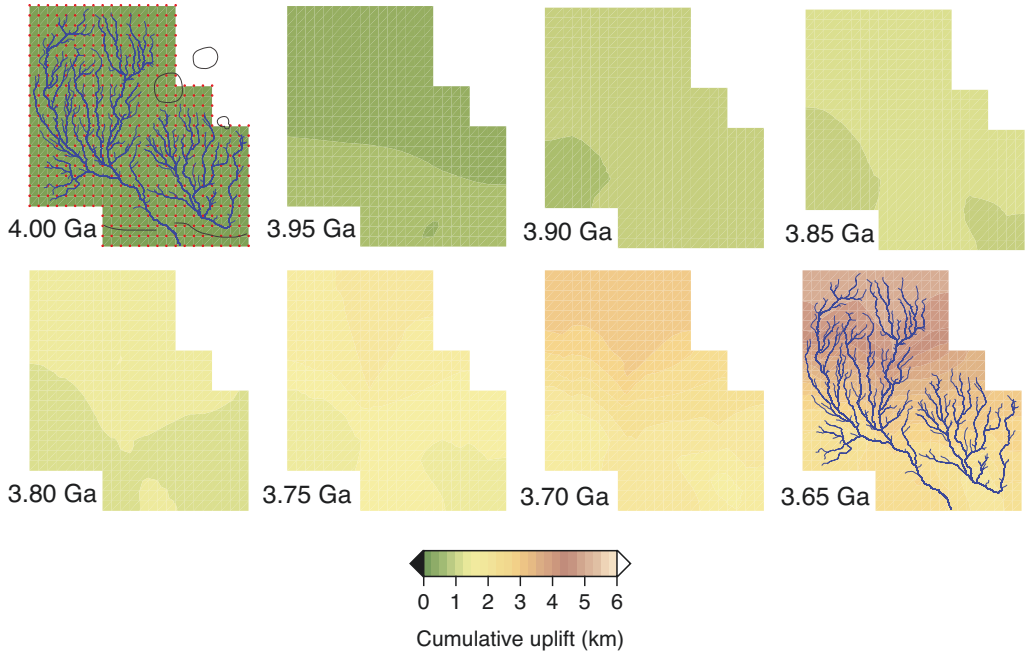


Figure 6.12: 2-D uplift history Warrego Valles. Blue lines = drainage inventory of 184 channels. Black lines = Thausmasia rise southern boundary. Black circles = craters. Red circles = nodes used for uplift model coverage.

ages describe only the time at which the channel stopped eroding, and little is known about the formation timescales of Warrego Valles or any other valley network on Mars.

As described in Section 5.5.2, I use a simplified version of the stream power model to invert an inventory of 184 rivers for a spatio-temporal uplift rate history. Erosional parameter v is not accurately constrained due to unknown valley formation timescales on Mars. For the inversion model I assume a maximum formation time where channels must form before 4 Ga (oldest age of Thaumasia region) and end before 3.5 Ga (approximate buffered crater age of Warrego Valles). We ran multiple joint-inversions which result in a best fitting $m = 0.2$ (Figure 6.11a). Model fits to channels are good (global residual rms misfit = 1.46). Fits to the channel profiles are shown in Figure 6.11, and spatial distribution of uplift is shown in Figure 6.12.

6.5.4 Uplift patterns and sources

Highest cumulative uplift (> 5 km) occurs in the northernmost parts of the Warrego Valles system and decreases uniformly towards the south. The spatial distribution and apparent one-dimensionality of this uplift is consistent with uplift of the Thaumasia highlands which took place during the Late Noachian (Frey, 1979). This uplift could have been generated from mantle convective processes, and the southern edge of the Thaumasia Highlands has been interpreted as the surface exposure of a large thrust fault, which would have been able to accommodate compressional stress field at the boundary between the uplifted and non-uplifted areas in the upper part of the lithosphere at the onset of hot spot activity (Webb and Head III, 2002). The uplift of Tharsis would have associated volcanoes and rift systems which would may have supported fluvial activity through increased hydrothermal action, precipitation, seismic disturbance of aquifers or unrecognised intrusions (Dohm and Tanaka, 1999; Phillips et al., 2000). Figure 6.13 depicts the erosion of Warrego Valles coincident with Thaumaria uplift increasing towards the north with increasing proximity to the Tharsis Bulge centre. These observations suggest Martian channels can successfully be used as tools for determining landscape evolution on Mars and the relative timing of significant uplift events.

6.6 Chapter Summary

The decay of the Martian atmosphere is a component of the long-term environmental change on Mars from a climate that once allowed rivers to flow to the cold and dry conditions of today. It is the only planet we know of to date that has undergone a complete, irreversible, and global climate change. This phenomenon has allowed the Martian surface to remain mostly intact for billions of years, preserving the geometries of surface processes that occurred close to the beginning of its planetary history. In this Chapter I applied similar tools used on terrestrial channels to the various types of channels observed on Mars to understand their origin and evolution. Drainage patterns on and near craters were mapped and analysis of their longitudinal profiles suggest they are morphologically similar to highly fluvial, modified terrestrial craters of similar

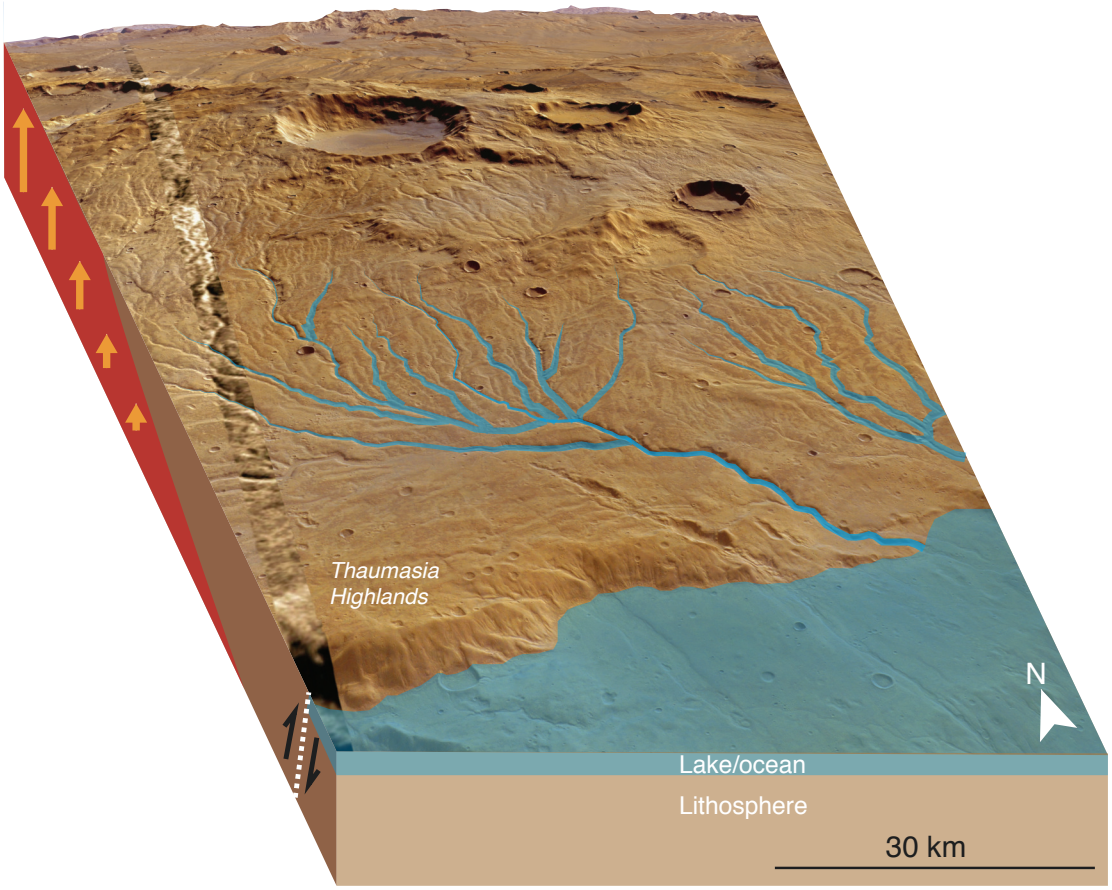


Figure 6.13: Schematic diagram of formation of Warrego Valles and uplift of the Thaumasia Rise (southern Tharsis Bulge). White dashed line = thrust fault; solid blue colour = rivers and lake/ocean; solid red colour = region of uplift; orange arrows = relative uplift magnitude.

size. In particular, Warrego Valles is a good example of a high-density dendritic system located at the very south of the uplifted Tharsis Bulge. Spectral analyses show, like terrestrial rivers, its power is contained within higher wavelengths of several tens of km and exhibits self-similarity. An inversion of its drainage indicates an uplift field which gradually increases towards the north. This is consistent with uplift of the Thaumasia region which could have originated as a result of mantle convective processes below Tharsis. These results indicate that, despite the poor temporal resolution of Martian fluvial timescales (thousands – millions of years), landscape evolution models are capable of generating uplift and erosion histories which are broadly consistent with observed geological and geodynamic constraints. Further, constraining the mechanics and driving forces of landscape evolution on Mars is fundamental to better understanding

how our own planet will evolve and respond to planetary processes at a variety of time and length scales.

Chapter 7

Conclusions

In this dissertation I showed how observations, including seismic data, well cores, organic geochemistry, UAV mapping, and cosmogenic dating can be combined with theory to constrain landscape evolution at a range of scales. The use of landscape evolution models to determine records of vertical motions is a powerful tool with significant applications for constraining regional histories of sub-surface processes. In the North Atlantic Ocean, sedimentary basins contain excellent evidence that the continental shelf experienced staged subaerial exposure. I used commercial wells and three-dimensional seismic data to reconstruct a 55–58 Ma landscape now buried $\sim$ 1.5 km beneath the seabed in the Bressay area of the northern North Sea. Geochemical analyses of organic matter from core samples intersecting the erosional landscape indicate the presence of angiosperm (flowering plant) debris. Combined with the presence of coarse clastic material, mapped beach ridges, and dendritic drainage patterns, these observations indicate that this landscape was of terrestrial origin. Longitudinal profiles of ancient rivers were extracted and inverted for an uplift rate history. The best-fitting uplift rate history has three phases and total cumulative uplift of $\sim$350 m. Biostratigraphic data from surrounding marine stratigraphy indicate that this landscape formed within 1–1.5 Ma. This uplift history is similar to that of a slightly older buried landscape in the Faeroe-Shetland basin 400 km to the west. These records of vertical motion can be explained by pulses of anomalously hot asthenosphere spreading out from the incipient Icelandic plume.

The dramatic landscapes observed in modern Iceland offer an opportunity to investigate dynamic support generated by the Icelandic plume located directly beneath it today. The ubiquity of waterfalls and canyons hints to an island-wide topographic control, however the processes which generate and maintain these large knickzones are poorly understood. I combined high-resolution drone photogrammetry and cosmogenic ^{3}He dating of fluvial terraces to constrain the erosional history of a broad knickzone in Jökulsá á Fjöllum, northeast Iceland. Progressive younging of terraces suggested knickzone propagation rates up to $\sim$70 cm yr^{-1} during the last 8 ka, contrary to previous models which suggest outburst floods as the dominant mode of canyon erosion. A calibrated inversion of Iceland's drainage networks indicates that rifting, sub-plate support, and isostatic adjustment result in tens to hundreds of meters of regional Holocene uplift, indicating gradual fluvial processes set the pace of erosion in postglacial volcanic landscapes.

On Mars, the abundance of drainage patterns suggest that base level change, fluvial erosion, and deposition of sedimentary rock have played important roles in determining the shape of its topography. Calculated uplift histories from joint inversion of the Warrego Valles system and wavelet power spectra indicate that regional uplift of >5 km at wavelengths greater than 40 km played an important role in determining the history of landscape evolution on the southern rim of the uplifted Tharsis Bulge.

The apparent success of inverse modelling of drainage inventories on a variety of geological settings is perplexing. Although it is acknowledged that the empirical stream power law is a crude approximation, its demonstrated ability to obtain excellent fits between observed and calculated river profiles implies that drainage networks behave simply and predictably at length scales of tens to hundreds of km, and timescales ranging from thousands to billions of years. This behaviour strongly supports the concept that fluvial channels, which set the pace for continental erosion, respond in a strikingly simple way to external tectonic forcing. Fundamentally, erosion and uplift histories from ancient and modern landscapes are powerful tools which allow us to probe sub-surface

processes and understand the generation, maintenance, and eventual decay of all planetary surfaces.

References

Adedosu, T., Sonibare, O., Ekundayo, O., and Tuo, J. (2010). Hydrocarbon-generative potential of coal and interbedded shale of Mamu Formation, Benue Trough, Nigeria. *Petroleum Science and Technology*, 28(4):412–427.

Alho, P., Russell, A. J., Carrivick, J. L., and Käyhkö, J. (2005). Reconstruction of the largest Holocene jökulhlaup within Jökulsá á Fjöllum, NE Iceland. *Quaternary Science Reviews*, 24(22):2319–2334.

Allen, R. M., Nolet, G., Morgan, W. J., Vogfjörd, K., Bergsson, B. H., Erlendsson, P., Foulger, G., Jakobsdóttir, S., Julian, B. R., Pritchard, M., et al. (2002). Imaging the mantle beneath Iceland using integrated seismological techniques. *Journal of Geophysical Research: Solid Earth*, 107(B12).

Amidon, W. H., Farley, K. A., Burbank, D. W., and Pratt-Sitaula, B. (2008). Anomalous cosmogenic 3He production and elevation scaling in the high Himalaya. *Earth and Planetary Science Letters*, 265(1-2):287–301.

Andrews, I., Long, D., Richards, P., Thomson, A., Brown, S., Chesher, J., and McCormac, M. (1990). United Kingdom offshore regional report: the geology of the Moray Firth. *British Geological Survey, HMSO, London*, 96.

Anell, I., Thybo, H., and Artemieva, I. (2009). Cenozoic uplift and subsidence in the North Atlantic region: Geological evidence revisited. *Tectonophysics*, 474(1-2):78–105.

Ansan, V. and Mangold, N. (2006). New observations of Warrego Valles, Mars: Evidence for precipitation and surface runoff. *Planetary and Space Science*, 54(3):219–242.

Ansan, V. and Mangold, N. (2013). 3D morphometry of valley networks on Mars from HRSC/MEX DEMs: Implications for climatic evolution through time. *Journal of Geophysical Research: Planets*, 118.

Árnadóttir, T., Lund, B., Jiang, W., Geirsson, H., Björnsson, H., Einarsson, P., and Sigurdsson, T. (2009). Glacial rebound and plate spreading: results from the first countrywide GPS observations in Iceland. *Geophysical Journal International*, 177(2):691–716.

Baker, V. R. (1978). The Spokane Flood controversy and the Martian outflow channels. *Science*, 202(4374):1249–1256.

Baker, V. R. and Milton, D. J. (1974). Erosion by catastrophic floods on Mars and Earth. *Icarus*, 23(1):27–41.

Barnett-Moore, N., Flament, N., Heine, C., Butterworth, N., and Müller, R. D. (2014). Cenozoic uplift of south Western Australia as constrained by river profiles. *Tectonophysics*, 622:186–197.

Barnhart, C. J., Howard, A. D., and Moore, J. M. (2009). Long-term precipitation and late-stage valley network formation: Landform simulations of Parana Basin, Mars. *Journal of Geophysical Research: Planets*, 114(E1).

Baynes, E. R., Attal, M., Dugmore, A. J., Kirstein, L. A., and Whaler, K. A. (2015a). Catastrophic impact of extreme flood events on the morphology and evolution of the lower Jökulsá á Fjöllum (northeast Iceland) during the Holocene. *Geomorphology*, 250:422–436.

Baynes, E. R., Attal, M., Niedermann, S., Kirstein, L. A., Dugmore, A. J., and Naylor, M. (2015b). Erosion during extreme flood events dominates Holocene canyon evolution in northeast Iceland. *Proceedings of the National Academy of Sciences*, 112(8):2355–2360.

Becker, T. W., Faccenna, C., O'Connell, R. J., and Giardini, D. (1999). The development of slabs in the upper mantle: Insights from numerical and laboratory experiments. *Journal of Geophysical Research: Solid Earth*, 104(B7):15207–15226.

Bell Jr, T. (1975). Statistical features of sea-floor topography. In *Deep Sea Research and Oceanographic Abstracts*, volume 22, pages 883–892. Elsevier.

Birnir, B., Smith, T. R., and Merchant, G. E. (2001). The scaling of fluvial landscapes. *Computers & geosciences*, 27(10):1189–1216.

Bishop, P. (2007). Long-term landscape evolution: linking tectonics and surface processes. *Earth Surface Processes and Landforms*, 32(3):329–365.

Bishop, P., Hoey, T. B., Jansen, J. D., and Artza, I. L. (2005). Knickpoint recession rate and catchment area: the case of uplifted rivers in Eastern Scotland. *Earth Surface Processes and Landforms*, 30(6):767–778.

Björnsson, H. (1980). Avalanche activity in Iceland, climatic conditions, and terrain features. *Journal of Glaciology*, 26(94):9–12.

Bjornsson, H. (2009). Jokulhlaups in Iceland: sources, release, and drainage. *Megaflooding on Earth and Mars. Cambridge University Press, Cambridge*, pages 50–64.

Blard, P.-H., Balco, G., Burnard, P., Farley, K., Fenton, C., Friedrich, R., Jull, A. T., Niedermann, S., Pik, R., Schaefer, J., et al. (2015). An inter-laboratory comparison of cosmogenic 3 He and radiogenic 4 He in the CRONUS-P pyroxene standard. *Quaternary Geochronology*, 26:11–19.

Blum, M. D. and Törnqvist, T. E. (2000). Fluvial responses to climate and sea-level change: a review and look forward. *Sedimentology*, 47(s1):2–48.

Braun, J. (2010). The many surface expressions of mantle dynamics. *Nature Geoscience*, 3(12):825.

Breddam, K., Kurz, M. D., and Storey, M. (2000). Mapping out the conduit of the Iceland mantle plume with helium isotopes. *Earth and Planetary Science Letters*, 176(1):45–55.

Brown, R. B., Holland, D., McKellip, R., and Navard, A. (2008). Creation of high resolution terrain models of Barringer meteorite crater (meteor crater) using photogrammetry and terrestrial laser scanning methods. In *Lunar and Planetary Science Conference*, volume 39, page 2453.

Bujak, J. P. and Williams, G. (1985). Mesozoic and Cenozoic dinoflagellates. *Plankton Stratigraphy. Cambridge University Press, Cambridge*, pages 847–965.

Burke, K. and Gunnell, Y. (2008). *The African erosion surface: a continental-scale synthesis of geomorphology, tectonics, and environmental change over the past 180 million years*, volume 201. Geological Society of America.

Cabrol, N. A. and Grin, E. A. (1999). Distribution, classification, and ages of Martian impact crater lakes. *Icarus*, 142(1):160–172.

Carr, M. H. (1979). Formation of Martian flood features by release of water from confined aquifers. *Journal of Geophysical Research*, 84:2995–3007.

Carr, M. H. (1996). Channels and valleys on Mars: Cold climate features formed as a result of a thickening cryosphere. *Planetary and Space Science*, 44(11):1411–1423.

Chapman, M. G., Gudmundsson, M. T., Russell, A. J., and Hare, T. M. (2003). Possible Juventae Chasma subice volcanic eruptions and Maja Valles ice outburst floods on Mars: Implications of Mars Global Surveyor crater densities, geomorphology, and topography. *Journal of Geophysical Research: Planets*, 108(E10).

Christensen, N. (1982). Seismic velocities, Handbook of Physical Properties of Rocks, II RS Carmichael, 1–228.

Cowie, P. a., Whittaker, A. C., Attal, M., Roberts, G., Tucker, G. E., and Ganas, A. (2008). New constraints on sediment-flux-dependent river incision: Implications for extracting tectonic signals from river profiles. *Geology*, 36(7):535–538.

Craddock, R. A. and Howard, A. D. (2002). The case for rainfall on a warm, wet early Mars. *Journal of Geophysical Research: Planets*, 107(E11).

Cramer, B., Toggweiler, J., Wright, J., Katz, M., and Miller, K. (2009). Ocean overturning since the Late Cretaceous: Inferences from a new benthic foraminiferal isotope compilation. *Paleoceanography*, 24(4).

Crochet, P., Jóhannesson, T., Jónsson, T., Sigurðsson, O., Björnsson, H., Pálsson, F., and Barstad, I. (2007). Estimating the spatial distribution of precipitation in Iceland using a linear model of orographic precipitation. *Journal of Hydrometeorology*, 8(6):1285–1306.

Crosby, B. T. and Whipple, K. X. (2006). Knickpoint initiation and distribution within fluvial networks: 236 waterfalls in the Waipaoa River, North Island, New Zealand. *Geomorphology*, 82(1-2):16–38.

Czarnota, K., Hoggard, M., White, N., and Winterbourne, J. (2013). Spatial and temporal patterns of Cenozoic dynamic topography around Australia. *Geochemistry, Geophysics, Geosystems*, 14(3):634–658.

Czarnota, K., Roberts, G. G., White, N. J., and Fishwick, S. (2014). Spatial and temporal patterns of Australian dynamic topography from river profile modeling. *Journal of Geophysical Research: Solid Earth*, 119(2):1384–1424.

d'Agostino, N., Jackson, J., Dramis, F., and Funiciello, R. (2001). Interactions between mantle upwelling, drainage evolution and active normal faulting: an example from the central Apennines (Italy). *Geophysical Journal International*, 147(2):475–497.

Dam, G., Larsen, M., and Sønderholm, M. (1998). Sedimentary response to mantle plumes: Implications from Paleocene onshore successions, West and East Greenland. *Geology*, 26(3):207–210.

Daradich, A., Mitrovica, J. X., Pysklywec, R. N., Willett, S. D., and Forte, a. M. (2003). Mantle flow, dynamic topographyn and rift-flank uplift of Arabia. *Geology*, 31:901–904.

Darbyshire, F. A., Priestley, K. F., White, R. S., Stefánsson, R., Gudmundsson, G. B., and Jakobsdóttir, S. S. (2000). Crustal structure of central and northern Iceland from analysis of teleseismic receiver functions. *Geophysical Journal International*, 143(1):163–184.

Davies, J. L. (1974). Geomorphology and Quaternary environments. In *Biogeography and ecology in Tasmania*, pages 17–27. Springer.

Dohm, J. M. and Tanaka, K. L. (1999). Geology of the Thaumasia region, Mars: Plateau development, valley origins, and magmatic evolution. *Planetary and Space Science*, 47(3-4):411–431.

Drury, L. O. (2012). Origin of cosmic rays. *Astroparticle Physics*, 39:52–60.

Dunne, J., Elmore, D., and Muzikar, P. (1999). Scaling factors for the rates of production of cosmogenic nuclides for geometric shielding and attenuation at depth on sloped surfaces. *Geomorphology*, 27(1-2):3–11.

Dziewonski, A. M. and Anderson, D. L. (1981). Preliminary reference Earth model. *Physics of the earth and planetary interiors*, 25(4):297–356.

Einarsson, M. Á. (1984). Climate of Iceland. *000072851*.

Einarsson, P. (1991). Earthquakes and present-day tectonism in Iceland. *Tectonophysics*, 189(1-4):261–279.

Elíasson, S. (1974). Eldsumbrot í Jökulsárgljúfrum. *JÖKULL*, 44.

Eneogwe, C., Ekundayo, O., and Patterson, B. (2002). Source-derived oleanenes identified in Niger Delta oils. *Journal of Petroleum Geology*, 25(1):83–95.

Evans, D. J., Lemmen, D. S., and Rea, B. R. (1999). Glacial landsystems of the southwest Laurentide Ice Sheet: modern Icelandic analogues. *Journal of Quaternary Science*, 14(7):673–691.

Eythorsson, J., Sigtryggsson, H., and Bertelsen, E. (1971). *Pt. 3: The Climate and Weather of Iceland*. Munksgaard.

Fanale, F. P., Postawko, S. E., Pollack, J. B., Carr, M. H., and Pepin, R. O. (1992). Mars-Epochal climate change and volatile history. *Mars*, pages 1135–1179.

Flament, N., Gurnis, M., Williams, S., Seton, M., Skogseid, J., Heine, C., and Müller, R. D. (2014). Topographic asymmetry of the South Atlantic from global models of mantle flow and lithospheric stretching. *Earth and Planetary Science Letters*, 387:107–119.

Förste, C., Bruinsma, S., Abrikosov, O., Flechtner, F., Marty, J.-C., Lemoine, J.-M., Dahle, C., Neumayer, H., Barthelmes, F., König, R., et al. (2014). EIGEN-6C4-The latest combined global gravity field model including GOCE data up to degree and order 1949 of GFZ Potsdam and GRGS Toulouse. In *EGU General Assembly Conference Abstracts*, volume 16.

Forte, A. M., Peltier, W. R., Dziewonski, A. M., and Woodward, R. L. (1993). Dynamic surface topography: a new interpretation based upon mantle flow models derived from seismic tomography. *Geophysical Research Letters*, 20(3):225–228.

Fox, M., Bodin, T., and Shuster, D. L. (2015). Abrupt changes in the rate of Andean Plateau uplift from reversible jump Markov Chain Monte Carlo inversion of river profiles. *Geomorphology*, 238:1–14.

Frey, H. (1979). Thaumasia: A fossilized early forming Tharsis uplift. *Journal of Geophysical Research: Solid Earth*, 84(B3):1009–1023.

Gallant, J. C., Moore, I. D., Hutchinson, M. F., and Gessler, P. (1994). Estimating fractal dimension of profiles: a comparison of methods. *Mathematical Geology*, 26(4):455–481.

Gallen, S. F. (2018). Lithologic controls on landscape dynamics and aquatic species evolution in post-orogenic mountains. *Earth and Planetary Science Letters*, 493:150–160.

Geirsdóttir, Á., Miller, G. H., and Andrews, J. T. (2007). Glaciation, erosion, and landscape evolution of Iceland. *Journal of Geodynamics*, 43(1):170–186.

Gilbert, G. K. and Murphy, E. C. (1914). *The transportation of debris by running water*. US Government Printing Office.

Glotzbach, C. (2015). Deriving rock uplift histories from data-driven inversion of river profiles. *Geology*, 43(6):467–470.

Gosse, J. C. and Phillips, F. M. (2001). Terrestrial in situ cosmogenic nuclides: theory and application. *Quaternary Science Reviews*, 20(14):1475–1560.

Gradstein, F., Kristiansen, I., Loemo, L., and Kaminski, M. A. (1992). Cenozoic foraminiferal and dinoflagellate cyst biostratigraphy of the central North Sea. *Micropaleontology*, pages 101–137.

Grant, J. A. and Schultz, P. H. (1993). Degradation of selected terrestrial and Martian impact craters. *Journal of Geophysical Research: Planets*, 98(E6):11025–11042.

Grant, J. A. and Wilson, S. A. (2011). Late alluvial fan formation in southern Margaritifer Terra, Mars. *Geophysical Research Letters*, 38(8).

Green, P. F., Lidmar-Bergström, K., Japsen, P., Bonow, J. M., and Chalmers, J. A. (2013). Stratigraphic landscape analysis, thermochronology and the episodic development of elevated, passive continental margins. *Geological Survey of Denmark & Greenland Bulletin*, 30.

Green, R. G., Priestley, K. F., and White, R. S. (2017). Ambient noise tomography reveals upper crustal structure of Icelandic rifts. *Earth and Planetary Science Letters*, 466:20–31.

Grieve, R. A. and Shoemaker, E. M. (1994). The record of past impacts on Earth. *Hazards due to comets and asteroids*, pages 417–462.

Grimaud, J.-L., Chardon, D., Beauvais, A., and Paola, C. (2014). Incision dynamics along river profiles: the influence of uplift and lithology. In *AGU Fall Meeting Abstracts*.

Gudmundsson, A. (2000). Dynamics of volcanic systems in Iceland: example of tectonism and volcanism at juxtaposed hot spot and mid-ocean ridge systems. *Annual Review of Earth and Planetary Sciences*, 28(1):107–140.

Gurnis, M., Mitrovica, J. X., Ritsema, J., and van Heijst, H.-J. (2000). Constraining mantle density structure using geological evidence of surface uplift rates: The case of the African superplume. *Geochemistry, Geophysics, Geosystems*, 1(7).

Gwinner, K., Jaumann, R., Hauber, E., Hoffmann, H., Heipke, C., Oberst, J., Neukum, G., Ansan, V., Bostelmann, J., Dumke, A., et al. (2016). The High Resolution Stereo Camera (HRSC) of Mars Express and its approach to science analysis and mapping for Mars and its satellites. *Planetary and Space Science*, 126:93–138.

Hager, B. H., Clayton, R., Richards, M. A., Comer, R. P., and Dziewonski, A. M. (1985). Lower mantle heterogeneity, dynamic topography and the geoid. *Nature*, 313:541–545.

Haq, B. U., Hardenbol, J., and Vail, P. R. (1988). Mesozoic and Cenozoic chronostratigraphy and cycles of sea-level change. *Sea-Level Changes - An Integrated Approach, SEPM Special Publications*, 42.

Hart, S., Schilling, J.-G., and Powell, J. (1973). Basalts from Iceland and along the Reykjanes Ridge: Sr isotope geochemistry. *Nature Physical Science*, 246(155):104.

Hartley, R. A., Roberts, G. G., White, N., and Richardson, C. (2011). Transient convective uplift of an ancient buried landscape. *Nature Geoscience*, 4(8):562.

Hayakawa, S., Ito, K., and Terashima, Y. (1958). Origin of cosmic rays. *Progress of Theoretical Physics Supplement*, 6:1–92.

Hofmann, A. W. and White, W. M. (1982). Mantle plumes from ancient oceanic crust. *Earth and Planetary Science Letters*, 57(2):421–436.

Hoggard, M. J., White, N., and Al-Attar, D. (2016). Global dynamic topography observations reveal limited influence of large-scale mantle flow. *Nature Geoscience*, 9(6):456.

Hoggard, M. J., Winterbourne, J., Czarnota, K., and White, N. (2017). Oceanic residual depth measurements, the plate cooling model, and global dynamic topography. *Journal of Geophysical Research: Solid Earth*, 122(3):2328–2372.

Hoke, M. R., Hynek, B. M., and Tucker, G. E. (2011). Formation timescales of large Martian valley networks. *Earth and Planetary Science Letters*, 312(1-2):1–12.

Hoorn, C., Guerrero, J., Sarmiento, G. A., and Lorente, M. A. (1995). Andean tectonics as a cause for changing drainage patterns in Miocene northern South America. *Geology*, 23(3):237–240.

Howard, A. D. (2007). Simulating the development of Martian highland landscapes through the interaction of impact cratering, fluvial erosion, and variable hydrologic forcing. *Geomorphology*, 91(3-4):332–363.

Howard, A. D., Dietrich, W. E., and Seidl, M. A. (1994). Modeling fluvial erosion on regional to continental scales. *Journal of Geophysical Research: Solid Earth*, 99(B7):13971–13986.

Howard, A. D., Keetch, M. E., and Vincent, C. L. (1970). Topological and geometrical properties of braided streams. *Water Resources Research*, 6(6):1674–1688.

Huang, J. and Turcotte, D. (1989). Fractal mapping of digitized images: application to the topography of Arizona and comparisons with synthetic images. *Journal of Geophysical Research: Solid Earth*, 94(B6):7491–7495.

Hynek, B. M., Beach, M., and Hoke, M. R. (2010). Updated global map of Martian valley networks and implications for climate and hydrologic processes. *Journal of Geophysical Research: Planets*, 115(E9).

Jackson, C. A.-L., Grunhagen, H., Howell, J. A., Larsen, A. L., Andersson, A., Boen, F., and Groth, A. (2010). 3D seismic imaging of lower delta-plain beach ridges: lower Brent Group, northern North Sea. *Journal of the Geological Society*, 167(6):1225–1236.

Japsen, P. and Chalmers, J. A. (2000). Neogene uplift and tectonics around the North Atlantic: overview. *Global and Planetary Change*, 24(3-4):165–173.

Jaumann, R., Tirsch, D., Hauber, E., Ansan, V., Di Achille, G., Erkeling, G., Fueten, F., Head, J., Kleinhans, M., Mangold, N., Michael, G., Neukum, G., Pacifici, a., Platz, T., Pondrelli, M., Raack, J., Reiss, D., Williams, D., Adeli, S., Baratoux, D., de Villiers, G., Foing, B., Gupta, S., Gwinner, K., Hiesinger, H., Hoffmann, H., Deit, L. L., Marinangeli, L., Matz, K.-D., Mertens, V., Muller, J., Pasckert, J., Roatsch, T., a.P. Rossi, Scholten, F., Sowe, M., Voigt, J., and Warner, N. (2015). Quantifying geological processes on Mars-Results of the High resolution stereo camera (HRSC) on Mars express. *Planetary and Space Science*.

Jöhannesson, H. and Sæmundsson, K. (1989). Geological map of Iceland (1: 500 000), Bedrock geology. *1st edn*.

Jones, R. W. and Milton, N. J. (1994). Sequence development during uplift: Palaeogene stratigraphy and relative sea-level history of the Outer Moray Firth, UK North Sea. *Marine and Petroleum Geology*, 11(2):157–165.

Jones, S. M. and White, N. (2003). Shape and size of the starting Iceland plume swell. *Earth and Planetary Science Letters*, 216(3):271–282.

Jones, S. M., White, N., Clarke, B. J., Rowley, E., and Gallagher, K. (2002a). Present and past influence of the Iceland Plume on sedimentation. *Geological Society, London, Special Publications*, 196(1):13–25.

Jones, S. M., White, N., and Maclennan, J. (2002b). V-shaped ridges around Iceland: Implications for spatial and temporal patterns of mantle convection. *Geochemistry, Geophysics, Geosystems*, 3(10):1–23.

Jones, S. M., White, N., and Maclennan, J. (2002c). V-shaped ridges around Iceland: Implications for spatial and temporal patterns of mantle convection. *Geochemistry, Geophysics, Geosystems*, 3(10):1–23.

Kirby, E. and Whipple, K. (2001). Quantifying differential rock-uplift rates via stream profile analysis. *Geology*, 29(5):415–418.

Kite, E. S., Williams, J.-P., Lucas, A., and Aharonson, O. (2014). Low palaeopressure of the martian atmosphere estimated from the size distribution of ancient craters. *Nature Geoscience*, 7(5):335–339.

Kjær, K. H., Korsgaard, N. J., and Schomacker, A. (2008). Impact of multiple glacier surges: a geomorphological map from Brúarjökull, East Iceland. *Journal of Maps*, 4(1):5–20.

Knox, R. O. and Holloway, S. (1992). Paleogene of the Central and Northern North Sea. *Lithostratigraphic Nomenclature of the UK North Sea. British Geological Survey, Nottingham*, pages 31–82.

Knox, R. O. and Morton, A. (1988). The record of early Tertiary N Atlantic volcanism in sediments of the North Sea Basin. *Geological Society, London, Special Publications*, 39(1):407–419.

Koppes, M. N. and Montgomery, D. R. (2009). The relative efficacy of fluvial and glacial erosion over modern to orogenic timescales. *Nature Geoscience*, 2(9):644.

Lal, D. (1991). Cosmic ray labeling of erosion surfaces: in situ nuclide production rates and erosion models. *Earth and Planetary Science Letters*, 104(2-4):424–439.

Lamb, M. P. and Dietrich, W. E. (2009). The persistence of waterfalls in fractured rock. *Geological Society of America Bulletin*, 121(7-8):1123–1134.

Lamb, M. P., Finnegan, N. J., Scheingross, J. S., and Sklar, L. S. (2015). New insights into the mechanics of fluvial bedrock erosion through flume experiments and theory. *Geomorphology*, 244:33–55.

Larsen, T. B., Yuen, D. A., and Storey, M. (1999). Ultrafast mantle plumes and implications for flood basalt volcanism in the Northern Atlantic Region. *Tectonophysics*, 311(1-4):31–43.

Lawver, L. A. and Müller, R. D. (1994). Iceland hotspot track. *Geology*, 22(4):311–314.

Layer, P. W. (2000). Argon-40/argon-39 age of the El'gygytgyn impact event, Chukotka, Russia. *Meteoritics & Planetary Science*, 35(3):591–599.

Le Breton, E., Dauteuil, O., and Biessy, G. (2010). Post-glacial rebound of Iceland during the Holocene. *Journal of the Geological Society*, 167(2):417–432.

Licciardi, J., Kurz, M., and Curtice, J. (2006). Cosmogenic 3 He production rates from Holocene lava flows in Iceland. *Earth and Planetary Science Letters*, 246(3):251–264.

Lifton, N. A., Bieber, J. W., Clem, J. M., Duldig, M. L., Evenson, P., Humble, J. E., and Pyle, R. (2005). Addressing solar modulation and long-term uncertainties in scaling secondary cosmic rays for in situ cosmogenic nuclide applications. *Earth and Planetary Science Letters*, 239(1-2):140–161.

Lithgow-Bertelloni, C. and Silver, P. (1998). Dynamic topography, plate driving forces and the African superswell. *Letters to Nature*, 395:345–348.

Liu, X. and Galloway, W. E. (1997). Quantitative determination of Tertiary sediment supply to the North Sea Basin. *AAPG bulletin*, 81(9):1482–1509.

Luterbacher, H., Ali, J., and Brinkhuis, H. (2004). The Paleogene Period: pp. 384–408 in FM Gradstein, JG Ogg, and AG Smith (eds.), A Geologic Time Scale 2004.

Lyle, P. (2000). The eruption environment of multi-tiered columnar basalt lava flows. *Journal of the Geological Society*, 157(4):715–722.

Mackay, L., Turner, J., Jones, S., and White, N. (2005). Cenozoic vertical motions in the Moray Firth Basin associated with initiation of the Iceland Plume. *Tectonics*, 24(5).

Maclennan, J. and Lovell, B. (2002). Control of regional sea level by surface uplift and subsidence caused by magmatic underplating of Earth's crust. *Geology*, 30(8):675–678.

Mangerud, J., Jakobsson, M., Alexanderson, H., Astakhov, V., Clarke, G. K., Henriksen, M., Hjort, C., Krinner, G., Lunkka, J.-P., Möller, P., et al. (2004). Ice-dammed lakes and rerouting of the drainage of northern Eurasia during the Last Glaciation. *Quaternary Science Reviews*, 23(11-13):1313–1332.

Marrero, S. M., Phillips, F. M., Borchers, B., Lifton, N., Aumer, R., and Balco, G. (2016). Cosmogenic nuclide systematics and the CRONUScalc program. *Quaternary Geochronology*, 31:160–187.

Martin, E., Paquette, J.-L., Bosse, V., Ruffet, G., Tiepolo, M., and Sigmarsson, O. (2011). Geodynamics of rift–plume interaction in Iceland as constrained by new 40Ar/39Ar and in situ U–Pb zircon ages. *Earth and Planetary Science Letters*, 311(1-2):28–38.

Masarik, J. and Reedy, R. C. (1995). Terrestrial cosmogenic-nuclide production systematics calculated from numerical simulations. *Earth and Planetary Science Letters*, 136(3-4):381–395.

Masursky, H. (1973). An overview of geological results from Mariner 9. *Journal of Geophysical Research*, 78(20):4009–4030.

Matthews, S., Shorttle, O., and Maclennan, J. (2016). The temperature of the Icelandic mantle from olivine-spinel aluminum exchange thermometry. *Geochemistry, Geophysics, Geosystems*, 17(11):4725–4752.

McElroy, M. B. and Donahue, T. M. (1972). Stability of the Martian atmosphere. *Science*, 177(4053):986–988.

McKenzie, D. (2010). The influence of dynamically supported topography on estimates of Te. *Earth and Planetary Science Letters*, 295(1-2):127–138.

Medvedev, S., Souche, A., and Hartz, E. (2013). Influence of ice sheet and glacial erosion on passive margins of Greenland. *Geomorphology*, 193:36–46.

Mège, D. and Masson, P. (1996). A plume tectonics model for the Tharsis province, Mars. *Planetary and Space Science*, 44(12):1499–1546.

Melles, M., Brigham-Grette, J., Minyuk, P., Koeberl, C., Andreev, A., Cook, T., Fedorov, G., Gebhardt, C., Haltia-Hovi, E., Kukkonen, M., et al. (2011). The Lake Elgygytgyn Scientific Drilling Project–Conquering Arctic Challenges through Continental Drilling. *Scientific Drilling*, 11:29–40.

Melosh, H. J. (1989). Impact cratering: A geologic process. *Research supported by NASA. New York, Oxford University Press (Oxford Monographs on Geology and Geophysics, No. 11), 1989, 253 p.*, 11.

Miller, K. G., Kominz, M. A., Browning, J. V., Wright, J. D., Mountain, G. S., Katz, M. E., Sugarman, P. J., Cramer, B. S., Christie-Blick, N., and Pekar, S. F. (2005). The Phanerozoic record of global sea-level change. *science*, 310(5752):1293–1298.

Moorbath, S., Sigurdsson, H., and Goodwin, R. (1968). KAr ages of the oldest exposed rocks in Iceland. *Earth and Planetary Science Letters*, 4(3):197–205.

Moore, J. M. and Howard, A. D. (2005). Large alluvial fans on Mars. *Journal of Geophysical Research: Planets*, 110(E4).

Moucha, R., Forte, A. M., Mitrovica, J. X., Rowley, D. B., Quéré, S., Simmons, N., and Grand, S. P. (2008). Dynamic topography and long-term sea-level variations: There is no such thing as a stable continental platform. *Earth and Planetary Science Letters*, 271(1-4):101–108.

Mudge, D. and Bujak, J. (2001). Biostratigraphic evidence for evolving palaeoenvironments in the Lower Paleogene of the Faeroe–Shetland Basin. *Marine and Petroleum Geology*, 18(5):577–590.

Mudge, D. C. (2015). Regional controls on Lower Tertiary sandstone distribution in the North Sea and NE Atlantic margin basins. *Geological Society, London, Special Publications*, 403(1):17–42.

Mudge, D. C. and Bujak, J. P. (1994). Eocene stratigraphy of the North Sea basin. *Marine and Petroleum Geology*, 11(2):166–181.

Mudge, D. C. and Bujak, J. P. (1996). An integrated stratigraphy for the Paleocene and Eocene of the North Sea. *Geological Society, London, Special Publications*, 101(1):91–113.

Mudge, D. C. and Copestake, P. (1992). Lower Palaeogene stratigraphy of the northern North Sea. *Marine and Petroleum Geology*, 9(3):287–301.

Mudge, D. C. and Jones, S. M. (2004). Palaeocene uplift and subsidence events in the Scotland–Shetland and North Sea region and their relationship to the Iceland Plume. *Journal of the Geological Society*, 161(3):381–386.

Murphy, B. P., Johnson, J. P., Gasparini, N. M., and Sklar, L. S. (2016). Chemical weathering as a mechanism for the climatic control of bedrock river incision. *Nature*, 532(7598):223.

Neal, J. (1996). A summary of Paleogene sequence stratigraphy in northwest Europe and the North Sea. *Geological Society, London, Special Publications*, 101(1):15–42.

Niem, A. R. (1974). WrightâĂŹs point, Harney County, Oregon: An example of inverted topography. *Ore Bin*, 36(3):33–49.

Nimmo, F. and Tanaka, K. (2005). Early crustal evolution of Mars. *Annu. Rev. Earth Planet. Sci.*, 33:133–161.

Nordhdahl, H., Ingólfsson, Ó., Pétursson, H. G., and Hallsdóttir, M. (2008). Late Weichselian and Holocene environmental history of Iceland. *Jökull*, 58:343–364.

Nordhdahl, H. and Pétursson, H. G. (2005). 3. Relative sea-level changes in Iceland: new aspects of the Weichselian deglaciation of Iceland. *Developments in Quaternary Sciences. Elsevier*, pages 25–78.

Ólafsson, H., Furger, M., and Brummer, B. (2007). The weather and climate of Iceland. *Meteorologische Zeitschrift*, 16(1):5–8.

Olsson, I. U. (1986). *Radiometric dating*. Journal of Quaternary Geoscience.

Oskarsson, N., Steinthorsson, S., and Sigvaldason, G. (1985). Iceland geochemical anomaly: origin, volcanotectonics, chemical fractionation and isotope evolution of the crust. *Journal of Geophysical Research: Solid Earth*, 90(B12):10011–10025.

Pagli, C., Sigmundsson, F., Lund, B., Sturkell, E., Geirsson, H., Einarsson, P., Árnadóttir, T., and Hreinsdóttir, S. (2007). Glacio-isostatic deformation around the Vatnajökull ice cap, Iceland, induced by recent climate warming: GPS observations and finite element modeling. *Journal of Geophysical Research: Solid Earth*, 112(B8).

Pálfy, J. and Smith, P. L. (2000). Synchrony between Early Jurassic extinction, oceanic anoxic event, and the Karoo-Ferrar flood basalt volcanism. *Geology*, 28(8):747–750.

Parker, R. L. (1994). *Geophysical inverse theory*. Princeton university press.

Parkin, C. J., Lunnon, Z. C., White, R. S., Christie, P. A., and of Margins Project (iSIMM) Team, I. S. I. . M. (2007). Imaging the pulsing Iceland mantle plume through the Eocene. *Geology*, 35(1):93–96.

Parnell-Turner, R., White, N., Henstock, T., Murton, B., Maclennan, J., and Jones, S. M. (2014). A continuous 55-million-year record of transient mantle plume activity beneath Iceland. *Nature Geoscience*, 7(12):914.

Paul, J. D., Roberts, G. G., and White, N. (2014). The African landscape through space and time. *Tectonics*, 33(6):898–935.

Pekeris, C. L. (1935). Thermal convection in the interior of the Earth. *Geophysical Journal International*, 3(8):343–367.

Pelletier, J. D. (1999). Self-organization and scaling relationships of evolving river networks. *Journal of Geophysical Research: Solid Earth*, 104(B4):7359–7375.

Perron, J. T. and Royden, L. (2013). An integral approach to bedrock river profile analysis. *Earth Surface Processes and Landforms*, 38(6):570–576.

Phillips, F. M., Zreda, M. G., Smith, S. S., Elmore, D., Kubik, P. W., Dorn, R. I., and Roddy, D. J. (1991). Age and geomorphic history of Meteor Crater, Arizona, from cosmogenic 36Cl and 14C in rock varnish. *Geochimica et Cosmochimica Acta*, 55(9):2695–2698.

Phillips, R., Bullock, M., Grinspoon, D., Hynek, B., Aharonson, O., Williams, R., and Hauck, S. (2000). Did Tharsis influence climate and fluvial activity on Mars. *Eos Trans. AGU*, 81:48.

Phillips, R. J. and Lambeck, K. (1980). Gravity fields of the terrestrial planets - Long-wavelength anomalies and tectonics. *Reviews of Geophysics and Space Physics*, 18(1):27–76.

Pieri, D. C. (1980). Martian valleys: Morphology, distribution, age, and origin. *Science*, 210(4472):895–897.

Pike, R. J. and Rozema, W. J. (1975). Spectral analysis of landforms. *Annals of the Association of American Geographers*, 65(4):499–516.

Poore, H., White, N., and Jones, S. (2009). A Neogene chronology of Iceland plume activity from V-shaped ridges. *Earth and Planetary Science Letters*, 283(1-4):1–13.

Poore, H., White, N., and Maclennan, J. (2011). Ocean circulation and mantle melting controlled by radial flow of hot pulses in the Iceland plume. *Nature Geoscience*, 4(8):558.

Pritchard, D., Roberts, G., White, N., and Richardson, C. (2009). Uplift histories from river profiles. *Geophysical Research Letters*, 36(24).

Protin, M., Blard, P.-H., Marrocchi, Y., and Mathon, F. (2016). Irreversible adsorption of atmospheric helium on olivine: A lobster pot analogy. *Geochimica et Cosmochimica Acta*, 179:76–88.

Ramezani, J., Bowring, S., Pringle, M., Winslow III, F., and Rasbury, E. (2005). The Manicouagan impact melt rock: A proposed standard for the intercalibration of U-Pb and 40Ar/39Ar isotopic systems. *Geochimica et Cosmochimica Acta Supplement*, 69:A321.

Rickers, F., Fichtner, A., and Trampert, J. (2013). The Iceland–Jan Mayen plume system and its impact on mantle dynamics in the North Atlantic region: evidence from full-waveform inversion. *Earth and Planetary Science Letters*, 367:39–51.

Roberts, G. G. and White, N. (2010). Estimating uplift rate histories from river profiles using African examples. *Journal of Geophysical Research: Solid Earth*, 115(B2).

Roberts, G. G. and White, N. (2017). The Importance of Long Wavelength Processes in Generating Landscapes. In *EGU General Assembly Conference Abstracts*, volume 19, page 4787.

Robinson, M. S. and Tanaka, K. L. (1990). Magnitude of a catastrophic flood event at Kasei Valles, Mars. *Geology*, 18(9):902–905.

Rodríguez Tribaldos, V., White, N. J., Roberts, G. G., and Hoggard, M. J. (2017). Spatial and temporal uplift history of South America from calibrated drainage analysis. *Geochemistry, Geophysics, Geosystems*.

Roe, G. H., Montgomery, D. R., and Hallet, B. (2002). Effects of orographic precipitation variations on the concavity of steady-state river profiles. *Geology*, 30(2):143–146.

Röhl, U., Westerhold, T., Bralower, T. J., and Zachos, J. C. (2007). On the duration of the Paleocene-Eocene thermal maximum (PETM). *Geochemistry, Geophysics, Geosystems*, 8(12).

Rose, E. R. (1955). *Manicouagan Lake-Mushalagan Lake Area, Quebec*. Ottawa: Department of Mines and Technical Surveys.

Rosenbloom, N. A. and Anderson, R. S. (1994). Hillslope and channel evolution in a marine terraced landscape, Santa Cruz, California. *Journal of Geophysical Research: Solid Earth*, 99(B7):14013–14029.

Rowley, D. B., Forte, A. M., Moucha, R., Mitrovica, J. X., Simmons, N. A., and Grand, S. P. (2013). Dynamic topography change of the eastern United States since 3 million years ago. *science*, 340(6140):1560–1563.

Rudge, J. F., Roberts, G. G., White, N. J., and Richardson, C. N. (2015). Uplift histories of Africa and Australia from linear inverse modeling of drainage inventories. *Journal of Geophysical Research: Earth Surface*, 120(5):894–914.

Rudge, J. F., Shaw Champion, M. E., White, N., McKenzie, D., and Lovell, B. (2008). A plume model of transient diachronous uplift at the Earth's surface. *Earth and Planetary Science Letters*, 267(1-2):146–160.

Sato, T. and Niita, K. (2006). Analytical functions to predict cosmic-ray neutron spectra in the atmosphere. *Radiation research*, 166(3):544–555.

Saunders, A., Fitton, J., Kerr, A., Norry, M., and Kent, R. (1997). The north Atlantic igneous province. *Large igneous provinces: Continental, oceanic, and planetary flood volcanism*, pages 45–93.

Schmidt, P., Lund, B., Arnadottir, T., and Schmeling, H. (2012). Glacial isostatic adjustment constrains dehydration stiffening beneath Iceland. *Earth and Planetary Science Letters*, 359:152–161.

Schoenbohm, L., Whipple, K., Burchfiel, B., and Chen, L. (2004). Geomorphic constraints on surface uplift, exhumation, and plateau growth in the Red River region, Yunnan Province, China. *Geological Society of America Bulletin*, 116(7-8):895–909.

Schoonman, C., White, N., and Pritchard, D. (2017). Radial viscous fingering of hot asthenosphere within the Icelandic plume beneath the North Atlantic Ocean. *Earth and Planetary Science Letters*, 468:51–61.

Schubert, G., Turcotte, D. L., and Olson, P. (2001). *Mantle convection in the Earth and planets*. Cambridge University Press.

Schultz, R. A. and Tanaka, K. L. (1994). Lithospheric-scale buckling and thrust structures on Mars: The Coprates rise and south Tharsis ridge belt. *Journal of Geophysical Research: Planets*, 99(E4):8371–8385.

Sclater, J. G. and Christie, P. A. (1980). Continental stretching: An explanation of the post-Mid-Cretaceous subsidence of the central North Sea Basin. *Journal of Geophysical Research: Solid Earth*, 85(B7):3711–3739.

Seeber, L. and Gornitz, V. (1983). River profiles along the Himalayan arc as indicators of active tectonics. *Tectonophysics*, 92:335–367.

Sen, B. and Sabale, A. (2011). Flow-types and lava emplacement history of Rajahmundry Traps, west of River Godavari, Andhra Pradesh. *Journal of the Geological Society of India*, 78(5):457–467.

Shaw Champion, M., White, N., Jones, S., and Lovell, J. (2008). Quantifying transient mantle convective uplift: An example from the Faroe-Shetland basin. *Tectonics*, 27(1).

Shorttle, O. and Maclennan, J. (2011). Compositional trends of Icelandic basalts: Implications for short–length scale lithological heterogeneity in mantle plumes. *Geochemistry, Geophysics, Geosystems*, 12(11).

Shorttle, O., Maclennan, J., and Jones, S. (2010). Control of the symmetry of plume-ridge interaction by spreading ridge geometry. *Geochemistry, Geophysics, Geosystems*, 11(7).

Sigmundsson, F., Vadon, H., and Massonnet, D. (1997). Readjustment of the Krafla spreading segment to crustal rifting measured by satellite radar interferometry. *Geophysical Research Letters*, 24(15):1843–1846.

Singh, A., Lanzoni, S., Wilcock, P. R., and Foufoula-Georgiou, E. (2011). Multiscale statistical characterization of migrating bed forms in gravel and sand bed rivers. *Water Resources Research*, 47(12).

Sinton, C. and Duncan, R. (1997). Potential links between ocean plateau volcanism and global ocean anoxia at the Cenomanian-Turonian boundary. *Economic Geology*, 92(7-8):836–842.

Sklar, L. and Dietrich, W. E. (1998). *River longitudinal profiles and bedrock incision models: Stream power and the influence of sediment supply*. Wiley Online Library.

Smith, D. E. and Zuber, M. T. (1996). The shape of Mars and the topographic signature of the hemispheric dichotomy. *Science*, 271(5246):184–188.

Smith, D. E., Zuber, M. T., Solomon, S. C., Phillips, R. J., Head, J. W., Garvin, J. B., Banerdt, W. B., Muhleman, D. O., Pettengill, G. H., Neumann, G. a., Lemoine, F. G., Abshire, J. B., Aharonson, O., Brown, C. D., Hauck, S. a., Ivanov, a. B., McGovern, P. J., Zwally, H. J., and Duxbury, T. C. (1999). The

global topography of Mars and implications for surface evolution. *Science (New York, N.Y.)*, 284(5419):1495–1503.

Smith, L. C., Alsdorf, D. E., Magilligan, F. J., Gomez, B., Mertes, L. A., Smith, N. D., and Garvin, J. B. (2000). Estimation of erosion, deposition, and net volumetric change caused by the 1996 Skeidharársandur jökulhlaup, Iceland, from synthetic aperture radar interferometry. *Water Resources Research*, 36(6):1583–1594.

Smith, W. and Wessel, P. (1990). Gridding with continuous curvature splines in tension. *Geophysics*, 55(3):293–305.

Smith, W. H. and Sandwell, D. T. (1997). Global sea floor topography from satellite altimetry and ship depth soundings. *Science*, 277(5334):1956–1962.

Solomon, S. C. and Head, J. W. (1982). Evolution of the Tharsis province of Mars - The importance of heterogeneous lithospheric thickness and volcanic construction. *Journal of Geophysical Research*, 87:9755–9774.

Som, S. M., Montgomery, D. R., and Greenberg, H. M. (2009). Scaling relations for large Martian valleys. *Journal of Geophysical Research: Planets*, 114(E2).

Spedding, N. and Evans, D. J. (2002). Sediments and landforms at Kvíárjökull, southeast Iceland: a reappraisal of the glaciated valley landsystem. *Sedimentary Geology*, 149(1-3):21–42.

Spice, H. E., Fitton, J. G., and Kirstein, L. A. (2016). Temperature fluctuation of the Iceland mantle plume through time. *Geochemistry, Geophysics, Geosystems*, 17(2):243–254.

Stephenson, S. N., Roberts, G. G., Hoggard, M. J., and Whittaker, A. C. (2014). A Cenozoic uplift history of Mexico and its surroundings from longitudinal river profiles. *Geochemistry, Geophysics, Geosystems*, 15(12):4734–4758.

Stixrude, L. and Lithgow-Bertelloni, C. (2005). Thermodynamics of mantle mineralsâĂŤI. Physical properties. *Geophysical Journal International*, 162(2):610–632.

Stock, J. D. and Montgomery, D. R. (1999). Geologic constraints on bedrock river incision using the stream power law. *Journal of Geophysical Research: Solid Earth*, 104(B3):4983–4993.

Stone, J. O. (2000). Air pressure and cosmogenic isotope production. *Journal of Geophysical Research: Solid Earth*, 105(B10):23753–23759.

Storey, M., Duncan, R. A., and Tegner, C. (2007). Timing and duration of volcanism in the North Atlantic Igneous Province: implications for geodynamics and links to the Iceland hotspot. *Chemical Geology*, 241(3-4):264–281.

Sturkell, E., Einarsson, P., Sigmundsson, F., Geirsson, H., Olafsson, H., Pedersen, R., de Zeeuw-van Dalfsen, E., Linde, A. T., Sacks, S. I., and Stefánsson, R. (2006). Volcano geodesy and magma dynamics in Iceland. *Journal of Volcanology and Geothermal Research*, 150(1-3):14–34.

Tackley, P. J., Xie, S., Nakagawa, T., and Hernlund, J. W. (2005). Numerical and laboratory studies of mantle convection: Philosophy, accomplishments, and thermochemical structure and evolution. *Earth's Deep Mantle: Structure, Composition, and Evolution*, 160(ii):83–99.

Tanaka, K. L. (1986). The stratigraphy of Mars. *Journal of Geophysical Research: Solid Earth*, 91(B13).

Tanaka, K. L., Dohm, J. M., Lias, J. H., and Hare, T. M. (1998). Erosional valleys in the Thaumasia region of Mars: Hydrothermal and seismic origins. *Journal of Geophysical Research: Planets*, 103(E13):31407–31419.

Tanner, W. F. (1971). The river profile. *The Journal of Geology*, 79(4):482–492.

Tarboton, D. G. (1997). A new method for the determination of flow directions and upslope areas in grid digital elevation models. *Water resources research*, 33(2):309–319.

Tentler, T. and Temperley, S. (2007). Magmatic fissures and their systems in Iceland: A tectonomagmatic model. *Tectonics*, 26(5).

Thiede, R., Sobel, E., Ballato, P., Gadoev, M., and Oimahmadov, I. (2014). Uplift and River Incision of the western Pamir Plateau - New insights from river-profile analysis and thermochronology. *Geophysical Research Abstracts*, 16(1):11864.

Thomas, J. (1996). The occurrence of the dinoflagellate cyst Apectodinium (Costa & Downie 1976) Lentin & Williams 1977 in the Moray and Montrose Groups (Danian to Thanetian) of the UK central North Sea. *Geological Society, London, Special Publications*, 101(1):115–120.

Thorarinsson, S. (1960). On the Geology and Geophysics of Iceland: Guide to Excursions 60. In *International Geological Congress, Reykjavik*.

Thorbergsson, G., Magnússon, I. T., and Pálmason, G. (1993). *Gravity data and a gravity map of Iceland*. Orkustofnun.

Thordarson, T. and Larsen, G. (2007). Volcanism in Iceland in historical time: Volcano types, eruption styles and eruptive history. *Journal of Geodynamics*, 43(1):118–152.

Tiley, R., McKenzie, D., and White, N. (2003). The elastic thickness of the British Isles. *Journal of the Geological Society*, 160(4):499–502.

Tomasson, H. (2002). Catastrophic floods in Iceland. *IAHS Publication*, pages 121–128.

Tomkeieff, S. I. (1940). The basalt lavas of the GiantâĂŹs Causeway district of Northern Ireland. *Bulletin volcanologique*, 6(1):89–143.

Torrence, C. and Compo, G. P. (1998). A practical guide to wavelet analysis. *Bulletin of the American Meteorological society*, 79(1):61–78.

Tryggvason, E. (1973). Seismicity, earthquake swarms, and plate boundaries in the Iceland region. *Bulletin of the Seismological Society of America*, 63(4):1327–1348.

Underhill, J. (2001). Controls on the genesis and prospectivity of Paleogene palaeogeomorphic traps, East Shetland Platform, UK North Sea. *Marine and Petroleum Geology*, 18(2):259–281.

Vandenberghe, N., Hilgen, F., Speijer, R., Ogg, J., Gradstein, F., Hammer, O., Hollis, C., Hooker, J., et al. (2012). The paleogene period. In *The geologic time scale*, pages 855–921. Elsevier.

Verhoeven, K., Louwye, S., Eiríksson, J., and De Schepper, S. (2011). A new age model for the Pliocene-Pleistocene Tjörnes section on Iceland: Its implication for the timing of North Atlantic-Pacific palaeoceanographic pathways. *Palaeogeography, Palaeoclimatology, Palaeoecology*, 309(1-2):33–52.

Vogt, P. (1971). Asthenosphere motion recorded by the ocean floor south of Iceland. *Earth and Planetary Science Letters*, 13(1):153–160.

Waitt, R. (2009). Great Holocene floods along Jökulsá á Fjöllum, north Iceland. *Flood and megaflood processes and deposits: recent and ancient examples. Int Assoc of Sed Spec Pub*, 32:37–51.

Webb, B. M. and Head III, J. (2002). Noachian tectonics of Syria Planum and the Thaumasia Plateau. In *Lunar and Planetary Science Conference*, volume 33.

Weissert, H. and Erba, E. (2004). Volcanism, CO2 and palaeoclimate: a Late Jurassic–Early Cretaceous carbon and oxygen isotope record. *Journal of the Geological Society*, 161(4):695–702.

Wenzel, M. J., Manga, M., and Jellinek, A. M. (2004). Tharsis as a consequence of Mars' dichotomy and layered mantle. *Geophysical research letters*, 31(4).

Whipple, K. X. and Tucker, G. E. (1999). Dynamics of the stream-power river incision model: Implications for height limits of mountain ranges, landscape response timescales, and research needs. *Journal of Geophysical Research: Solid Earth*, 104(B8):17661–17674.

Whipple, K. X. and Tucker, G. E. (2002). Implications of sediment-flux-dependent river incision models for landscape evolution. *Journal of Geophysical Research: Solid Earth*, 107(B2).

White, N. (1990). Does the uniform stretching model work in the North Sea. In *Tectonic evolution of the North Sea rifts*, volume 181, pages 217–239. Oxford University Press Oxford.

White, N. and Lovell, B. (1997). Measuring the pulse of a plume with the sedimentary record. *Nature*, 387(6636):888.

White, R., Bown, J., and Smallwood, J. (1995). The temperature of the Iceland plume and origin of outward-propagating V-shaped ridges. *Journal of the Geological Society*, 152(6):1039–1045.

White, R. and McKenzie, D. (1989). Magmatism at rift zones: the generation of volcanic continental margins and flood basalts. *Journal of Geophysical Research: Solid Earth*, 94(B6):7685–7729.

White, R. and McKenzie, D. (1995). Mantle plumes and flood basalts. *Journal of Geophysical Research: Solid Earth*, 100(B9):17543–17585.

Whittaker, A. C., Attal, M., Cowie, P. a., Tucker, G. E., and Roberts, G. (2008). Decoding temporal and spatial patterns of fault uplift using transient river long profiles. *Geomorphology*, 100(3-4):506–526.

Williams, R. M., Irwin III, R. P., and Zimbelman, J. R. (2009). Evaluation of paleohydrologic models for terrestrial inverted channels: Implications for application to martian sinuous ridges. *Geomorphology*, 107(3-4):300–315.

Wilson, J., Roberts, G., Hoggard, M., and White, N. (2014). Cenozoic epeirogeny of the Arabian Peninsula from drainage modeling. *Geochemistry, Geophysics, Geosystems*, 15(10):3723–3761.

Wolfe, C. J., Bjarnason, I. T., VanDecar, J. C., and Solomon, S. C. (1997). Seismic structure of the Iceland mantle plume. *Nature*, 385(6613):245.

Wordsworth, R. D. (2016). The climate of early Mars. *Annual Review of Earth and Planetary Sciences*, 44:381–408.

Wünnemann, K. and Ivanov, B. (2003). Numerical modelling of the impact crater depth–diameter dependence in an acoustically fluidized target. *Planetary and Space Science*, 51(13):831–845.

Wyllie, M. R. J., Gregory, A. R., and Gardner, L. W. (1956). Elastic wave velocities in heterogeneous and porous media. *Geophysics*, 21(1):41–70.

Zhang, H., Zhang, P., and Fan, Q. (2011). Initiation and recession of the fluvial knickpoints: A case study from the Yalu River-Wangtian'e volcanic region, northeastern China. *Science China Earth Sciences*, 54(11):1746.

Ziegler, P. A. (1992). European Cenozoic rift system. *Tectonophysics*, 208(1-3):91–111.